# Novel Cosmological Constraints on Dark Matter

by

Harrison Winch

A thesis submitted in conformity with the requirements
for the degree of Doctor of Philosophy

Department of Astronomy and Astrophysics
University of Toronto

Novel Cosmological Constraints on Dark Matter

Harrison Winch
Doctor of Philosophy

Department of Astronomy and Astrophysics
University of Toronto
2024

# Abstract

The nature of dark matter (DM) is one of the most significant unsolved problems in modern particle physics and cosmology. While we have overwhelming evidence for its existence through gravitational interactions with light and visible matter, the origins and particle nature of DM remain mysterious. This thesis involves three interrelated projects that aim to probe the fundamental particle nature of DM through novel tests of its structure on various scales. In the first project [210], we compute microlensing forecasts using the Vera Rubin Observatory, estimating future constraints on dark compact objects with various spherical and disk-like distributions within our galaxy. These forecasts allow us to probe models of dissipative and mirror-sector DM components at fractions of $\lesssim 10^{-4}$, and we illustrate the dependence of these constraints on the size and tilt of the "dark disk". In the second project [208], we develop a novel computational method for modeling extreme axions DM (axions with a large starting field angle) as a cosmological fluid, allowing for rapid calculation of the linear $z = 0$ matter power spectrum (MPS), and comparison to MPS estimates from the Lyman-$\alpha$ forest using the extended Baryonic Oscillation Spectroscopic Survey (eBOSS). We demonstrate that extreme axion models can alleviate axion constraints with a non-trivial range of starting angles, motivating and enabling a reevaluation of current cosmological constraints on axion DM. In the third project [209], we develop and implement a new test of mixed-axion DM using measurements of galaxy UV luminosities from the Hubble and James Webb space telescopes. By marginalizing over a parametric model connecting halo mass and UV luminosity, we can exclude a single axion as all the DM for $m_{\rm ax} < 10^{-21.6}$ eV and limit axions with $-26 \leq \log(m_{\rm ax}/{\rm eV}) \leq -23$ to be less than 22% of the DM (both at 95% confidence limit, or c.l.). These limits utilize UV data probing a previously unexplored range of high redshifts and small scales, ruling out a previously unconstrained region of axion DM parameter space. Throughout these projects, I have developed a number of innovative techniques, allowing us to model, forecast, and constrain exotic models of dark matter by comparing them to a variety of astronomical and cosmological observables, shedding light on the most mysterious substance in the universe.

For Grandpa,
for showing me the stars,
and
for Mr. van Bemmel,
for showing me how to get there.

# Acknowledgements

I would like to express my profound thanks to my supervisor, Renée Hložek, for letting me explore a series of semi-related forays into the uncharted wilds of dark matter theory. Thank you for showing me the way, either by zooming in with me to the intractable swamp of code debugging, or zooming out to remind ourselves of the bigger picture and goals for these projects. In the end, the journey has been fascinating, rewarding, and entirely worth the effort.

I would also like to thank my committee members, Gwen Eadie and David Curtin, for keeping me on track, and providing invaluable guidance on statistics, particle physics, and everything else. I also want to thank my co-authors (in roughly chronological order): Jo Bovy, Jack Setford, David J. E. Marsh, Daniel Grin, and Keir K. Rogers.

I acknowledge the financial support of NSERC from the CGS-Masters and CGS-Doctoral scholarships.

I also wish to acknowledge that the land on which the University of Toronto is built is the traditional territory of the Haudenosaunee, and most recently, the territory of the Mississaugas of the New Credit First Nation. We are grateful to have the opportunity to work in the community, on this territory.

Lastly, I would like to thank my family, Mom and Dad, and of course, my dearest wife Annie. I couldn't have done it without all of you.

# Contents

# Chapter 1

# Introduction

This thesis involves multiple projects developing novel tests of dark matter (DM) physics using astrophysics and cosmology. This includes forecasting microlensing constraints on dark compact objects in disk distributions, developing innovative computational methods for simulating extreme axion DM models, and computing constraints on mixed axion cosmologies using galaxy UV luminosities. This work draws a number of interdisciplinary connections between theoretical DM models and concrete astronomical and cosmological observables, developing multiple new tools to aid in our search for the nature of DM.

Before presenting the novel cosmological tests of DM, we first introduce some of the scientific background relating to both the theoretical DM cosmology and the astronomical observables that my work draws connections between. In Section 1.1 I provide some background on cosmology, going from the basics of general relativity in Section 1.1.1 to a description of background cosmological evolution in Section 1.1.2 and metric perturbations in Section 1.1.3. We then introduce the primary components of our cosmological model in Section 1.1.4, including baryons, radiation, dark matter, and dark energy, as well as describing their behaviour as homogeneous cosmic fluids in Section 1.1.5. These components can be combined under the assumptions of our homogeneous and isotropic background cosmology to write the Friedmann equations describing the evolution of a universe containing baryons, radiation, cold dark matter (CDM), and a cosmological constant ($\Lambda$), introduced in Section 1.1.6. This solution, sometimes referred to as the $\Lambda$CDM paradigm, is sufficient to describe the entire background evolution of the universe we live in.

All of these methods are useful in modeling the evolution of the universe at the background level, but it does not resolve some of the key mysteries of the universe, such as the nature of dark matter (DM). In Section 1.2, We provide some background on DM, introducing some of the key models investigated in my work. These include cold dark matter (CDM) in Section 1.2.1, ultralight axion DM in Section 1.2.2, and dark compact objects arising from dissipative or mirror-sector models of DM in Section 1.2.3.

In Section 1.3 I introduce some methods for computing the linear and nonlinear dynamics of DM overdensities, allowing us to make predictions for inhomogeneous cosmic structure on various scales and under various assumptions about the nature of DM. The perturbative dynamics of a scalar field are introduced in Section 1.3.1, while the effective fluid formalism for efficiently approximating a rapidly oscillating scalar field is presented in Section 1.3.2. These linear dynamics can be used to

compute cosmological observables, including the matter power spectrum (MPS) in Section 1.3.3, the halo mass function (HMF) in Section 1.3.4, and the distribution of dark compact objects (DCOs) in Section 1.3.5.

I then introduce some of the observational signatures used to probe these aspects of DM structure in Section 1.4, along with some of the telescopes and surveys that are conducting these observations. Section 1.4.1 introduces microlensing, and how it can be used to search for DCOs using the Legacy Survey of Space and Time (LSST) with the Vera Rubin Observatory. Section 1.4.2 introduces the Lyman-$\alpha$ forest and how it can be used to estimate the linear MPS using surveys like the extended Baryon Oscillation Spectroscopic Survey (eBOSS). Section 1.4.3 describes the UV luminosity function (UVLF), which can be measured using both the Hubble and James Webb space telescopes. And finally, Secion 1.4.4 introduces the Cosmic Microwave Background (CMB), as measured by the *Planck* space telescope. All of these telescopes and observables play an important role in testing theories of DM, and all of them play a role in this thesis.

Finally, Section 1.5 introduces some of the statistical tools I use to compare the theoretical DM models to cosmological observations. Section 1.5.1 gives an overview of Bayesian probability, defining the likelihood, prior, and posterior. Section 1.5.2 introduces some illustrative forms of the likelihood, including the chi-squared statistic ($\chi^2$), which is useful for approximately Gaussian likelihood distributions, and the Poisson distribution, which involves the frequency of random events, and is useful both in microlensing computations, as well as estimating the UV luminosity function. Section 1.5.3 introduces Markov-Chain Monte-Carlo (MCMC) methods for efficiently estimating the posterior distribution on a high-dimensional parameter space. Lastly, Section. 1.5.4 introduces the Akaike information criterion (AIC), which can be useful in distinguishing between competing models claiming to explain the same observation with differing numbers of parameters.

After introducing this background, we present the three papers that make up the body of this thesis. This includes forecasting microlensing constraints on disk distributions of DCOs using LSST in Chapter 2, modeling the dynamics of extreme axion DM in Chapter 3, and testing mixed axion cosmologies with the UV luminosity function (UVLF) in Chapter 4. Chapter 5 presents general conclusions from this work, along with a discussion of future research projects building on these results in order to shed further light on the nature of DM.

## 1.1 Relativistic Cosmology

Currently, all confirmed probes of Dark Matter (DM) physics occur through gravitational interactions. This section explains the basics of General Relativity and how it used to model the evolution of the structure and contents of the universe, both at a background level and at first-order perturbative fluid dynamics. We also introduce the components of the standard $\Lambda$ - cold dark matter ($\Lambda$CDM) cosmological model, and how a universe containing these components can be modeled at a background level.

### 1.1.1 General Relativity

In simple terms, Einstein's theory of General Relativity (GR) states that mass and energy both impact the curvature of nearby spacetime. When objects (or light) travel through these regions

of curved spacetime, their trajectories appear to curve, giving rise to the phenomenon we know as gravity.

Mathematically, this law can be written as the Einstein Field Equations (EFE),

$$R_{\mu\nu} - \frac{1}{2}Rg_{\mu\nu} + \Lambda g_{\mu\nu} = \frac{8\pi G}{c^4}T_{\mu\nu}, \tag{1.1}$$

where $g_{\mu\nu}$ is the spacetime metric tensor, $R_{\mu\nu}$ and $R$ are the Ricci tensor and scalar curvature (respectively) of the metric, $\Lambda$ is the cosmological constant, $G$ is the Newtonian gravitational constant, $c$ is the speed of light, and $T_{\mu\nu}$ is the stress-energy tensor. The metric tensor, $g_{\mu\nu}$ describes how the components of two vectors should be multiplied together to get the line element. This equation explains how the spacetime metric tensor ($g_{\mu\nu}$) reacts to the presence of matter or energy ($T_{\mu\nu}$), allowing us to solve for the shape of spacetime given a certain distribution of matter.

If we assume the Cosmological constant term can be incorporated into the stress-energy tensor as negative density, use natural units so $c \equiv 1$, and define the Einstein Tensor as,

$$G_{\mu\nu} = R_{\mu\nu} - \frac{1}{2}Rg_{\mu\nu}, \tag{1.2}$$

we can rewrite our EFE as

$$G_{\mu\nu} = 8\pi G T_{\mu\nu}. \tag{1.3}$$

### 1.1.2 Background Cosmology

For cosmological applications of GR, we assume that the spacetime solution is extremely close to a homogeneous, isotropic, time-dependent background solution (also known as the Friedmann-Robertson-Walker, or FRW, metric). This allows us to separate our systems of equations into background and perturbation components. The metric can be written as,

$$g_{\mu\nu} = g_{\mu\nu 0}(t) + g_{\mu\nu 1}(t, \mathbf{x}), \tag{1.4}$$

where $g_{\mu\nu 0}(t)$ is the background FRW metric which depends only on time $t$, and $g_{\mu\nu 1}(t, \mathbf{x})$ is the metric perturbation which depends on both time $t$ and location $\mathbf{x}$. The position, $\mathbf{x}$ is a 3-vector, which we denote with bold font for the duration of this introduction. We assume that the perturbations $g_{\mu\nu 1}$ and its derivatives are all small, and assume that the background solution is spatially flat. This flatness assumption can be violated in some cosmological analysis, but we will assume flatness for computational simplicity, and since it appears to agree with current observations. The convention of using subscripts of 0 and 1 for the background and first-order perturbations will be used throughout this work.

This separation allows us to write the EFE as,

$$G_{\mu\nu 0} = 8\pi G T_{\mu\nu 0} \tag{1.5}$$

$$G_{\mu\nu 1} = 8\pi G T_{\mu\nu 1}, \tag{1.6}$$

where the background (subscript 0) and first-order perturbations (subscript 1) can be solved separately.

The assumptions of homogeneity and isotropy at a background level allow the background space-

time metric to be written as,

$$ds^2 = g_{\mu\nu 0} dx^\mu dx^\nu = -dt^2 + a^2(t) d\mathbf{x}^2, \tag{1.7}$$

where $a(t)$ is the scale factor describing the scale of the universe at time $t$, scaled such that the value of $a_{\text{today}} = 1$. Under these assumptions, the background EFE can be used to derive the Friedmann equations for the evolution of $a(t)$,

$$\left(\frac{\dot{a}}{a}\right)^2 = H^2 = \frac{8\pi G}{3}\rho \tag{1.8}$$

$$\frac{\ddot{a}}{a} = -\frac{4\pi G}{3}(\rho + 3P), \tag{1.9}$$

where dots represent derivatives with respect to time $t$, $H$ represents the Hubble parameter describing the expansion rate of space time (defined as $H \equiv \dot{a}/a$) and $\rho$ and $P$ are the average density and pressure of the contents of the universe, respectively. Again, we are defining density and pressure perturbatively, so $\tilde{\rho}(t, \mathbf{x}) = \rho(t) + \delta\rho(t, \mathbf{x})$ and $\tilde{P}(t, \mathbf{x}) = P(t) + \delta P(t, \mathbf{x})$, where $\rho$ and $P$ are the average density and pressure at time $t$, while $\delta\rho$ and $\delta P$ represent inhomogeneous perturbations that are assumed to be small relative to the background values.

It will also be useful for our purposes to use conformal time $\tau$ where

$$d\tau = \frac{dt}{a(t)}, \tag{1.10}$$

such that the conformal time at a given physical time $t$ can be written as,

$$\tau = \int_0^t \frac{dt'}{a(t')} \tag{1.11}$$

Conformal time is related to real time, $t$, but also scales with the past expansion of spacetime, $a$. In technical terms, it is the amount of time it would take a photon to travel from where we are located to the furthest observable distance, provided the universe ceased expanding. We will use apostrophes ($'$) to represent derivatives with respect to conformal time. The conformal Hubble parameter can be written as,

$$\mathcal{H} \equiv \frac{a'}{a} = aH = \dot{a}. \tag{1.12}$$

We can also relate the scale factor to cosmological redshift of photons, which occurs due to the "stretching" of photon wavelengths due to cosmic expansion. Redshift can be defined as,

$$z = \frac{\lambda_{\text{obs}} - \lambda_{\text{emit}}}{\lambda_{\text{emit}}}, \tag{1.13}$$

where $\lambda_{\text{obs}}$ and $\lambda_{\text{emit}}$ are the observed and emitted wavelengths of light, respectively. The wavelength of a photon observed today (when the scale factor $a = 1$), is longer than when it was emitted by a factor of $1/a_{\text{emit}}$. Therefore, we can relate scale factor and redshift by,

$$a = \frac{1}{1+z}. \tag{1.14}$$

This means we can refer to earlier cosmic times (lower $a$) as "higher redshift", and vice versa.

### 1.1.3 Metric Perturbations and the Synchronous Gauge

At the level of the first-order perturbations, $g_{\mu\nu 1}$, there is some freedom in selecting how the space and time metric perturbations are defined. This choice is known as the choice of gauge. Most of our work is conducted in the Synchronous Gauge, which is defined as the gauge such that $g_{001} = g_{0i1} = 0$ (where $i$ and $j$ are indices over the spatial dimensions), so all metric perturbations are in the portion of the spacetime metric tensor describing the curvature of space (as opposed to time),

$$g_{\mu\nu 1} = 0_{\mu\nu} + h_{ij}. \tag{1.15}$$

This spatial metric perturbation, $h_{ij}$, can be decomposed into its trace, $\beta \equiv h_{ii}$, and three traceless components, $h^{||}_{ij}$, $h^{\perp}_{ij}$, and $h^{T}_{ij}$, such that,

$$h_{ij} = \beta\delta_{ij}/3 + h^{||}_{ij} + h^{\perp}_{ij} + h^{T}_{ij}, \tag{1.16}$$

and,

$$\epsilon_{ijk}\partial_j\partial_l h^{||}_{lk} = 0 \tag{1.17}$$

$$\partial_i\partial_j h^{\perp}_{ih} = 0 \tag{1.18}$$

$$\partial_i h^{T}_{ij} = 0. \tag{1.19}$$

Therefore, we can write $h^{||}_{ij}$ in terms of some scalar field $\mu$, such that,

$$h^{||}_{ij} = \left(\partial_i\partial_j - \frac{1}{3}\delta_{ij}\nabla^2\right)\mu, \tag{1.20}$$

and write $h^{\perp}_{ij}$ in terms of some divergenceless vector $A_i$, such that,

$$h^{\perp}_{ij} = \partial_i A_j + \partial_j A_i. \tag{1.21}$$

Therefore, we can describe our metric perturbations in the synchronous gauge entirely in terms of two scalars ($\beta$ and $\mu$), one vector ($A_i$), and one tensor ($h_{ij}$).

### 1.1.4 The Contents of the Universe

Up until this point, we have been discussing the properties of the spacetime metric in a largely homogeneous and isotropic cosmology without specifying the contents of the universe. However, the evolution of both the background and perturbations of the cosmology depend on the nature of the contents of the universe. Each of the major cosmological components included in our model are introduced below.

#### Baryons

The Standard Model of particle physics is a description of all the forms of matter we have detected on Earth. It includes multiple classes of leptons (including the electron and the neutrinos) as well

as quarks (which can combine to form neutrons and protons, and other exotic combinations). The Standard Model also describes the possible interactions between these particles, including via the electromagnetic force (with a force mediator known as a "photon", or a light particle), as well as gluons mediating the strong nuclear force, and W and Z bosons mediating the weak nuclear force. Lastly, the Standard Model includes the Higgs boson, which represents excitations of the Higgs field which gives mass to all other particles. The standard model does a good job of explaining almost all particle phenomena we observe on Earth – however, it fails to include any explanation of dark matter, discussed more below and in Section 1.2, which we know to make up the majority of matter in the universe.

In cosmology, we use the term "baryons" to refer to all non-relativistic forms of matter that fit into the Standard Model (SM) of particle physics. This is because true "baryons" (groups of three bound quarks, which include neutrons and protons) make up the majority of the mass of standard matter in the Universe. Therefore, this category includes all forms of atomic and molecular gas, dust, stars, planets, and so on that are formed from non-relativistic SM particles.

#### Radiation

Radiation refers to all forms of relativistic particles and force mediators in the universe. The most prominent example of a radiation component is the photon, although some forms of light neutrino species, gravitational waves, or hypothetical forms of dark radiation beyond the Standard Model would also be included in this category.

#### Dark Matter

Dark matter (DM) refers to the massive gravitationally-interacting substance in our universe that does not appear to interact with light or baryonic matter through the strong, weak, or electromagnetic forces. As explained in Section 1.2, the exact nature of DM is unknown. Although DM could be composed of certain forms of SM matter (such as black holes or exotic quark nuggets), most models involve some additional particle or form of matter beyond the standard model of particle physics. The most prominent model of DM is that of cold DM (discussed in Section 1.2.1), where DM is assumed to be a new non-relativistic, massive, and completely non-interacting particle. However, this thesis involves investigations of a number of alternative DM models, which are discussed in more detail in Sections 1.2.2 and 1.2.3.

#### Dark Energy

Due to the observed acceleration of spacetime, the universe is believed to also contain a mysterious force known as dark energy (DE). Like DM, there are many hypothetical models of what DE could be, but its true nature remains unknown. In this work, we assume DE to be a cosmological constant, $\Lambda$, of the same form that appeared in the Einstein Field Equations of GR, Eq. (1.1). This means that the energy density of DE would remain constant with time, regardless of the expansion of spacetime. This is a popular default model in cosmology, and, when combined with the cold DM (CDM) model, this default cosmology is often refereed to as $\Lambda$CDM. This $\Lambda$CDM model does not make any claims about the fundamental nature of either DM or DE, but it is able to describe their behaviour and match current data with minimal complexity in the model.

### 1.1.5 Cosmic fluid dynamics

In order to understand the growth of structure under different DM models, we need to model the density evolution of different cosmic components at both a background and perturbative level. In this section, we will start with the background density evolution, and then move on to the evolution of the perturbations.

The average background density changes as the universe expands, but it also changes more at high density or pressure. This can be summarized by the continuity equation, which can be derived from the Friedmann equations (Equation (1.8)) and written in conformal coordinates as

$$\rho' = -3\mathcal{H}(\rho + P). \tag{1.22}$$

This equation is true for total density, as well as the densities for each cosmological component (DM, baryons, etc.). We will denote variables associated with different cosmological components by the subscript $X$, where $X = \mathrm{c}$ refers to CDM (discussed more in Section 1.2.1), $X = \mathrm{a}$ refers to axions or axion-like particles (discussed more in Section 1.2.2), and $X = \mathrm{b}$ refers to baryons.

In order to relate the pressure and density of a given cosmological component, it will also be useful to define two background quantities that describe the behaviour of a given cosmological component. These two quantities are the equation of state parameter,

$$w_X \equiv \frac{P_\mathrm{X}}{\rho_\mathrm{X}}, \tag{1.23}$$

and the adiabatic sound speed squared,

$$c^2_{\mathrm{ad}X} \equiv \frac{\dot{P}_\mathrm{X}}{\dot{\rho}_\mathrm{X}} = \frac{P'_\mathrm{X}}{\rho'_\mathrm{X}}. \tag{1.24}$$

In order to solve Eq (1.8) (the Friedmann equations) for the background evolution of the universe, we need to understand how the average density, $\rho$, varies with the scale factor, $a$. This depends on the nature of the dominant component in the universe at any given time. If we assume the universe is dominated by a single component $X$, we can rewrite Eq. (1.22) as,

$$\frac{d\rho_\mathrm{X}}{d\tau} = -3\frac{\frac{da}{d\tau}}{a}\rho_\mathrm{X}(1 + w_\mathrm{X}). \tag{1.25}$$

This can be rearanged into,

$$\frac{d\rho_\mathrm{X}}{\rho_\mathrm{X}} = -3(1 + w_\mathrm{X})\frac{da}{a}. \tag{1.26}$$

We can then integrate both sides to get

$$\ln(\rho_\mathrm{X}) = -3(1 + w_\mathrm{X})\ln(a) + C \tag{1.27}$$

which can be simplified into,

$$\rho_\mathrm{X} = \rho_{\mathrm{X}0}a^{-3(1+w_\mathrm{X})}, \tag{1.28}$$

where $\rho_{\mathrm{X}0}$ is the density of component $X$ today (at $a = 1$). This tells us how the densities of different cosmological components vary with cosmic expansion. For example, dust, baryons, and many DM

| Component | Subscript | $w_X$ | $\rho_X(a)$ |
|---|---|---|---|
| Baryons | b | 0 | $\propto a^{-3}$ |
| Radiation | r | 1/3 | $\propto a^{-4}$ |
| Cold Dark Matter | c | 0 | $\propto a^{-3}$ |
| Cosmological Constant | $\Lambda$ | -1 | $\propto a^{0}$ |

Table 1.1: The primary components of the ΛCDM cosmology, as introduced in Section 1.1.4. The $w_X$ column shows the equation of state parameter, $w_X = P_X/\rho_X$ for each component, while the $\rho_X(a)$ column shows the evolution of the background density of that component with scale factor, as computed using Eq. (1.28).

models (including cold dark matter, introduced in Section 1.2.1) have zero pressure, meaning that $w_c = 0$, so,

$$\rho_{\rm c}(a) = \rho_{\rm c0} a^{-3}. \tag{1.29}$$

Physically, this can be understood as the energy density of a pressureless substance (such as dust) diluting with volume, which scales as the cube of the scale factor.

Different cosmological components will behave differently, with different equation of state parameters and different background density evolution. The properties of the different components introduced in Section 1.1.4 are summarized in Table 1.1.

### 1.1.6 The Friedmann Equation in ΛCDM

Now that we have introduced the primary cosmological components, and their dependence on scale factor, we can rewrite the Friedmann equation Eq. (1.8) as

$$H^2 = \frac{8\pi G}{3} \sum_X \rho_{X0} a^{-3(1+w_X)}. \tag{1.30}$$

This is often rewritten to be in terms of the densities of the different cosmological components today relative to the critical density required for a flat universe,

$$\rho_{\rm crit} = \frac{3H^2}{8\pi G}, \tag{1.31}$$

This allows us to write the fractional density of component $X$ today as,

$$\Omega_X = \frac{\rho_{X0}}{\rho_{\rm crit,0}} = \frac{8\pi G \rho_{X0}}{3H_0^2}. \tag{1.32}$$

Therefore, the Friedmann equation can be written with the ΛCDM cosmological components from Table 1.1 as,

$$H^2 = H_0^2 \left[ (\Omega_b + \Omega_c) a^{-3} + \Omega_r a^{-4} + \Omega_\Lambda \right] \tag{1.33}$$

where

$$\sum_X \Omega_X = 1 \tag{1.34}$$

in a flat universe. This equation efficiently describes the background evolution and expansion of a flat, homogenous, isotropic universe containing baryons, CDM, radiation, and a cosmological constant, which appears to describe our universe at a background level.

## 1.2 Dark Matter Models

Dark matter (as introduced in Section 1.1.4) is a general term for a massive invisible component in our universe which interacts with other forms of matter via gravity but apparently not via the other three fundamental forces (strong, weak, and electromagnetic). There are numerous pieces of evidence for the existence of DM, including galaxy rotation curves [21], gravitational lensing [4], the growth of structure [165], and the cosmic microwave background [9]. Many of these pieces of evidence are discussed in more detail in the section on astronomical observables, including gravitational lensing in Section 1.4.1, the growth of structure in Sections 1.3.3 and 1.3.4, and the cosmic microwave background in Section 1.4.4. Studying the inferred distribution and structure of DM in our universe can help to distinguish between different DM models. Furthermore, multiple models of DM may be correct, and the DM we observe could be combination of two or more different types. These multi-component models of DM are sometimes referred to as mixed DM. In this section, we introduce some of the DM models studied in this thesis, including cold dark matter (CDM), ultralight axions (ULAs), and mirror sector DM.

### 1.2.1 Cold Dark Matter

CDM describes a class of DM models consisting of non-relativistic particles that interact only via gravitational forces (i.e. they do not interact with photons, baryons, or themselves). Since these CDM particles are pressureless, non-relativistic and non-interacting, their cosmic energy density dilutes only by the volume factor ($\rho_c \propto a^{-3}$, as shown in Eq. (1.29)). The growth of structure in CDM models can be explained entirely through gravitational interactions, either with linear perturbation theory (introduced in Section 1.1), models of non-linear halo collapse (described in Section 1.3.4), or N-body simulations (including the IllustrisTNG [150] and THESAN [110] simulations).

The CDM paradigm has been shown to match many observational probes of DM structure. These include measurements of the CMB [9], large scale structure [165], and galaxy rotation curves [21]. In addition, it is theoretically simple, with minimal novel mechanisms or extensions to the SM (only one new massive particle, and no new force carriers). For these reasons, CDM is treated as the default description of DM by much of the cosmology community, and is used as the fiducial model in simulations and descriptions of structure formation. However, it is important to note that the CDM paradigm can encompass a wide range of models and mechanisms by which these particles are created, and purely astrophysical measurements of CDM cannot distinguish between non-interacting CDM-like models. Instead, the CDM paradigm simply describes the minimal astrophysical properties of DM that fit the data (ie. being non-relativistic and only interacting via gravity). This means that many models of DM could look like CDM in certain regions of parameter space. For example, ultralight axions (described in Section 1.2.2) with a sufficiently high particle mass would be virtually indistinguishable from CDM. In addition, a variety of well-motivated weakly interacting massive particles (WIMPs) with low interaction cross-sections would manifest astrophysically as CDM.[1]

[1]Note that WIMPs with higher cross-sections can be constrained by observables such as the CMB [193, 132].

### 1.2.2 Ultralight axions

Ultralight axions and axion-like particles (with masses $m_{\rm ax} \lesssim 10^{-18}$ eV) are a class of well-motivated dark matter particle candidates that provide a compelling alternative to the CDM paradigm and a possible explanation for the theoretical origins of DM. The term axion was originally proposed to describe a pseudo-Nambu-Goldstone boson arising from a broken Peccei-Quinn symmetry in quantum chromodynamics (QCD)[157, 205, 206, 24, 63]. A Nambu-Goldstone boson arises from a periodic degree of freedom associated with a broken symmetry, while a pseudo-Nambu-Goldstone boson has some irregularity in its period degree of freedom, resulting in a preferred region of the periodic loop with a slightly lower field potential and a low but non-zero particle mass. However, since the proposal of the QCD axion, axion-like particles (ALPs) have been found to arise from broken symmetries more generally, and are produced naturally from a variety of string theories as a result of compactified higher dimensions [64, 163, 2, 195, 68, 18, 135, 6]. While the QCD axion involves a particular coupling to the electromagnetic field, ALPs do not require such a coupling, allowing them to be a purely dark particle that interacts with the standard model only via gravitation. These particles are therefore not only a compelling DM candidate, but also a powerful probe of string theory and high-energy physics. Throughout this work, we will use axion and ALP interchangeably to refer to this broad class of low-mass pseudo-Nambu-Goldstone boson DM candidates.

The extremely flat pseudo-Nambu Goldstone field potential gives axions a very low particle mass $m_{\rm ax}$, potentially on the order of $10^{-22}$ eV.[2] This low mass results in a de Broglie wavelength that manifests on astrophysical scales. This de Broglie wavelength smooths out structure below the axion Jeans scale $\lambda_J$, which depends on the axion particle mass as $\propto m_{\rm ax}^{-1/2}$ [15, 68, 18, 155, 90, 135, 99, 117]. High mass axions would have a very small Jeans scale, resulting in them looking effectively like CDM on all but the smallest scales. The astrophysical (roughly kpc to Gpc) scale of these axion wave features necessitates the use of cosmological observables in order to search for their effects. These searches often constrain both the axion particle mass and the axion DM fraction ($f_{\rm ax} = \Omega_{\rm ax}/\Omega_{\rm DM}$) through their observational signatures [90, 135, 112, 117, 171, 170]. The discovery of a subdominant DM fraction of axions would have profound implications for fundamental physics. Indeed, many axion DM models motivated by string theory propose a range of axion particle masses existing simultaneously (sometimes called the 'string axiverse', see [18, 136, 81]). Some of these particles (such as the QCD axion, see [157, 205, 206, 24, 63]) would manifest as a CDM component when the axions have sufficiently high mass. Therefore, it is relevant to consider models of mixed DM consisting of both a primary CDM-like component as well as an ultralight axion-like subcomponent at fractions of 10% or less.

Large-scale (ie. tens of megaparsecs and larger) measurements of the CMB and galaxy clustering have put tight constraints on the axion fraction for low-mass ($m_{\rm ax} \leq 10^{-25}$ eV) axions [90, 89, 117, 171]. Small-scale measurements of the Lyman-$\alpha$ forest (explained in more detail in Section 1.4.2) rule out higher-mass ($10^{-23}$ eV $\lesssim m_{\rm ax} \lesssim 10^{-20}$ eV) axions at higher DM fractions [101, 112, 169]. Analyses of the kinematics of dwarf galaxies have claimed to rule out axions with mass of $m_{\rm ax} = 10^{-19}$ eV as 100% of the DM [137, 60]. Other low-$z$ astrophysical probes of axions include galaxy weak lensing [62], galaxy strong lensing [187], galaxy rotation curves [21] and supermassive

[2] For a rough sense of scale, this means that the mass of an axion ($\sim 10^{-22}$ eV) is to the mass of an electron ($\sim 10^{6}$ eV) what the mass of an electron is to the mass of a basketball (50 g $\approx 10^{35}$ eV), which is roughly what the mass of a basketball is to the mass of the moon ($10^{26}$ g $\approx 10^{58}$ eV).

black holes [61]. Future 21-cm measurements also have the potential to detect signatures of axion DM at high redshift [197, 5, 95, 75, 125]. A joint analysis of CMB (see Section 1.4.4) and Lyman-$\alpha$ forest measurements from the Extended Baryon Oscillation Spectroscopic Survey [eBOSS; 11] finds that a non-zero axion density ($m_{\rm ax} \sim 10^{-25}\,$eV) alleviates an apparent tension in measurements of the small-scale power [170], while respecting existing limits. Axions of intermediate mass ($m_{\rm ax} \sim 10^{-25}\,$eV) are also found to address the $S_8$ cosmological parameter discrepancy [171].

In conclusion, there are many sophisticated ways of probing the unique observational signature of axion DM. However, there are still many regions of axion parameter space that remain unexplored. Finally, the tantalizing hints at axion signatures from observables such as the Ly-$\alpha$ forest motivate a further examination of axion DM astrophysics, testing a variety of unexplored scales and redshifts. One such exploration is introduced in Chapter 4.

### 1.2.3 Mirror Sector Dark Matter

Another interesting class of DM models that we consider in my thesis are models of *dissipative* dark matter, i.e., dark matter that emits dark radiation and can therefore cool efficiently. Similarly to how baryonic matter can cool via electromagnetic radiation and form into compact structures including stars and galaxies, dissipative dark matter can cool via a dark analogue to radiation (sometimes called dark radiation or a "dark photon"), which standard CDM models are incapable of doing. In most models, dissipative dark matter is constrained to be only a subcomponent, making up at most around 5-10% of the total dark matter density [74, 59, 45]. Dissipative dark matter can form radically different structures compared to ordinary CDM; for instance, it can cool to form a *dark disk* of DM and dark compact objects, in analogy to the baryonic disk of our own Galaxy [74, 73, 114, 115].

One well-motivated example of dissipative DM arises in the Mirror Twin Higgs framework [44] with asymmetric reheating [47, 53]. This model is representative of a broad class of "neutral naturalness" solutions to the little hierarchy problem, which refers to the fact that quantum corrections destabilize the mass of the Higgs boson in the standard model, as introduced in Section 1.1.4. This problem motivates the existence of new particles to cancel those quantum corrections (see [139, 56] for a review). The Mirror Twin Higgs hypothesis proposes a separate "mirror sector" of particles, similar to our own SM. Due to a larger Higgs Vacuum Expectation Value (VEV) in the mirror sector, fundamental particles in the mirror sector would all be more massive than their SM counterparts, by a factor of between ∼3-7 in the simplest and most natural models. This mass enhancement is a free parameter of the model that can be constrained either by Higgs decay measurements in collider experiments [39] or by searching for astrophysical signatures of mirror baryons [46]. These mirror sector particles mostly interact with themselves, being endowed with the dark equivalents of electromagnetism and nuclear physics, and acting effectively like a small self-interacting and dissipative sub-component of DM. As discussed in Section 1.3.5, a dissipative DM component can form dark compact objects – in the case of Mirror Sector DM these objects are referred to as "Mirror Stars", as they would likely behave much the same way as baryonic stars, only using the dark equivalents of hydrogen, helium, photons, and so forth. The creation of these dark compact objects is discussed in more detail in Section 1.3.5, and the prospects of future observational constraints are introduced in Chapter 2.

## 1.3 Dark Matter Structure

Utilizing the framework of linear cosmological perturbation theory explained in Section 1.1, we can now build up our models of DM structure on different scales, allowing us to compute various observables for different DM models in both linear and non-linear regimes.

### 1.3.1 Scalar field wave dynamics

Many DM models (particularly ultralight axions, explained in Section 1.2.2) can be modeled as a scalar field in our cosmology. This scalar field $\phi$ has a Lagrangian of the form,

$$\mathcal{L} = -\frac{1}{2}(\partial\phi)^2 - V(\phi), \tag{1.35}$$

where $\partial\phi$ refers to the vector of the partial derivative of $\phi$ along all three spatial dimensions plus time, and $V(\phi)$ is some field potential. For now, we will keep $V(\phi)$ in its general form, although specific forms of the potential will become relevant later. For example, the axion field (as introduced in Secion 1.2.2) has a period potential of the form,

$$V_{\rm a}(\phi_{\rm a}) = m_{\rm a}^2 f_{\rm a}^2[1 - \cos(\phi_{\rm a}/f_{\rm a})], \tag{1.36}$$

where $f_{\rm a}$ is the axion decay constant describing the scale of the periodicity, and $m_{\rm a}$ is the axion particle mass describing the curvature of the potential near the minimum. When $\phi_{\rm a} \approx 0$, we can Taylor expand to get,

$$V_{\rm a}(\phi_{\rm a}) \approx m_{\rm a}^2\phi_{\rm a}^2/2. \tag{1.37}$$

This quadratic form of the potential is conveniently used for many cosmic scalar fields that are assumed to be close to a potential minimum, simplifying some analysis. However, it is prudent to remember that scalar fields like the axion may start with a variety of starting values close to either a minimum or maximum in the periodic field potential, and that evolution far from the quadratic regime may look substantially different. One approach to modeling these anharmonic starting field angles is presented in Chapter 3.

#### Background Scalar Field Dynamics

As with the spacetime metric tensor (explained in Section 1.1.3), we can separate our scalar field into background and perturbation components,

$$\phi(\tau, \mathbf{k}) = \phi_0(\tau) + \phi_1(\tau, \mathbf{k}), \tag{1.38}$$

where the background $\phi_0$ depends only on conformal time $\tau$ (defined in Equation (1.10)), and the small perturbations $\phi_1$ depends on both $\tau$ and co-moving Fourier spatial wavenumber, $\mathbf{k}$.

At the background level, we can use variation of our scalar field Lagrangian to write the stress-energy tensor $T_{\mu\nu}$ and use the components of that to derive expressions for the average density and

pressure of our field,

$$\rho_\phi = \frac{a^{-2}}{2}\dot{\phi}_0^2 + V(\phi_0) \tag{1.39}$$

$$P_\phi = \frac{a^{-2}}{2}\dot{\phi}_0^2 - V(\phi_0). \tag{1.40}$$

We can also derive the equation of motion for the evolution of the background field,

$$\ddot{\phi}_0 + 2\mathcal{H}\dot{\phi}_0 + a^2 V'(\phi_0) = 0, \tag{1.41}$$

where $V'(\phi_0) = \frac{\partial V}{\partial \phi}\big|_{\phi_0}$ is the first derivative of the field potential computed at the average background field value $\phi_0$.

We can use these definitions of density and pressure along with this equation of motion to re-derive Eq.(1.22). To do this, we take the time derivative of our expression for $\rho_\phi$ and cancel out the terms corresponding to the equation of motion:

$$\dot{\rho}_\phi = -a^{-2}\mathcal{H}\dot{\phi}_0^2 + a^{-2}\dot{\phi}_0\ddot{\phi}_0 + V'(\phi_0)\dot{\phi}_0 \tag{1.42}$$

$$= a^{-2}\dot{\phi}_0\big[-3\mathcal{H}\dot{\phi}_0 + 2\mathcal{H}\dot{\phi}_0 + \ddot{\phi}_0 + a^2 V'(\phi_0)\big] \tag{1.43}$$

$$= a^{-2}\dot{\phi}_0[-3\mathcal{H}\dot{\phi}_0 + 0] \tag{1.44}$$

$$= -3\mathcal{H}(a^{-2}\dot{\phi}_0^2) \tag{1.45}$$

$$= -3\mathcal{H}(\rho_\phi + P_\phi). \tag{1.46}$$

We can also find how the scalar field energy density, given in Eq. (1.39), varies with scale factor, $a$, using Eq. (1.28). At early times, when $2\mathcal{H}\dot{\phi}_0 \gg a^2 V'(\phi_0)$, the field will remain effectively "fixed" at a specific value, resulting in the potential energy $V(\phi)$ being dominant over the kinetic energy $\frac{a^{-2}}{2}\dot{\phi}_0^2$. This means that, at early times,

$$w_\phi = \frac{P_\phi}{\rho_\phi} = \frac{\frac{a^{-2}}{2}\dot{\phi}_0^2 - V(\phi_0)}{\frac{a^{-2}}{2}\dot{\phi}_0^2 + V(\phi_0)} \approx -1, \tag{1.47}$$

and therefore,

$$\rho_\phi \propto a^{-3(1+w_\phi)} = a^0. \tag{1.48}$$

In other words, fixed scalar fields at early times evolve like a cosmological constant.

However, at late times, the scalar field will have decayed into the minimum of the field potential. We can approximate the potential near this minimum as quadratic, and the oscillations of the backgorund field as harmonic, allowing us to use the equipartition of energy to conclude that the potential and kinetic energy terms at late times should be equal. Therefore, we can assume that $V(\phi) \approx \frac{a^{-2}}{2}\dot{\phi}_0^2$ such that at late times $P_\phi \approx 0$ and $w_\phi \approx 0$. From this, we can conclude that,

$$\rho_\phi \propto a^{-3(1+w_\phi)} = a^{-3}. \tag{1.49}$$

Therefore, a scalar field at late times that has decayed into a potential minimum behaves behaves like pressureless cold dark matter on an average background level, as in Eq. (1.29).

### Scalar Field Perturbations

The field perturbations $\phi_1$ evolve according to their own equations of motion (in the synchronous gauge) which can be derived from varying the Lagrangian to be,

$$\ddot{\phi}_1 + 2\mathcal{H}\dot{\phi}_1 + \big(a^2 V''(\phi_0) + k^2\big)\phi_1 = -\frac{1}{2}\dot{\phi}_0\dot{\beta}, \tag{1.50}$$

where $k = |\mathbf{k}|$ is the amplitude of the comoving Fourier wavenumber, and $\beta$ is the trace of the scalar metric perturbations (see Section 1.1.3 on the synchronous gauge).

We can also derive expressions for the density and pressure perturbations of our scalar field from the stress energy tensor:

$$\delta\rho_\phi = a^{-2}\big(\dot{\phi}_0\dot{\phi}_1 - \dot{\phi}_0^2 A\big) + V'(\phi_0)\phi_1 \tag{1.51}$$

$$\delta P_\phi = a^{-2}\big(\dot{\phi}_0\dot{\phi}_1 - \dot{\phi}_0^2 A\big) + V'(\phi_0)\phi_1 \tag{1.52}$$

$$(\rho_\phi + P_\phi)(v_\phi - B) = a^{-2}k\dot{\phi}_0\phi_1 \tag{1.53}$$

where $A$ and $B$ are the scalar potential and vector perturbations in the synchronous gauge, respectively, and $v_\phi$ is the fluid velocity.

In the comoving synchronous gauge (chosen such that $\dot{\phi}_1 = 0$), we can use the above equations combined with background and perturbation equations of motion to derive equations of motion for the density perturbations $\delta_\phi = (\delta\rho_\phi)/\rho_\phi$, along with the coupled equations of motion for the dimensionless heat flux $u_\phi = (1 + w_\phi)v_\phi$. These equations of motion are as follows:

$$\dot{\delta}_\phi = -ku_\phi - (1 + w_\phi)\dot{\beta}/2 - 3H(1 - w_\phi)\delta_\phi - 9\mathcal{H}^2(1 - c^2_{\mathrm{ad}\phi})u_\phi/k \tag{1.54}$$

$$\dot{u}_\phi = 2\mathcal{H}u_\phi + k\delta_\phi + 2\mathcal{H}(w_\phi - c^2_{\mathrm{ad}\phi})u_\phi. \tag{1.55}$$

Therefore, we can model the evolution of overdensities of a scalar field as a cosmic fluid once we compute the values of $w_\phi$ and $c^2_{\mathrm{ad}\phi}$ from the background solution.

## 1.3.2 The Effective Fluid Formalism

The above system of equations is analytically exact and computationally feasible for slowly varying scalar fields. However, when a scalar field is rapidly oscillating (at late times, when Hubble friction is lower), integrating over these rapid oscillations with a large seperation of time scales can be computationally prohibitive. Therefore, it will become necessary to average over these rapid oscillations and model the field perturbations as an effective fluid. During this period of rapid oscillations, the equation of state parameter and adiabatic sound speed of the scalar field both average to zero, and the behaviour of the effective fluid can instead be modeled by the effective fluid sound speed,

$$c^2_{\mathrm{ef}} \equiv \frac{\delta P}{\delta\rho}, \tag{1.56}$$

so the equations of motion become,

$$\dot{\delta}_\phi = -ku_\phi - \frac{\dot{\beta}}{2} - 3\mathcal{H}^2 c_{\rm ef}^2 \delta_\phi - 9\mathcal{H}^2 c_{\rm ef}^2 u_\phi/k \tag{1.57}$$

$$\dot{u}_\phi = -\mathcal{H}u_\phi + c_{\rm ef}^2 k\delta_\phi + 3c_{\rm ef}^2 \mathcal{H}u_\phi. \tag{1.58}$$

In the case of uniform harmonic oscillations of the background field, the effective fluid sound speed can be approximated as,

$$c_{\rm ef}^2 \simeq \frac{k^2/(4m_\phi^2 a^2)}{1 + k^2/(4m_\phi^2 a^2)}, \tag{1.59}$$

which can be derived from the assumption of harmonic oscillations, where $m_\phi$ is the mass of the scalar field defined at the potential minimum where the field is oscillating. This encodes the effect of the axion Jeans scale discussed in Section 1.2.2, causing a suppression of structure below $k \sim 2m_\phi a$. However, this effective sound speed only holds when the field is oscillating near the minimum of the potential where it can be approximated as quadratic. Implementing the effective fluid formalism for fields starting near the peak of their potential is computationally challenging, and is explored more in Chapter 3.

### 1.3.3 The Matter Power Spectrum

One of the most widely-used measurements of DM structure is the matter power spectrum (MPS), which describes the amplitude of the DM overdensities on different wavenumbers, $k$. The MPS is the Fourier transform of the autocorrelation function, $\xi(r)$, which is defined as,

$$\xi(r) = \frac{1}{V}\int_V d^3x \delta(\mathbf{x})\delta(\mathbf{x}-\mathbf{r}), \tag{1.60}$$

where $r = |\mathbf{r}|$ is the amplitude of the vector distance between the two points where the fractional overdensity, $\delta = (\delta\rho - \rho)/\rho$, is being measured, and $V$ is the volume being integrated over. In other words, this autocorrelation function is telling us how much the overdensity at any given point is correlated to the overdensity a given distance away ($r$) in any direction. Therefore, we can relate the autocorrelation function $\xi(r)$ to its Fourier transform, the MPS, denoted $\mathcal{P}(k)$,

$$\xi(r) = \int \frac{d^3\mathbf{k}}{(2\pi)^3}\mathcal{P}(k)e^{i\mathbf{k}\cdot\mathbf{r}}, \tag{1.61}$$

where $k = |\mathbf{k}|$ is the amplitude of the Fourier spatial wavenumber. The MPS can also be related directly to the Fourier transform of the overdensities, expressed as $\delta(k)$, by the relation,

$$\langle\delta(\mathbf{k})\delta^*(\mathbf{k}')\rangle = (2\pi)^3\mathcal{P}(k)\delta^3(\mathbf{k}-\mathbf{k}') \tag{1.62}$$

where $\delta^3$ is a three-dimensional dirac delta function.

At early times or on large scales, the evolution of the overdensities can be computed entirely using linear perturbation theory, allowing us to estimate the linear matter power spectrum with great precision. However, at later times and at smaller scales, nonlinear physics becomes significant, and the shape of the matter power spectrum becomes modified by models of halo collapse or baryonic feedback [186]. The linear MPS can thus be computed for different cosmologies, as well as estimated

from observables, either directly through tests of large-scale structure at early times (such as the CMB or galaxy clustering), or inferred indirectly from small-scale probes of structure, such as the Lyman-$\alpha$ forest (discussed further in Section 1.4.2). Fig. 1.1 shows various measurements of the linear MPS along with predictions for both a pure CDM cosmology (as discussed in Section 1.2.1), as well as both pure and mixed axion DM cosmologies at two different axion masses (as discussed in Section 1.2.2).

### 1.3.4 The Halo Mass Function

While the linear MPS describes the amplitude of structure on all scales evolving under purely linear interactions, small-scale structure has a tendency to clump together through the effects of gravity, forming halos of DM governed by highly non-linear interactions that are not described well by the MPS. To describe the mass distribution of these non-linear DM halos, we use the halo mass function (HMF). The HMF is the number density of dark matter halos of total mass $M_h$. By encoding models of nonlinear gravitational collapse, the HMF encodes information about how nonlinear DM structure is forming on different scales. This function, which varies with redshift, can be calculated for both $\Lambda$CDM and non-CDM models.

The HMF can be computed using the method described in [107, 51, 173, 203], and is presented in detail below. The HMF is defined as

$$n(M_h, z) \equiv \frac{1}{M_h} \frac{d\tilde{n}}{d \ln M_h}, \tag{1.63}$$

where $M_h$ is halo mass and $\tilde{n}$ is halo number density. Following the ellipsoidal collapse model of halo formation, we can write the HMF as

$$n(M_h, z) = \frac{1}{2} \frac{\bar{\rho}(z)}{M_h^2} f(\nu) \left| \frac{d \ln \sigma^2}{d \ln M_h} \right|, \tag{1.64}$$

where $\bar{\rho}(z)$ is the average total matter density at the relevant redshift and $\sigma^2$ is the variance of linear fluctuations, which is described in more detail below. The multiplicity function $f(\nu)$ is chosen to be the Sheth-Tormen fitting function [186]:

$$f(\nu) = A \sqrt{\frac{2}{\pi}} \sqrt{q} \nu (1 + (\sqrt{q}\nu)^{-2p}) e^{-\frac{q\nu^2}{2}}, \tag{1.65}$$

where $\nu = \delta_{\rm crit}/\sigma(M_h, z)$, with $\delta_{\rm crit}$ being the critical linear density threshold for halo collapse. This functional form was proposed by [186] based on models of ellipsoidal collapse, with parameters set to match the halo number densities from numerical simulations. The fitting parameters are set to be $A = 0.3222$, $p = 0.3$, $q = 0.707$ and $\delta_{\rm crit} = 1.686$ in order to match simulations described in [186], following what was done in [173, 203].

$\sigma^2(M_{\rm h}, z)$ is the variance of linear fluctuations at redshift $z$ using a spherical real-space top hat filter $\hat{W}(M_h, r)$ with a radius $R_h$ such that the average enclosed mass is equal to $M_h$. We use the Fourier transform of $\hat{W}(M_h, r)$, which we denote $W(M_h, k)$. The variance can be written as,

$$\sigma^2(M_h, z) = \int \frac{d^3k}{(2\pi)^3} W^2(M_h, k) P^{\rm L}(k, z), \tag{1.66}$$

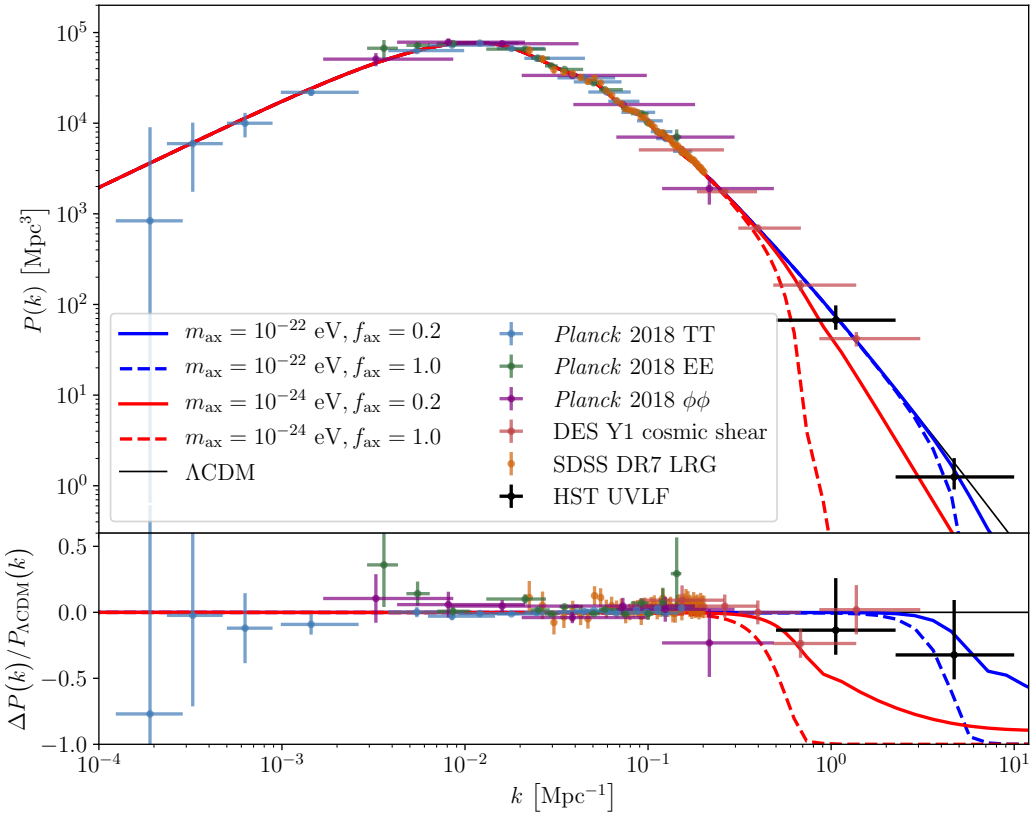


Figure 1.1: The MPS as a function of wavenumber $k$ for both cold dark matter (shown in black, introduced in Section 1.2.1) and axion (in red and blue, introduced in Section 1.2.2) cosmologies with different axion mass ($m_{\mathrm{ax}}$) and DM fraction ($f_{\mathrm{ax}} = \Omega_{\mathrm{ax}}/\Omega_{\mathrm{DM}}$). These axion cosmologies are modeled as an effective scalar field, as introduced in Sections 1.3.1 and 1.3.2. Blue, green, and magenta error bars represent constraints on the MPS from *Planck* 2018 measurements of the CMB [9] temperature TT, polarization EE and lensing $\phi\phi$ angular power spectra, respectively, which are introduced in Section 1.4.4. Red error bars are from galaxy weak lensing shear estimates made with the Dark Energy Survey (DES)[4], while orange error bars are from galaxy clustering estimates using the Sloan Digital Sky Survey [165]. Black error bars represent constraints on the MPS based on both *Planck* CMB and Hubble Space Telescope (HST) measurements of the UV luminosity function as computed in [174], explained in Section 1.4.3. We do not show Lyman-$\alpha$ forest inference on the MPS as existing estimates do not account for the tension with *Planck* cosmology in the tilt of the small-scale power (as discussed in [170]). This plot was constructed using the script from [174] as well as the axion Boltzmann code `axiCLASS` [162]. Previous iterations of this plot were presented in [196, 91, 43].

where $k$ is the physical wavenumber and $P^{\rm L}(k,z)$ is the linear MPS at redshift $z$ (discussed in Section 1.3.3). In this work, we use the `axiCLASS` code [162, 190] to compute the linear MPS.

It follows that the final component of the HMF expression can be written as:

$$\frac{d\ln\sigma^2}{d\ln M_h} = \frac{3}{\sigma^2 R_h^4 \pi^2}\int_0^\infty dk \frac{P^{\rm L}(k)}{k^2} I(k,R_h), \tag{1.67}$$

where

$$I(k,R_h) \;=\; (\sin(kR_h) \,-\, kR_h\cos(kR_h)) \,\times\, \left[\sin(kR_h)\left(1 \,-\, \frac{3}{(kR_h)^2}\right) \,+\, \frac{3}{kR_h}\cos(kR_h)\right], \tag{1.68}$$

which is derived from the derivative of $W(M_h,k)$.

Other forms of the mass function $f(\sigma)$ have been proposed in order to capture more complex aspects of halo formation history. One example is the Reed model [164] where Eq. (1.65) is replaced by:

$$f_{\rm Rd}(\sigma_{M_{\rm h}}) = A_{\rm Rd}\sqrt{\frac{2a_{\rm Rd}}{\pi}}\left[1+\left(\frac{\sigma^2_{M_{\rm h}}}{a_{\rm Rd}\delta^2_{\rm Rd}}\right)^{p_{\rm Rd}} + 0.2\exp\left(-\frac{(\ln\sigma^{-1}_{M_{\rm h}} - 0.4)^2}{2(0.6)^2}\right)\right]\frac{\delta_{\rm Rd}}{\sigma_{M_{\rm h}}}\exp\left(-\frac{c_{\rm Rd}a_{\rm Rd}\delta^2_{\rm Rd}}{2\sigma^2_{M_{\rm h}}}\right), \tag{1.69}$$

where $A_{\rm Rd} = 0.3235$, $a_{\rm Rd} = 0.707$, $p_{\rm Rd} = 0.3$, $c_{\rm Rd} = 1.081$ and $\delta_{\rm Rd} = 1.686$ [164, 174]. In our work (Chapter 4) we primarily use the Sheth-Tormen model, although a comparison to the result of the Reed model is included. The Reed model was developed using a novel method of accounting for finite simulation box size, including more baryonic physics and the effect of the slope of the power spectrum [164]. These adjustments improved the accuracy of predicting rare objects, which the Sheth-Tormen model overpredicted by around 50%. In addition, the Reed model has been found to be more accurate beyond redshifts of $z = 10$ (since halos in this regime are more rare, a better handling of rare objects becomes more significant), suggesting that future analysis in that redshift range might require more complex halo mass functions.

### 1.3.5 Dark Compact Objects

As discussed in Sec. 1.2.3, some models of dark matter can include the dissipation of "dark photons". Within such models, *compact* dark objects (DCOs) can form — see [48] for a simple model featuring only an asymmetric dark electron and a dark photon. The size and mass of these compact objects depends on the details of the model, essentially being set essentially by the self-interactions and cooling rate of the dissipative subcomponent and possible sources of feedback. These dissipative DM models will generally form DCOs in disk distributions due to cooling earlier in the process of galactic formation, analogous to the creation of baryonic galactic disks. These disk distributions of dark stars can be probed by microlensing observations (see Sec. 1.4.1 and Chapter 2). Other gravitational tests of dark disks include measurements of the local matter density, which can constrain extremely thin dark disks with thickness $< 100$ parsecs to contain $< 1\%$ of the Milky Way's DM [181, 38]

Given a particular model of dissipating DM, such as mirror-sector DM, the properties of that model may be related to the spatial and mass distribution of the dark compact objects it can form. Some work has been done calculating the cosmological implications of such a mirror sector, particularly in [46], in addition to earlier work on fully symmetric mirror DM such as [76]. However,

we are only beginning to understand the astrophysical implications of this model. Depending on the model parameters, these baryon-like DM particles can form dark galactic disks and coalesce into "mirror stars" that fuse mirror nuclei and shine in mirror light. These stars would be cohabiting our halo but be largely invisible to us, except for the possibility of faint characteristic optical and X-ray signatures in the presence of mixing between the mirror and SM photons [58, 57]. (For earlier work on the possibility of dark matter stars, see [142, 143, 77, 25, 26].) The details of how the properties of the mirror-sector model would connect to the mass and spatial distributions of the mirror stars are complicated and as-yet unsolved [57]. Therefore, it is important to formulate model-independent constraints on DCOs in Galactic distributions, so that they might eventually be applied to a variety of Dark Disk models. Such constraints are computed in Chapter 2.

DCOs arising at late times from dissipative models of DM can be contrasted to DCOs arising primordially from large fluctuations collapsing gravitationally into primordial black holes (PBHs). Some reviews of PBHs can be found at [72, 27]. These PBHs are also a popular DM candidate, capable of being probed by many of the same observables as dissipative DCOs, but with a different galactic distribution since they do not dissipate energy at late times and do not collapse into dark disk distributions. Instead, PBHs would be found in a spherically-symmetric galactic distribution, much like traditional CDM. Chapter 2 explains how we might be able to distinguish between PBHs and DCOs arranged in dark disk configurations through the use of microlensing. In general, any galactic distribution of DCOs can be probed with microlensing.

## 1.4 Observables

The work presented in this thesis utilizes a number of astronomical and cosmological observables in order to directly measure the structure and distribution of DM. This section introduces the various observables used in the rest of the thesis, as well as the telescopes and surveys used to measure these observables. These include measurements of microlensing by the LSST with the Vera Rubin Observatory, measurements of the Lyman-$\alpha$ forest with eBOSS, measurements of the UV luminosity function (UVLF) with the Hubble and James Webb space telescopes (HST and JWST), and measurements of the Cosmic Microwave Background (CMB) with the *Planck* telescope. The approximate range of scales and redshifts probed by these observables (as well as others) are shown in Fig. 1.2.

### 1.4.1 Microlensing

Gravitational lensing is a phenomenon whereby a massive object passes directly in front of a bright background source, gravitationally lensing the light as a result of general relativity [153, 12]. When the viewer, lens, and source are all in direct alignment, this results in the the source appearing as an "Einstein ring" around the lens, with a radius given by $r_E$. We can derive an expression for this "Einstein radius" using general relativity (introduced in Section 1.1.1). In [71], Einstein showed that the angular deflection of light, $\alpha$ around a source of mass $M$ and distance $b$ can be written as,

$$\alpha = \frac{4GM}{c^2 b}. \tag{1.70}$$

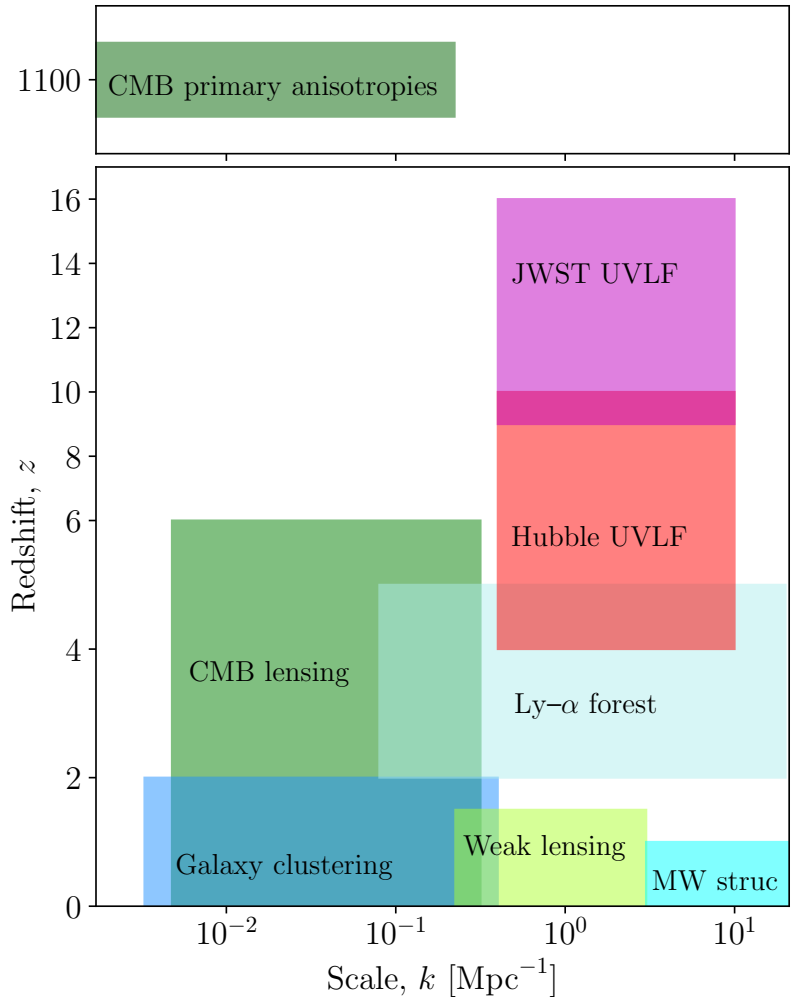


Figure 1.2: The approximate range of wavenumbers $k$ and redshifts $z$ explored by various astrophysical probes of DM structure. Microlensing (Sec.1.4.1) is included as one of multiple $z = 0$ probes of small scale milky way (MW) structure included in "MW struc" [13, 212]. The "Ly-$\alpha$ forest" box includes measurements from both eBOSS (Sec. 1.4.2) well as high-resolution spectroscopy from the XQ-100 survey [127, 112]. The UVLF boxes from HST [30] and JWST [87] are discussed in Sec. 1.4.3. Both CMB primary anisotropies and gravitational lensing are discussed in Sec. 1.4.4.

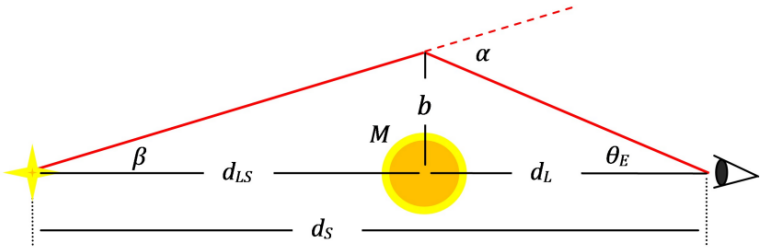


Figure 1.3: A diagram showing the physical arrangement of gravitational lensing, with the source on the left, the lens of mass $M$ in the middle, and the observer on the right. Diagram reproduced from source [85].

Note that this is only a factor of 4 greater than the Newtonian solution assuming a ballistic model of light.

From the geometric picture shown in Figure 1.3, we can see that the angle of deflection, $\alpha$, is equal to the sum of the angle of the emitted light ray relative to a straight path to the lens and observer ($\beta$) and the observed angle of the incoming light ray by the viewer ($\theta_E$). In addition, using the small angle approximation, we can write both $\beta$ and $\theta_E$ as their tangent ratios, such that:

$$\beta \approx \tan(\beta) = \frac{b}{d_{LS}} \tag{1.71}$$

$$\theta_E \approx \tan(\theta_E) = \frac{b}{d_L} \tag{1.72}$$

where $d_L$ is the distance from the observer to the lens, and $d_{LS}$ is the distance from the lens to the source. Therefore, we can equate the geometric and gravitational expressions for $\alpha$to get

$$\frac{4GM}{c^2 b} = \frac{b}{d_L} + \frac{b}{d_{LS}} \tag{1.73}$$

We can then rewrite this to solve for $b$, which we here denote as the Einstein radius $r_E$. We also can substitute $L = d_L + d_{LS}$ as the total distance to the source, and $x = d_L/L$ as the fractional distance to the lens relative to the distance to the source. From this, we can write the Einstein radius as,

$$r_E = \sqrt{\frac{4MLGx(1-x)}{c^2}}. \tag{1.74}$$

This result was first presented by Albert Einstein in [71], and a recent pedagogical derivation can be found in [158].

In many cases involving low-mass lenses, the Einstein ring created by the strong lensing is too small to be resolved by the telescope being used, so the event manifests only as a temporary brightening of the background object. This temporary brightening can be detected with long-term photometric survey telescopes, and can be distinguished from other transients by its achromatic and time-symmetric lightcurve (meaning that the event looks the same in all wavelengths, and the starting and ending periods look the same in reverse). The relative amplitude of this brightening depends on the minimum separation of the lens from the observer-source line, $b$, as a fraction of

Einstein radius $r_E$, where,

$$A = \frac{u^2+2}{u\sqrt{u^2+4}},$$

and $u = b/r_E$. Characterizing the number of microlensing events we see in a given survey can put constraints on the number of dark compact objects in our Galaxy, allowing us to constrain models of compact DM. This technique has been used in the past to rule out MAssive Compact Halo ObjectS (MACHOS) for a variety of mass ranges comprising 100% of the DM in our halo [12, 211].

In order to compute the forecasts and constraints that microlensing surveys place on dark compact objects, we would need to calculate the expected number of detectable microlensing events. As a conservative estimate, most forecasts only consider something to be a microlensing event if the fractional separation $u$ is less than 1 (so $A \geq 1$) since this is necessary for multiple images to be formed. for a given survey. The differential microlensing event rate, which describes the number of microlensing event rates per unit time per unit crossing time ($\hat{t}$, how long the microlensing event lasts), is given in [12] and [40] to be

$$\frac{d\Gamma}{d\hat{t}} = \frac{32L}{\hat{t}^4 m v_c^2}\int_0^1 \rho_{\rm DM}(x) r_E^4(x,m)\exp\left(-\frac{4r_E^2(x,m)}{\hat{t}^2 v_c^2}\right)dx, \tag{1.75}$$

where $\hat{t}$ is the event crossing time, $L$ is the distance from the observer to the source, $m$ is the lens mass, $x$ is the fractional distance of the lens compared to the source, $v_c$ is velocity of the DCOs transverse to the line of sight at location $x$ relative to the line of sight, $\rho_{\rm DM}(x)$ is the compact DM density at that distance along the line of site, and $r_E(x,m)$ is the Einstein radius for a given distance and mass, given by Eq. (1.74). The derivation of this formula can be found in [12] and [85].

This microlensing rate must then be multiplied by the range of possible start times for an event to be observable. This range depends on whether the event is being detected using traditional microlensing or paralensing, which is the oscillatory lensing amplification caused by the Earth's orbit instead of the transverse velocity of the object itself. For traditional microlensing, the event must fully overlap with the survey in order to be considered detectable, as we would need to see both the rising and falling sections of the light curve to confirm that the event is achromatic and time symmetric. Therefore, the range of possible event start times for events of duration $\hat{t}$ that could be detectable with a survey of length $t_{\rm survey}$ would be $T_{\rm micro} = t_{\rm survey} - \hat{t}$. However, for paralensing events the event can start or end before or after the actual observing period, as long as it overlaps with the observing period for at least one year in order to detect one full parallax oscillation. Therefore, the length of time over which an event of duration $\hat{t}$ can start and still be seen by paralensing is $T_{\rm para} = t_{\rm survey} + \hat{t} - (2\text{ years})$. This includes both events that start during the survey but not in the final year (so a range of $t_{\rm survey} - (1\text{ year})$) and events that start up to $\hat{t} - (1\text{ year})$ before the survey (so they end at least one year after the survey begins, providing the necessary overlap). Therefore, for a given event duration $\hat{t}$, the range of possible start times for it to be detectable by either microlensing or paralensing is the greater of the two ranges provided above. For short-duration events this would be traditional microlensing, while longer events would be detectable with paralensing. The total number of expected microlensing events is then,

$$N_{\rm observed} = n_{\rm sources}\int_0^\infty \frac{d\Gamma}{d\hat{t}} T_{\rm micro/para}\,\xi(\hat{t})\,d\hat{t}, \tag{1.76}$$

which integrates the differential microlensing rate over all possible crossing times, $\hat{t}$, multiplied by the possible range of start times $T$ to get the total number of events that would be seen in the survey. The integrand is also multiplied by $\xi(\hat{t})$, which is the fractional detectibilty of events with crossing time $\hat{t}$, and depends on the systematics of the survey being used, including the cadence and sensitivity. The total number of events is also multiplied by $n_{\rm sources}$, which is the total number of sources in the survey. Using this method for calculating microlensing event numbers, we can compute constraints on the compact object DM fraction, as is done in Chapter 2.

**LSST**

In principle, any large survey with regular cadence could search for microlensing events. In particular, surveys such as the Legacy Survey of Space and Time (LSST) that will be taken by the Vera C. Rubin Observatory, should be able to place tight microlensing constraints on the DCO DM fraction due to increased sensitivity and large number of target sources [176, 66]. The Rubin Observatory is an upcoming astronomical facility in Northern Chile which will conduct a 10-year survey of the southern sky (known as the LSST) using its 3200 megapixel camera attached to an 8.4-meter telescope. A survey of this size with more than a billion stellar sources and over 10 years of images taken only a few days apart will be ideal for microlensing as it will have the potential to detect a very high number of events. It will also be able to use paralensing to detect microlensing events with arbitrarily long crossing times [84]. Paralensing has been observed in past surveys [211, 83] but never with the large number of sources available to LSST.

The detectability of events with crossing time $\hat{t}$ was modeled by [66] using well-informed assumptions about the cadence and sensitivity of the LSST survey. In particular, [66] calculated the projected sensitivity by injecting microlensing lightcurves into LSST OpSim cadence simulations, incorporating realistic assumptions of LSST cadence and sensitivity. Since the sensitivity of the LSST instrument and analysis pipeline is outside the scope of this work, we used an analytic function to describe this detectability, $\xi(\hat{t})$, with parameters fit to match the mass-dependent sensitivity presented in [66]. We used a logarithmic logistic function of the form

$$\xi(\hat{t}) = \frac{1}{1 + \left(\frac{\hat{t}}{t_0}\right)^{-1/t_r}}. \tag{1.77}$$

This function was chosen because it varies smoothly with $\log \hat{t}$ between complete detectability and no detectability. The parameters of $t_0$ and $t_r$ were fit to the results of the rigorous systematic analysis done in [66]. Therefore, we ignore questions of observing conditions, depth, and issues with the point spread function.[3] In practice, these microlensing events would be flagged by the LSST transient pipelines due to their time-symmetric and achromatic nature, and a collection of these events could be compared to theoretical predictions to test for populations of dark compact objects.

[3]Additionally, looking ahead to Fig. 2.1, we can see that the mass range where this sensitivity is the most relevant is the same mass range where our microlensing constraints will be complicated by the presence of rogue interstellar planets, making it difficult to compute exact constraints. Therefore, the most robust constraints from Rubin will be in the high-mass regime explored by paralensing, where questions of cadence, observing conditions, and issues with the point spread function are less relevant.

### 1.4.2 Lyman-$\alpha$ forest

One of the best ways of probing the small-scale linear matter power spectrum is with the Lyman-$\alpha$ (or Ly-$\alpha$) forest. The Ly-$\alpha$ forest is measured using the absorption of light from high-redshift quasars (super-luminous active galactic nuclei typically observed at high redshifts) by foreground neutral hydrogen. The neutral hydrogen absorbs light with the Lyman-$\alpha$ transition at rest wavelengths of $\lambda_{\text{Ly-}\alpha} = 121.6$ nm, but depending on the redshift at which this absorption occurs, the absorption feature will be detected at different places in the quasar spectrum. This allows the observer to sample the neutral hydrogen density along the entire line of sight to the quasar. This can result in extremely high-resolution estimates of the matter power spectrum if we use a high number of quasars and high-resolution spectroscopy to analyze the quasar spectra.

However, this estimate is dependent on hydrodynamic modeling of the hydrogen gas clouds in order to relate the Lyman-$\alpha$ absorption flux to the underlying DM density. In practice, cosmological predictions of the MPS must then be fed through either a hydrodynamical simulation, or an emulator of such a simulation (as was done in [169]) in order to produce predicted values for the Ly-$\alpha$ flux power spectrum. Alternatively, these simulations can be run many times in order to reconstruct estimates of the linear MPS from the Ly-$\alpha$ flux spectrum. All of these simulations involve making assumptions about both dark and baryonic physics, making it difficult to use this observable to probe alternative models of DM.

#### eBOSS

We use the estimates of the linear MPS from the eBOSS DR14 Ly-$\alpha$ forest data. eBOSS (or the Extended Baryon Oscillation Spectroscopic Survey) us the 5th data release from the Sloan Digital Sky Survey collaboration (SDSS). The survey includes 210,005 quasars with $z_q > 2.10$ that are used to measure the signal of Ly-$\alpha$ absorption [67]. The flux power spectrum is then used to compute estimates of the linear MPS at $z = 0$. It should be noted that these estimates assume $\Lambda$CDM in their reconstruction, limiting their validity when used to test models of non-cold DM.

### 1.4.3 UV Luminosity Function

The UVLF $\Phi_{\text{UV}}$ is the number density of galaxies with a given UV magnitude $M_{\text{UV}}$ at a redshift $z$. The UVLF is dependent on the number density of galaxy halos with a given mass (the HMF $n(M_h, z)$ described in Section 4.3) and the average UV magnitude of galaxies in halos with a given mass. This makes the UVLF a powerful probe of small-scale structure at high redshifts, but is dependent on the modeling of galaxy UV luminosities in order to infer fundemantal physics.

The UVLF can be expressed as

$$\Phi_{\text{UV}}(M_{\text{UV}}, z) = \int n(M_h, z) P(M_{\text{UV}}|M_h, z) dM_h, \tag{1.78}$$

where $P(M_{\text{UV}}|M_h, z)$ is the probability of a galaxy having a UV magnitude $M_{\text{UV}}$ given a halo mass $M_h$ at redshift $z$ (using the conditional luminosity function formalism developed by [214] and implemented in the software package `GALLUMI` by [173]). This probability can be modeled as a

Gaussian distribution:

$$P(M_{\rm UV}|M_h,z) = \frac{1}{\sqrt{2\pi}\sigma_{M_{\rm UV}}} \exp\left[ - \frac{\left(M_{\rm UV} - \overline{M_{\rm UV}}(M_h,z)\right)^2}{\sigma^2_{M_{\rm UV}}}\right], \tag{1.79}$$

where $\sigma_{M_{\rm UV}}$ is the scatter in UV magnitude (driven by, for example, bursty star formation), which we treat as a nuisance parameter that we fit to the data. $\overline{M_{\rm UV}}(M_h,z)$ is the average UV magnitude of galaxies in halos with mass $M_h$ at redshift $z$, which is computed according to the model specified below. The relation given in Eq. (1.79) is illustrated in Fig. 1.4.

We relate the mean UV magnitude $\overline{M_{\rm UV}}$ to the halo mass $M_h$ using models presented in [173]. First, the mean UV luminosity $\overline{L_{\rm UV}}$ is related to the mean UV magnitude by the definition

$$0.4(51.63 - \overline{M_{\rm UV}}) = \log_{10}\left(\frac{\overline{L_{\rm UV}}}{\text{erg s}^{-1}}\right). \tag{1.80}$$

The mean UV luminosity $\overline{L_{\rm UV}}$ can be related to the mean star formation rate $\overline{\dot{M}_\star}$:

$$\overline{L_{\rm UV}} = \frac{\overline{\dot{M}_\star}}{\kappa_{\rm UV}}, \tag{1.81}$$

where $\kappa_{\rm UV} = 1.15 \times 10^{-28} M_\odot$ s erg$^{-1}$ yr$^{-1}$ is derived from stellar synthesis population modeling (see [131] for details). This relation physically captures how UV photons are generated in young star-forming regions.

We can then relate the mean star formation rate to the mean stellar mass $\overline{M_\star}$:

$$\overline{\dot{M}_\star} = \frac{H(z)}{t_\star}\overline{M_\star}, \tag{1.82}$$

which assumes that stellar accretion rate is proportional to the dynamical time of DM halos, as done in [156] and [82]. This relationship is parameterized by the dimensionless $t_\star$ which we vary as a free parameter.

Finally, we relate the average stellar mass $\overline{M_\star}$ to the halo mass $M_h$ using a parametric broken power law equation:

$$\frac{\overline{M_\star}}{M_h} = \frac{\epsilon_\star}{\left(\frac{M_h}{M_c}\right)^{\alpha_\star} + \left(\frac{M_h}{M_c}\right)^{\beta_\star}}, \tag{1.83}$$

where $\epsilon_\star$, $M_c$, $\alpha_\star$, and $\beta_\star$ are functions over which we marginalize when fitting to data. $\epsilon_\star \geq 0$ is the overall amplitude of stellar mass function relative to the halo mass, $M_c \geq 0$ is the mass at which mean stellar mass peaks relative to halo mass. $\alpha_\star \leq 0$ regulates the slope of the low-mass end of the function, while $\beta_\star \geq 0$ regulates the high-mass end. This broken power law accurately reflects the physical model of star formation, since the galaxies in low-mass halos will have insufficient star formation, while those in high mass halos will have used up most of the available gas and will thus also have supressed star formation. The exact slope of these two effects, and the pivot mass at which star formation peaks, are all free parameters in this model. Following the parameterization in [173],

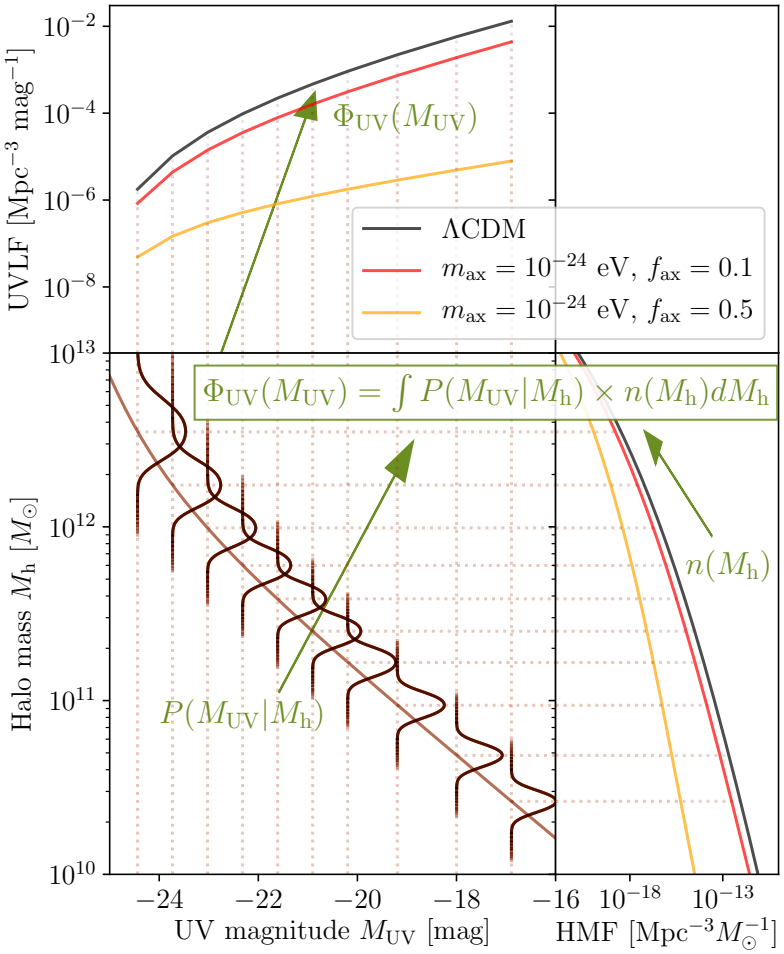


Figure 1.4: A schematic illustrating how the UVLF ($\Phi_{\rm UV}(M_{\rm UV})$, upper left) can be computed from the HMF ($n(M_h)$, lower right) and the average UV magnitude $\overline{M_{\rm UV}}$ for halos of a given mass $M_h$ (lower left) following Eq. (1.78). The solid Gaussian-like curves in the lower left panel represent the conditional probability of a halo having mass $M_{\rm h}$ given a UV magnitude $M_{\rm UV}$ (i.e., the inverse of the probability given in Eq. (1.79), as this better illustrates the construction of the UVLF by integrating over multiple distributions of Eq. (1.79) for different values of $M_h$). We show a pure CDM universe in black, a mixed-DM universe with 10% axions and $m_{\rm ax} = 10^{-24}$ eV in red, and one with 50% axions of the same mass in orange. All scenarios are plotted for $z = 6$. Axions suppress the HMF (lower right) and thus the UVLF (upper left) but do not impact the average UV magnitudes for halos of a given mass (lower left).

we assume the $z$-dependence of these parameters is:

$$\alpha_\star(z) = \alpha_\star, \tag{1.84}$$

$$\beta_\star(z) = \beta_\star, \tag{1.85}$$

$$\log_{10}\epsilon_\star(z) = \epsilon_\star^s \times \log_{10}\left(\frac{1+z}{1+6}\right) + \epsilon_\star^i, \tag{1.86}$$

$$\log_{10} M_c(z) = M_c^s \times \log_{10}\left(\frac{1+z}{1+6}\right) + M_c^i, \tag{1.87}$$

where both $\epsilon_\star$ and $M_c$ are parameterized by a power law with slopes $[\epsilon_\star^s, M_c^s]$ and intercepts $[\epsilon_\star^i, M_c^i]$, both pivoting at $z = 6$ (chosen by [174] to be representative of the HST UVLF estimates, shown in Fig. 4.2). Since $\epsilon_\star$ is fully degenerate with $t_\star$ from Eq. (1.82), we combine $t_\star$ into our nuisance function $\epsilon_\star(z)$ (as done in [173]).

When combined together, Eqs. (1.80) to (1.87) allow us to compute the average UV luminosity for a given halo mass, which we then use to calculate the UVLF [Eqs. (1.78) and (1.79)]. [173] demonstrates that this model can reproduce the UVLF as calculated in the detailed Illustris TNG hydrodynamical simulations [202]. This test means that we can marginalize over uncertainty in the relation between UV luminosity and halo mass as seen in hydrodynamical simulations, but without the need to run a large number of computationally-expensive models. The results of this model (with HST best-fit parameters) are shown in Fig. 1.5 along with HST data.

**Hubble and James Webb space telescopes**

We use estimates of the UVLF from the Hubble Space Telescope (HST) presented in [30]. The HST is a space-based optical telescope capable of observing UV galaxies at high redshifts (since the UV light will have been redshifted into the optical). The sample we use contains $> 24,000$ UV sources, at redshifts $z = 4$ to $z = 10$. The UV sources are grouped into $M_{\rm UV}$ bins of 0.5 magnitudes. These measurements of the UVLF are shown in Fig. 1.5.

These UVLF estimates have recently been improved by groundbreaking new results from the James Webb space telescope (JWST), which is an infrared space-based telescope capable of resolving UV sources at much higher redshifts, up to $z \sim 16$ [28, 87]. Some early analyses of JWST observations have suggested that its estimates of the $z > 10$ UVLF may be substantially higher than the $\Lambda$CDM expectations based on the $z < 10$ HST estimates [32, 49]. If true, this overabundance of structure at high redshifts could imply tight constraints on DM models that predict a suppression in the MPS, such as axions (see Section 1.2.2).

In order to test whether these preliminary JWST results are in tension with our model, we consider a spectroscopically-confirmed sample of 25 JWST UV sources presented in Table 1 of source [87]. We restrict ourselves to only spectroscopically-confirmed sources as photometric samples are known to be contaminated by low-$z$ interlopers, and it is only with mid- and far-infrared spectroscopy that redshifts can be definitively determined. Indeed, many of the initial high-$z$ sources that were claimed to be in tension with $\Lambda$CDM cosmology were later found to be interlopers, and determining their true redshift is still an active area of research [215, 79, 88]. The sources to which we restrict our analysis have spectroscopic redshifts in the range $8.61 < z < 13.20$, allowing [87] to compute the UVLF at $z = 9$ and $z = 10$. They also compute lower bounds at $z = 12$ and upper bounds at

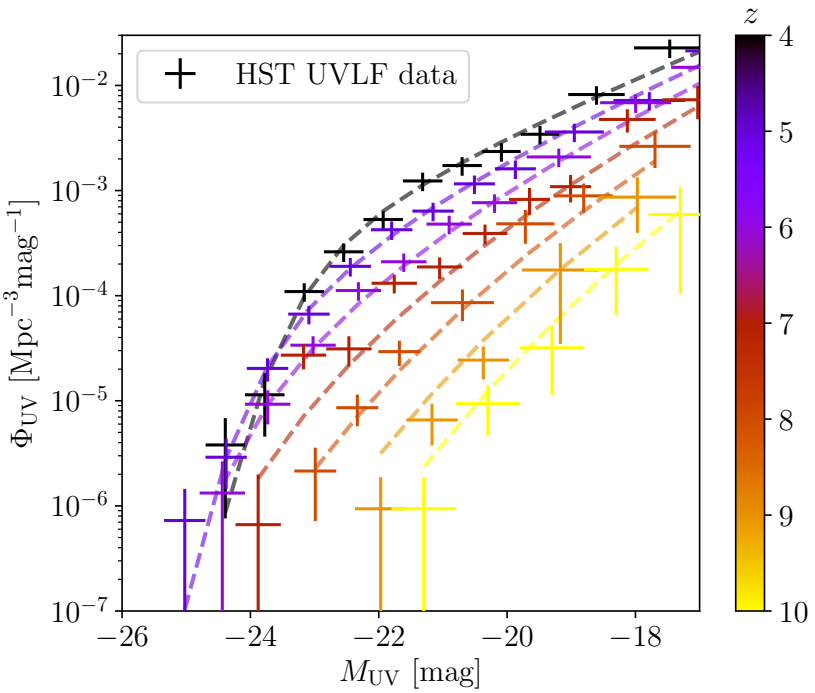


Figure 1.5: The UVLF for redshifts $z = 4-10$, assuming a pure CDM cosmology fit to Hubble Space Telescope (HST) data (dashed lines), alongside the HST data presented with error bars showing 68% c.l. uncertainties and magnitude bin widths [30].

$z = 16$ (from non-detection in their field).

### 1.4.4 The Cosmic Microwave Background

One of the most powerful cosmological observables is the Cosmic Microwave Background (CMB). The CMB consists of photons that are emitted at very early times, when the universe first transitions from a hot, opaque, ionized plasma into neutral, transparent hydrogen gas. During this transition, photons that were previously scattered by the opaque plasma are suddenly free to stream through the universe. Apart from occasional interactions with astrophysical objects at late times, these photons have freely streamed to us from this surface of last scattering. This transition occurred at a redshift of $z \approx 1100$, meaning that these photons have been redshifted into the microwave range by the expansion of spacetime. Overdensities and underdensities in the primordial plasma at this point result in hot and cold spots in this microwave background, allowing us to probe linear structure at very early times on comoving scales that are as large as the entire observable universe. These scalar overdensities can be traced either with the temperature of the CMB (denoted as $T$) or by the curl-free component of the photon polarization (denoted as $E$). These observables are often plotted on an angular power spectrum, which resembles the matter power spectrum except it uses spherical harmonics instead of comoving Fourier wavenumber. For example, the map of temperature on the spherical sky $T(\theta, \phi)$ (where $\theta$ and $\phi$ are spherical coordinates) can be decomposed into the spherical

harmonic basis functions $Y_{\ell,m}$ indexed by the multipole number $\ell$ and azimuthal number $m$ as,

$$T(\theta,\phi) = \sum_{\ell,m} a_{\ell m}^{TT} Y_{\ell m}(\theta,\phi). \tag{1.88}$$

The temperature power spectrum can then be written as the average of the $a_{\ell m}^{TT}$ values squared, averaged over all values of $m$ at a certain $\ell$ (where $m \leq \ell$),

$$C_\ell^{TT} = \langle |a_{\ell m}^{TT}|^2 \rangle. \tag{1.89}$$

A similar process can be used to compute the E-mode polarization power spectrum.

The CMB can also be used as a probe of late-time structure. As the CMB photons travel to us from the surface of last scattering, they can interact with other astrophysical objects – for example, these photons can be gravitationally lensed by massive halos, allowing us to reconstruct the lensing potential map $\phi$. In addition, the photons can be scattered by gas or dust, leading to numerous other signals which can either be removed as a noise contamination or examined as interesting signals in their own right. In this work, however, we only use the temperature, $E$-mode polarization, and lensing power spectra as probes of cosmology. The redshifts and scales probed by both primary CMB anisotropies and late-time CMB lensing are shown in Fig. 1.2.

#### *Planck*

The *Planck* telescope has produced some of the most accurate measurements of the CMB on a wide range of scales [9]. As a space-based telescope, it is capable of measuring the largest modes of the CMB, but also has the resolution to probe angular scales down to $\ell \sim 2500$. *Planck* measurements of the temperature ($TT$), curl-free polarization ($EE$), and lensing ($\phi\phi$) can all be used to estimate the linear MPS – these estimates are shown in Fig. 1.1.

## 1.5 Statistics

All of the projects in this thesis involve some sort of comparison between theories of dark matter and astronomical observations or forecasts. The goal of these comparisons is to compute estimates (or constraints) on the properties of dark matter given various observation datasets. This section introduces some of the statistical tools which are used in these comparisons.

### 1.5.1 Bayesian probability

In cosmology, we often wish to compute the probability of different values for theoretical cosmological parameters, given a certain observational dataset. This allows us to estimate the value and uncertainty of cosmological parameters, such as the DM density or ULA particle mass. In order to compute these probabilities, we make use of Bayes' theorem.

If we observe some astronomical data $\mathbf{x}$, and wish to compute estimates of cosmological parameters $\boldsymbol{\theta}$, Bayes' theorem states that the conditional probability of $\boldsymbol{\theta}$ given $\mathbf{x}$ (also known as the *posterior*) can be written as,

$$P(\boldsymbol{\theta}|\mathbf{x}) = \frac{P(\mathbf{x}|\boldsymbol{\theta})P(\boldsymbol{\theta})}{P(\mathbf{x})}. \tag{1.90}$$

$P(\mathbf{x}|\boldsymbol{\theta})$ is the probability of observing the data $\mathbf{x}$ given the parameters $\boldsymbol{\theta}$, and is commonly referred to as the *likelihood* and denoted $\mathcal{L}$. $P(\boldsymbol{\theta})$ is referred to as the *prior* and represents the probability of the cosmological parameters having a value of $\boldsymbol{\theta}$. $P(\mathbf{x})$, also known as the *evidence* (or the prior predictive density) is the probability of observing data $\mathbf{x}$ integrated over all possible values of $\boldsymbol{\theta}$. The evidence can be written as,

$$P(\mathbf{x}) = \int P(\mathbf{x}|\boldsymbol{\theta})P(\boldsymbol{\theta})d\boldsymbol{\theta}. \tag{1.91}$$

Since the final value of the evidence does not change for different values of $\boldsymbol{\theta}$, it acts only as a normalizing term. When computing the relative probabilities of different $\boldsymbol{\theta}$ values, it is often ignored.

### 1.5.2 Forms of the Likelihood

The Bayesian posterior requires computations of the likelihood $\mathcal{L}$, which describes the probability of observing a certain result $\boldsymbol{x}$ given some theoretical model parameters $\boldsymbol{\theta}$.

#### Chi-squared

One of the simplest forms of the likelihood is the normal distribution, quantified by the chi-squared test statistic $\chi^2$. For some set of observed values $x_i$ with uncorrelated Gaussian uncertainty $\sigma_i$, the log of the likelihood can be written as

$$\log(\mathcal{L}_{\chi^2}) = \chi^2 = \sum_i \frac{[x_i - \hat{x}_i(\boldsymbol{\theta})]^2}{\sigma_i^2}, \tag{1.92}$$

where $\hat{x}_i(\boldsymbol{\theta})$ is the predicted value of the observable $x_i$ given the theoretical model parameters $\boldsymbol{\theta}$.

#### Poisson statistics

If our observed value of interest $x$ is a discrete number of events with an average of $\lambda$, we can write the probability mass function (PMF) of observing $x$ using the Poisson distribution,

$$P_{\mathrm{Poi}}(x;\lambda) = e^{-\lambda}\frac{\lambda^x}{x!}, \tag{1.93}$$

Both the expectation value and variance of this distribution can be estimated as $\lambda$. This means that for high values of $\lambda$, this distribution converges to a Gaussian with mean $\lambda$ and uncertainty $\sqrt{\lambda}$. If you collect a series of observations $x_i$, then the likelihood given a mean rate $\lambda$ can be written as the product of the PMF distributions,

$$\mathcal{L}_{\mathrm{Poi}}(x_i|\lambda) = \prod_i e^{-\lambda}\frac{\lambda_i^x}{x_i!}. \tag{1.94}$$

### 1.5.3 Markov-Chain Monte-Carlo analysis

Computing the likelihood $\mathcal{L}$ typically involves using a theoretical model to compute expected values for certain observable values, and then using either chi-squared or Poisson statistics to compare them to observed parameters. This theoretical computation can often take a few seconds or minutes, depending on the cosmological model involved. However, calculating the posterior distribution using

Eq. (1.90) for all possible combinations of model parameters can become computationally prohibitive for large numbers of parameters.[4]

Fortunately, there are alternatives to evaluating the posterior using a grid. Markov-chain Monte Carlo (MCMC) algorithms are a class of methods for randomly drawing samples from a probability distribution such that the distribution of samples matches the underlying probability distribution. A popular example of a MCMC method is the Metropolis-Hastings algorithm, which can efficiently sample a high-dimensional posterior distribution $P(\boldsymbol{\theta}|\mathbf{x})$, where $\boldsymbol{\theta}$ is a vector of model parameters and $\mathbf{x}$ is the given data. A description of the algorithm is as follows:

1. Select an arbitrary starting value $\boldsymbol{\theta}_0$, and set some proposal function $g(\boldsymbol{\theta}'|\boldsymbol{\theta})$. Both of these choices are arbitrary, but the algorithm converges faster if the starting value is near the posterior mean, and the proposal function closely resembles the shape of the posterior. In practice, we typically use a multivariate Gaussian matching the estimated variance and covariance of the posterior.

2. For each iteration $i$ starting with $i = 0$:

   (a) Propose a new candidate value $\boldsymbol{\theta}'$ by drawing from the proposal distribution $g(\boldsymbol{\theta}'|\boldsymbol{\theta}_i)$.

   (b) Calculate the acceptance ratio $\alpha = P(\boldsymbol{\theta}'|\mathbf{x})/P(\boldsymbol{\theta}_i|\mathbf{x})$. Since only the ratio of the posterior distribution matters, we can ignore the evidence term in Bayes theorem, and only compute the likelihoods and priors.

   (c) Generate a uniform random number $u \in [0, 1]$. If $u \leq \alpha$, then *accept* the candidate value by setting $\boldsymbol{\theta}_{i+1} = \boldsymbol{\theta}'$. If $u > \alpha$, then *reject* the candidate and keep the value the same, setting $\boldsymbol{\theta}_{i+1} = \boldsymbol{\theta}_i$.[5]

3. Repeat the previous iterations for some number of steps $N$. This can be done with multiple chains in parallel, speeding up computation time.

Over time, the chains will approach a stationary distribution that approximates the posterior distribution. whilr it is impossible to know whether a distribution has reached perfect convergence, we can run various diagnostic tests to asses apparent convergence. Often the first part of the chains will have to be discarded as "burn in", since it has not yet reached the stationary distribution. There are various methods of determining how many points to remove, but in practice the only requirement is that the number of points after burn-in is enough to achieve convergence, which is discussed below.

[4]For example, the flat ΛCDM cosmology model typically involves six model parameters, so sampling each of these at a thousand value would require computing the posterior on a grid with $(1000)^6 = 10^{18}$ points. If each computation requires one second, this would take around twice the age of the observable universe. Each additional model parameter added (for example, when probing mixed models of DM, or marginalizing over astrophysical nuisance parameters) would increase this runtime by a factor of a thousand per parameter.

[5]In other words, if the proposed value is "better" than the current value (ie. $P(\boldsymbol{\theta}'|\mathbf{x}) > P(\boldsymbol{\theta}_i|\mathbf{x})$), then $\alpha > 1$, so the proposed value will always be accepted. However, if the proposed value is "worse" than the current one, it may or may not be accepted, depending on how much worse it is. Points that are much worse have a low value of $\alpha$, so the uniform random $u$ will probably be greater then $\alpha$ and the point will probably be rejected. However, if the proposed point is only slightly worse, then $\alpha$ will be closer to 1, so $u$ will be more likely to be less than $\alpha$ and the point will probably (but not certainly) be accepted.

**Gelman-Rubin tests for convergence**

Convergence for a series of Markov chains can be quantified using the Gelman-Rubin (GR) statistic [80]. This statistic can be computed from a series of $J$ chains (indexed by $j$), each containing $L$ points (indexed by $i$). The value of the point itself is denoted $x$, and the GR statistic can be computed for each parameter in a multivariate MCMC analysis. It is assumed that burn-in phases have already been discarded.

The mean value of each chain $j$ is denoted as $\bar{x}_j$, while the mean of all chains is denoted as $\bar{x}_\star$. The variance of the means of the chains can be written as,

$$B = \frac{L}{J-1}\sum_{j=1}^{J}(\bar{x}_j - \bar{x}_\star)^2, \tag{1.95}$$

while the mean of the variance averaged across all chains can be written as

$$W = \frac{1}{J}\sum_{j=1}^{J}\left(\frac{1}{L-1}\sum_{i=1}^{L}(x_i^j - \bar{x}_j)^2\right). \tag{1.96}$$

Finally, the GR statistic can be written as,

$$R = \frac{\frac{L-1}{L}W + \frac{1}{L}B}{W}. \tag{1.97}$$

As the chains run to $L \to \infty$, the average variance $W$ approaches a fixed value, while the variance of the averages $B$ approaches zero. Therefore, the GR statistic approaches 1. Often, we use $R-1$ as the relevant statistic, as this value approaches zero. A threshhold for convergence must be chosen, typically set to $R-1 < 0.1$ for all parameters. Once this threshold has been reached for all parameters, the chain is likely converged and the distribution of the chains can be used as an approximation of the posterior distribution. Discarding different amounts of the initial chains as burn-in will change the GR statistic, but in practice a series of chains of any length that satisfy the GR convergence criteria can be used as an estimate of the posterior distribution.

### 1.5.4 Model Comparison

Bayes' theorem is useful when computing estimates of the model parameters given a certain cosmological model. This is often used in cosmology when the ΛCDM paradigm is assumed (see Section 1.2.1), and we only wish to estimate the values of cosmological model parameters. However, when considering models of DM beyond CDM, it often becomes necessary to compare the probability of different models, each with their own set of parameters. In general, models with more parameters have greater flexibility in fitting a given dataset, so the maximum likelihood ($\hat{\mathcal{L}}$) tends to be higher. In order to distinguish when more complex models are actually warranted by the data, we use the Akaike information criterion (AIC), presented in [10]. The AIC can be written as,

$$\mathrm{AIC} = 2K - 2\ln(\hat{\mathcal{L}}) \tag{1.98}$$

where $K$ is the number of parameters in the model, and $\hat{\mathcal{L}}$ is the maximum likelihood value. Given some set of possible models, the preferred model is the one with the minimum AIC value. In other

words, if a certain model involves $n$ more parameters than a different model, then those additional parameters are only warranted if the improvement in fit is such that $\Delta \ln(\hat{\mathcal{L}}) > n$.

# Chapter 2

# Microlensing of Dark Disks

Article published in the Astrophysical Journal, as Harrison Winch et al. "Using LSST Microlensing to Constrain Dark Compact Objects in Spherical and Disk Configurations". In: *The Astrophysical Journal* 933.2 (July 2022), p. 177. DOI: 10.3847/1538-4357/ac7467. URL: https://dx.doi.org/10.3847/1538-4357/ac7467. As first author, this project was primarily my idea, in collaboration with co-author David Curtin. I developed the model for computing dark disk microlensing, wrote all of the code used to calculate forecasts, generated all figures and wrote the almost all of the paper text, with editorial input from co-authors. Section 2.3.4 on dark compact object velocities was computed and written by co-author Jack Setford. The probabilistic comparison in Section 2.3.3 was largely written by co-author Jo Bovy. Some sections of the introduction providing background on the Mirror Twin Higgs hypothesis was written by co-author David Curtin.

## 2.1 Abstract

The Legacy Survey of Space and Time (LSST) with the Vera Rubin Observatory will provide strong microlensing constraints on dark compact objects (DCOs) in our Galaxy. However, most current forecasts limit their analysis to Primordial Black Holes (PBH). It is unclear how well LSST microlensing will be able to constrain alternative models of DCOs with different Galactic spatial profile distributions at a subdominant DM fraction. In this work, we investigate how well LSST microlensing will constrain spherical or disk-like Galactic spatial distributions of DCOs, taking into account extended observing times, baryonic microlensing background, and sky distribution of LSST sources. These extensions represent significant improvements over existing microlensing forecasts in terms of both accuracy and versatility. We demonstrate this power by deriving new LSST sensitivity projections for DCOs in spherical and disk-like distributions. We forecast that LSST will be able to constrain one solar mass PBHs to have a DM fraction under $4.1 \times 10^{-4}$. One-solar-mass objects in a dark disk distribution with the same dimensions as the Galactic disk will be constrained below $3.1 \times 10^{-4}$, while those with $m = 10^5 M_\odot$ will be constrained to below $3.4 \times 10^{-5}$. We find that compressed dark disks can be constrained up to a factor of $\sim 10$ better than ones with identical dimensions to the baryonic disk. We also find that dark disks become less tightly constrained when they are tilted with respect to our own disk. This forecasting software is a versatile tool, capable of constraining any model of DCOs in the Milky Way with microlensing, and is made publically available.

## 2.2 Introduction

As discussed in Section 1.4.1, microlensing is a phenomenon whereby a massive object passes directly in front of a bright background source, gravitationally lensing the light [153, 12]. However, the Einstein ring created by the strong lensing in these cases is too small to be resolved by most telescopes, so the event manifests only as a temporary brightening of the background object. This temporary brightening can be detected with long-term photometric survey telescopes, and can be distinguished from other transients by its achromatic and time-symmetric lightcurve. Characterizing the number of microlensing events we see in a given survey can put constraints on the number of dark compact objects in our Galaxy, allowing us to constrain models of compact DM. This technique has been used in the past to rule out MAssive Compact Halo ObjectS (MACHOS) for a variety of mass ranges comprising 100% of the DM in our halo [12, 211]. Future surveys, such as the Legacy Survey of Space and Time (LSST) at the Vera C. Rubin Observatory, should be able to push the constraint on MACHO DM fraction much lower due to its increased sensitivity and number of target sources [176, 66]. It will also be able to use paralensing (a periodic feature imposed on the lensing signal due to parallax effects) to detect microlensing events with arbitrarily long crossing times [84]. Paralensing has been observed in past surveys [211, 83], but never with the large number of sources available to LSST.

Fig. 2.1 shows forecast constraints on the fraction of halo DM consisting of DCOs. It is clear that LSST will do much better than past experiments detecting microlensing in either the Milky Way (MW$\mu$L) or the Andromeda Galaxy (M31$\mu$L) (based on past microlensing surveys [13, 198, 212, 152]). The past LSST forecasts (in orange) are taken from [66]. The new forecast for this compact DM distribution (in blue) are one subject of this paper.

It is not obvious how these constraints would translate onto alternative theories of compact dark matter that do not follow a spherically symmetric galactic distribution. This is due to the fact that these forecasts, [66] assume that the compact objects being investigated by LSST are Primordial Black Holes (PBH). Primordial Black Holes have a strong theoretical justification (only requiring minor adjustments to early-universe physics and minimal extensions to the SM) and their existence has been suggested as an explanation of some of the higher-mass binary black hole pairs detected by LIGO. Thus it is understandable for past microlensing analysis to focus on them as the primary compact DM candidate [3, 65, 106]. PBHs are assumed to have a spherically symmetric Navarro-Frenk-White (NFW) galactic distribution [149] of the form

$$\rho_{\mathrm{NFW}}(r) = \frac{\rho_0}{\left(\frac{r}{r_s}\right)\left(1+\frac{r}{r_s}\right)^2} \tag{2.1}$$

with the parameters of $\rho_0 = 0.014\ \mathrm{M}_\odot\ \mathrm{pc}^{-3}$ and $R_s = 16$ kpc [151, 35, 33]. This assumption, along with several other simplifications made in the calculations of [66], play a significant role in deriving Rubin's sensitivity to the dark object DM fraction. Therefore, alternative models of compact dark matter – beyond the leading PBH candidate – would be constrained differently by the same survey.

Particularly interesting are models of *dissipative* dark matter, i.e., dark matter that emits dark radiation and can therefore cool efficiently. One example of a dissipative DM model is mirror sector DM, introduced in Section 1.2.3, which can form mirror stars and a mirror galactic disk. The size and mass of these compact objects depends on the details of the model, being set essentially by

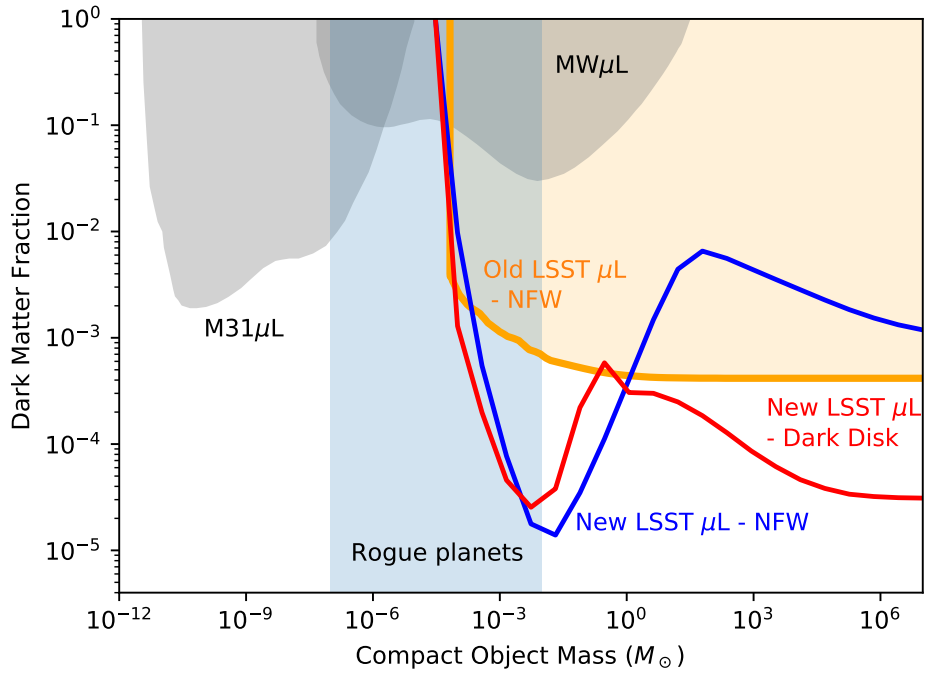


Figure 2.1: Past and future constraints on the DM fraction of dark compact objects in our Galaxy as a function of object mass, with shaded regions being constrained. The MW$\mu$L curves are from the MACHO and OGLE surveys of the LMC and Galactic bulge [13, 198, 212]. The M31$\mu$L curve is from detecting microlensing in stars in the M31 galaxy [152]. The orange curve represents current forecast microlensing constraints from LSST, as described in [66]. The blue curve shows the new constraints calculated in this paper, using full observing runtime, baryonic microlensing background rates, multiple lines of sight, and variable lens velocity distributions. Both the orange and blue curves assume a spherically-symmetric NFW distribution of dark compact objects [149]. See Section 2.4 for a more details on this computation. The red curve shows the forecast constraints on dark compact objects in a benchmark dark disk distribution, parameterized as a fraction of total dark matter. This dark disk has a double exponential profile with the same size and shape as our Galactic disk, but with a delta function mass distribution. See Section 2.5.2 for details and constraints for generalized dark disks. The pale blue band indicates the mass range where unknown numbers of rogue planets may exist in interstellar space, creating an irreducible systematic that would impede searches for dark compact objects in that range. Note that the Roman space telescope will eventually impose constraints on this plot as well (as discussed in [108]), but that these constraints will likely not surpass those from Rubin.

the self-interactions and cooling rate of the dissipative subcomponent, as well as possible sources of feedback. In principle. any such model can be constrained by microlensing observations, and the Rubin observatory will be able to offer the best constraints yet for a broad region of the parameter space.[1]

The Rubin Observatory should be able to probe the existence and properties of such a mirror star population in our Galaxy, independent of any electromagnetic signals they may or may not generate. However, the different mass and spatial Galactic distributions of mirror stars compared to PBH's change how well Rubin will be able to constrain the fraction of our DM halo consisting of mirror stars with microlensing. The details of how the properties of the mirror-sector model would connect to the mass and spatial distributions of the mirror stars are complicated and as-yet unsolved [57]. Therefore, it is important to formulate model-independent microlensing constraints on DCOs in Galactic distributions that are more general than that of PBHs, so that they might eventually be applied to a variety of Dark Disk models.

Other exotic compact objects that can appear in new physics models are boson stars [199, 94, 113], including axion stars [113, 23, 70]. A wide range of masses are possible for such objects, depending on the parameters of the model in question. We also direct the reader to a recent study on the effect of size and density distribution of extended structures on microlensing signals [54, 55].

Given the variety of dark sector models that can give rise to exotic compact objects, it would be helpful to anticipate how well the Rubin Observatory can constrain dark compact objects with an arbitrary Galactic spatial and mass distribution. This would give a flexible way to calculate constraints that could change depending on the uncertainties in our understanding of mirror sector astrophysics, or other models of dark compact objects. In this paper, we produce numerical forecasts for microlensing with the Rubin observatory that take as input an arbitrary functional form for the Galactic spatial distributions of dark compact objects, and predict the constraints Rubin will be able to impose on the DM fraction. Our software is made publicly available at [207], and can be used to compute forecast constraints for any arbitrary spatial distribution of dark compact objects. These constraints also include a number of systematic improvements over the initial forecasts by [66] by including variable survey length, background baryonic microlensing events, and the contribution from multiple lines of sight. Note that these constraints might be subject to change, depending on the final choice of observing strategies decided upon by the Rubin collaboration; further discussion on the impact of observing strategies can be found in [176]. In addition to being very helpful for the development of mirror-sector astrophysics (being able to anticipate the constraining power for different Galactic and stellar models), this code is generally applicable for any theory of complex self-interacting DM that could produce dark compact objects.

One potential difficulty in detecting dark objects in the $\sim 10^{-3} M_\odot$ range is that past microlensing surveys have suggested the presence of wandering Jovian planets in our Galaxy, which would be indistinguishable from dark compact objects [188, 189]. Until we better understand this population of Jovian lenses, the prospects for positively detecting dark objects in this mass range are uncertain. (We should also note that the mass range most impacted by rogue Jovian planets (from roughly $10^{-7}$ to $10^{-2} M_\odot$) is also the mass range most impacted by changes in the observing cadence or sensitivity of LSST, adding to the uncertainties in this range.)

[1] Other gravitational probes of dark disks include measurements of the local matter density, which can constrain extremely thin dark disks with thickness $< 100$ pc to contain $< 1\%$ of the Milky Way's DM [181, 38]

In Section 3.3, we explain how the microlensing constraints were calculated from theoretical microlensing rates. We also explain several of the novel improvements to our calculations of microlensing sensitivity, such as the inclusion of extended observing times in 2.3.1, baryonic microlensing background events in 2.3.2 and 2.3.3, realistic velocity distributions in 2.3.4, and combined constraints from multiple lines of sight in 2.3.5. In Section 2.4, we show the effect that including each of these improvements has on our forecast microlensing constraints for spherical distributions of dark compact objects. Finally, in Section 2.5, we discuss constraints on alternative distributions of dark compact objects, such as a flattened halo in 2.5.1, a dark disk rescaled with respect to our own baryonic disk in 2.5.2 that may apply to mirror stars, and a dark disk that is tilted with respect to our own in 2.5.3. Section 2.5.4 presents some possible trivial and non-trivial extensions to this work using the software. Final conclusions are presented in Section 2.6.

## 2.3 Methods: Microlensing Computations

In order to put constraints on the quantity of dark objects in the Galaxy, we need to estimate the average number of microlensing events by dark compact objects that should be seen, given an assumed density of dark compact objects, and then calculate the probability of observing some actual number of observed events. This actual number could be zero, in the case of no positive events, or simply the estimated number of microlensing events caused by baryonic compact objects (also known as stars and planets). We can then determine the maximum dark matter fraction that could be consistent with some fiducial result in order to estimate the resulting constraints. We set the mass distribution of dark compact objects to be delta functions in the calculations that follow, both for simplicity and for comparison to earlier calculations. This overestimates the sensitivity of microlensing to small dark matter fractions compared to more realistically spread-out mass distributions, but we leave a quantitative analysis of LSST sensitivity to continuous mass distributions of DCOs for future study.

### 2.3.1 The expected number of microlensing events in a survey

In [66], the expected number of microlensing events was calculated using only the optical depth to microlensing, which estimates the number of sources undergoing a microlensing event at any single point in time. However, this calculation does not take into account the full survey time, as short events could experience more detections if the telescope operates for $\sim 12$ years, as Rubin is expected to. As discussed in Section 1.4.1 and presented in Eq. (1.76), in order to calculate the expected number of microlensing events over an extended period of time ($N_{\rm expected}$), we need to calculate the differential microlensing event rate per unit crossing time, multiply by the detection efficiency for events with that crossing time ($\xi(\hat{t})$), multiply by the range of times over which an event of a given crossing time could start and we would still detect it, and then integrate over crossing time. This gives some total number of microlensing events observed per source, which can then be scaled to the $\approx 4$ billion stars anticipated to be seen by LSST in each observation [66, 128] [2]. This

[2]Technically, microlensing can occur with either a star or a quasar as the source. However, for our analysis, we have used the expected number of stars resolvable by Rubin (4 billion), and neglected the number of quasars. This is because LSST is expected to observe only 10 million quasars, representing a correction of roughly 0.25% to our number of sources, and thus our estimated number of microlensing events [102, 128]. Some work has been done using microlensing from quasars, such as [19].

technique can be used to estimate both the number of dark and baryonic microlensing events, using different mass and Galactic distribution functions.

### 2.3.2 Baryonic microlensing comparison

The calculations in [66] assume that we will observe zero microlensing events with Rubin, and then calculate the DM fraction required to make the predicted number of events fall below one. However, in reality, we should observe many microlensing events, simply from ordinary baryonic stars crossing the lines of sight to background sources. Taken in isolation, these events would be indistinguishable from microlensing events caused by DCOs. This is due to the fact that the lens star would be so close to the background source star that they would likely be unresolvable with the telescope used (otherwise the lensing event would be classified as strong lensing and not microlensing). Although it would be theoretically possible to conduct a spectroscopic or multi-band analysis to determine the presence of two stars, we make the conservative assumption that this analysis is not done. Barring such analysis, the only way to distinguish the dark and baryonic microlensing events is by computing their statistical distribution (in both crossing time $\hat{t}$ and location on the sky $\vec{y}$) and comparing it to the distribution expected from baryonic stars. One microlensing event is not enough to be a detection — we can only claim to have detected a number of DCO microlensing events if that number is greater than the uncertainty on the number of baryonic microlensing events of the same crossing time. This uncertainty must incorporate both inherent Poisson uncertainty on the number of baryonic microlensing events, and measurement uncertainty on the number of stars in our Galaxy, which we estimate to be roughly a 5% uncertainty on the number of stars in any given mass bin, consistent with [34].

In order to calculate the baryonic microlensing event rate, we use the same procedure for calculating the dark object event rate discussed in Section 2.3.1, replacing the dark object density profile with a simple double-exponential Galactic disk model

$$\rho_{\rm star}(R,z) = A_b \exp\left(-\frac{(R-R_0)}{h_R}\right)\exp\left(-\frac{|z|}{h_z}\right) \tag{2.2}$$

where $A_b = 0.04 M_\odot\,{\rm pc}^{-3}$ is the local stellar density [34], $R_0 = 8.2$ kpc is the Sun's distance from the Galactic center, and $h_R = 3$ kpc and $h_z = 400$ pc are the radial and vertical scale lengths, respectively [33]. We also must take into account the mass distribution of baryonic stars, using a normalized Kroupa initial mass function (IMF) [116] of

$$N_*(m) = C m^{-\alpha}, \tag{2.3}$$

where

$$\alpha = \begin{cases} 0.3\,, & m \leq 0.08\,M_\odot \\ 1.3\,, & 0.08\,M_\odot < m \leq 0.5\,M_\odot \\ 2.3\,, & 0.5\,M_\odot < m \end{cases}. \tag{2.4}$$

This distribution is intended to reflect the population of both stellar lenses and compact stellar remnants, which are still produced according to the stellar IMF and could act as non-luminous lenses. It is of course the case that compact stellar remnants will be less massive than the high-mass stars

that created them, meaning the IMF overestimates the abundance of high-mass objects compared to the real present-day mass distribution. On the other hand, the stellar remnant contribution to lower mass populations is negligible in relative terms. This overestimation of the baryonic lens population means that our projections for the Rubin sensitivity to DCOs must be regarded as a conservative estimate, and the real constraints may be slightly more stringent in the high-stellar-mass range.

The distinction between luminous and non-luminous baryonic lenses is not relevant for our work, as the resulting microlensing events would only be distinguishable via spectroscopic or multi-band analysis, which we assume is not done, though it could be the subject of dedicated additional observations. If such an analysis were conducted, some of the microlensing events from luminous baryonic lenses could be positively identified, potentially tightening the resulting constraints on DCOs. However, the feasibility of such an analysis is outside the scope of this work, so we defer to the conservative assumption that no attempt to spectrally identify baryonic lensing events is conducted. Therefore, microlensing events from DCOs, compact stellar remnants, and luminous stars are all considered indistinguishable, with the only defining features being the event crossing time and location on the sky.

### 2.3.3 Probabilistic comparison of Dark and Baryonic Microlensing

Next we calculate the probability of a certain dark matter fraction given a certain observed number of events, and the theoretical expectation of how many dark and baryonic events we should see. We also need to incorporate our uncertainty on the total amount of baryonic stars in the Galaxy. This can be done by leveraging Bayes' theorem, described in Section 1.5.1. Let us first assume that our basic model of the observations is characterized by two parameters: $f_{\rm DM}$, that sets the fraction of DM in compact objects in our assumed distribution, and a parameter $\alpha_b$, that scales the expected baryon density, with $\alpha_b = 1$ corresponding to our fiducial baryon model from equation (2.2) above. We also assume a prior constraint on $\alpha_b$ that it has an uncertainty of 5%, that is, $p(\alpha_b) = \mathcal{N}(\alpha_b|1, 0.05^2)$, where $\mathcal{N}(x|\mu, \sigma^2)$ is the Gaussian distribution for $x$ with mean $\mu$ and variance $\sigma^2$. We assume a uniform prior on $f_{\rm DM}$ between 0 and 1, so $p(f_{\rm DM}) = 1$ on $0 \leq f_{\rm DM} \leq 1$, and $= 0$ elsewhere. We use a simulated set of microlensing events calculated using the method above, consisting of event rates for $N_{LoS}$ lines of sight, each representing $n_s$ number of actual sources. For a given simulated set of data consisting of numbers of microlensing events $D = \{N(\hat{t}^*, \vec{y})\}$ observed in bins in duration $\hat{t}^*$ and line-of-sight $\vec{y}$, the posterior distribution is

$$p(f_{\rm DM}, \alpha_b|\{N(\hat{t}^*, \vec{y})\}) \propto p(\{N(\hat{t}^*, \vec{y})\}|f_{\rm DM}, \alpha_b)\, p(\alpha_b)\, p(f_{\rm DM}) \tag{2.5}$$

where the likelihood is given by

$$p(\{N(\hat{t}^*, \vec{y})\}|f_{\rm DM}, \alpha_b) = \prod_{\hat{t}^*, \vec{y}} \left[\mathrm{Poi}(N(\hat{t}^*, \vec{y})|\left[N_{\rm DM}(\hat{t}^*, \vec{y}; f_{\rm DM}) + \alpha_b\, N_{\rm star}(\hat{t}^*, \vec{y})\right])\right]^{n_s} \tag{2.6}$$

where $\mathrm{Poi}(N, \lambda)$ is the Poisson distribution (see Section 1.5.2) for the number of events $N$ given average expected number of events $\lambda$. $N_{\rm DM}(\hat{t}^*, \vec{y}; f_{\rm DM})$ is the number of dark matter events predicted for the given $f_{\rm DM}$, and $N_{\rm star}(\hat{t}^*, \vec{y})$ is the number of baryonic events for the fiducial model (and is therefore scaled by $\alpha_b$). The power of $n_s$ represents the fact that this probability is being computed for $n_s$ individual sources along each line of sight, but that we are approximating the event rates

as all being equal to $N(\hat{t}^*, \vec{y})$. We thus take the product of all the likelihoods, corresponding to the joint likelihood from all the real sources that each line of sight represents. Marginalizing the posterior distribution over $\alpha_b$ then gives

$$p(f_{\rm DM}|\{N(\hat{t}^*,\vec{y})\}) \propto p(f_{\rm DM}) \times \int {\rm d}\alpha_b\, p(\alpha_b) \prod_{\hat{t}^*,\vec{y}} \left[{\rm Poi}(N(\hat{t}^*,\vec{y})|[N_{\rm DM}(\hat{t}^*,\vec{y};f_{\rm DM}) + \alpha_b\, N_{\rm star}(\hat{t}^*,\vec{y})])\right]^{n_s}. \tag{2.7}$$

Constraining $f_{\rm DM}$ to a given confidence level $C$ (e.g., $C = 0.95$ for 95% confidence $\approx 2\sigma$) then requires us to (a) simulate a set of events $\{N(\hat{t}^*, \vec{y})\}$ assuming that $f_{\rm DM} = 0$ and $\alpha_b = 1$ and (b) for a given DM distribution, find $f_{\rm DM}$ such that $\int {\rm d}f_{\rm DM}\, p(f_{\rm DM}|\{N(\hat{t}^*,\vec{y})\}) = C$.

If we were performing this analysis with a real survey, in addition to modifying the survey parameters that go into $N_{\rm DM}(\hat{t}_\star, \vec{y})$ and $N_{\rm star}(\hat{t}_\star, \vec{y})$, we would also replace the expected number of events $N(\hat{t}_\star, \vec{y})$ with the actual number of events seen along a given sight line $\vec{y}$ and with given crossing time $\hat{t}_\star$. In the case of Rubin, this actual collection of microlensing events will be assembled using the LSST transient pipeline to flag and save probable microlensing transient events, as described in Sec. 1.4.1. The resulting limits on $f_{\rm DM}$ may or may not be consistent with zero, depending on whether this dataset prefers the presence or absence of a DCO population.

### 2.3.4 Dark Compact Object Velocity Distributions

In addition to having a different density distribution function from the DM, microlensing with baryonic stars or a disk of dark compact objects also involves a different velocity distribution function because we can no longer assume that the lens velocities are isotropic, but are instead co-rotating along with us. This requires more complicated calculations of lens velocities.

For this first treatment of dark compact objects in disk-like distributions, we assume that the circular velocity and velocity dispersion profiles are identical to those of the Milky Way. This should be a reasonable approximation for dark disks that are subdominant in mass to the baryonic disk. The rotation curves are generated using the Galactic dynamics Python library `galpy`, assuming a standard NFW halo dominating the galactic gravitational potential [33]. Thus the average velocity at a given radius from the Galactic center is fixed by the object's position (and the angular tilt of the dark disk). In this case the relative velocity $v_c$ to be used in equation (1.75) is the relative velocity of the lens and source transverse to the line of sight, that is,

$$v_c = |\vec{v}^{\perp}_{source} - \vec{v}^{\perp}_{lens}|, \tag{2.8}$$

where the superscript $\perp$ indicates the component transverse to the line of sight connecting the Earth and the source. Since both the source and the lens can be co-rotating with the sun with a similar circular velocity, $v_c$ can be significantly less than the average value of $220\,{\rm km\,s^{-1}}$ that one would expect for an isotropic dark matter halo profile.

### 2.3.5 Simulating LSST sources

Calculations of the microlensing event rate require integrating the DM density along the line of sight to a source. In order to greatly simplify their calculation, [66] placed all of the expected LSST sources at the centre of the Galactic bulge, so they only needed to calculate the event rate along a

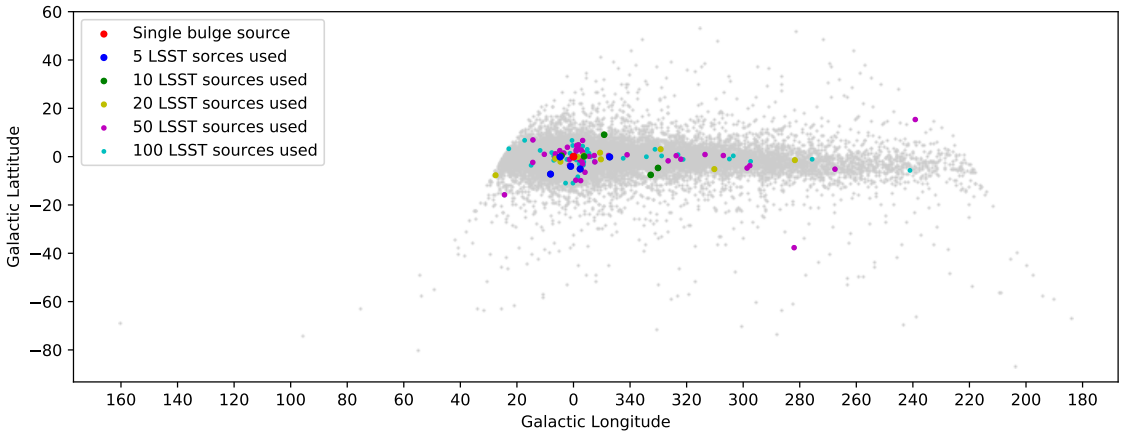


Figure 2.2: Sky distribution in Galactic coordinates of the simulated LSST stars generated using Galaxia, along with the randomly chosen 5, 10, 20, 50, and 100 sources used to calculate microlensing event rates. It is clear that the locations of these random stars is fairly representative of the total coordinate distribution of LSST objects.

single line of sight, and then multiplied by the number of sources to get the final expected number of events. Although this is a reasonable assumption for a crude first estimate, because the amount of dark matter between us and the Galactic bulge is fairly typical of a source star [204] and many of the sources are in the Galactic bulge, having a single line of sight makes it difficult to understand how sensitive Rubin would be to alternative dark object density distributions that may vary over multiple lines of sight.

Ideally, we would calculate the microlensing event rate to every one of the $\sim 4 \times 10^9$ sources that Rubin will observe in the r-band with each pass, but given that each calculation takes around 20 seconds on a single CPU core, this calculation is computationally unfeasible[128]. Instead, we simulate a smaller number of LSST sources with a statistically representative distribution of coordinates and distances, calculate the microlensing event rate along each of these lines of sight, and then multiply the sum of microlensing events by the number of real sources per line of sight to get our total number of sources up to $4 \times 10^9$.

To create a list of representative LSST sources, we use the software `Galaxia` [184], which produces simulated surveys based on a complex model of the Milky Way's stellar populations and given survey parameters. We used the Rubin Observatory's single-visit magnitude limit of 24.5, using just the i band (to reflect the superior point spread function in the i-band, maximizing the number of resolvable sources) [103]. Since microlensing is an achromatic event, the band chosen for this simulated survey should not have a large impact on our results, as long as the simulated survey approximately captures the distribution of stars resolvable by Rubin. We centred the Galaxia simulated survey on the equatorial south pole, covering an area of 18000 square degrees (to approximately match the observing area of the LSST survey described in [66]). We apply a filter to only return a random fraction of the sources in order to produce a manageable amount of data. Setting this fraction to $f_{\text{sample}} = 10^{-6}$ returned a manageable number of sources, while still providing a representative sampling of the Galactic distribution. The Galactic coordinates of these 86,186 sources are plotted in grey in Fig. 2.2, where a clear disk and bulge structure can be seen. This simulated survey is

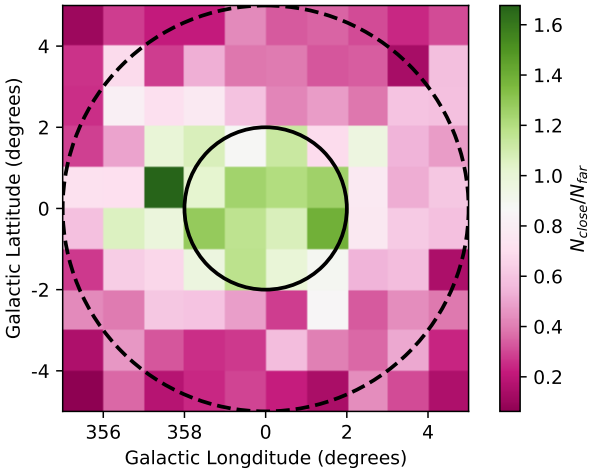


Figure 2.3: Ratio of the number of simulated sources that would be indistinguishable from their neighbours with an LSST resolution of 0.65 arcseonds ($N_{\rm close}$) compared to the number that are sufficiently far away from their neighbours ($N_{\rm far}$) for each 1-pixel square on the sky around the Galactic bulge. Green squares have the majority of their sources indistinguishable from a neighbour, suggesting that LSST will have difficulty measuring individual lightcurves of sources in this region. The circle radii indicate a 2-degree and 5-degree mask of the core, limiting the sources considered to be ones that LSST is likely to be able to resolve.

used as a placeholder for LSST sources, and it would be ideal in future work to use a real source catalogue from Rubin once the survey is operational.

Even this number of sources is impractically large to perform microlensing calculations on every line of sight. Instead, we randomly select some number of these sources, calculate microlensing rates along those lines of sight, and then multiply the resulting event numbers by an appropriate normalization factor to get the correct total number of sources. The subsamples of sources are shown in various colors in Fig. 2.2.

One limitation of this simulated survey is that the Galaxia software does not include the Large and Small Magellanic Clouds (LMC and SMC) in their source catalogues. This is unfortunate, as the LMC and SMC will provide some key lines of sight that cut through the Dark Matter Halo while avoiding much of the Galactic plane, therefore probing the spatial lens distribution. Not including these key sightlines makes all of our constraints conservative, as the real LSST source catalogue will include these helpful sightlines. Analyzing the impact of LMC and SMC sightlines of LSST microlensing is left for future work.

There is some concern that LSST will be unable to resolve closely-spaced sources in dense regions of the sky, such as the Galactic bulge [204, 167]; this will make microlensing with these unresolved sources difficult to analyze. In order to estimate how many sources might be unresolved, we calculate the number of simulated Galaxia sources that are close enough to a neighbour that most of the real sources represented by that Galaxia source would be unresolved, based on the estimated resolution of Rubin of 0.65 arcseconds[104]. We use this to calculate where on the sky the majority of sources are likely to be unresolved as opposed to resolvable. Figure 2.3 shows which 1-degree regions of the sky around the Galactic bulge are expected to have more resolved or unresolved sources according

to our simulated source catalogue. Since these regions present possible difficulties for microlensing, we create duplicate source catalogues with all sources within either two degrees or five degrees of the Galactic core completely masked from the sample. These masked catalogues provide the opportunity to test the dependence of forecasted constraints on this less reliable bulge region. This masking of of the core will not appreciably change the total number of sources, as Rubin is expected to observe around 172 thousand sources per square degree in that area [128], meaning that a circular mask with radius of five degrees would only mask around $1.4 \times 10^7$ sources, which is less than 0.4% of the $4 \times 10^9$ total sources expected to be resolved each visit. This correction is negligible compared to the uncertainty in the estimated number of LSST sources, and as such is ignored. [3]

## 2.4 Results: Improved Projected Microlensing Constraints on Primordial Black Holes

In this section, we explain how each of the changes to the [66] methodology mentioned above affected the microlensing rates, and thus changed the constraints on $f_{\rm DM}$ for a sherically-symmetric NFW distribution of PBHs. The mass-dependent constraints on $f_{\rm DM}$ are shown in Fig. 2.4 and Fig. 2.5 for a variety of assumptions, such that we can see the impact of each of the improvements implemented.

The first improvement involved using the microlensing rate integrated over a longer period of time, instead of simply using the optical depth to microlensing at a fixed moment in time. These results are shown in Figure 2.4. When we use the full LSST length of 12 years, our constraints improve considerably for low masses (shown by the solid line). This is due to the fact that objects of mass $10^{-2} M_\odot$ would have an average crossing time of  1 day, so we should detect around three orders of magnitude more over the entire length of the twelve-year survey. This improvement is irrespective of the fractional detectability of these events, as longer survey times will provide more events that could possibly be detected. Therefore, our constraint projections for objects of this mass improve by around three orders of magnitude. The dashed lines in Fig. 2.4 shows an intermediate cases of 1 year or 4 years spent surveying the Milky Way.

Secondly, we can see in Fig. 2.5 the effects of considering baryonic microlensing, and how these baryonic microlensing rates differ for different choices of line of sight. We can see that including baryonic microlensing backgrounds weakens the constraints around the $1 M_\odot$ range, as this is where we would expect many baryonic microlensing events from stars, and thus would require more dark events to warrant a significant detection. This figure also shows how the constraints (and the impact of baryons) changes depending on which lines of sight we use to represent the entire Rubin source catalogue in our sensitivity projections. The three colors (red, green, and blue) respond to approximating all the sources as either: living in the Galactic core, living in the Large Magellanic Cloud (LMC; outside the disk and on the far side of the Galaxy), or using 100 random sources drawn from our simulated Rubin catalogue respectively [4].

[3] We recognize that there is significant uncertainty on the estimated density of LSST sources in the Galactic core, and that work such as [179], [177], and [166] have reached different estimates than the LSST Science book cited above. However, the key value for our analysis is the total number of sources *outside* the Galactic core, which have fewer uncertainties than the core density. Therefore, we feel comfortable using the internally-consistent values quoted in [128]. Real data from LSST will, of course, determine whether these estimated source counts were accurate, and may require future revisions to our estimates.

[4] The LMC is chosen for comparison because it has been used in the past for microlensing surveys such as MACHO [13]. However, placing the LMC constraints alongside those for the core or for a sample of LSST sources is somewhat

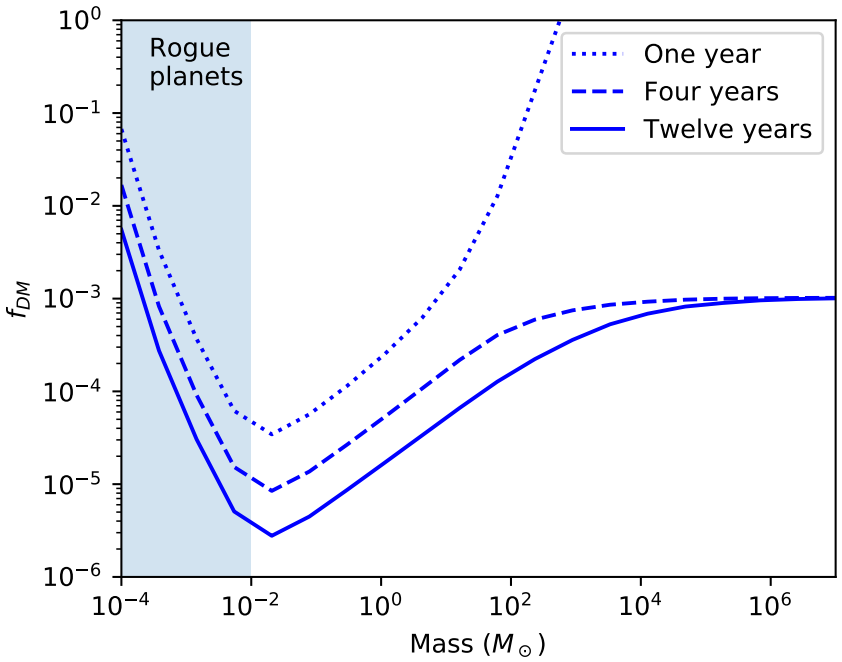


Figure 2.4: Constraints on the DM fraction of dark objects in a spherical NFW distribution as a function of object mass, with variable survey lengths. All constraints here are calculated using a sampling of the sky distribution with 100 lines of sight. Baryonic foregrounds were not included in this calculation. Depending on the length of time LSST spends surveying the Milky Way, constraints could be significantly improved on low mass objects, as we would expect much higher numbers of these events over the course of the survey. Note that the high-mass constraints are considerably weaker for a survey just one year in length, as this reduced survey time would make it almost impossible to conduct paralensing with the data, which is essential for constraining high-mass objects.

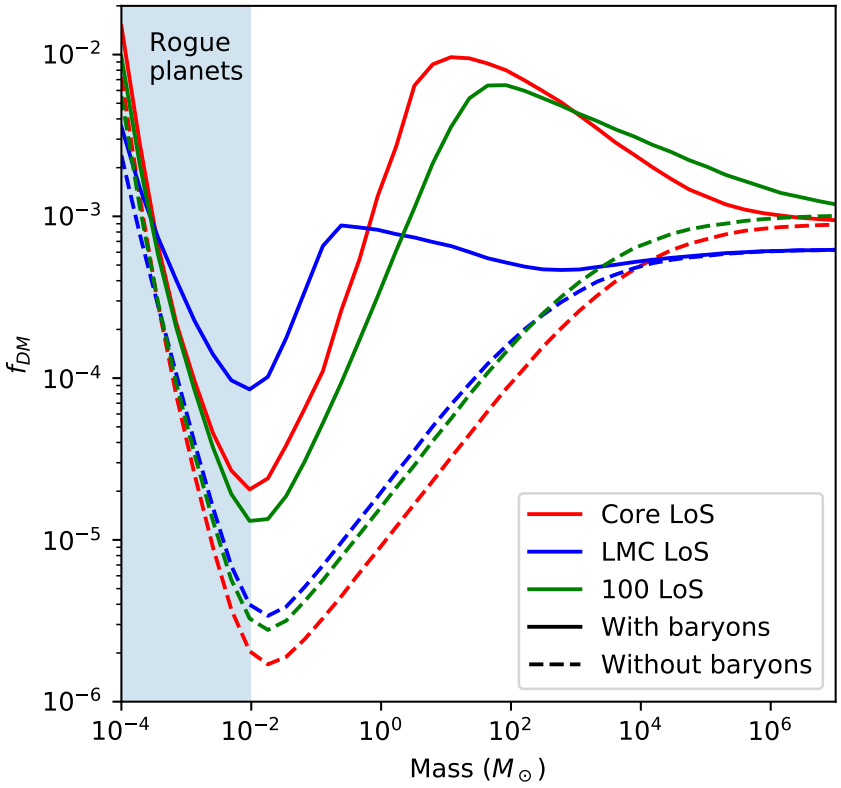


Figure 2.5: Constraints on the DM fraction of dark objects in a spherical NFW distribution as a function of object mass, showing the effects of multiple lines of sight and incorporating baryonic microlensing. The dashed lines reflect constraints assuming zero baryonic microlensing, while the solid lines represent constraints weakened by the confusion with baryonic microlensing events. With a single line of sight to the Galactic core, the baryon-free constraints are the strongest due to the large amount of DM between us and the core, but adding baryons significantly weakens our core constraints. However, the constraints computed using a more realistic 100 representative lines of sight is less impacted by baryons, as some lines of sight are slightly out of the Galactic disk, and thus less impacted by baryonic microlensing. Note that the blue curve represents constraints using the same total number of sources as the other constraints, but assuming these sources are all located in the LMC. We understand that the LSST survey will not contain this many sources in the LMC, but we have including these fictional constraints for comparison purposes, to demonstrate the qualitative impact of the LMC sightlines and to show the strengths and weaknesses of using a range of sources instead of just the LMC, as has been done in past microlensing surveys [13].

The slight mass-shift of the baryonic bump in the three cases is primarily the result of different perpendicular velocities of baryonic stars along each of the three lines of sight. The core constraints (in red) are made in a region with a lot of baryonic stars (along the plane of the Galactic disk), and as a result the bump there is quite large. The LMC constraints, on the other hand, have a line of sight that passes through the far side of the Galactic disk as well, so it will encounter stars moving in the opposite direction to Earth's orbit. This will lead to the baryonic microlensing events being shorter in duration, so they would be confused for lower-mass dark microlensing events, which is why the baryon-bump for the LMC source is shifted to the left. For the 100 LSST lines of sight, some lines of sight will be looking along the disk either to the left or right of the Galactic core, resulting in the transverse velocities of the baryonic stars being much smaller than when looking directly into the core. This makes those microlensing events longer in duration, so they will be confused for more massive dark objects. We also note that the distribution of objects along the line of sight (ie. the distance) can also impact the crossing times, and thus which mass ranges are most impacted by baryonic microlensing. However, since the distance distribution of dark and baryonic objects for most lines of sight is qualitatively similar (increasing towards the Galactic centre, and decreasing away from it), we conclude that changes in the transverse velocities are the driving reason behind the mass-shifts of the bumps seen in Figure 2.5. This result illustrates the importance of properly incorporating the effects of different lines of sight and velocities on baryonic microlensing.

Lastly, we can characterize the impact of including multiple lines of sight, as opposed to calculating the microlensing rate for a single line of sight between us and the Galactic bulge. We can see in Fig. 2.5 that using 100 lines of sight as opposed to one core line of sight changes the impact of baryonic microlensing rates over a range of object masses. Fig. 2.6 shows how the constraints for one solar-mass dark objects change depending on the number of lines of sight. For reference, the red line shows the constraints for a single line of sight between us and the Galactic bulge, while the blue line is a reference for constraints using the LMC. We can see that the constraints change as we use more lines of sight, but begin to stabilize after around 50 lines of sight. We use 100 lines of sight for all other calculations in this paper, as it is within 0.1 orders of magnitude of the limit at 1000 lines of sight, but is still able to be computed in a reasonable amount of time. Our final projected sensitivity constraints can therefore be interpreted as having a $\sim 30\%$ level of statistical error, which is sufficient for our purposes.

## 2.5 Results: Projected Constraints on Alternative Density Models

In the previous section, we explained how our estimates of microlensing constraints improve upon previous calculations, and how they are sensitive to events at many locations in the Galaxy. These modifications produce a more realistic forecast of constraints on regular spherically-distributed models of compact DM, as shown in Fig. 2.1. Another important advantage of these improvements is that they allow us to reliably predict the sensitivity of Rubin for non-spherical distributions of compact DM, as was motivated in the Introduction. For example, one interesting case is that of

fictitious, as we assume the same number of total sources located at each of these locations, and it would be impossible to get $4\times10^9$ sources in the LMC using existing telescopes. Also note that LSST may end up using a different observing cadence for the LMC than for the rest of the Galactic plane, and this should be incorporated into any serious analysis of LSST microlensing in the LMC.

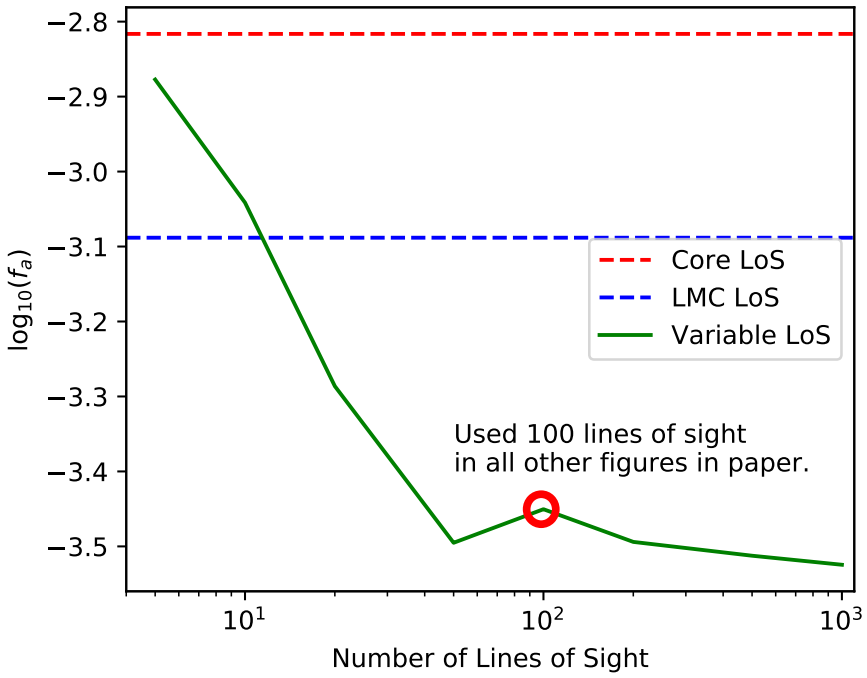


Figure 2.6: Constraints on the fraction of 1 $M_\odot$ dark objects, as more sight lines representing the sky distribution of LSST sources are added to our analysis. We are assuming a spherical NFW dark object distribution, and including the effects of baryonic backgrounds. It is clear that convergence to the realistic sensitivity is achieved with about $\sim 100$ lines of sight. This also gives much better constraints than approximating all sightlines as being in either the Galactic core or the LMC. For this reason, we have chosen to use 100 lines of sight for all other plots in this paper, as it is shown here to be accurate to within around 0.1 orders of magnitude, or 30%, of the fully converged result.

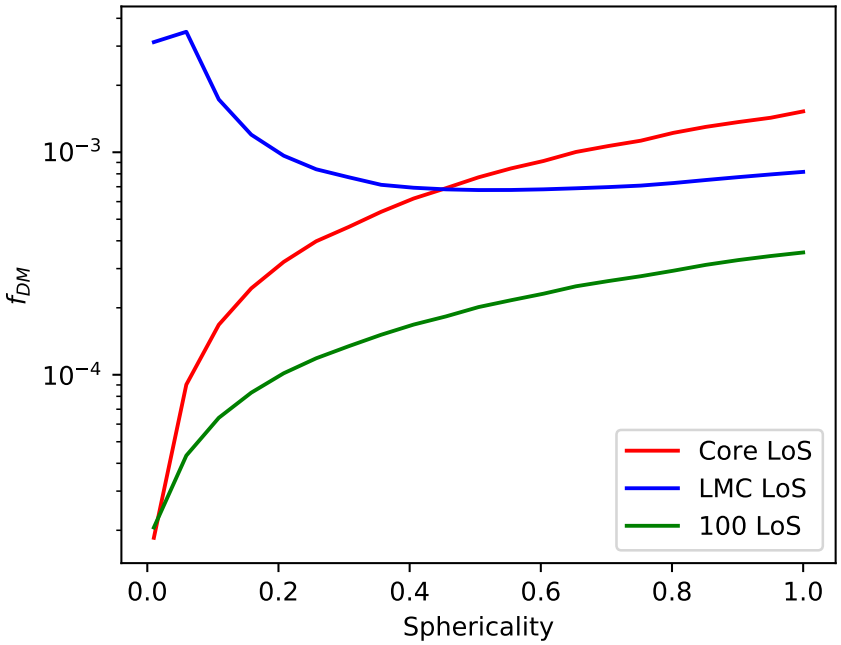


Figure 2.7: Constraints on the compact DM fraction for one-solar-mass objects as a function of the sphericality ($q$) of the DCO Galactic distribution. The NFW halo is being flattened with respect to parameter $q$ as shown in Equation (10). We can see that using sources in the LMC is less helpful at constraining flattened distributions of DCOs, while approximating all sources to be at the core runs the risk of overestimating the impact of compressed sphericality on the constraints. From this we conclude that using a representative distribution of lines of sight is essential for constraining non-spherical distributions of DCOs.

a mirror disk of dark compact objects resembling our baryonic Galactic disk up to some rescaling or rotation and comprising only a few percent of the total dark matter in our Galaxy (as was introduced in Section 1.2.3). Note that only a fraction of the total mirror matter in the dark disk would be expected to have formed compact objects, just as in the visible disk, and it is this compact dark object density distribution that we are concerned with. Their low fraction of the total DM abundance makes it difficult for these dark disks to be constrained by Galactic dynamics, especially if they have non-negligible disk height (for constraints on a very "thin" disk scenario from stellar kinematics, see [180] and [38]). Fortunately, microlensing has the potential to set tight constraints on the compact-object fraction for arbitrary Galactic distributions.

### 2.5.1 Flattened NFW halo

In principle, any Galactic density function could be used for the dark compact objects in our extended calculation. To get a basic understanding of the role that flatness plays in our compact DM constraints, we first consider a simple 'squashed' NFW distribution. This connects straightforwardly to our previous constraints on a spherical NFW distribution. For all previous tests, we were using a spherical NFW distribution of equation (2.1). To convert this profile into a squashed NFW distribution, we convert the above spherically-symmetric distribution to cylindrical coordinates, and

rescale the $z$-axis by some factor $q$, being sure to add a normalization factor to maintain constant total mass:

$$\rho_{\mathrm{NFW};q}(r,z) = \frac{\rho_0}{q\big(\frac{\sqrt{r^2+(z/q)^2}}{R_s}\big)\big(1+\frac{\sqrt{r^2+(z/q)^2}}{R_s}\big)^2}. \tag{2.9}$$

We can think of this new parameter $q$ as the 'sphericality', where $q = 1$ corresponds to a normal spherical NFW distribution, and $q = 0$ corresponds to an infinitely thin delta-function disk. We can then re-run our microlensing constraints with a range of sphericalities, and for a variety of source locations. The results are shown in Fig. 2.7. We can see that the constraints on the compact dark object fraction get tighter for flatter distributions. This is not unexpected, as more of the dark objects are located along the lines of sight to stars in the Galactic disk. We can also see that the dependence on sphericality changes for different collections of lines of sight. This reinforces the importance of using a representative sample of sightlines when investigating non-standard distributions of dark compact objects, and not simply approximating all sources to be at the Galactic core.

### 2.5.2 Rescaled mirror disk

A more realistic model of aspherically-distributed dark compact objects would be a dark disk with a similar distribution to our own. Therefore, it is interesting to ask what constraints we could put on a dark object distribution resembling the double-exponential model used in our baryonic microlensing. We can try rescaling this model disk in both the vertical and radial directions (renormalizing to maintain a given total mass), and observe how our constraints on the total mass ratio between mirror and baryonic matter changes. This new density formula for a dark disk would have the form

$$\rho_{\mathrm{DD};\mathrm{q_r},\mathrm{q_z}}(r,z) = \frac{A_{DD}}{q_r^2 q_z}\exp\left(-\frac{(r/q_r - R_0)}{h_R}\right)\exp\left(-\frac{|z/q_z|}{h_z}\right) \tag{2.10}$$

with $A_{DD}$ being the amplitude of the dark disk distribution, and $q_R$ and $q_z$ being the radial and vertical rescaling factors, respectively. We use 100 lines of sight to calculate the constraints on the rescaled dark disk. Fig. 2.8 shows the projected constraints on dark compact objects of mass $10^{-2}M_\odot, 1M_\odot$, and $10^5 M_\odot$ as a function of vertical and radial rescaling, while Fig. 2.9 highlights how these constraints depend on the mass of dark compact objects, computed for dark disks rescaled equally in the horizontal and vertical directions. Note that although the Galactic distribution of the dark and baryonic objects is similar, the mass distributions are nonetheless different (with dark objects having a delta-function mass distribution, while baryonic stars have a Kroupa IMF as described above). A more thorough investigation of dark object mass distributions is left for future work.

These results show that constraints on dark compact objects with a disk distribution can get significantly tighter if the disk is concentrated towards the centre of the Galaxy. This is reasonable, as the density along some lines of sight increases as the disk is compacted. However, it is interesting to note that this is only true down to a rescaling of around 0.3 – beyond this point the constraints get weaker again. This is likely due to the fact that highly compressed dark disks only overlap with a small number of sources, so the increase in statistical power for these central lines of sight is offset by a reduction in some of the more peripheral lines of sight.

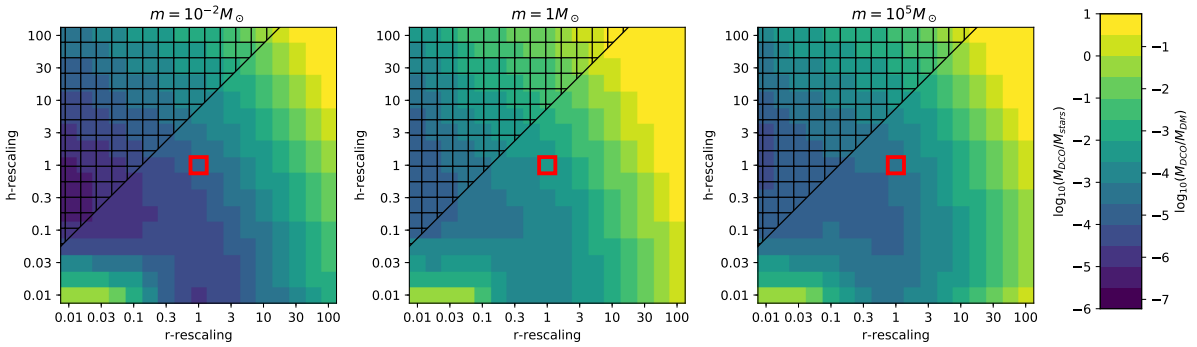


Figure 2.8: Constraints on the ratio of the total mass of dark compact objects (DCOs) to ordinary stars, depending on how the vertical and radial length scales of the dark disk compare to those of the Milky Way (see Eq. (11)). The color indicates maximum allowed DM mass, either as a fraction of total baryonic matter or a fraction of total dark matter (hence the two number scales on the colorbar). The red square indicates a perfectly symmetrical mirror disk (with the same dimensions as the Milky Way's baryonic disk), and we can see that the constraints get tighter when the disk is compressed. However, this improvement soon reaches a saturation, as further compression (beyond around 0.3 in radial compression, and 0.1 in vertical compression) weakens the constraints. Note that these bounds only apply quantitatively to sharply peaked mass distributions for the DCOs. The black cross-hatched region corresponds to 'disks' that are taller than they are wide, which is unphysical, but we still show the corresponding results as a demonstration of the versatility of our forecasting software.

### 2.5.3 Tilted mirror disk

Another possible distribution of mirror matter that could be considered is a dark disk that is tilted with respect to our own disk. This could be caused by imperfect coupling between the dark and baryonic sectors as our Galactic disks were forming, resulting in imperfect alignment between the angular momentum vectors (although gravitationally they should eventually align). We can see in Fig. 2.10 how the constraints on the disk mass ratios get weaker with a tilted disk, likely due to the fact that we have fewer sources outside the Galactic plane, and thus less statistical power. These constraints are for $10^{-2} M_\odot, 1 M_\odot$, and $10^{5} M_\odot$ objects, using 100 lines of sight.

It is interesting to note that although the constraints get weaker when the dark disk is tilted in any direction, there is a consistent difference in how much weaker depending on the tilt angle. Tilting the disk to the left or right (from the perspective of our Sun looking into the Galactic core) preserves some of the key lines of sight through the dark disk into the Galactic bulge (where many sources are located), so the constraints only get slightly weaker. Tilting towards or away from us, on the other hand, results in no good lines of sight that go along the plane of the dark disk, so they get significantly weaker. The differences between left and right, as well as the differences between towards and away, could be the result of rotation of the dark and baryonic disks, or asymmetries in the region of the sky seen by LSST (as seen in Fig. 2.2).

Finally, we point out that it is unlikely that a dark disk would exhibit a tilting angle as high as the maximum of 45° that we show in our plot, but our calculation demonstrates that more reasonable tilting angles might be detectable, even if their impact on microlensing sensitivity is quite modest.

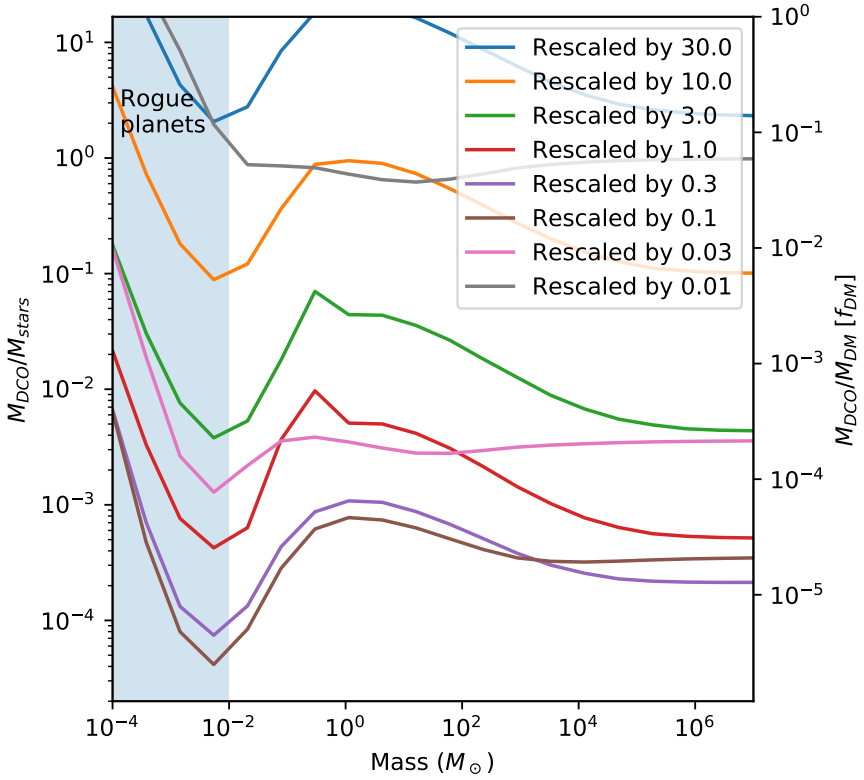


Figure 2.9: Forecast constraints on the total mass of DCOs in a dark disk distribution as a function of object mass. The lines show constraints for various spatial rescaling factors, where the radial and vertical rescaling with respect to the baryonic disk are identical (see Eq. (11)). The total mass of the dark disk is kept fixed during this rescaling, so the smaller dark disk has much more mass concentrated near the centre of the Galaxy, corresponding to tighter constraints on the total allowed mass. Note that these bounds only apply quantitatively to sharply peaked mass distributions for the DCOs. The left axis shows the constraints on dark compact object mass as a fraction of total stellar mass in the Milky Way, while the right axis shows the constraints as a fraction of total dark matter in the Galaxy (in other words, $f_{\rm DM}$). As was seen in Fig. 2.8, the improvements in constraints for compact disks reaches a saturation point at around 0.1 before it begins to weaken again. We can also see that the role of baryonic backgrounds becomes slightly less important for highly compact disks, as seen by the reduced 'bump' in the pink and grey curves. The constraints for disks rescaled by a factor of 100 are not shown on this plot, as they lie completely above the top of the figure, and cannot be constrained to be anything less than 100% of the DM for any mass range.

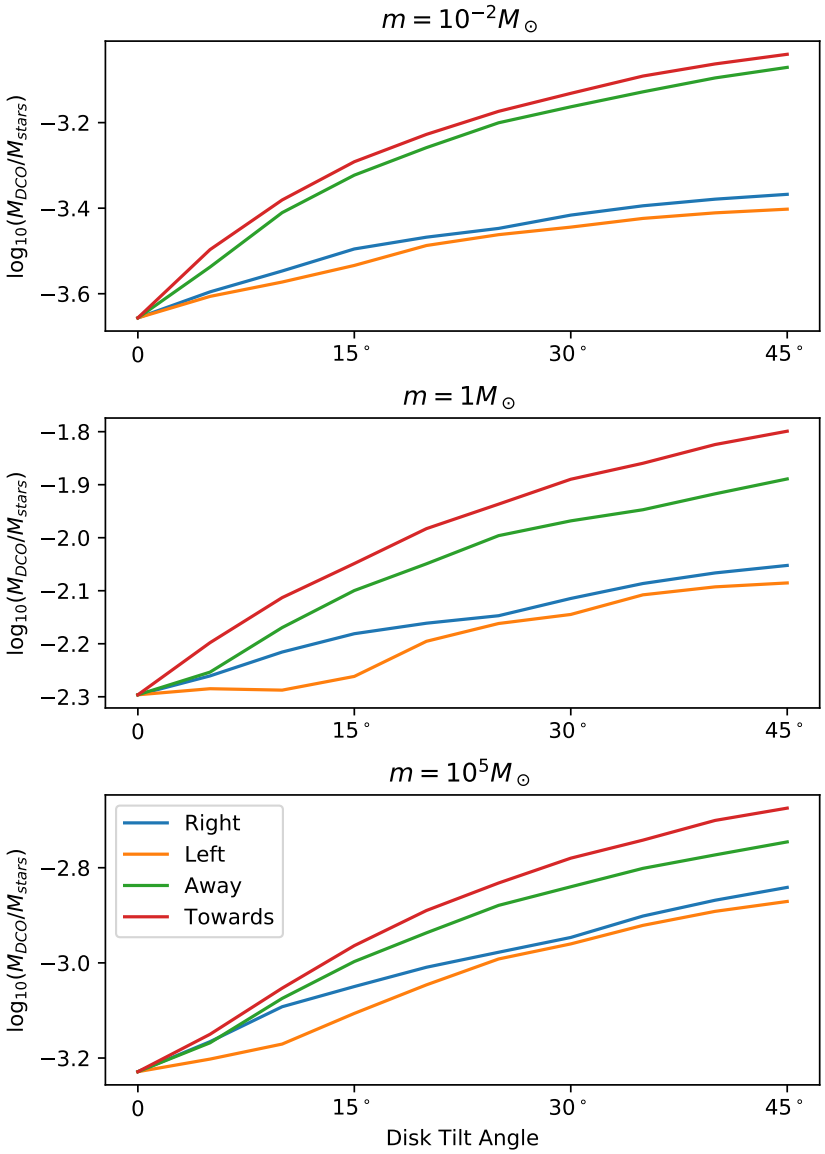


Figure 2.10: Forecasted constraints on the ratio of the total masses of dark compact objects (DCOs) in a dark disk and ordinary stars, depending on the tilt of the dark disk relative to our own. The four lines illustrate the result of tilting the dark disk in different directions, as viewed from Earth looking towards the Galactic centre. We can see that the constraints get weaker when we tilt the dark disk, regardless of the direction of tilt. This plot assumes a dark disk with the same dimensions as the Milky Way's baryonic disk, and each subplot shows constraints for a different mass of dark compact object. We use 100 lines of sight in order to achieve a representative sample of the dark object distribution.

### 2.5.4 Future Applications of Microlensing Code

In addition to the spherical and flattened NFW profile, and the rescaled and tilted double-exponential disk, our code for calculating these microlensing constraints could be used on any conceivable distribution of dark compact objects, corresponding to more exotic theories of compact DM, or more precise future predictions for the distribution of dark compact objects in a given theory of dissipative DM. These investigations could be performed very easily by supplying the code with a new functional form of the Galactic spatial distribution of DCOs. A simple example would be to investigate dark disks that are simultaneously rescaled and tilted, which was not done in this work. Another possibility would be to consider distributions of dark compact objects that mirror some other component of our baryonic Galaxy, perhaps only forming a 'dark bulge' or 'dark bar'. More complex models could include dark compact objects that are clustered, similar to baryonic globular clusters. These dark object distributions could also be informed from specific models of compact dark matter, such as dissipative dark matter, axion stars, and mirror dark matter. This would require theoretical predictions for the Galactic distribution of these specific models of dark compact objects, perhaps dependent on the free parameters of the underlying model, which has yet to be done for most of the models of compact DM mentioned here. In these cases of theoretically-motivated Galactic distributions, our constraints on the parameters of the distribution function could translate into interesting constraints on the parameters of the underlying model.

An only slightly more-involved extension of our analysis that we have not yet investigated is constraints on more general distributions of dark object masses, instead limiting our investigations to delta-function mass distributions of DCOs. As a first approximation, one might simply convolve the mass distribution with the mass-dependent constraints on dark object fraction that the code currently produces. However, this would fail to accurately capture the effect of baryonic "background events" in crossing time. The correct approach would be to compare the distributions of dark and baryonic events as a function of crossing time. This would require some modification to the code, in order to compute dark event rates for a range of masses, and then weighting those distributions of events by some mass function to get a total distribution of events in crossing time. Comparing this to the distribution of baryonic microlensing events could produce interesting effects. For example, when we restricted our baryonic star mass distribution to a delta function, we found that our constraints got significantly weaker when the masses overlapped perfectly. Similarly, we expect that a dark object mass distribution perfectly mirroring a stellar IMF would have significantly weaker constraints, as the event distribution would perfectly match the baryonic events. In this case, the constraints would be limited only by the inherent uncertainty on baryonic star abundance, which we currently assume to be around 5% (consistent with [34]). Realistic sensitivities likely lie between these two extremes, depending on how much a given DCO mass distribution "stands out" against the background of the baryonic stellar mass distribution. We leave a more thorough investigation of the impact of DCO mass distribution to future work.

## 2.6 Conclusion

The Vera Rubin Observatory is expected to produce some of the strongest microlensing constraints on dark compact objects in our Galaxy. As this paper has shown, LSST will not just be able to constrain models of PBHs, but it has the potential to constrain many other more exotic models of

dark compact objects that could make up a fraction of the DM in our Galaxy.

Of special interest is the potential to constrain models of dissipative dark matter, such as the Mirror Twin Higgs and related models. These models predict that a subcomponent of dark matter could be in the form of mirror baryons and electrons, forming atomic dark matter that can cool and collapse into mirror stars. These compact objects can have unusual Galactic distributions, which motivates more complex microlensing constraint calculations. This paper has improved on older LSST microlensing constraints by including variable observing times, baryonic microlensing foregrounds, and multiple lines of sight characteristic of LSST sources.

Using these improvements, we are not only able to improve sensitivity projections for primordial black holes, but also forecast novel constraints on a variety of alternative DM distributions. Some example models that were constrained include a squashed NFW distribution, a rescaled mirror disk, and a tilted mirror disk. For example, we forecast that LSST will be able to constrain dark compact objects with one solar mass in an NFW distribution to have a DM fraction under $4.1 \times 10^{-4}$. One-solar-mass objects with a delta function mass distribution and a dark disk spatial distribution with the same dimensions as the baryonic Galactic disk will be constrained to below $f_{\rm DM} < 3.1 \times 10^{-4}$, while those with masses of $10^5 M_\odot$ will be constrained to below $f_{\rm DM} < 3.4 \times 10^{-5}$ This represents a significant advance in our understanding of microlensing probes of non-minimal dark matter, and suggests that realistic DCO distributions could be detected with percent or permille dark matter fractions in our Milky Way disk. Our results motivate further work to understand the fraction of mirror dark matter that actually forms DCOs, as well as their mass distributions, which will have a major impact on the interpretation of these bounds in terms of more fundamental particle physics theory parameters. The software created for this paper can easily be re-purposed to constrain any arbitrary spatial distribution of compact objects. All the code used to produce the figures in this paper, as well as compute new constraints on custom Galactic distributions, is available at this GitHub link [207].

# Chapter 3

# Modeling of Extreme Axions

Article submitted to Physical Review D, as Harrison Winch et al. "Extreme Axions Unveiled: a Novel Fluid Approach for Cosmological Modeling". In: (Nov. 2023). arXiv: `2311.02052 [astro-ph.CO]`. As first author, this project was primarily my idea, in collaboration with co-author Renée Hložek. I developed the computational methods that form the core of the paper, implemented them into existing code packages, generated all results and figures, and wrote almost all of the paper text, with editorial input from co-authors Renée Hložek, David J. E. Marsh. Daniel Grin, and Kier K. Rogers.

## 3.1 Abstract

Axion-like particles (ALPs) are a well-motivated dark matter candidate that solve some of the problems in the clustering of large scale structure in cosmology. ALPs are often described by a simplified quadratic potential to specify the dynamics of the axion field, and are included in cosmological analysis codes using a modified fluid prescription. In this paper we consider the extreme axion: a version of the axion with a high initial field angle that produces an enhancement (rather than a suppression) of structure on small scales around the Jeans length, which can be probed by measurements of clustering such as the eBOSS DR14 Ly-$\alpha$ forest. We present a novel method of modeling the extreme axion as a cosmological fluid, combining the Generalized Dark Matter model with the effective fluid approach presented in the `axionCAMB` software, as well as implementing a series of computational innovations to efficiently simulate the extreme axions. We find that for axion masses between $10^{-23}$ eV $\lesssim m_{\rm ax} \lesssim 10^{-22.5}$ eV, constraints on the axion fraction imposed by the eBOSS DR14 Ly-$\alpha$ forest can be significantly weakened by allowing them to be in the form of extreme axions with a starting angle between $\pi - 10^{-1} \lesssim \theta_0 \lesssim \pi - 10^{-2}$. This work motivates and enables a more robust hydrodynamical analysis of extreme axions in order to compare them to high-resolution Ly-$\alpha$ forest data in the future.

## 3.2 Introduction

Axion-like particles (ALPs) are a broad class of DM particle candidates that possess both a strong theoretical justification and a variety of potentially observable signatures, as discussed in Section 1.2.2. While the traditional quantum chromodynamics (QCD) axion is a pseudo-Nambu-

Goldstone boson arising from a broken Peccei-Quinn symmetry [157], ALPs can arise from broken symmetries more generally, and are produced naturally from a variety of string theories as a result of compactified higher dimensions, making them a well-motivated DM particle candidate [64, 163, 2, 195, 68, 18, 135, 6]. Throughout this work, we will use axion and ALP interchangeably to refer to this broad class of low-mass pseudo-Nambu-Goldstone boson DM candidates.

The extremely flat field potential of ALPs gives them a very low particle mass $m_{\rm ax}$, potentially on the order of $10^{-22}$ eV. This extremely low mass results in a de-Broglie wavelength that "smoothes" cosmic power on small ($\sim$ kpc - Mpc) scales, which is why these models are sometimes called "fuzzy dark matter" [97, 62]. The scale of this power suppression is directly related to the ALP mass, with lower masses suppressing structure on larger scales [119]. This has allowed us to put strong lower bounds on the axion mass (or upper bounds on the axion fraction), using a variety of observables such as galaxy clustering, the Lyman-$\alpha$ forest, and the CMB[15, 93, 89, 169, 62]. For a more detailed review of axions and their role in cosmology, see, e.g., Refs. [135] and [86].

However, most analyses of dark matter structure formation ignore the periodic nature of the Nambu-Goldstone field, which creates a cosine field potential for the axion. While the mass of the ALP $m_{\rm ax}$ characterizes the field potential curvature at a stable minimum, the scale of the periodicity of the field potential is related to the energy scales of the broken symmetry giving rise to the Nambu-Goldstone field, parameterized by the axion decay constant $f_{\rm ax}$ [135]. We can write the field potential $V(\phi)$ for the axion field $\phi$ as

$$V(\phi) = m_{\rm ax}^2 f_{\rm ax}^2 \big[1 - \cos(\phi/f_{\rm ax})\big], \tag{3.1}$$

with a stable minimum at $\phi = 0$, and periodicity on the order of $\phi \sim 2\pi f_{\rm ax}$. If the axion field exhibits only small oscillations around this minimum, we can approximate the potential near the minimum as quadratic, of the form

$$V(\phi) \approx \frac{m_{\rm ax}^2}{2}\phi^2. \tag{3.2}$$

All dependence on the symmetry-breaking scale $f_{\rm ax}$ cancels out, and we get a harmonic potential with curvature dependent on the axion mass $m_{\rm ax}$.

Modeling a scalar field in a harmonic potential is a good approximation of the ALP behaviour both at late times or if you assume a low starting field value relative to $f_{\rm ax}$. As a result, most past work in axion cosmology has assumed a low starting angle and thus a purely quadratic potential, allowing the ALP field to be approximated as a generalized dark matter fluid, and efficient predictions can be made of cosmological observables (i.e., the suppression in small-scale power mentioned earlier) [96, 92, 119].

However, despite the computational simplicity of the quadratic potential, the full cosine nature of the potential becomes significant if you start the axion field near the "top" of the potential (so $\theta_i \equiv \phi_i/f_{\rm ax} \to \pi$, where $\theta_i$ is the initial value of the axion field angle, $\theta$). In this work, we will refer to models where the axion field starts near the top of the cosine potential as "extreme", following the convention in existing literature labeling these models as "extreme axion dark matter" or "extreme wave dark matter" [41, 216]. These models are sometimes also referred to as "large-misalignment angle" axions [eg. 17]. In contrast to these "extreme" models, we will refer to axions with low starting angles well within the quadratic regime as "vanilla" axions.

Past work modeling perturbations to the axion field have shown that starting near the top of the potential results in significant enhancements to the Matter Power Spectrum (MPS) around the

same scales that are ordinarily suppressed in the vanilla axion case [41, 121, 123]. This enhancement arises in the scalar field as it evolves over a region of field potential with negative curvature[1]. These enhancements have been shown to weaken, or even reverse, the suppression of power due to the low axion mass, resulting in a weakening of existing observational constraints on these axion models. The scale of these enhancements is related to how close the axion field angle, $\theta_i$, starts to $\pi$, as this results in the field remaining "balanced" on the top of the potential for longer, and spending more time in this region of negative potential curvature. Thus, developing ways of efficiently modeling these extreme axions can allow us to reevaluate the robustness of past axion constraints, and explore new and interesting models of DM that are still consistent with the data.

Past work has suggested this "balanced" starting value requires some degree of fine tuning of the initial conditions, but models have been proposed that could explain this fine tuning, with an inverted potential at an earlier phase driving the axion field to start near the potential maximum at $\phi \sim 2\pi f_{\rm ax}$ [50, 17]. Being able to efficiently model the extreme axions for a range of parameters, and comparing the results to cosmological observables, would allow us to test the required degree of fine tuning of the initial field angle, and thus put constraints on the range of possible axion models.

Some work has been done to model the evolution of the axion field with these extreme starting angles [41, 217, 121, 216]. However, the rapidly-oscillating nature of these axion fields (both at the background and perturbation level) necessitates extremely high temporal resolution for the computations, requiring long computation times for a brute force solution [217, 216]. This makes running repeated estimates of the axion evolution, of the sort required for a Markov Chain Monte Carlo (MCMC) or other likelihood sampler method, prohibitively expensive.

In this work, we present a novel method of efficiently and accurately modeling the behaviour of these extreme axions as a cosmological fluid. We follow the structure of the vanilla axion modeling code `axionCAMB`, explained in more detail in Ref. [92]. We implement a number of innovations and improvements to `axionCAMB` compute predictions for cosmological observables such as the linear MPS. These innovations, described in more detail in the Section 3.3, include a restructuring of the initial conditions, and a novel effective sound speed of the extreme axion fluid. All of these innovations reduce the runtime to model extreme axions down to $\sim 7$ seconds. This opens up new opportunities to put observational constraints on extreme axion models with higher-dimensional MCMC algorithms that require tens of thousands of calls to the axion evolution code.

In addition to explaining our various novel innovations to model extreme axions as a cosmological fluid, we also present predictions for some cosmological observables, in order to assess the potential observability of these models. We compare our predictions for the linear MPS to estimates of the linear MPS from the eBOSS DR14 Ly-$\alpha$ forest [67]. We find that moderately extreme axions can

[1] Two explanations of why negative potential curvature leads to an enhancement in power are presented here. Firstly, on an intuitive level, we can imagine these negatively curved potentials to be like a fixed pendulum located near the peak of its range of movement. A collection of closely-spaced pendulums starting near the peak (representing a variety of "perturbations" around some mean value) would spread out as they swing down from their peak. This represents a growth of perturbations, which is in contrast to a collection of pendulums starting near the minimum of their movement, which would simply oscillate around their mean.
For a more mathematical understanding of why negative potential curvature leads to an enhancement of power, consider the following argument: if the curvature of the field potential is related to $m_{\rm ax}^2$ in the case of a free particle, negative curvature is a negative $m_{\rm ax}^2$ term, and thus can be thought of as "imaginary mass", as the square root of a negative number. Since the mass governs the frequency of the field oscillations, this gives rise to an "imaginary frequency". Oscillations with an imaginary frequency are just hyperbolic sine and cosine functions, so the field perturbations exhibit exponential growth instead of harmonic oscillation during this regime of negative potential curvature.

alleviate tensions between vanilla axions and the Ly-$\alpha$ estimates for a range of masses and axion fractions, and that the improvements in the fit are significant enough to warrant the addition of the extra parameter to our vanilla axion model. For example, we show that for axion masses between $10^{-23}$ eV $\lesssim m_{\rm ax} \lesssim 10^{-22.5}$ eV, constraints on the axion fraction imposed by the eBOSS DR14 Ly$\alpha$ forest can be significantly weakened by considering extreme axions with a starting angle between $\pi - 10^{-1} \lesssim \theta_0 \lesssim \pi - 10^{-2}$. This motivates future hydrodynamical simulations of the Ly-$\alpha$ forest in extreme axion cosmologies, in order to compute more robust comparisons to these models, similar to the analysis done in Ref. [169].

In addition to acknowledging the full cosine nature of the standard axion potential, some theoretical models have been proposed which could involve a more complex potential function. One example is a larger background quadratic component to the potential in addition to the smaller-scale cosine wiggles. Such a 'monodromic' potential could allow each axion particle to carry significantly more energy, relaxing previous cosmological constraints on mass and coupling strength [105]. In addition, some models of axion-like particles consider a self-interacting axion field, adding quartic corrections to the traditional harmonic potential [42]. Recently, models have even been proposed with a hyperbolic cosine potential [200]. Since the axion potential function will be implemented into `axionCAMB` in a totally generic way, it will be possible to use our software to constrain any interesting axion potential with minimal modifications. Calculating cosmological constraints on axion potentials of a variety of arbitrary forms would be a powerful tool in understanding what role axions or axion-like particles could have played in the evolution of our universe, and open a new window into distinguishing between otherwise indistinguishable ALP DM models.

## 3.3 Methods

In order to model the behavior of extreme axions, we modified `axionCAMB` to include an arbitrary field potential shape (in our case, a cosine of the form given in Equation 3.1), and reconfigured the code to sample the extreme starting angles necessary to probe these potentials. We also modified the effective sound speed of the axions after the onset of oscillations to reflect the growth in structure resulting from the tachyonic field dynamics. Lastly, we implemented a computationally-efficient 'lookup table' of the axion background fluid evolution in order to speed up the computation of the perturbation equations of motion. The details of implementing extreme axions into `axionCAMB` are presented below [2].

The numerical treatment of axions in `axionCAMB` is described in detail in Ref. [92], as well as in Sections 1.1.5, 1.3.1, and 1.3.2 of the Introduction. In theory, the best way of modeling the dynamics of axion dark matter is to model the behaviour of the field throughout all of cosmic history, as discussed in Section 1.3.1, and derive all cosmological parameters from those primary variables. However, since this field evolution includes periods of extremely rapid oscillations at late times, simulating this is computationally prohibitive and numerically unstable. Instead, the axion field is modeled directly at early times, but the code switches to a simplified fluid approximation detailed in Section 1.3.2 at late times [92]. This piecewise background evolution could then be called when solving the equations of motion for the fluid perturbations (axion density perturbation $\delta_{\rm ax}$ and axion heat flux $u$), allowing for efficient and stable computation of the final axion power spectrum.

[2] `axionCAMB` is in turn based on the cosmological Boltzmann code, `CAMB` [122].

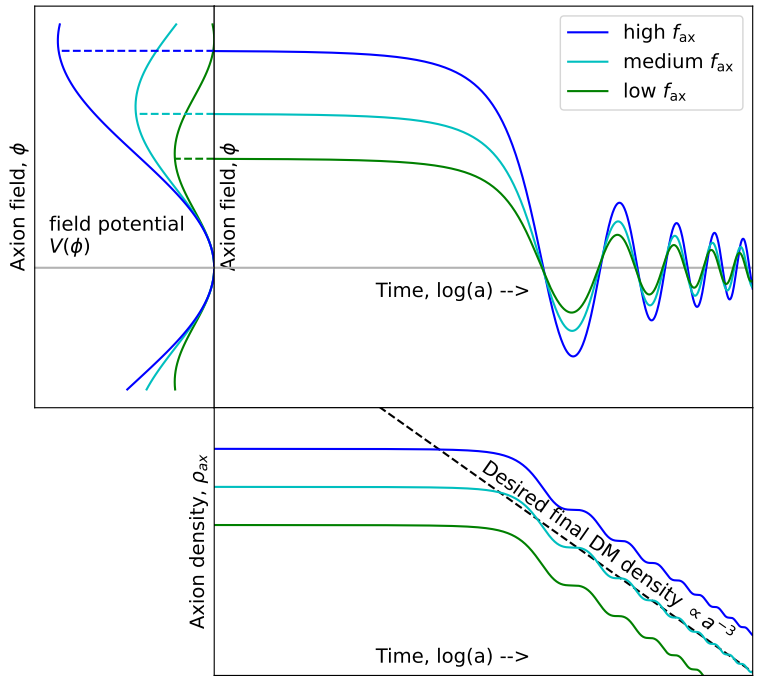


Figure 3.1: This diagram illustrates our novel shooting method for determining the axion initial conditions, as explained in Section 3.3.1. Three possible axion potential scales are shown here in blue, cyan, and green. The initial value of the axion field is determined by the axion starting angle (in radians, set here to be 3.0), and the scale of the axion potential. We then evolve the axion field forward in time using equation 1.41, as it starts to oscillate at late times, as shown in the top panel. Once the axion density has started to evolve like CDM, we can compare the final densities of all of these test cases to the desired final axion density (shown in a black dashed line in the bottom-right plot), and we use a cubic spline interpolation to determine the correct potential scale to reproduce the desired final density.

### 3.3.1 Finely tuned initial conditions

In the original formulation of `axionCAMB`, the initial field angle was found by testing a range of starting field values $\phi_i$ in a fixed potential, evolving them all forward in time to find the final axion density, and then interpolating to find the initial field value that best reproduces the desired final density via this "shooting method". However, in order to explore the tachyonic enhancements arising from extreme starting angles, we need to set the starting angle ($\theta_{\rm ax} = \phi_{\rm ax}/f_{\rm ax}$) extremely close to $\pi$, which is impossible to do manually in the original formulation of `axionCAMB`.

In order to specify both the initial axion field angle $\theta_i$ *and* the final axion density $\Omega_{a0}h^2$, we had to restructure the initial shooting regime. In our new regime, the free parameter in the shooting regime is the scale of the cosine field potential, $f_{\rm ax}$. We test a range of field potential scales for a fixed axion mass $m_{\rm ax}$, start all of the axion fields at the same *angle* ($\phi_i = f_{\rm ax}\theta_i$) within the cosine potential, and then evolve them all forward in time using Equation 1.41 to find the final axion density. This process is illustrated in Figure 3.1. We are then able to interpolate from these final densities in order to find the field potential scale that correctly reproduces the desired final axion density given a certain starting angle.

Restructuring the initial shooting methods to specify the field starting angle allows us to probe

the effects of extreme starting angles in new ways. We can specify starting angles arbitrarily close to $\pi$, in order to see the effects of these extremely finely tuned angles on other observables. In addition, when performing MCMC analysis, having the starting angle as a free parameter allows us to impose arbitrary priors on this starting angle. We can use these priors to test the dependence of any constraints on the level of fine tuning of the axion starting angle.

### 3.3.2 Modeling the early-oscillatory effective axion sound speed

While the pre-oscillatory behaviour of the extreme axion perturbations can be precisely modeled by the equation of state parameter $w_{\rm ax}$ and the adiabatic sound speed $c^2_{\rm ad}$, as explained in Section 1.3.1, this is no longer the case after the onset of oscillations. This is because the adiabatic sound speed, defined by Equation 1.24, becomes undefined when $\dot{\rho}_{\rm ax} = 0$, or when $w_{\rm ax} = -1$, and these poles are difficult to integrate around. Therefore, after the onset of oscillations, we must switch over to an effective-fluid formalism, shown in Section 1.3.2, where we time-average over the oscillations. This gives us $w_{\rm ax} = 0$ and $c^2_{\rm ad} = 0$, and the behaviour of the perturbation equations of motion are instead governed by the effective axion sound speed $c^2_{\rm ax}$, as seen in Eq. 1.57. This sound speed is an approximation, which, in the case of harmonic oscillations of a vanilla axion, can be approximated analytically to be, the expression given in Eq. **??**.

However, in the case of an extreme axion, particularly during the early anharmonic phase of oscillations, the assumptions of regular harmonic oscillations do not hold. The nature of anharmonic oscillations resists easy analytic approximation of the effective fluid sound speed, so instead we developed methods of approximating this sound speed numerically. Since the effective fluid sound speed describes the frequency of oscillations, exponential growth of the axion perturbations can be modeled by a negative value of $c^2_{\rm ax}$, much like the negative mass squared term in the field equations. In this case, a negative $c^2_{\rm ax}$ term does not actually mean spacelike sound speeds, but instead is merely an effective fluid model of the axion field instabilities. The impact of this negative sound speed on the growth of the fluid perturbations is roughly proportional to the integral of the sound speed over conformal time.

To get a sense of the effects of the anharmonic potential on the axion fluid sound speed, we first solve the axion field perturbation equations of motion,

$$\ddot{\phi}_1 + 2\mathcal{H}\dot{\phi}_1 + \left[k^2 + a^2 V''(\phi_0)\right]\phi_1 = -\frac{1}{2}\dot{\phi}_0\dot{\beta}, \tag{3.3}$$

where $\phi_1 = \phi - \phi_0$ is the axion field perturbation. For this integration, we use the metric term $\dot{\beta}$ from the `axionCAMB` solution with the vanilla axion sound speed as the driving source term. This approach is accurate in the adiabatic mode before equality when radiation dominates the gravitational potential. We can then use this $\{\phi_0, \dot{\phi}_0, \phi_1, \dot{\phi}_1\}$ solution to compute the fluid sound speed in synchronous gauge,

$$c^2_{\rm ax} = \frac{\delta P_{\rm ax}}{\delta \rho_{\rm ax}} = \frac{a^{-2}\dot{\phi}_0\dot{\phi}_1 - V'(\phi_0)\phi_1}{a^{-2}\dot{\phi}_0\dot{\phi}_1 + V'(\phi_0)\phi_1}. \tag{3.4}$$

This approximation of the fluid sound speed is shown in red in the lower subplot of Figure 3.2.

In order to approximate the boost in the axion sound speed shown in the field equations without changing the late-time evolution of the perturbations, we modified the vanilla axion fluid sound

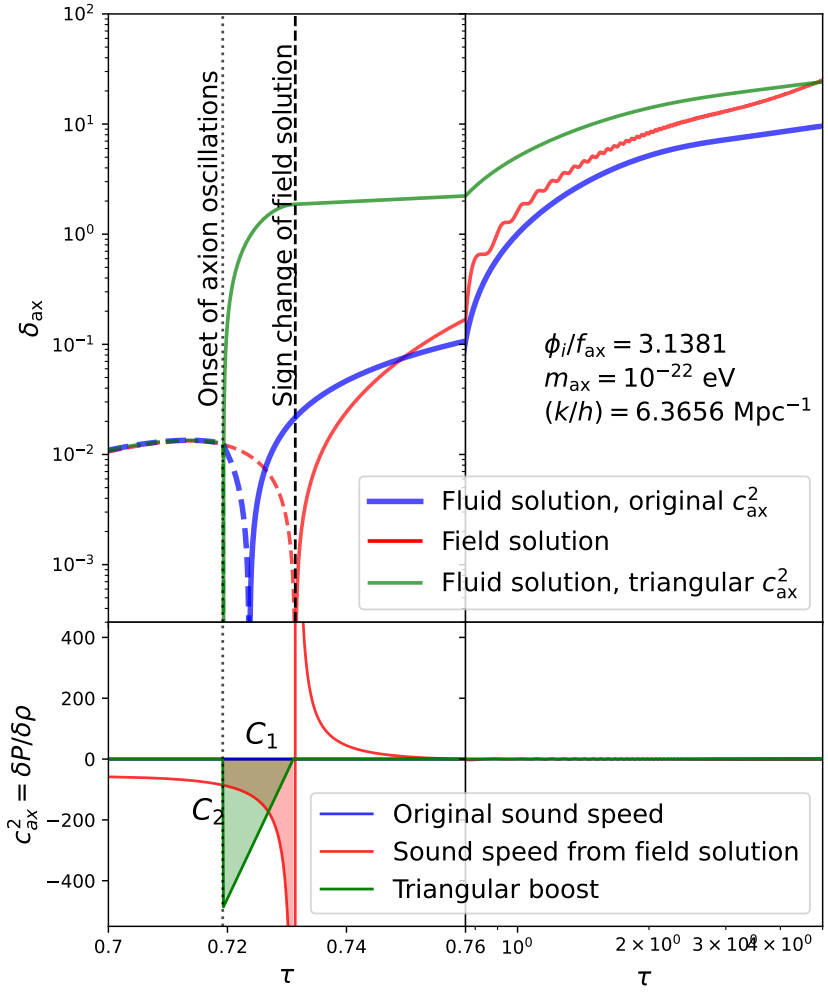


Figure 3.2: The evolution of axion perturbations during and soon after the onset of oscillations for different treatments of the axion sound speed. The horizontal axis is divided between a linear scale on the left and a log scale on the right, to capture both the early and late time behaviour. The blue line represents the generalized dark matter (GDM) fluid equations with the default vanilla axion sound speed [96] The red line in the upper plot uses the Klein-Gordon field equations with the metric term sourced from the vanilla fluid solution. The red line in the lower plot shows the axion sound speed computed from this field solution ($c^2_{ax} = \delta P/\delta\rho$) in the synchronous gauge. This sound speed is used to fit the approximate height and width of a triangular boost to this sound speed - this boost is shown in green on the lower plot. In the upper plot, the green curve shows the solution to the fluid GDM equations with this triangular boost in the sound speed, reproducing the expected power at late times.

speed to include a large negative spike just after the onset of oscillations. This negative triangular spike is shown in green in the lower subplot of Figure 3.2. The width and height of this spike were fit to match the approximate sound speed computed from the field perturbation solution. The width ($C_1$) was fit to the delay in scale factor $a$ between the onset of axion oscillations and the asymptotic sign change in the field solution sound speed. This numerical width was then approximated as a power law function of the scale factor $k$ of the perturbation, depends linearly on the scale factor at the onset of oscillations, which in turn depends on the axion mass, fraction, and starting angle,

$$C_1(k, a_{\rm osc})_{\{A_1, M_1, B_1\}} \approx \frac{a_{\rm osc}}{A_1}\left(\frac{k}{B_1}\right)^{M_1}, \tag{3.5}$$

where $A_1$, $M_1$, and $B_1$ are all fit parameters, chosen to match the dependance of the scale factor delay in the field solutions over a range of values for $k$ and $a_{\rm osc}$.

The height of this triangle ($C_2$)was chosen such that the total area of the triangle was equal to the area enclosed by the sound speed over the same conformal time period. As mentioned earlier, since the axion equations motion are differential equations in conformal time $\tau$, the integral of the $c^2_{\rm ax}$ over $\tau$ approximates the impact that this sound speed spike has on the evolution of the perturbations. Once this height was calculated for a certain field evolution, it is effectively fit by an power law of the sale factor $k$ and the logarithm of the initial axion field angle seperation from $\pi$ (since more extreme starting angles should result in exponentially larger boosts to the perturbation growth)[3],

$$C_2(k, \theta_{\rm ax,0})_{\{Q_2, M_2, B_2\}} \approx \left[\log\left(\frac{\pi - \theta_{ax,0}}{Q_2}\right)\right]\left(\frac{k}{B_2}\right)^{M_2}, \tag{3.6}$$

where $Q_2$, $M_2$, and $B_2$ are all fit parameters, chosen to match the area of the effective sound speed calculated from the field solutions over a range of $k$ and $\theta_{{\rm ax},i}$ values..

With these two functions for $C_1$ and $C_2$, we can compute a sound speed boost for any combination of axion parameters, approximating the effect of the fluid sound speed for a rapidly oscillating extreme axion. This modifies the vanilla axion sound speed with the following triangular boost,

$$c^2_{\rm ax} = \tilde{c}^2_{\rm ax} - \left[C_2 * \frac{(a_{\rm osc} + C_1) - a}{C_1}; a \in (a_{\rm osc}, a_{\rm osc} + C_1)\right] \tag{3.7}$$

The power spectrum results for this method can be compared to the literature, where other groups have used the exact field perturbation equations of motion to compute the matter power spectrum for extreme axions, such as Ref. [121]. In Figure 3.3 we can see the comparison in the matter power spectrum for both a vanilla axion and an extreme axion with a starting angle deviating from $\pi$ by 0.2 degrees, and we find that they are in remarkably close agreement with Ref. [121]. However, this close agreement seems to hold best at $z = 0$, when these power spectra are computed, while the higher redshifts comparison may be more nuanced. Figure 3.2 suggests that while the exact field solution and the new approximate fluid solution agree at very late times, their evolution at early times are not fully equivalent, so more work may need to be done on this approximation in order to perform comparisons to high-redshift observables.

[3] A logarithmic dependence for the background field can be derived analytically for the anharmonic corections to the relic density [130].

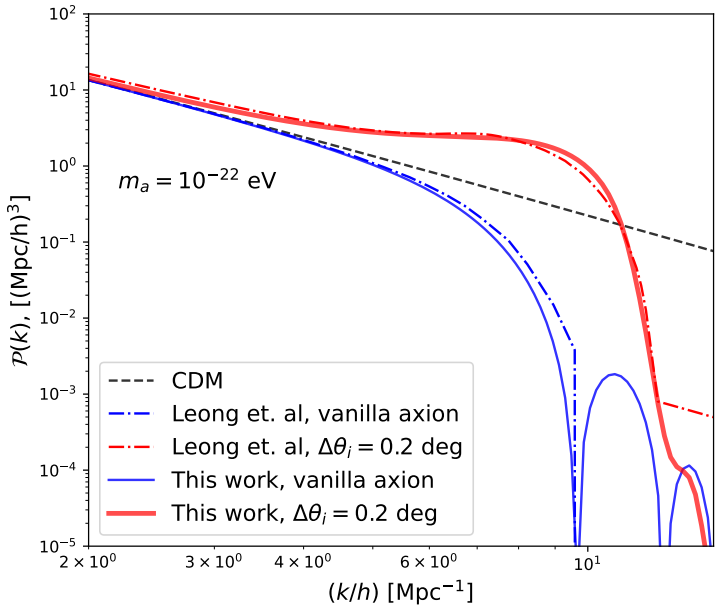


Figure 3.3: This figure compares the predicted matter power spectra for our technique of fitting a triangular boost to the axion sound speed, to that predicted in Ref. [121], which used the full field perturbation equation solution to compute the matter power spectrum for an extreme axion.

### 3.3.3 Using lookup tables for efficient modeling of field

Extending the full field evolution so much later past the onset of oscillations requires far more computational resources than ending the field evolution as soon as oscillations begin. Greater numerical resolution, in both time and possible field potential scale, is also required to integrate these rapidly oscillating variables. With these increases to computational time, the new version of `axionCAMB` takes around seventy seconds to complete. While this may be feasible when computing a single power spectrum result, this is computationally intensive with which to run an MCMC analysis, which may require tens to hundreds of thousands of separate calls to `axionCAMB`.

Fortunately, there is an opportunity here to streamline the process through the use of a precomputed lookup table of smoothed axion background variables. The background evolution of the axion depends only on the axion mass $m_{\rm ax}$, axion density $\Omega_{\rm ax}h^2$, and axion starting angle $\theta_0$. In turn, the only output from the axion background module that is used by the rest of the code are the arrays of $w_{\rm ax}$, $c^2_{\rm ad}$, and $\rho_{\rm ax}$.

We generated a lookup table of `axionCAMB` results $-24 < \log(m_{\rm ax}) < -22$, $0.0012025 < \Omega_{\rm ax}h^2 < 0.12025$, and $\pi - 1 < \theta_i < \pi - 10^{-4}$, saving the arrays of the three background variables presented above, in addition to $\log(a)$ as a time variable. We were then able to write a new version of the axion background module that, instead of computing the axion background evolution from scratch, computes it instead from this lookup table. When this new version of `axionCAMB` is called, the new values of $m_{\rm ax}$, $\Omega_{\rm ax}h^2$, and $\theta_i$ are used to determine the eight reference combinations closest to the desired values. The proximity of the new values to these eight reference values is used to calculate a weighted average of the eight background evolutions of $w_{\rm ax}$, $c^2_{\rm ad}$, $\rho_{\rm ax}$, and $\log(a)$. This lookup

table method was tested extensively against the full computation, showing consistent results, and the required runtime was reduced from $\sim 70$ seconds down to $\sim 7$ seconds.

### 3.3.4 Summary of changes to `axionCAMB`

In order to model axions with extreme starting angles in a cosine field potential using the computationally efficient field formalism used in `axionCAMB`, we have introduced a number of modifications to `axionCAMB` which are explained above, but summarized here.

- We replaced the quadratic approximation of the field potential with an arbitrary potential function, currently set to the canonical cosine potential.
- We restructured the initial conditions to specify the starting angle relative to this cosine, as well as the desired final axion density, and test a variety of potential scales $f_{\rm ax}$ to determine the correct one using a shooting method.
- We modified the effective axion fluid sound speed to reproduce the growth in structure seen in the exact field perturbation equations of motion.
- We precomputed a lookup table for the axion background evolution which significantly reduced the runtime.

The result is an accurate modeling of extreme axion background and perturbation evolution for an arbitrary axion mass, density, and starting angle that only takes $\sim 7$ seconds to run. This powerful tool can shed new light on the behaviour and detectability of these extreme axion models, as discussed below.

## 3.4 Phenomenology

We discuss the observed changes to the axion background variables and cosmological observables as a result of the cosine potential and extreme starting angle. While we leave a full MCMC analysis to future work, we provide a simple comparison of these models to an approximate likelihood (using a $\chi^2$ comparison to the eBOSS DR14 Ly-$\alpha$ forest estimates of the linear MPS) to illustrate the potential constraining power of the data on the extreme axion model. A description of the Ly-$\alpha$ forest isprovided in Section 1.4.2, while a discussion of the $\chi^2$ likelihood is provided in Section 1.5.2.

### 3.4.1 Changes to axion background variables

Before the onset of oscillations, when the axion field is slowly evolving over the negatively-curved potential, the axion perturbation equations of motion depend only on the derived background variables $w_{\rm ax}$ and $c^2_{\rm ad}$, defined in Eq. **??** and Eq. 1.24. In this section, we will discuss the effect of changing the axion starting angle and axion mass on the evolution of these background variables, as they help shed light on how the extreme starting angles impact the fluid equations of motion during these early times.

There has not been a thorough treatment of extreme axions in the fluid formalism previously. The impacts of starting angle on the background evolution of $w_{\rm ax}$ and $c^2_{\rm ad}$ can be seen in Figure 3.4. For low starting angles (blue lines near $\theta_0 = 1.0$ on the plot), the equation of state parameter

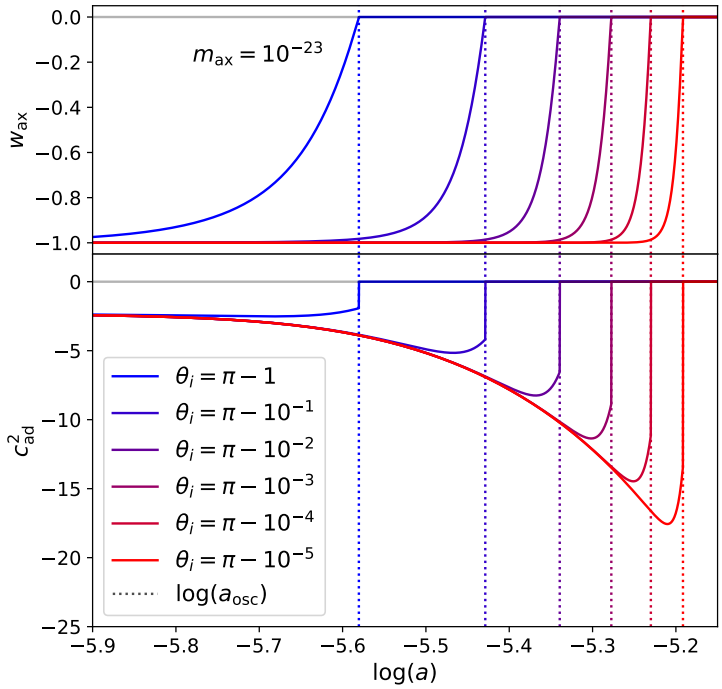


Figure 3.4: This plot shows the effect of varying the axion starting angle $\theta_0$ on the evolution of the axion background variables, $w_{\rm ax}$ and $c^2_{\rm ad}$, in the case of an axion mass of $10^{-24}$ eV. The dotted vertival lines represent the onset of axion oscillations, denoted as the first time when $w_{\rm ax} = 0$. We can see that for extreme starting angles, close to $\pi$ (in red), a number of features can be seen. The onset of oscillations is delayed, $w_{\rm ax}$ approaches zero more rapidly just before the onset of oscillations, and $c^2_{\rm ad}$ becomes much more negative before returning to zero.

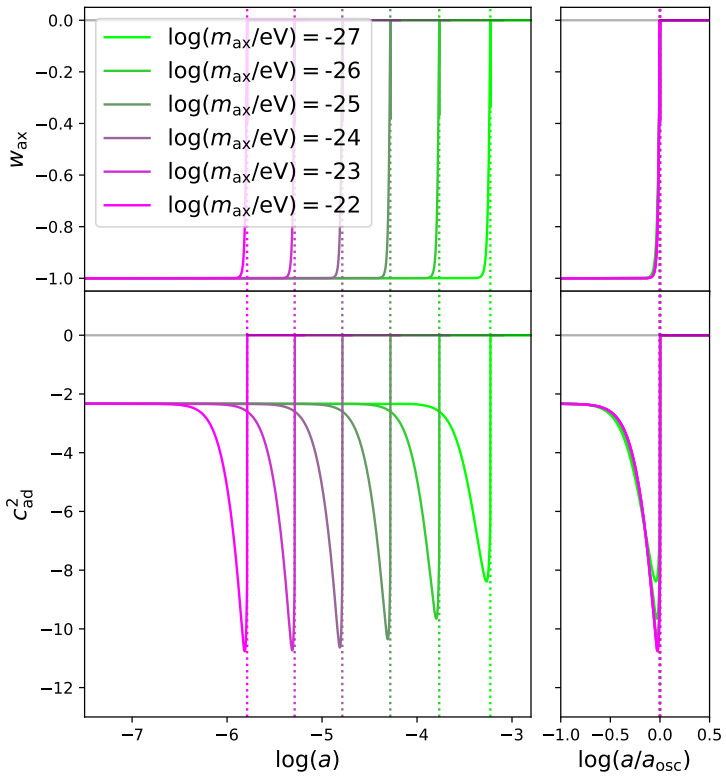


Figure 3.5: This plot shows the effect of varying the axion mass $m_{\rm ax}$ on the evolution of the axion background variables, $w_{\rm ax}$ and $c^2_{\rm ad}$, with a moderately extreme axion starting angle of $\theta_0 = 3.14$. The right plots show the axion background variables normalized to the scale of the onset of oscillations ($a_{\rm osc}$). We can see that the shape of the background variables changes only slightly with mass, and the largest change is a delayed onset of oscillations for low mass (in green)

$w_{\rm ax}$ starts at $-1$ at early times, as the fixed axion field behaves like a cosmological constant at these times. However, as the axion field starts to roll within the potential, the equation of state parameter rises from $-1$, crossing zero at the point when oscillations are defined to begin. However, for extreme axion starting angles (in purple and red in Figure 3.5), the onset of these oscillations in $w_{\rm ax}$ is delayed to later times, due to a flatter initial potential slope when the field starts near the cosine peak. Once the field does start to evolve, the evolution to $w_{\rm ax}$ rises to zero much faster, due to the fact that the Hubble friction has been allowed to become lower by the time the field starts to evolve. Therefore, as soon as the field enters the steeply sloped region of the potential, there is less holding it back from oscillating rapidly.

The adiabatic sound speed ($c^2_{\rm ad}$), shown in the lower subplot of Figure 3.5, exhibits some of the same features as the equation of state parameter $w_{\rm ax}$, but with some notable differences. Like $w_{\rm ax}$, the evolution of $c^2_{\rm ad}$ starts at the same negative value for all starting field angles (in this case, starting at $-7/3$, as predicted by Ref. [97]), evolving up to zero at the onset of oscillations, for the low field angles in blue. For extreme starting angles (purple/red lines with e.g. $\theta_0 = \pi - 10^{-8}$) also have a delayed onset of evolution in the adiabatic sound speed, similar to those seen in $w_{\rm ax}$. However, one interesting new feature seen in $c^2_{\rm ad}$ for extreme starting angles is that the value of $c^2_{\rm ad}$ becomes extremely negative just before the onset of oscillations. This can be understood since $c^2_{\rm ad} = \dot{P}_{\rm ax}/\dot{\rho}_{\rm ax}$ (Eq. 1.24), and when the field starts to slowly roll along the top of a cosine potential, the density $\rho_{\rm ax}$ is not decreasing as quickly as it would if the field were evolving down the side of a quadratic potential. This smaller denominator results in a larger absolute value for the adiabatic sound speed.

These features of the smooth background variables can help explain the tachyonic growth of structure in the fluid formalism, as an extremely negative value of $c^2_{\rm ad}$ just before the onset of oscillations drives growth in certain terms in the fluid density perturbation equations of motion (Eq. 1.57).

We can also examine how the axion mass changes the evolution of these key background fluid variables in the case of an extreme axion, as seen in Figure 3.5. This plot also shows the equation of state parameter $w_{\rm ax}$ in the upper subplot, and the adiabatic sound speed $c^2_{\rm ad}$ in the lower subplot, for a fairly extreme starting angle of $\theta_0 = 3.14$ and a range of axion masses. We can see that the shape of the evolution of these background variables is largely independent of mass, other than the onset of oscillations begins later (at larger values of the scale factor) for more massive axions.

### 3.4.2 Matter Power Spectrum Signatures

These changes to the background fluid variables also impact the MPS (introduced in Section 1.3.3) which is what gives us the cosmological observables that can be seen in Ly-$\alpha$ forest. In this section, we describe the impact of axion mass, starting angle, and axion DM fraction on the MPS, and compare the results to the linear MPS estimated using the eBOSS DR14 Ly-$\alpha$ forest data and the $\Lambda$CDM model, as described in Section 1.4.2 . Note that we are not doing a full hydrodynamical simulation of the Ly-$\alpha$ flux power spectrum, but are instead using the $z = 0$ linear matter power spectrum estimated using the Ly-$\alpha$ forest data. This estimation has a number of limitations. The linearization of the Ly-$\alpha$ power spectrum, and the evolution to $z = 0$, both assume pure CDM physics. In addition, these estimates marginalise over a number of astrophysical parameters describing the nonlinear fluid dynamics, which may have non-trivial degeneracies with both cosmological and axion parameters, which would need to be investigated more thoroughly in a robust comparison to Ly-$\alpha$

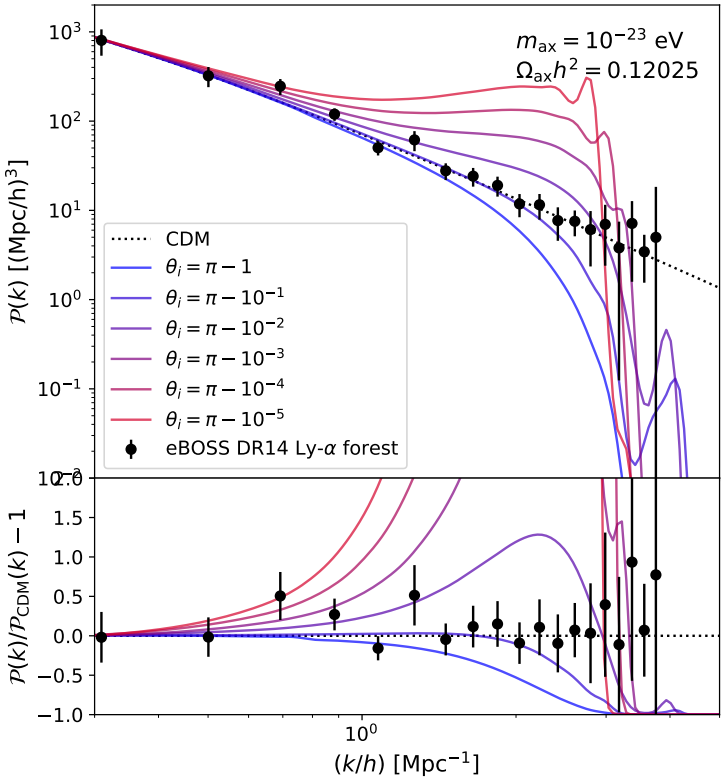


Figure 3.6: The effect of varying the axion starting angle ($\theta_0$) on the axion matter power spectrum. The black data points with error bars are the published MPS data from the eBOSS DR14 Ly-$\alpha$ forest results. These models shown were computed with an axion mass of $m_{ax} = 10^{-23}$ eV, and an axion density of $\Omega_{ax}h^2 = 0.12025$, or constituting 100% of the dark matter.

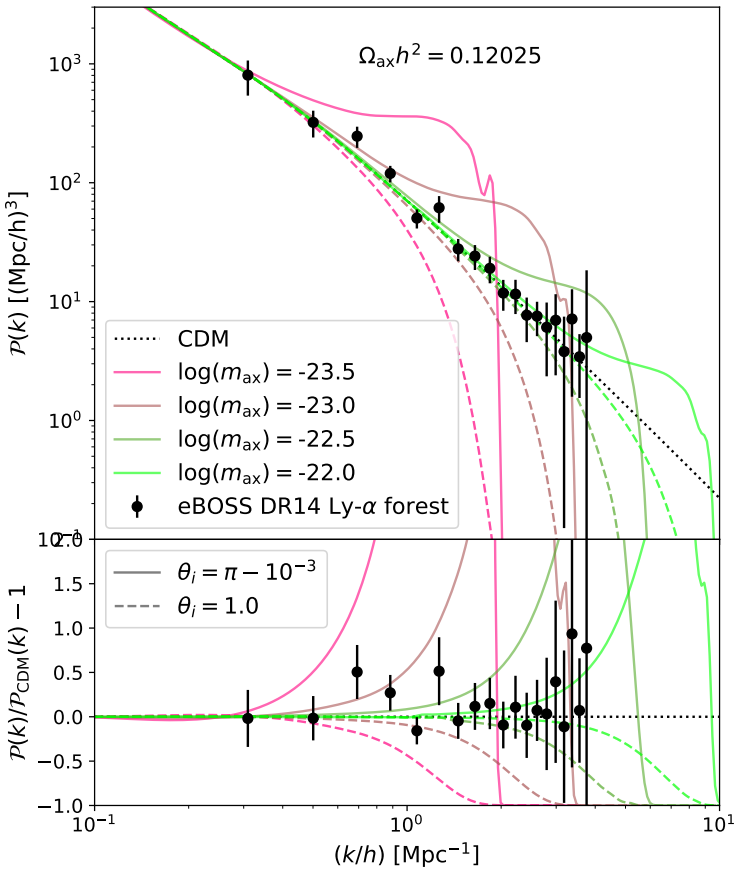


Figure 3.7: The effect of varying the axion mass ($m_{ax}$) on the axion matter power spectrum, for both a low and extreme axion starting angle ($\theta_0 = 1.0$ in dashed and $\pi - 10^{-8}$ in solid). As in Figure 3.6, the black data points with error bars are the linear MPS estimates from the eBOSS DR14 Ly-$\alpha$ forest data. These results were computed with an axion density of $\Omega_{ax}h^2 = 0.12025$, or constituting 100% of the dark matter.

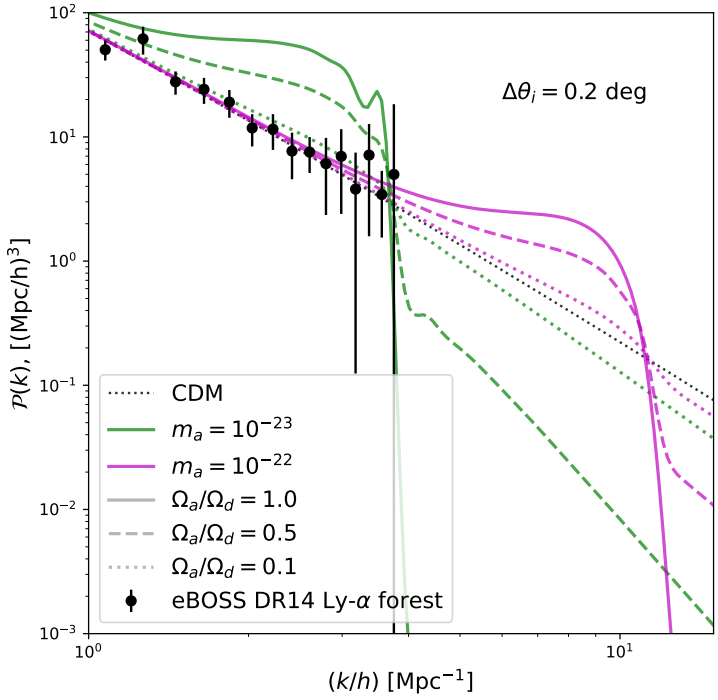


Figure 3.8: The effect of varying the axion fraction ($\Omega_{\rm ax}/\Omega_d$) for two axion masses and a fixed extreme starting angle of $\Delta\theta_i = 0.2$ deg. As in Figures 3.6 and 3.7, the black data points with error bars are the linear MPS estimates from the eBOSS DR14 Ly-$\alpha$ forest data.

forest data. Therefore, this comparison should not be considered quantitatively robust, but instead as a qualitative demonstration of how and where extreme axions can alleviate previous Ly-$\alpha$ forest constraints on vanilla axion models.

Figure 3.6 shows the matter power spectrum for a variety of starting axion field angles, all for a fixed axion mass ($m_{\rm ax} = 10^{-23}$ eV) and fixed dark matter density ($\Omega_{\rm ax}h^2 = 0.12025$). We can see here that for a low starting angle well within the quadratic regime ($\theta_0 = \pi - 1$, in blue) there is a reduction in power at small scales [111], which drives well-known limits on the fuzzy dark matter particle mass [92, 135, 101, 169, 62]. However, when we go to extreme starting angles (with $\theta_0 \to \pi$, in red) we can see an enhancement in power around the cutoff scale, eventually even surpassing the CDM results in black [consistent with the the results of 41, 42, 216, 217, 121, 17]. The eBOSS DR14 Ly-$\alpha$ forest estimates of the linear MPS are plotted in black with error bars, for visual comparison to the axion power spectra. We can see by eye that while both extremely low and extremely high starting angles appear to be strongly ruled out by the data, there is a range of starting angles around $\theta_0 \approx \pi - 10^{-2}$ that agree with the data more, suggesting that for a certain axion mass and energy density, the starting angle may be able to be constrained from both sides.

Figure 3.7 shows how the matter power spectrum depends on axion mass, for both low and high axion starting angle, again overlaid with the eBOSS DR14 Ly-$\alpha$ forest data. The axion mass changes the cutoff scale in the matter power spectrum for the low-angle vanilla axions, with lower mass axions exhibiting a reduction in power at larger scales (lower $k$ values), in agreement with Ref. [92]. The axion mass also changes the scale at which enhancement in the matter power spectrum occurs for the extreme axions. Similarly to the vanilla axion cutoff, the extreme axion enhancement occurs at larger scales (smaller $k$ values) for lower axion mass. The two effects appear to be synchronized, with a similar shift in $k$ for both the vanilla cutoff and the extreme enhancement. By comparing the eBOSS DR14 Ly-$\alpha$ forest data to the models we can see that measurements at smaller scales allow us to constrain both the vanilla and extreme axion models at higher masses.

Figure 3.8 shows how the MPS depends on the axion fraction, for two masses and a fixed extreme starting angle. As expected, lower axion fractions result in the MPS converges to the CDM solution, suggesting that any extreme axion model can be unconstrained at a low enough axion DM fraction.

### 3.4.3 Comparison to Ly-$\alpha$ forest estimates of the MPS

These MPS results can be compared to the eBOSS DR14 Ly-$\alpha$ forest estimates of the linear matter power spectrum and these estimates can be used to compute a simple $\chi^2$ to gauge the goodness of fit. The results of these likelihood comparisons are shown for $m_{\rm ax} = 10^{-23}$ eV in Figure 3.9. In this figure, we plotted the difference in log likelihoods between our extreme axion fits and a CDM fit, so that this difference should approach zero for extremely low axion fractions as we approach a pure CDM universe. In this case, the 'likelihood' being computed was a simple $\chi^2$ metric (introduced in Section 1.5.2) to the eBOSS DR14 estimates of the linear MPS for model $m$, where the log likelihood is given by the equation,

$$\log(\mathcal{L}_m) \approx \chi^2_m = \sum_i \frac{(\mathcal{P}_i - \mathcal{P}_m(k_i))^2}{\sigma^2_{\mathcal{P}i}}, \tag{3.8}$$

where the eBOSS DR14 estimates of the MPS are $\mathcal{P}_i$ at wavenumber $k_i$ with uncertainty $\sigma_{\mathcal{P}i}$. This chi-squared likelihood can be computed for both an axion model and $\Lambda$CDM, and the difference of the logarithm of these results is plotted in Figure 3.9. A low value means the axion model is almost

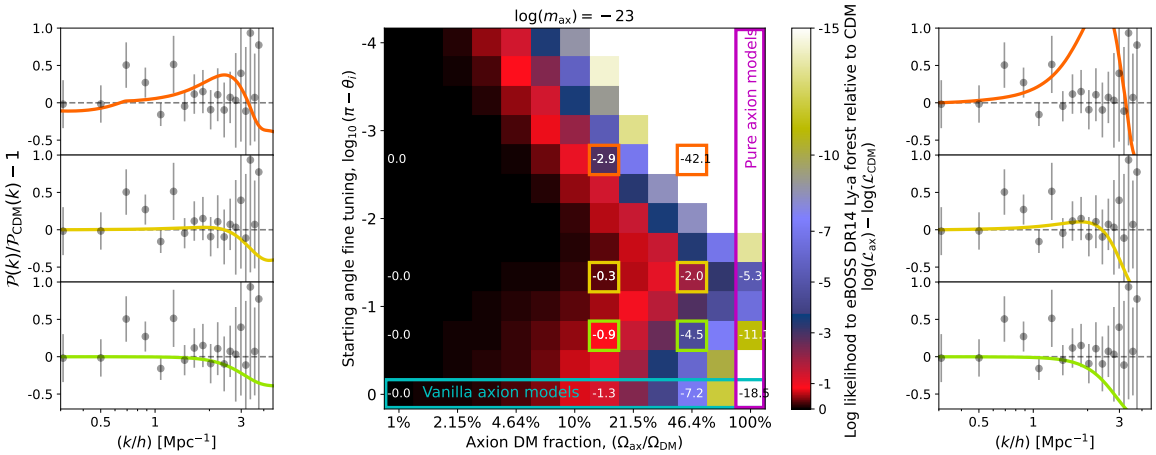


Figure 3.9: Simple fits of our linear MPS predictions to estimates from the eBOSS DR14 Ly-$\alpha$ forest, for a range of axion fractions and axion starting angles, and with a mass of $\log_{10}(m_{ax}/\text{eV}) = -23$. The middle plot shows a grid of the relative log likelihood values of this fit (using the chi-squared likelihood given in equation 3.8), relative to the fit with pure CDM (value close to zero on the colorbar means a fit that is almost as good as CDM, while a more negative value means a worse fit). The horizontal axis shows different axion fractions, on a logarithmic scale, so the models on the far right (within the magenta box) are pure axion models with no CDM. The vertical axis shows different degrees of fine tuning for the axion starting angle. The row along the bottom (in the cyan box) have very low starting angles, so these results approximate those of a vanilla quadratic axion, while the row along the top have starting angles separated from $\pi$ by just $10^{-4}$ radians. The six plots along the left and right show the fractional differences of the matter power spectra for six examples on the grid, highlighted by the orange, yellow, and green boxes, to allow a visual comparison to the eBOSS DR14 Ly-$\alpha$ forest estimates of the linear MPS.

as good a fit as CDM, while higher values mean the axion model has an increasingly worse fit to the eBOSS data. As expected, the best fits are for low axion fractions, indicating that CDM is still the best fit to the eBOSS data. However, if we compare models with different starting angles and a fixed axion fraction, we can see that for fractions above $\sim 10\%$, varying the starting angle can result in a significantly better fit to the Ly-$\alpha$ forest estimates of the MPS.

In order to compare multiple different models, each with a different maximum likelihood and number of free parameters, it is useful to use the Akaike Information Criterion, given in Section 1.5.1. The best model (able to achieve the best fit with the minimum number of parameters) is the model with the lowest AIC. Therefore, when comparing two different models, the improvement is considered worth the added complexity if the difference in the natural logarithm of the maximum likelihood ($\Delta \log(\hat{L})$) is greater than the number of added parameters in the model. Here, we are using a $\chi^2$ comparison to the linearized matter power spectrum estimate (eq. 3.8) instead of a full likelihood computation of the Ly-$\alpha$ forest data, and we are also not maximizing the likelihood over all possible cosmological parameters. Despite these caveats, the AIC can still help to assess the improvement in our fit to the MPS estimates, and compare that improvement to the number of added parameters necessary to achieve that improvement.

When comparing extreme axion models to the standard axion implementation, one extra parameter is needed (either the axion starting angle $\theta_i$, or the potential scale parameter $f_{\rm ax}$, depending on how you formulate the problem). This added complexity to the model is justified if it yields $\Delta \log(\hat{L}) > 1$. Although we are not computing the maximum $\hat{L}$ marginalized over all cosmological parameters, we can still see the difference in $\log(L)$ in Figure 3.9, and we can see that considering extreme axions can improve the relative $\log(L)$ by several orders of unity, suggesting that the improvement in fit will be worth the extra parameter to the axion model. The extreme starting angles can also significantly improve the fits for a range of other axion fractions. Although pure CDM is still a better fit to the eBOSS MPS estimates than axions with this mass of $m_{\rm ax} = 10^{-23}$ eV, we can see that moderately extreme axions (with a starting angle of $\theta_i \approx \pi - 10^{-1}$) offer a significantly better fit than vanilla axions for a range of axion fractions, while for very extreme starting angles ($\theta_i \gtrsim \pi - 10^{-3}$) the results once again are in tension with the eBOSS estimates.

This mass of $m_{\rm ax} = 10^{-23}$ eV has a dramatic difference between vanilla and extreme axions, due to the large amount of overlap between the scales measured by the eBOSS Ly-$\alpha$ forest, and the scales affected by the extreme axion enhancements. However, even the maximum likelihood for pure axions, with a starting angle of $\theta_0 = \pi - 10^{-1}$, still gives a difference to CDM of $\Delta \log \hat{L} \sim 5$, indicating that is still a poor fit to the Ly-$\alpha$ forest data, and a significantly worse fit than CDM. We can get better agreement, however, if we go to slightly higher masses.

Figure 3.10 shows the same log likelihood comparison for a range of axion fractions and starting angles, but this time for a mass of $m_{\rm ax} = 10^{-22.5}$ eV. Once again, we can see that pure CDM still gives the best fit, but for a fixed axion fraction, axions with a starting angle between $3 \lesssim \theta_i \lesssim 3.13$ have higher likelihoods than vanilla axions (along the lowest row). In particular, for pure axion models (along the far right), the maximum likelihood around $\theta_0 = \pi - 10^{-1} \approx 3.01$ gives log likelihood values that are actually 0.1 higher than CDM, whereas vanilla axions are 2.1 less than CDM. This suggests that extreme axions with $m_{\rm ax} = 10^{-22.5}$ eV may actually be slightly preferred by the Ly-$\alpha$ data, while vanilla axions with the same mass would be ruled out. In addition, the improvement is likely significant enough to warrant the addition of one extra parameter, based on

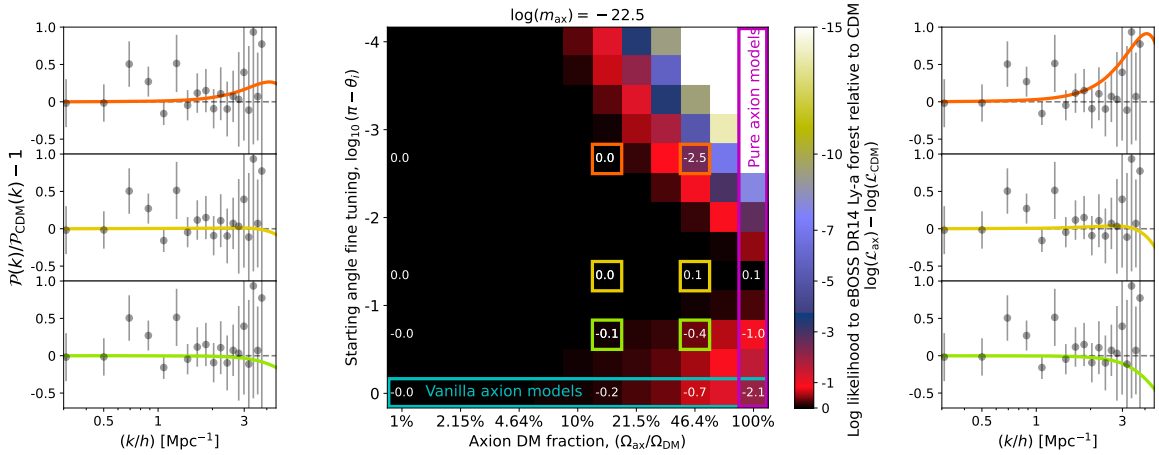


Figure 3.10: As Fig. 3.9, except for $\log_{10}(m_{\rm ax}/{\rm eV}) = -22.5$. The middle plot shows a grid of the relative log likelihood values of this fit, relative to the fit with pure CDM The horizontal axis shows different axion fractions, and the vertical axis shows different degrees of fine tuning for the axion starting angle. The six plots along the left and right show the fractional differences of the matter power spectra for six examples on the grid, highlighted by the orange, yellow, and green boxes, to allow a visual comparison to the eBOSS DR14 Ly-$\alpha$ forest estimates of the linear MPS. The best fits to Lym-$\alpha$ forest data can be achieved with a starting angle roughly between $3 \lesssim \theta_i \lesssim 3.13$, but fits can be achieved with lower axion fraction for a wider range of angles than that.

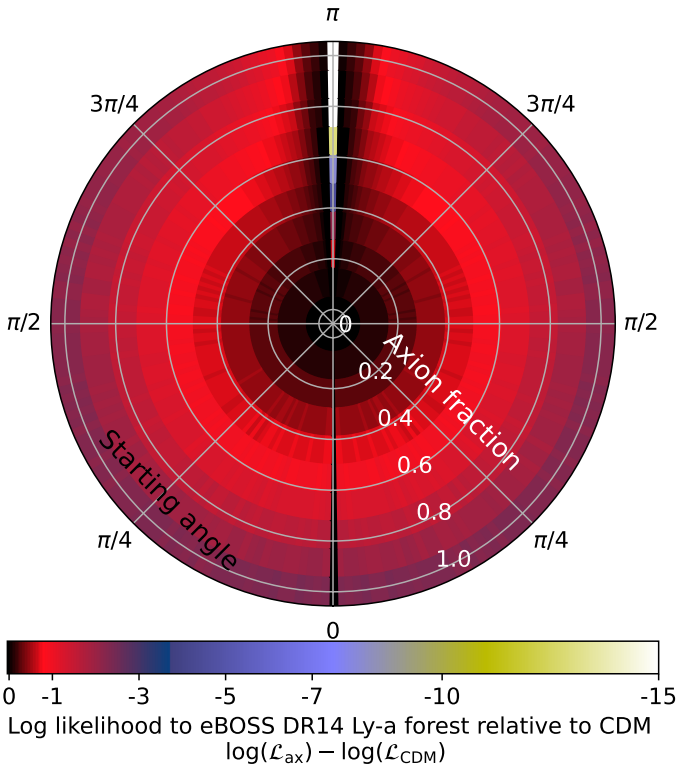


Figure 3.11: As Fig. 3.10, with $\log_{10}(m_{\rm ax}/{\rm eV}) = -22.5$, but plotted radially for a full range of starting angles. The color represents the relative log likelihood values of this fit, relative to the fit with pure CDM The radial axis shows different axion fractions, and angle represents the axion starting angle. The black region represents scenarios that can fit the data as well as CDM, which include a non-trivial fraction of starting angles at high axion fraction.

the AIC. This conclusion could be verified with a full hydrodynamical simulation and comparison to Ly-$\alpha$ forest data, and the exact mass where axions can go from forbidden to permitted might change slightly. However, we can be confident that extreme axions can alleviate tensions with Ly-$\alpha$ data for some mass range, drawing into question our previous upper bounds on the axion mass, and motivating future work into Ly-$\alpha$ constraints on extreme axions.

The range of possible starting angles that can relieve axion constraints is non-trivial. Fig. 3.11 shows the relative difference in log likelihood for $m_{\rm ax} = 10^{-21.5}$ relative to CDM for a full range of starting angles, where the polar angle is the axion starting field angle, and the radius is the axion fraction. The dark region of the plot (with fits that are almost as good as CDM) covers the low-fraction region in the centre of the plot, as well as a non-trivial portion of the outer region around starting angles close to $\pi$. From this plot, we can conclude that even with a uniform prior on starting angle, the existince of these extreme solutions should have a nontrivial impact on estimated constraints on axion mass and fraction.

While Figures 3.10 and 3.9 show that a moderately extreme axion can help alleviate tensions with Ly-$\alpha$ forest data for axions with a mass of $10^{-22.5}$ eV, this is not necessarily true for all axion masses. Figure 3.12 shows this same log likelihood grid for masses of $10^{-22}$ eV and $10^{-24}$ eV. We can see that for $m_{\rm ax} = 10^{-24}$ eV, the effects are at low enough $k$ that they remain ruled out regardless of initial field angle. In this case, the constraints become entirely dependent on axion fraction. On the other hand, at $m_{\rm ax} = 10^{-22}$ eV, the effects are at high enough $k$ that they are completely unconstrained by the eBOSS Ly-$\alpha$ forest estimates of the MPS, regardless of starting field angle or axion density fraction. Evidently, extreme axion starting angles can only alleviate constraints on the axion density fraction with Ly-$\alpha$ forest data for a specific range of masses, around $m_{\rm ax} \sim 10^{-23}$ eV. It is important to note that the relevant mass range in question will depend heavily on the maximum $k$ being probed by the relevant survey. This mass range will change slightly if we use Ly-$\alpha$ estimates at different scales [such as high-resolution surveys using Keck or the Very Large Telescope, 129, 100], but the effect will likely still be limited to a certain mass range.

## 3.5 Discussion and Future Work

The methods presented in this work allow for rapid computations of cosmological observables in extreme axion models, and their rapid comparison to real data, and opens up a range of interesting applications and areas of further study. In general, moderately extreme starting angles seem to alleviate tensions with existing measurements of the MPS for a certain range of axion mass $m_{\rm ax}$, axion density $\Omega_{\rm ax}h^2$, and initial axion field angle $\theta_i$, but establishing the exact limits of these alleviated tensions is an interesting question that would require an extensive MCMC analysis. We can see from Fig. 3.11 that even with uniform priors on the starting angle (ie. no fine tuning mechanism), the existence of these extreme solutions capable of alleviating the constraints would make up a non-trivial fraction of model parameter space. Such an analysis would involve repeated computations of our extreme axion model (made possible by the rapid runtimes of our modified `axionCAMB`), and the repeated comparison to cosmological likelihoods for galaxy clustering and the CMB. Such an analysis would tell us exactly how much weaker our constraints on axion mass and density could be if we are allowed to vary the starting field angle. It would also tell us about any degeneracies between these three axion parameters and any other cosmological parameters being

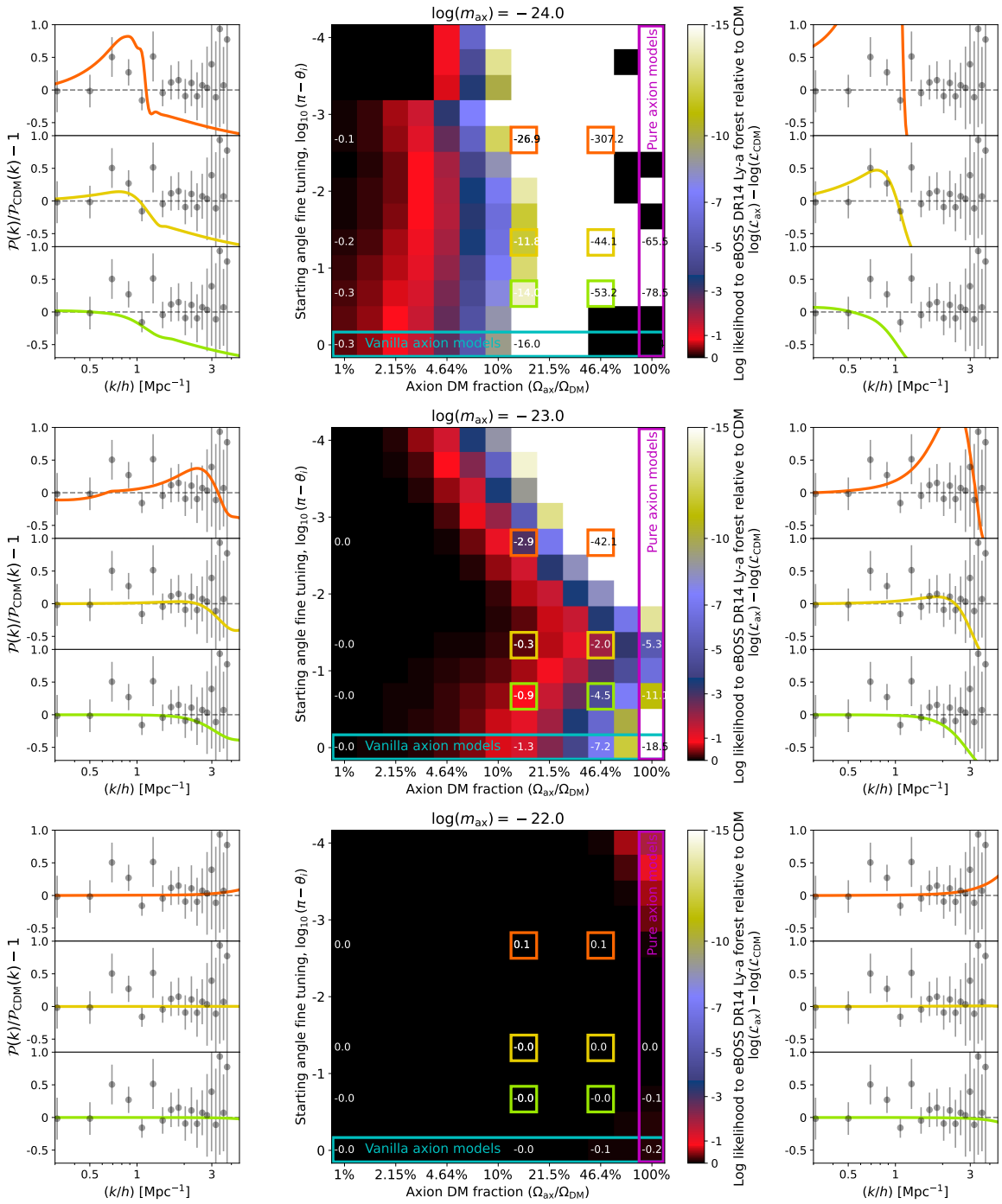


Figure 3.12: The fit of our extreme mixed axion model to the eBOSS Ly-$\alpha$ forest data for a larger range of masses, showing that axions with masses of $10^{-24}$ or $10^{-22}$ are not impacted by considering extreme axions as opposed to vanilla axions.

varied.

Although comparison to LSS likelihoods from galaxy surveys, and CMB likelihoods for the lensing, temperature, and polarization power spectra are the most straightforward, the tightest current constraints on axions come from measurements of the Ly-$\alpha$ forest, as these are able to probe the MPS at much smaller scales than either galaxy surveys or the CMB [169]. However, comparing MPS predictions for extreme axions to data from the Ly-$\alpha$ forest is more difficult, as it requires hydrodynamical simulations of the small-scale nonlinear structure, which in principle could depend on the nonlinear behaviour of the extreme axion model. In this paper, we used the estimates of the linear $z = 0$ MPS from the Ly-$\alpha$ forest data, which assumed CDM for the small-scale structure evolution, but this method is only valid in the low-axion-density regime, where CDM makes up most of the dark matter.[4] Some work has been done modeling the nonlinear Ly-$\alpha$ forest for extreme axions[121], but this simulation is computationally expensive. Ideally, the best approach would be to train an emulator to produce extreme axion predictions of the Ly-$\alpha$ data, similar to what was done in Ref. [169]. When combined with our modified `axionCAMB`, this could allow for rapid computation and direct comparison to Ly-$\alpha$ forest data, which would give the most informative constraints on the small-scale behaviour of these extreme axion models. This analysis would also require a more robust model of the extreme axion sound speeds in order to model the effects at higher redshifts, while the current model has only been validated for $z = 0$. In addition, direct comparison to Ly-$\alpha$ observables would allow us to use higher resolution spectroscopic surveys, such as those done with Keck or VLT [129, 100].

Accurate simultaneous constraints on the axion mass, density fraction, and starting angle, would quantitatively address an important question that, so far, has only been approached qualitatively: namely, the required degree of fine-tuning for these extreme axion models to work. Fig. 3.10 shows that a good agreement with data can be reached with axion starting angles that are close to the peak, seperated by less than 10%. Fig. 3.11 shows that the range of starting angles that can fit the Ly-$\alpha$ forest data with a large axion fraction is non-trivial, suggesting that extreme starting angles are an important factor to consider when computing axion constraints, even without a fine tuning mechanism. This required degree of fine-tuning could also depend on other cosmological parameters. With our modified `axionCAMB`, we could create estimates of the necessary degree of fine-tuning for a range of axion and cosmological parameters, helping to inform the plausibility of these models that produce starting angles close to $\pi$.

Another area worth exploring is comparing these constraints to forecast sensitivities by future CMB experiments, such as the Simons Observatory, and CMB-S4 [93, 120, 69, 1]. Although Planck is already cosmic-variance limited for temperature at low-$\ell$, there may be substantial improvements to be made with an experiment with better polarization and/or high-$\ell$ data [7]. CMB lensing also offers the ability to probe the DM MPS at a range of scales[171]. We could also experiment with simultaneous constraints from CMB and MPS sources. Direct probes of the MPS can also be used to constrain the extreme axion model, including the Dark Energy Survey [which we used to constrain the vanilla axion model in 62], *Euclid* [14], JWST [154], and the Vera Rubin Observatory [134]. Lensing or Galactic dynamics could also be used to search for DM substructure on sub-galactic scales [145, 210, 144].

[4]Ref. [170] finds that pure CDM, with the hydrodynamical model used in the eBOSS analysis, is insufficient to explain both the *Planck* CMB and eBOSS Ly-$\alpha$ forest data, further motivating a more robust mixed-axion hydrodynamical treatment of the Ly-$\alpha$ forest.

It is important to note that these ultralight axion models can also be probed by late-time astrophysical effects, including the formation of dwarf galaxies [60], or dark matter rotation curves [22, 21]. These e-time astrophysical probes would not be impacted by the early-time imprints of extreme starting angle, and thus these constraints appear to be independent of axion starting angle. However, these constraints depend on astrophysical modeling in dense baryonic environments (for example, modeling the structure of the soliton core), which makes it difficult to probe to low axion fraction. Cosmological constraints sensitive to the linear MPS (such as the CMB, Ly-$\alpha$ forest, or the UV luminosity function) remain superior in probing low axion fractions [eg. 92, 171, 209], and thus a rigorous understanding of extreme starting angles is necessary to compute accurate constraints using these experiments. While these observables probe different axion masses (ranging from $10^{-27}$ eV up to $10^{-19}$ eV), we anticipate that the alleviation of mass and fraction constraints due to extreme axion starting angle will be qualitatively similar across that range. The comparison to eBOSS Ly-$\alpha$ forest constraints is intended as an illustrative proof of concept, and is not intended to be a comprehensive reevaluation of cosmological axion constraints.

Lastly, we could try constraining potentials beyond just the standard cosine shape. Models have been proposed with axions possessing quartic, hyperbolic cosine, or monodromic potentials [42, 200, 105, 124]. In addition, axion-like scalar fields with a variety of potentials have been proposed as an early dark energy component potentially capable of relieving the Hubble tension [109, 161]. Axion perturbations in all of these potentials could conceivably be modeled using our modified `axionCAMB`, since the potential function is implemented generically. The only requirement would be that the potential being tested must simplify to a quadratic at small $\phi$ values, in order for the particle DM approximation to be valid at late times.

## 3.6 Conclusions

Extreme axions represent an interesting class of dark matter models, possessing both interesting theoretical justifications from string theory, as well as concrete cosmological observables. Previously, their one major drawback was the high computational cost of modeling the rapid field oscillations. In this work, we have introduced a new extension to the existing `axionCAMB` software, allowing it to compute MPS and CMB observables for extreme axion models in $\sim 7$ seconds, where previous models have taken multiple days. These observables can be computed for a range of values for the axion mass, axion DM density fraction, and extreme axion starting angle, as well as a range of ordinary cosmological parameters. We achieved this rapid modeling of the extreme axions by using a modified version of `axionCAMB`'s fluid approximation, reconfiguring the initial conditions to allow for finely tuned starting angles, modifying the effective fluid sound speed to reflect the tachyonic growth during the oscillatory phase, and implementing an efficient lookup table of the axion background fluid variables to allow for rapid computation.

We also compared the results of our extreme axion model to estimates of the linear matter power spectrum from the eBOSS DR14 Ly-$\alpha$ forest data. While there are limitations to this approach, as the estimation of the linear $z = 0$ MPS from Ly-$\alpha$ forest data assumes CDM physics, and integrates over a number of astrophysical parameters, we can still use this comparison to give us estimates of the effect of these extreme axion models on cosmological axion constraints more generally. We find that when considering the eBOSS DR14 Ly-$\alpha$ forest data, for a range of axion masses around

$m_{\rm ax} \approx 10^{-22.5}$ eV, constraints on the axion fraction can be significantly weakened by considering extreme axions with a starting angle between $\pi - 10^{-1} \lesssim \theta_i \lesssim \pi - 10^{-2}$. This motivates future work running robust MCMC comparisons of this extreme axion model to Ly-$\alpha$ observables, as well as CMB and other cosmological axion measurements. With the help of this new, efficient fluid model of extreme axions, we can compute more nuanced constraints on axion mass and fraction, as well as shed new light on the possible high-energy origins of these ALPs through estimates of the axion decay constant $f_{\rm ax}$.

# Chapter 4

# Testing Axions with the UV Luminosity Function

Article submitted to the Astrophysical Journal, as Harrison Winch et al. "High-redshift, small-scale tests of ultralight axion dark matter using Hubble and Webb galaxy UV luminosities". In: (Apr. 2024). arXiv: `2404.11071 [astro-ph.CO]`. As first author, this project was primarily my idea, in collaboration with co-author Keir K. Rogers. I developed and modified the code used in this project, created all figures, and wrote almost all of the paper text, with editorial input from co-authors, including Keir K. Rogers, Renée Hložek, and David J. E. Marsh.

## 4.1 Abstract

We calculate the abundance of UV-bright galaxies in the presence of ultralight axion (ULA) dark matter (DM), finding that axions suppress their formation with a non-trivial dependence on redshift and luminosity. We set limits on axion DM using UV luminosity function (UVLF) data, excluding a single axion as all the DM for $m_{\rm ax} < 10^{-21.6}$ eV and limiting axions with $-26 \leq \log(m_{\rm ax}/{\rm eV}) \leq -23$ to be less than 22% of the DM (both at 95% confidence limit). These limits use UVLF measurements from 24,000 sources from HST at redshifts $4 \leq z \leq 10$. We marginalize over a parametric model connecting halo mass and UV luminosity. Our results bridge a window in axion mass and fraction previously unconstrained by cosmological data, between large-scale CMB and galaxy clustering and the small-scale Lyman-$\alpha$ forest. These high-$z$ measurements provide a powerful consistency check of low-$z$ tests of axion DM, including the recent hint for a sub-dominant ULA DM fraction in Lyman-$\alpha$ forest data. We also consider a sample of 25 spectroscopically-confirmed high-$z$ galaxies from JWST, finding these data to be consistent with HST. Combining HST and JWST UVLF data does not improve our constraints beyond HST alone, but future JWST measurements have the potential to improve these results. We also find an excess of low-mass halos ($< 10^9 M_\odot$) at $z < 3$, which could be probed by sub-galactic structure probes (e.g., stellar streams, satellite galaxies and strong lensing).

## 4.2 Introduction

Ultralight axions and axion-like particles (with masses $m_{\rm ax} \lesssim 10^{-18}$ eV) are well-motivated dark DM particle candidates, which are discussed in detail in Section 1.2.2 of the Introduction. Large-scale measurements of the CMB and galaxy clustering have put tight constraints on the axion fraction for low-mass ($m_{\rm ax} \leq 10^{-25}$ eV) axions [90, 89, 117, 171]. Small-scale measurements of the Lyman-$\alpha$ forest rule out higher-mass ($10^{-23}$ eV $\lesssim m_{\rm ax} \lesssim 10^{-20}$ eV) axions at higher DM fractions [101, 112, 169]. A joint analysis of CMB and Lyman-$\alpha$ forest measurements from eBOSS [11] finds that a non-zero axion density ($m_{\rm ax} \sim 10^{-25}\,$eV) alleviates tension in measurement of the small-scale power [170], while respecting existing limits. Axions ($m_{\rm ax} \sim 10^{-25}\,$eV) are also found to address other cosmological parameter discrepancies relating to the amplitude of small-scale power [171].

However, there remains a substantial gap of unconstrained axion masses, around $10^{-25}$ eV $\lesssim m_{\rm ax} \lesssim 10^{-23}$ eV, which have evaded current cosmological constraints. Claimed constraints in this mass range from strong lensing [187] and galaxy rotation curves [21] depend on modeling the complex astrophysics of the soliton core in dense galactic environments, making it difficult to probe low axion fractions, which motivates the use of complementary cosmological probes to further probe this gap. In addition, all other axion probes use either low ($z \lesssim 5$) or recombination ($z \sim 1100$) redshifts, with no powerful probes during the redshifts of early structure formation ($4 \lesssim z \lesssim 16$). Any claimed evidence of axion DM as a resolution to low-$z$ tensions [e.g., 170, 171] needs to be corroborated by high-$z$ consistency checks that can probe similarly small scales.

In this paper, we investigate the use of the galaxy UVLF (introduced in Section 1.4.3 as an independent probe of ultralight axions, capable of probing a novel range of scales and redshifts unexplored by observations (as seen in Fig. 1.2). The UVLF, $\Phi_{\rm UV}(M_{\rm UV}, z)$, is the number of UV sources (galaxies) per unit volume per unit UV magnitude $M_{\rm UV}$ at redshift $z$. This function depends on the astrophysical model of star formation within the galaxy which contributes to the UV luminosity through the number of bright young stars, as well as depending on the halo mass function (HMF), which describes the number density of halos of a given mass. Since the de Broglie wavelength of ultralight axions prevents them from clustering into halos below a certain scale, this will impact the HMF, which will in turn impact the UVLF [36, 178, 52]. Thus, the UVLF has the potential to probe axion physics on small scales, beyond the reach of more established large-scale structure observations. We use the UVLF likelihood package `GALLUMI` [174], which computes the UVLF using the formalism we describe in Sections 4.3 and 4.4. [174, 173] already demonstrated the power of the high-$z$ UVLF in testing the standard cosmological model. We present here the first use of this modeling of the UVLF in testing a concrete example of beyond Standard Model physics.

Previous studies constraining axions with the UVLF include [36, 178, 52]. [178, 52] use $N$-body simulations to compute the observables and were therefore unable to perform a detailed statistical analysis being limited by the number of simulations they could calculate. [36] use similar semi-analytic methods to those we use here, but did not perform a full statistical analysis of constraints on mass and fraction. These previous works find consistent results with one another, validating the semi-analytic methods. In the present work, we perform, for the first time, a complete statistical analysis combining CMB and UVLF data (see Fig. 4.1 for a summary of our main result).

The HST has observed over 24,000 UV sources between different surveys at redshifts $4 \leq z \leq 10$ [30, 31]. These UVLF measurements have recently been augmented by groundbreaking new results from JWST, which can observe UV sources at much higher redshifts, up to $z \sim 16$ [28, 87]. We find

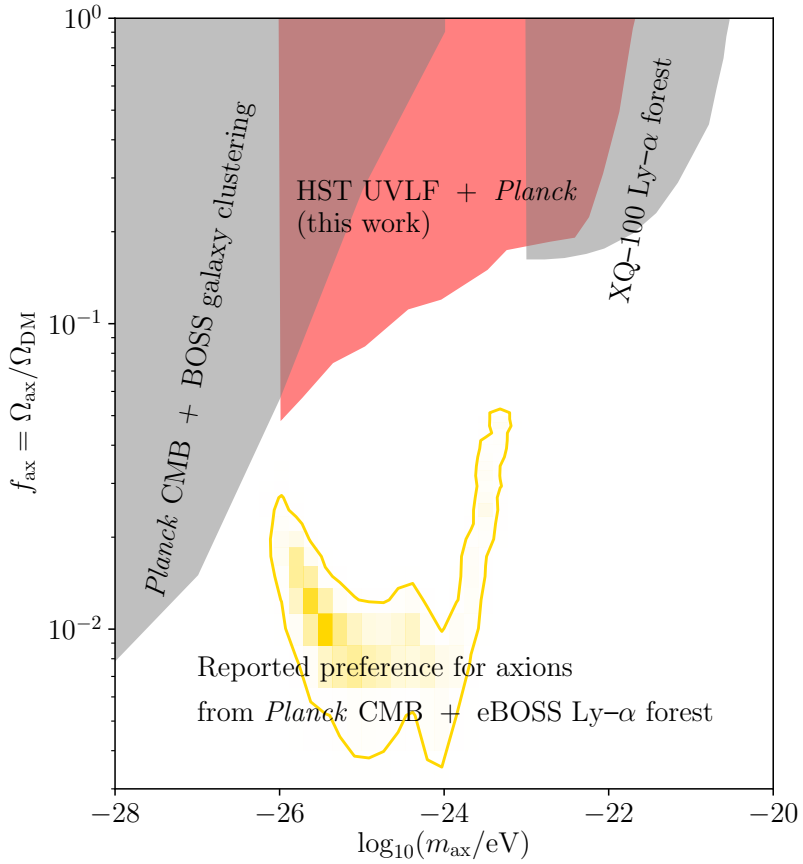


Figure 4.1: $2\sigma$ constraints on axion mass and DM fraction from cosmological probes (astrophysical constraints are neglected due to their complex dependence on soliton modeling). The right shaded region represents constraints using the Lyman-$\alpha$ forest computed in [112], with data from the XQ-100 survey [127] and the MIKE and HIRES spectrographs, which only considered axions down to a mass of $10^{-23}$ eV. The left shaded region represents joint constraints from *Planck* CMB and BOSS galaxy clustering, as computed in [171]. This work (in red, also shown in Fig. 4.9) crucially fills a gap between these two other methods. The gold contours represent the reported preference for axion DM presented in [170], computed using both *Planck* CMB and eBOSS Ly-$\alpha$ forest data, which is consistent with our UVLF limits.

that while the JWST data do constrain the axion fraction on their own, the quality of the HST data still provides tighter constraints on axion physics.

Some early analyses of JWST observations have suggested that its estimates of the $z > 10$ UVLF may be substantially higher than the ΛCDM expectations based on the $z < 10$ HST estimates [32, 49]. If true, this overabundance of structure at high redshifts could imply tight constraints on the allowed axion fraction, given that axions would decrease this UVLF (though this is a mass-dependent statement, as shown in Figure 4.6).

However, there are significant uncertainties in star and galaxy formation at these high redshifts that need to be marginalized over, and so a full statistical analysis including a robust model of these uncertainties is essential to draw conclusions regarding the nature of DM. In addition, the discrepency appears to be higher in photometric JWST samples, where low-$z$ interlopers may impact the distribution of UV magnitudes.

In Section 4.3, we introduce our method for computing the HMF and present the impacts of mixed axion models on the HMF, while Section 4.4 does the same for the UVLF. In Section 4.5, we present the results of a statistical comparison with data, using measurements of both HST UVLF and *Planck* CMB. In Section 4.6, we compare these constraints to those from other probes and discuss the prospects for future improvements. We conclude in Section 4.7.

## 4.3 The Halo Mass Function

The halo mass function (HMF) is the number density of dark matter halos of total mass $M_h$. This function, which varies with redshift, can be calculated for both ΛCDM and mixed axion models. It is a key component for calculating the UVLF, our primary observable, which is discussed in Section 4.4. Through this section and Sec. 4.4, we will consider three possible impacts of axions on the UVLF, which are listed below:

- **Cosmological impact of axions** refers to the impact of axions on the linear matter power spectrum, which goes into the computation of the HMF. We find that this mechanism has the dominant effect on the UVLF.
- **Axion halo pressure** refers to the effect of axions preventing the creation of halos below the halo Jeans limit due to their quantum pressure effects.
- **Axion astrophysics** refers to the impact of axions on the baryonic sector for halos below the Jeans limit. Halos below this limit will lack an axion component, due to axion halo pressure, and thus will have a greater ratio of baryons to DM. This will lead to increased star formation relative to total halo mass, which impacts the UVLF as described in Section 4.4.2.

### 4.3.1 Computing the HMF

The HMF can be computed from the linear MPS with the Sheth-Tormen model of ellipsoidal collapse, using the method described in [107, 51, 173, 203], and outlined in Section 1.3.4.

When the cosmological model contains both axions and CDM, the computation of the HMF will be impacted by the presence of axions. Galaxy halos are being formed from a mixture of axions and CDM [118]. As such, these halos will use the combined axion-and-CDM values of $P^{\rm L}(k, z)$,

$\sigma(M_h, z)$, and $\bar{\rho}(z)$. Since axions alter the form of $P^{\rm L}(k, z)$ (and thus $\sigma(M_h, z)$), this will impact the shape of the HMF, even for large halos that may be above the axion Jeans scale.

In addition to the cosmological impact through $P^{\rm L}(k, z)$, axion physics can impede the formation of halos of size equal to or smaller than the axion Jeans scale. This is due to the macroscopic de Broglie wavelength of ultralight axions preventing axions from clustering into small halos. In this work, we refer to this effect as "axion halo pressure" to distinguish its effects from the cosmological impact on the HMF, or the astrophysical impacts of axions on the UVLF (discussed in Sec 4.4.2). The axion Jeans wavenumber

$$k_J \approx \sqrt{m_{\rm ax} H}, \tag{4.1}$$

where $m_{\rm ax}$ is the axion mass and $H$ is the Hubble parameter [90]. [138] and [203] compute a critical halo mass below which the average virial radius is below the axion Jeans scale, indicating that axion halo pressure would play a non-negligible role in halo formation. Such a critical halo mass

$$M_{\rm crit} = \frac{4}{3}\pi\left(\frac{\lambda_J}{2}\right)^3 \rho_{\rm m}, \tag{4.2}$$

where $\lambda_J$ is the Jeans scale, related to the Jeans wavenumber by $\lambda_J/2 = \pi/k_J$.

The critical halo mass is always much smaller than the halo masses already impacted by the linear axion power spectrum. For many axion particle masses, the critical halo mass is too small even to be probed with the HST UVLF. Fig. 4.2 shows the range of halo masses probed by the HST UVLF at different redshifts (based on the UVLF model presented in Sec. 4.4), compared to the maximum halos impacted by both the halo pressure and linear cosmology of axion DM with $m_{\rm ax} = 10^{-23}$ eV. The maximum halo mass impacted by axion halo pressure is not only smaller than the minimum halo probed by HST, but is also at least two orders of magnitude smaller than the maximum halo mass impacted by the axion linear cosmology. Both of these halo mass limits vary with axion mass in the same way, meaning that axion cosmology always impacts a substantially larger range of halo masses than the axion astrophysics [see Fig. 2 in 138]. In this work, we ignore these axion halo pressure effects as negligible and consider only the cosmological impacts of axions on the HMF via $P^{\rm L}(k, z)$. This is consistent with the results of past works, including [62], which found that axion constraints from galaxy weak lensing using the Dark Energy Survey [4] were not sensitive to the critical halo mass. We illustrate the negligible role of the axion halo pressure in Fig. 4.3.

### 4.3.2 Impact of axions on the HMF

Considering only the cosmological impacts of axions on the HMF, there is a suppression in the number of halos below a certain mass. This suppression physically arises since, below their macroscopically-sized de Broglie wavelength, axions suppress the amplitude of density fluctuations that form halos. Fig. 4.3 (right-hand side) shows the impact of axions with a mass of $m_{\rm ax} = 10^{-24}$ eV on the HMF at $z = 8$ for different axion fractions, showing how a higher axion fraction causes an increased suppression. Fig. 4.3 illustrates how allowing just 10% of the DM to be in the form of axions can result in a significant suppression in the number of DM halos at that redshift ($\sim 80\%$). We consider $z = 8$ as representative of the redshifts probed by the UVLF (see Figs. 1.2, 4.2 and 1.5).

The left-hand side of Fig. 4.3 shows that higher mass axions (of order $m_{\rm ax} \approx 10^{-21}$ eV) result in

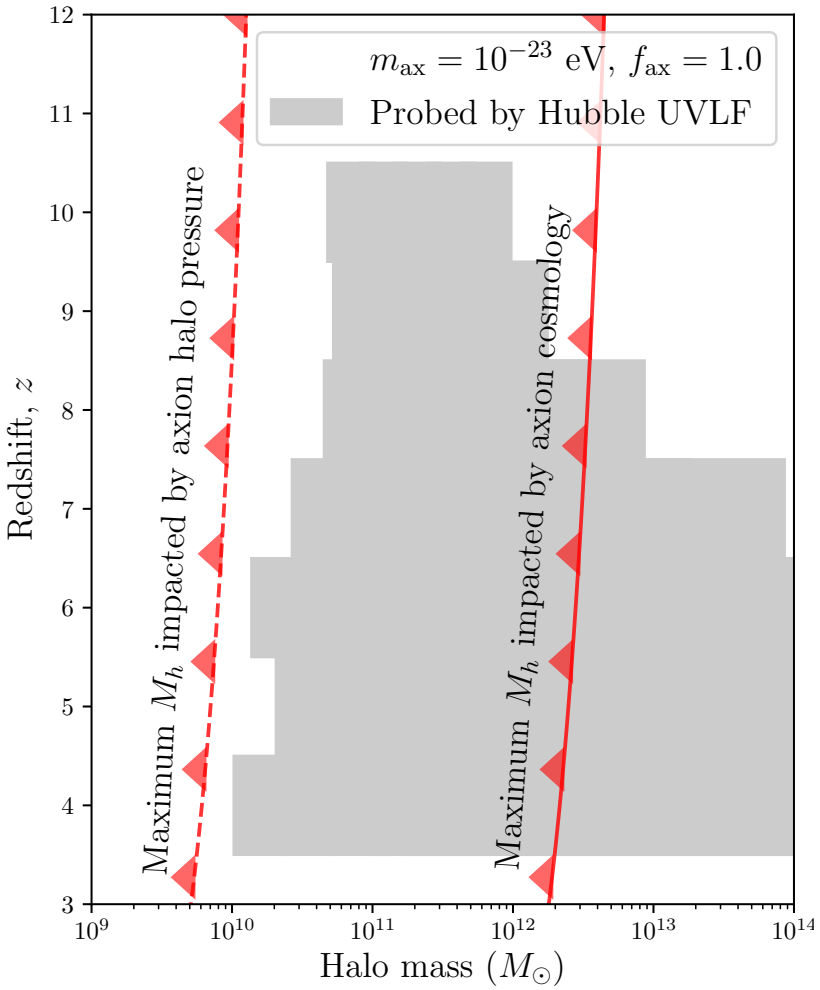


Figure 4.2: The redshifts and halo masses probed by HST measurements of the UVLF (grey boxes), along with the masses impacted by axion halo pressure and cosmology at $m_{\rm ax} = 10^{-23}$ eV (red lines). The halo masses impacted by axion astrophysics are always much smaller than those impacted by axion cosmology. This includes both the prevention of axion halo formation, as discussed in Sec. 4.3, as well as the indirect effects on the star formation rate below the Jeans scale, which is discussed in Sec. 4.4.

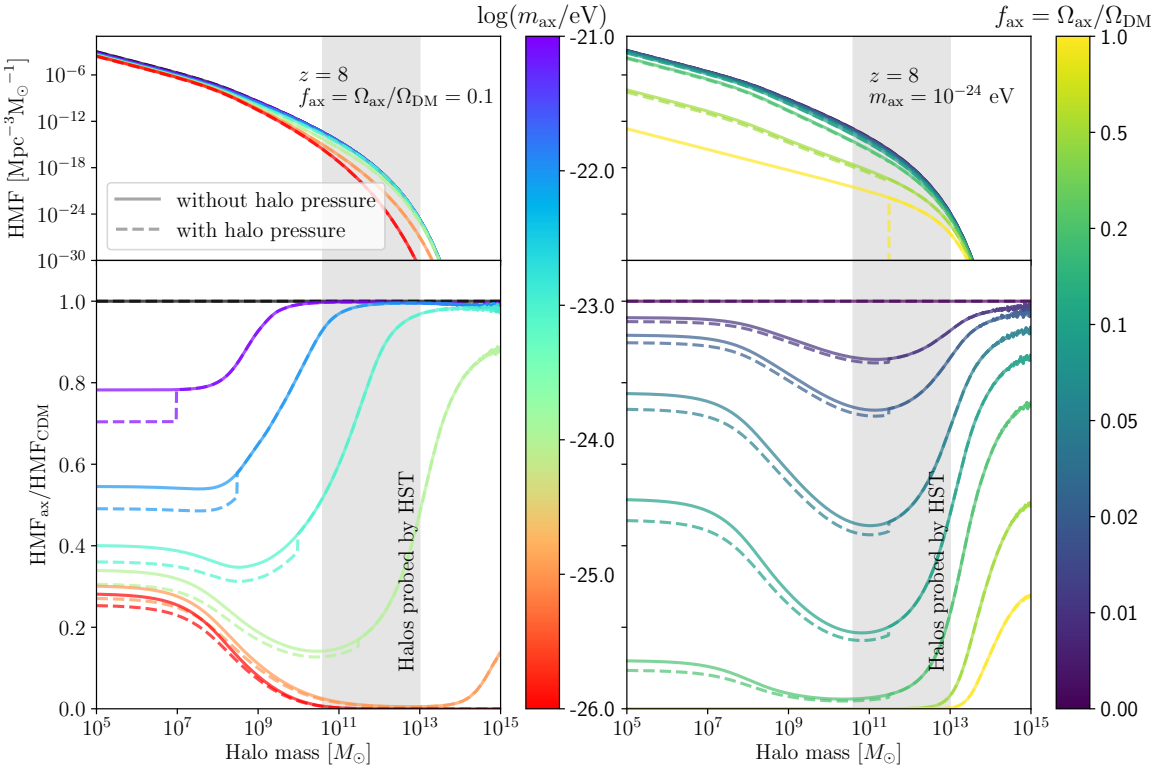


Figure 4.3: The left panels show the impact of axions with varying mass and fixed axion fraction of $f_{ax} = \Omega_{ax}/\Omega_{DM} = 0.1$ on the HMF, while the right panels show the impact of varying the axion DM fraction at a fixed mass of $m_{ax} = 10^{-24}$ eV. The top panels show the HMF, while the lower panels show the ratio of the HMF relative to a pure ΛCDM cosmology, all computed at $z = 8$. Lower mass axions result in a stronger suppression of the HMF, along with a higher maximum impacted halo mass. The scale of axion fractions in the right panels is not linear. Higher axion fractions result in stronger suppressions of the HMF; for intermediate axion fractions the suppression is less pronounced at lower halo masses, as a result of delayed structure formation due to the suppression of initial small-scale fluctuations (see Fig. 4.5 for an illustration of this process). We also plot the impact of axion halo pressure suppressing halo formation below the critical Jeans scale, shown with dashed lines. These corrections are negligible compared to the cosmological impact of axions on the HMF for the range of halo masses probed by HST. This is true for all axion masses and DM fractions that we consider.

a suppression of around 20% for halos lighter than $\sim 10^9 M_\odot$. However, lower mass axions (of order $m_{\rm ax} \approx 10^{-24}$ eV) result in a significant suppression of halos with mass between $10^8$ and $10^{14} M_\odot$, with the suppression of halo formation reaching as much as 80% compared to the ΛCDM model. The cutoff halo mass is roughly inversely proportional to the axion mass, as shown in [138], since heavier axions have smaller wavelengths. However, the suppression for the lowest axion masses is less severe at low halo masses, plateauing at a suppression of less than 50% for halo masses below $10^7 M_\odot$ for axion masses below $10^{-23}$ eV. This plateauing is due to the suppression of primordial structure on small scales causing a delay in hierarchical growth, resulting in more residual low-mass halos at late times that have not yet had a chance to merge into larger objects. We discuss this effect further below. This plateau is unlikely to be observed with the UVLF, where most galaxy halos that contribute to the Hubble and Webb UVLF have masses greater than $10^{10} M_\odot$ (as seen in Fig. 4.2 and by the grey bars in Figs. 4.3 and 4.4). We discuss the potential observability of this signature using low-$z$ probes of galaxy substructure in Sec. 4.6.

Figure 4.3 also shows the impact of axion halo pressure with dashed lines, which prevents the formation of axion halos below the critical Jeans halo mass (given in Eq. (4.2)). The critical halo mass depends on the axion mass, where higher-mass axions have a shorter Jeans scale and thus suppress the formation of smaller halos. The amplitude of this suppression depends on the axion fraction, where models with higher axion DM fraction exhibit a greater suppression of halo formation on small scales. In both the left- and right-hand sides of Fig. 4.3, the impact of axion halo pressure is always subdominant to the impact of axion cosmology, particularly in the range of halo masses probed by HST (in the light grey bar). Therefore, we safely neglect the effects of axion pressure on halo formation when computing the UVLF. Further, we explicitly check in Section 4.4 the effect on the UVLF from axion halo pressure combined with "axion astrophysics."

Figure 4.4 shows that the suppression of the HMF due to axion DM is more pronounced at higher redshift, motivating the use of JWST and other high-redshift measurements of the UVLF. Fig. 4.4 shows the ratio of the 10%-axion HMF to the ΛCDM HMF for an axion mass of $10^{-25}$ eV at the same redshift. For $z = 12$, the HMF is suppressed by more than five orders of magnitude for halos of mass $10^{13} M_\odot$. However, for lower redshifts such as $z = 0$, the maximum suppression is only around $\sim 25\%$. The halo suppression is stronger at earlier times since the halos are a cleaner probe of the primordial axion suppression. At later times, non-linearities tend to erase the axion suppression. In fact, for $z \leq 3$, we see more low mass halos for 10% axion models relative to ΛCDM. As mentioned above, this enhancement effect is due to the delay in hierarchical growth of halos, resulting in an overabundance of low-mass halos at late times, as shown in the lower panel of Fig. 4.4. Fig. 4.5 shows that reducing the primordial scalar amplitude $A_{\rm s}$ results in a similar overabundance of low-mass halos at $z = 0$, which is also due to the suppression of structure leading to a delay in hierarchical growth. Although, the scale dependence of the effect is different in the case of axions due to the additional Jeans suppression. Axion enhancement effects are only relevant for very low halo masses ($M_h \lesssim 10^9 M_\odot$) and late times ($z \lesssim 3$), which are well beyond the scope of the UVLF (see Fig. 4.2). This overabundance of low-mass halos in a mixed axion cosmology is nonetheless a novel theoretical result. We discuss the potential observability with low-$z$ probes in Sec. 4.6.

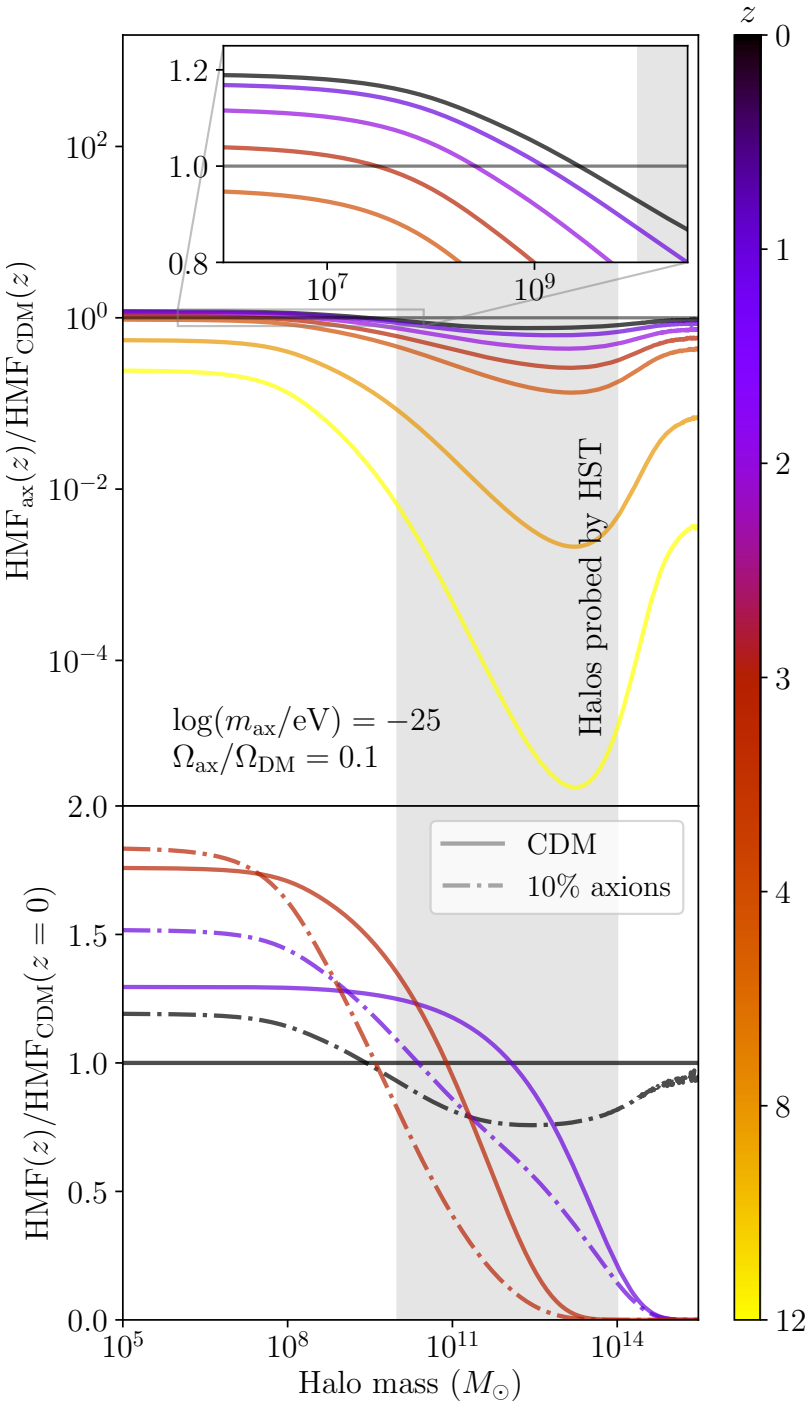


Figure 4.4: As Fig. 4.3, but for varying redshift, $m_{\mathrm{ax}} = 10^{-25}\,\mathrm{eV}$ and $f_{\mathrm{ax}} = 0.1$. The upper plot shows the mixed-axion HMF relative to the ΛCDM HMF at the same redshift, with the inset focusing on low redshifts (between $z = 0$ and $z = 4$) where the HMF enhancement occurs. The lower plot shows a ΛCDM HMF (in solid) and a 10%, $m_{\mathrm{ax}} = 10^{-25}$ eV mixed-axion HMF (in dashed) at $z = 3,\ 1,$ and 0, all relative to the ΛCDM HMF at $z = 0$, in order to show how the excess low-mass HMF in the mixed axion model results from the delay in the growth of intermediate-mass halos. The grey band indicates halo masses probed by the HST UVLF across all redshifts, although the range for a particular redshift might be narrower than indicated (see Fig. 4.2 for an illustration of typical halo masses probed at a certain redshift).

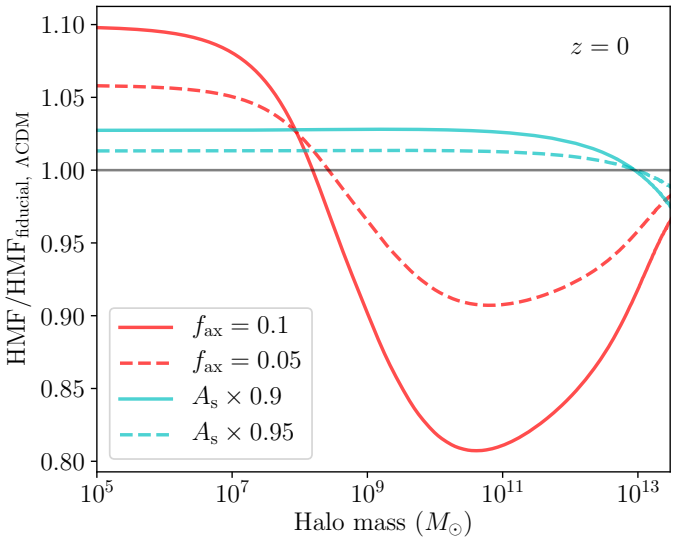


Figure 4.5: A comparison of the effect of axion fraction and primordial scalar amplitude $A_{\rm s}$ on the HMF at $z = 0$. All lines are the ratio of the HMF with respect to a pure-CDM cosmology with a fiducial value of $A_{\rm s} = 2.1132 \times 10^{-9}$. Red curves represent non-zero axion DM fraction $f_{\rm ax}$ with $m_{\rm ax} = 10^{-24}$ eV. Turquoise curves represent reduced $A_{\rm s}$ relative to the fiducial cosmology, mimicking the suppression of structure caused by axion DM. Both effects, by suppressing the initial matter power spectrum, lead to an increase in the number of low-mass halos at late times, due to the delay in the onset of hierarchical growth.

## 4.4 The Galaxy UV Luminosity Function

### 4.4.1 Computing the UVLF

The UVLF $\Phi_{\rm UV}$ is the number density of galaxies with a given UV magnitude $M_{\rm UV}$ at a redshift $z$, and can be computed using the method described in Section 1.4.3.

In addition to the effects of axions on the halo mass function discussed in Section 4.3, we consider here the effects of axion astrophysics on the relation between UV luminosity and halo mass. As in the discussion regarding axion halo pressure, axions do not cluster into halos below a critical mass equivalent to the Jeans scale within the halo [203]. Therefore, the relation between halo mass and stellar mass (Eq. (1.83)) can deviate from the CDM expectation below this critical mass. Halos in that regime are missing the axion DM component and thus have a higher ratio of baryons to DM. For a given stellar mass, the halo mass is multiplied by a factor equal to the CDM fraction, i.e. by $(1 - \Omega_{\rm ax}/\Omega_{\rm DM})$, where $\Omega_{\rm ax}$ and $\Omega_{\rm DM}$ are the axion and total DM densities, respectively, relative to the critical density. This reduction in halo mass means that the ratio of the stellar mass relative to the total halo mass, $\overline{M_\star}/\overline{M_h}$, is enhanced by a factor of $1/(1 - \Omega_{\rm ax}/\Omega_{\rm DM})$. This only applies for halos below the cutoff mass given in Eq. (4.2), modifying Eq. (1.83) with a piecewise enhancement below the critical mass. We illustrate the negligible role of this "axion astrophysics" in Fig.4.6. We discuss the UVLF model and how it may change in the presence of axions further in Section 4.6.

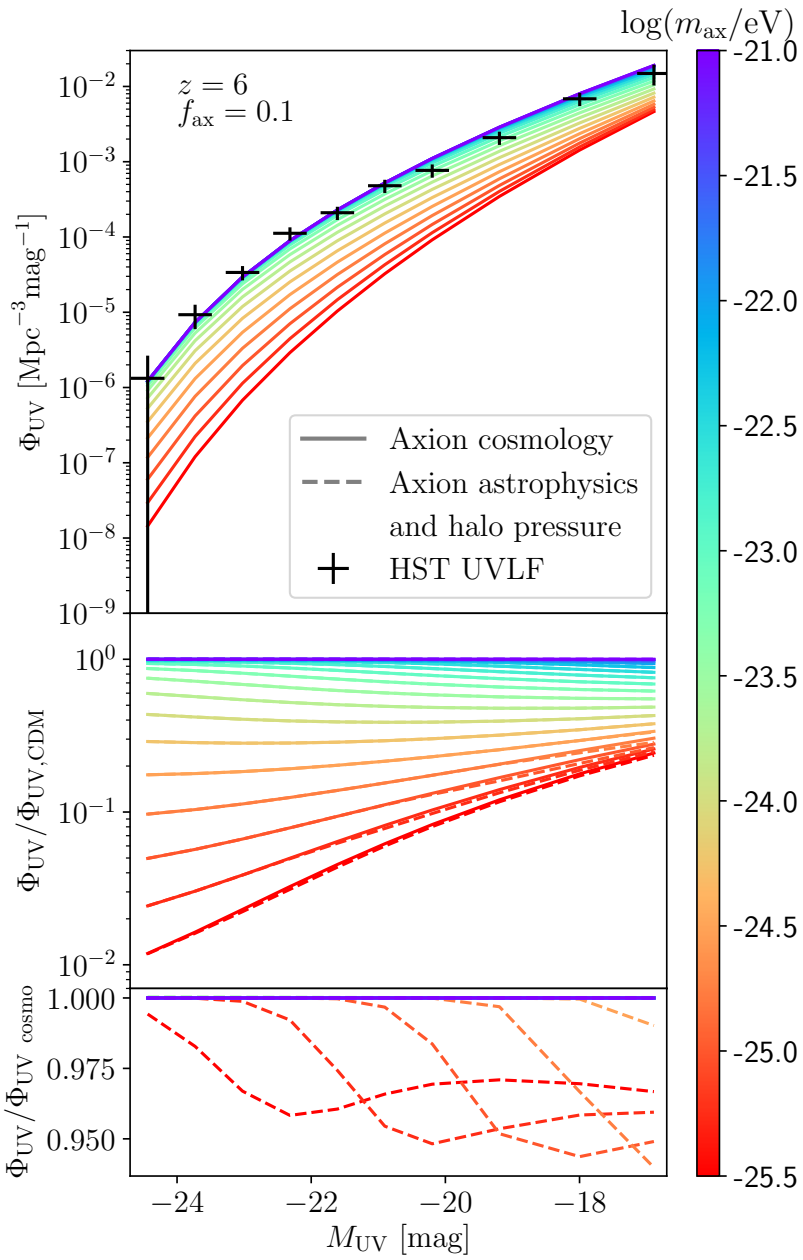


Figure 4.6: The UVLF for a range of axion masses, all with a 10% axion fraction and at $z = 6$. Black error bars show HST data at the same redshift (68% c.l. and magnitude bin widths). The upper panel shows the cosmological impact of axion mass on the UVLF without considering axion astrophysics. The middle panel shows the impact of both axion cosmology (in solid lines) and axion halo pressure and astrophysics (in dashed lines) relative to the pure CDM model. The UVLF is more suppressed for axions with lower mass, due to the larger de Broglie wavelength. Higher mass axions cause more suppression at lower halo masses (and hence fainter galaxies), while lower mass axions cause more suppression at higher halo masses (and hence brighter galaxies). This effect is due to the same overabundance of low-mass halos shown in Figs. 4.3, 4.4 and 4.5. The lowest panel shows the impact of both axion halo pressure and axion astrophysics relative to the UVLF with only the cosmological impacts. Axion halo pressure and astrophysics only impact the UVLF for $m_{ax} \lesssim 10^{-24.5}$eV, with about 5% additional suppression, whereas axion cosmology suppresses the UVLF by one to two orders of magnitude for similarly low axion masses.

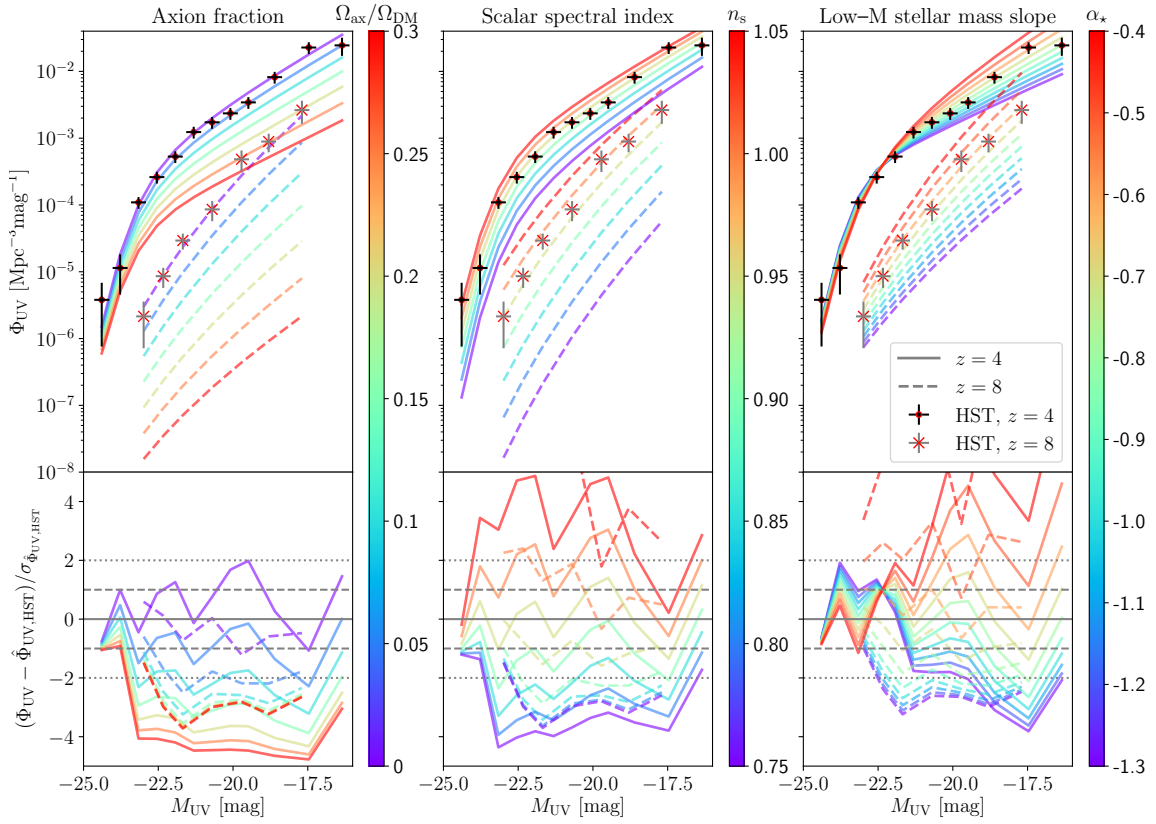


Figure 4.7: The impact on the UVLF (all other parameters fixed at best-fit values for HST UVLF + *Planck* CMB) from axion fraction (for $m_{ax} = 10^{-24}$ eV), primordial scalar spectral index $n_s$ and the low-mass slope of the stellar mass - halo mass relation $\alpha_\star$. The UVLF is shown at $z = 4$ and $z = 8$, alongside the HST measurements at the same redshifts (respectively black and grey error bars; 68% c.l. uncertainties and magnitude bin widths). The lower panels show the model difference to the HST data rescaled by the data uncertainties. All three variables have qualitatively similar impacts on the UVLF, meaning that a higher axion fraction is degenerate with higher $n_s$ and/or $\alpha_\star$.

### 4.4.2 Impact of axions on the UVLF

Fig. 4.6 shows that axions suppress the UVLF due to the suppression of structure on small scales as captured in the HMF. Lower mass axions tend to suppress structure more. Higher mass axions cause more suppression at faint luminosities, while low mass axions ($m_{\rm ax} < 10^{-22.5}$ eV) cause more suppression at higher luminosities. This is due to the same overabundance of low-mass halos shown in Figures 4.3, 4.4, and 4.5.

The first column in Fig. 4.7 shows how an axion with $m_{\rm ax} = 10^{-24}$ eV impacts the UVLF at different axion fractions. Increasing the axion density increases the suppression of faint UV galaxies, which are typically hosted by lower mass halos. However, the impact is qualitatively similar to varying the primordial scalar spectral index $n_{\rm s}$ (shown in column 2 of Fig. 4.7) or by varying the the low-mass slope of the stellar mass - halo mass relation $\alpha_\star$ (in the third column). These degeneracies mean that higher axion fractions can be permitted by increasing $n_{\rm s}$ and/or $\alpha_\star$, i.e., by allowing for more primordial small-scale structure or by increasing the stellar to halo mass ratio at the low mass end. Further, the top panels show that the axion effect is relatively stronger at higher redshift, driven by the effect on the HMF shown in Fig. 4.4. However, the lower panels show that HST data, which have fewer high-$z$ sources, are less constraining at higher redshift. We discuss in Section 4.6 the utility of higher redshift observations from JWST.

## 4.5 Comparison to Observations

| Shorthand | Likelihoods and priors | Color |
|---|---|---|
| HST UVLF | HST UVLF + Pantheon<br>+ BBN $\omega_{\rm b}$ prior<br>+ fixed $\theta_{\rm s}$ + fixed $\tau$ | Blue |
| *Planck* CMB | *Planck* high-$\ell$ TT, TE, EE<br>+ *Planck* low-$\ell$ TT, EE<br>+ *Planck* lensing + BOSS BAO | Green |
| HST UVLF<br>+ *Planck* CMB | HST UVLF + Pantheon<br>+ *Planck* high-$\ell$ TT, TE, EE<br>+ BBN $\omega_{\rm b}$ prior<br>+ *Planck* low-$\ell$ TT, EE<br>+ *Planck* lensing + BOSS BAO | Red |
| JWST UVLF | JWST UVLF + Pantheon<br>+ BBN $\omega_{\rm b}$ prior<br>+ fixed $\theta_{\rm s}$ + fixed $\tau$ | Pink |
| HST<br>+ JWST joint | HST UVLF + JWST UVLF<br>+ Pantheon + BBN $\omega_{\rm b}$ prior<br>+ fixed $\theta_{\rm s}$ + fixed $\tau$ | Magenta |

Table 4.1: The different combinations of likelihoods, priors and fixed parameters that we use, along with the shorthand used in the text and the color used for contour plots. HST UVLF measurements are given in [30], Pantheon supernovae magnitudes are given in [183], all *Planck* CMB likelihoods are given in [9], BOSS BAO measurements are given in [16] and JWST UVLF measurements are given in [87]. The prior on $\omega_{\rm b}$ and the fixed $\theta_{\rm s}$ and $\tau$ values are described in Sec. 4.5.1.

We now use UVLF data from HST, combined with other cosmological observations, to compute

constraints on mixed axion models. We use the Markov chain Monte Carlo (MCMC, described in Section 1.5.3 of the Introduction) code `MontePython` [37], along with the `axiCLASS` axion Boltzmann solver [162, 190] based on the `CLASS` code [29], to sample the posterior distribution. We use a modified version of the `GALLUMI` UVLF likelihood (presented in [173]) to compare our axion models to HST measurements of the UVLF (see Section 4.5.1). We also use *Planck* measurements of the CMB in order to constrain larger scales in the matter power spectrum than we probe in the UVLF. We summarize the different data combinations we consider in Table 4.1, including the JWST data we consider in Section 4.6. All posterior corner plots are generated using the `corner` package [78].

### 4.5.1 Hubble UV luminosities

We use estimates of the UVLF from the Hubble Space Telescope (HST) from [30]. This sample contains $> 24,000$ UV sources, at redshifts $z = 4$ to $z = 10$. The UV sources are grouped into $M_{\rm UV}$ bins of 0.5 magnitudes. These estimates of the UVLF are shown in Fig. 1.5.

We use the `GALLUMI` likelihood [presented in 173] to compute the UVLF and compare it to the HST estimates using a Gaussian likelihood $\mathcal{L}$:

$$\log(\mathcal{L}) = \sum_{M_{\rm UV},z} \left( \frac{\Phi_{\rm UV}(M_{\rm UV}, z) - \hat{\Phi}_{\rm UV,HST}(M_{\rm UV}, z)}{\sigma_{\Phi_{\rm UV,HST}}(M_{\rm UV}, z)} \right)^2, \tag{4.3}$$

where $\Phi_{\rm UV}(M_{\rm UV}, z)$ is the UVLF computed using Eq. (1.78) and $\hat{\Phi}_{\rm UV,HST}(M_{\rm UV}, z)$ and $\sigma_{\Phi_{\rm UV,HST}}(M_{\rm UV}, z)$ are the HST measurements of the value and uncertainty, respectively, of the UVLF at redshift $z$ and UV magnitude $M_{\rm UV}$. We vary all seven UVLF model parameters $[\alpha_\star, \beta_\star, \epsilon^s_\star, \epsilon^i_\star, M^s_c, M^i_c, \sigma_{M_{\rm UV}}]$ (defined in Eqs. (1.79) and (1.83) - (1.87)) as astrophysical nuisance parameters with uniform priors (see Table 4.2).

Following [173], we combine the HST UVLF likelihood with supernovae magnitudes from the Pantheon survey [using the Pantheon likelihood presented in 183]. However, we do not calibrate the supernovae magnitudes with Cepheid variable star data. This likelihood adds one additional nuisance parameter $M$, a calibration magnitude related to the intrinsic supernova luminosity, which we allow to vary as a free parameter with a uniform prior (see Table 4.2). We also impose a Gaussian prior on $\omega_b \times 10^2 = \Omega_b h^2 \times 10^2$ of $\mathcal{N}(2.233, 0.036)$ from Big Bang nucleosynthesis (BBN) measurements [159] and fix the values of the acoustic angular scale $100\theta_s = 1.040827$ and optical depth of reionization $\tau = 0.0544$ to be consistent with *Planck* values [9]. Including both the Pantheon supernovae data with the *Planck* value of $100\theta_s = 1.040827$ tightly constrains both the total matter density $\Omega_{\rm m}$ and the dimensionless Hubble parameter $h$. We also impose a uniform prior on both axion and CDM density. Some past analysis has assumed a loguniform prior on axion density in order to probe extremely low axion DM fractions. However, we opt for a uniform prior in order to compute conservative results and not bias our analysis towards low axion fractions. This is because loguniform priors give equal weight to each logarithmic range, and depending on where you set the lower limit, this can result in a preference towards lower fractions, which are already less constrained by the data. Future work could involve experimenting with loguniform priors on the axion fraction to test the dependence of these constraints on the prior form.

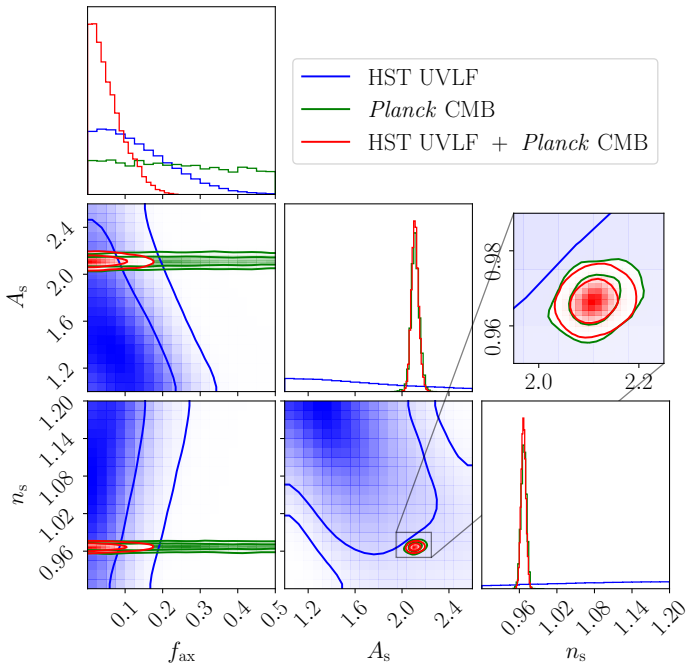


Figure 4.8: Marginalized posterior of axion fraction $f_{ax} = \Omega_{ax}/\Omega_{DM}$ for axion mass of $10^{-24}$ eV, the primordial scalar amplitude $A_s$ and spectral index $n_s$. The blue contours are from HST UVLF data shown in Fig. 1.5 (plus Pantheon supernovae data and a BBN prior on $\omega_b$, as explained in Table 4.1). The green contours are from *Planck* CMB plus BAO data from BOSS. The red contours are the joint constraints from both sets of observables. $A_s$ is given in units of $10^{-9}$.

### 4.5.2 *Planck* cosmic microwave background

We use *Planck* measurements of the CMB in order to anchor the values of cosmological parameters, in particular, $A_s$ and $n_s$ as these are measures of the large-scale matter power that the UVLF does not probe. We use the *Planck* 2018 foreground-marginalized likelihood, using the high-multipole $\ell$ TT, TE and EE angular power spectra, along with the low-$\ell$ TT and EE angular power spectra [8]. We also use CMB lensing $\phi\phi$ power spectra and measurements of the galaxy baryon acoustic oscillations (BAO) from the Baryon Oscillation Spectroscopic Survey (BOSS 2014) [16]. For constraints using *Planck* CMB data, we allow $100\theta_s$ and $\tau$ to vary as cosmological parameters and also vary the calibration parameter $A_{\rm Planck}$ [9]. We use uniform priors given in Table 4.2.

### 4.5.3 Results

In Fig. 4.8, we show the marginalized posterior of the axion fraction $f_{\rm ax} = \Omega_{\rm ax}/\Omega_{\rm DM}$, the primordial scalar amplitude $A_{\rm s}$ and spectral index $n_{\rm s}$, for an axion of mass $10^{-24}$ eV. We illustrate the degeneracy between axion and cosmological parameters at this fixed mass as the power of adding UVLF data is clear. The *Planck* likelihood (combined with BOSS BAO, as described in Tab. 4.1) limits the axion fraction

$$f_{\rm ax}[m_{\rm ax} = 10^{-24}{\rm eV}] < 0.93 \ (95\% \ {\rm c.l.}) \quad [\textit{Planck} \ {\rm CMB}]. \tag{4.4}$$

This limit is consistent with the *Planck* + BOSS galaxy clustering constraints presented in [171]. The HST UVLF likelihood already sets a stronger constraint, limiting the axion fraction

$$f_{\rm ax}[m_{\rm ax} = 10^{-24}{\rm eV}] < 0.28 \ (95\% \ {\rm c.l.}) \quad [{\rm HST \ UVLF}]. \tag{4.5}$$

The UVLF is a more powerful probe, since for $m_{\rm ax} \geq 10^{-25}\,{\rm eV}$, the axion wavelength is smaller than the smallest modes currently modeled in *Planck* (and other CMB experiments') data. Whereas, as illustrated in Fig. 1.1, the UVLF probes much smaller scales than current CMB data where axion effects manifest.

The lower-left panel of Fig. 4.8 shows that for the UVLF constraints, slightly higher values of $f_{\rm ax}$ are allowed with higher values of $n_{\rm s}$[1]. High values of $n_{\rm s}$ are strongly inconsistent with *Planck* CMB data, which constrain $n_{\rm s} = 0.9665 \pm 0.0038$ [8]. Therefore, if we combine the HST UVLF measurements of smaller-scale structure with the *Planck* CMB large-scale measurements of $A_{\rm s}$ and $n_{\rm s}$, we break the degeneracy between axion and cosmological parameters. We thus significantly improve our axion fraction limit

$$f_{\rm ax}[m_{\rm ax} = 10^{-24}{\rm eV}] < 0.15 \ (95\% \ {\rm c.l.}) \quad [{\rm HST \ UVLF} + \textit{Planck} \ {\rm CMB}]. \tag{4.6}$$

The constraints shown in Fig. 4.8 have a fixed axion mass $m_{\rm ax} = 10^{-24}$ eV. However, we also explore how joint HST UVLF and *Planck* CMB likelihoods constrain axions of different masses. In Fig. 4.9, we show constraints on axion fraction given both likelihoods while varying the axion mass $\log(m_{\rm ax}/{\rm eV})$ between $-21$ and $-26$, in addition to varying all cosmological and astrophysical

[1]Larger axion fractions can be consistent with the HST UVLF when combined with a higher $n_{\rm s}$, as $n_{\rm s}$ raises small-scale power while the axion fraction suppresses it. The impact of $\Omega_{\rm ax}$ and $n_{\rm s}$ can be compared in Fig. 4.7.

| Parameter | Prior | Posterior ($m_{\rm ax} = 10^{-24}$ eV) HST UVLF + *Planck* CMB |
|---|---|---|
| $\Omega_{\rm CDM}$ | $\mathcal{U}$[0.0, 0.3] | $0.247^{+0.015}_{-0.008}$ |
| $\Omega_{\rm ax}$ | $\mathcal{U}$[0.0, 0.3] | $< 0.036$ (95% c.l.) |
| $\omega_{\rm b} \times 10^2$ | $\mathcal{N}(2.233, 0.036)$ | $2.241^{+0.013}_{-0.013}$ |
| $A_{\rm s} \times 10^9$ | $\mathcal{U}$[0.5, 3.0] | $2.112^{+0.029}_{-0.033}$ |
| $n_{\rm s}$ | $\mathcal{U}$[0.7, 2.0] | $0.9666^{+0.0036}_{-0.0039}$ |
| $100 \times \theta_{\rm s}$ | $\mathcal{U}$[1.037, 1.043] | $1.0419^{+0.00028}_{-0.00029}$ |
| $\tau$ | $\mathcal{U}$[0.01, 0.2] | $0.0580^{+0.0069}_{-0.0080}$ |
| $\alpha_\star$ | $\mathcal{U}$[-3.0,0.0] | $-0.575^{+0.089}_{-0.114}$ |
| $\beta_\star$ | $\mathcal{U}$[0.0,3.0] | $0.9804^{+0.0024}_{-0.6897}$ |
| $\epsilon^s_\star$ | $\mathcal{U}$[-3.0,3.0] | $0.56^{+0.57}_{-0.33}$ |
| $\epsilon^i_\star$ | $\mathcal{U}$[-3.0,3.0] | $-0.49^{+0.14}_{-0.11}$ |
| $M^s_c$ | $\mathcal{U}$[-3.0, 3.0] | $1.66^{+1.28}_{-0.41}$ |
| $M^i_c$ | $\mathcal{U}$[7.0,15.0] | $11.87^{+0.21}_{-0.15}$ |
| $\sigma_{M_{\rm UV}}$ | $\mathcal{U}$[0.001, 3.0] | $0.45^{+0.18}_{-0.19}$ |
| $M$ | $\mathcal{U}[-\infty, \infty]$ | $-19.417^{+0.012}_{-0.012}$ |
| $A_{\rm Planck}$ | $\mathcal{U}$[0.9,1.1] | $1.0018^{+0.0025}_{-0.0025}$ |

Table 4.2: The priors and posteriors of all cosmological and astrophysical parameters in our joint HST UVLF and *Planck* CMB constraints on mixed axion models with $m_{\rm ax} = 10^{-24}$ eV. $\mathcal{U}$ represents uniform priors over the specified range, while $\mathcal{N}$ represents a Gaussian prior with the stated mean and standard deviation. In the right-most column, we give the posterior mean with the 68% c.l. uncertainties, except where the 95% c.l. upper limit is given.

parameters as above.[2] The 68% and 95% upper limits on $f_{\rm ax}$ for different axion masses (with a bin width in $\log(m_{\rm ax}/{\rm eV})$ of $\pm 0.5$) are shown in Table 4.3. Axions for $\log(m_{\rm ax}/{\rm eV}) \leq -23$ are limited $\leq 22\%$ of the DM. Axions for $\log(m_{\rm ax}/{\rm eV}) \leq -21.6$ are ruled out as each contributing 100% of the dark matter at 95% credibility, thus confirming previous results that exclude axion models as a solution to the so-called cold dark matter "small-scale crisis" [169, 148]. The UVLF loses sensitivity as the axion mass increases, as the axion wavelength falls below the smallest scales probed. We show degeneracies with astrophysical parameters in Appendix 4.8.1.

## 4.6 Discussion

### 4.6.1 Halo mass function model

In this work, we use the Sheth-Tormen model of ellipsoidal collapse [186] to compute the HMF, using parameters fit to pure-CDM simulations, as described in Sec. 4.3. This model has been used in the past (such as by [203]) to model the formation of halos in mixed-axion cosmologies, and compared to simulations in pure axion cosmologies in [62]. We show in Appendix 4.8.3 that alternative forms for the mass function (such as those proposed in [164]) are impacted by the linear axion power spectrum

[2]Following the examples in [169, 62, 170], we set the upper bound on $\log(m_{\rm ax})$ in a data-informed way, i.e., that the upper bound is set by the sensitivity of the data. In this way, the limits are not affected by the infinite prior volume as $m_{\rm ax} \to \infty$.

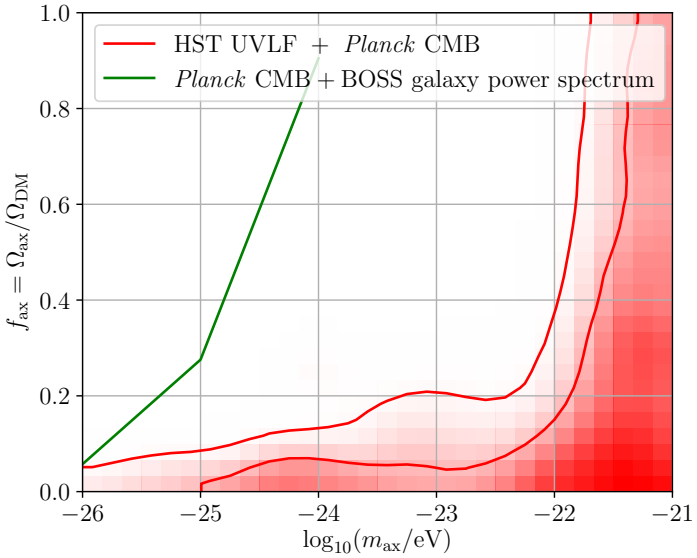


Figure 4.9: Marginalized posterior on axion mass and DM fraction from joint HST UVLF and *Planck* CMB likelihoods. The red contours indicate the allowed 68% and 95% limits, in contrast to the UVLF results in Fig. 4.1. We also show (in green) the 95% upper limit from *Planck* CMB combined with BOSS galaxy power spectrum, as reported in [171]. Combining *Planck* CMB with HST UVLF substantially tightens constraints on the axion fraction.

| | Upper limits on $f_{\rm ax}$ | |
|---|---|---|
| $\log(m_{\rm ax}/{\rm eV})$ | 68% c.l. | 95% c.l. |
| -21.0 | 0.620 | 0.930 |
| -22.0 | 0.321 | 0.790 |
| -23.0 | 0.110 | 0.224 |
| -24.0 | 0.071 | 0.151 |
| -25.0 | 0.052 | 0.079 |
| -26.0 | 0.021 | 0.043 |

Table 4.3: 68% and 95% c.l. upper limits on the axion DM fraction $f_{\rm ax} = \Omega_{\rm ax}/(\Omega_{\rm ax} + \Omega_{\rm CDM})$ for different masses $m_{\rm ax}$. These constraints are computed using joint HST UVLF + *Planck* CMB data. The mass-varying posterior chain is divided into bins with width in $\log(m_{\rm ax}/{\rm eV})$ of $\pm 0.5$. Although the limits at $m_{\rm ax} = 10^{-21}$ eV are less than unity, this is expected for a nearly uniform distribution, i.e., we do not contradict Fig. 4.9 that shows that this mass is unconstrained by our data.

in almost identical ways. We find that the impact of axion halo pressure on the HMF is limited to either low halo masses beyond the sensitivity of the UVLF or there is a negligible suppression relative to the impact of the linear matter power spectrum (see Fig. 4.3). Since the impact of axions on the HMF from the primordial linear matter power spectrum is found to be largely independent of the choice of halo formation model and the effects of axion halo pressure are negligible for the axion mass and fraction ranges that we consider, we conclude that our estimates of the HMF are sufficiently accurate compared to the data uncertainties.

Future inferences of the HMF, including using JWST UVLF to probe higher redshifts and smaller scales, will become more sensitive to the small-scale effects of axion halo pressure, necessitating more robust modeling of the impact of axion physics on halo formation, e.g., the role of axion quantum pressure in the collapse of overdensities. This would require comprehensive Schrodinger-Poisson simulations in order to capture the combination of axion, baryonic and CDM physics involved in halo formation in mixed-axion cosmologies, such as those conducted by [182, 98, 141, 118]. A consequence of our findings, that the impacts of small-scale axion physics on halo formation are negligible given current data, is that our methods can be used to test other DM models with a suppressed linear power spectrum (such as warm [e.g., 201, 172, 133, 126] or interacting [e.g., 168] DM).

### 4.6.2 UV luminosity model

Our results depend on the mean UV luminosity of halos as described in Sec. 4.4. The flexible parametric model that we use is shown in [174] to capture the results of hydrodynamical simulations such as Illustris TNG [202] and to fit Hubble UVLF data well under the ΛCDM model. In Appendix 4.8.2, we also test an alternative model of UV magnitude, informed by empirical measurements of low-$z$ galaxies, and we find that our chosen model gives constraints that are either consistent or conservative in comparison. We then relate the HMF and UVLF using a Gaussian scatter of UV magnitudes around this mean relation, in order to account for stochasticity from galaxy composition and bursty star formation [e.g., 194, 88]. Importantly, when searching for the signature of axions, we marginalize over uncertainty in the stellar mass to halo mass relation in both its scale and time dependence, covering the uncertainties seen in simulations. Remarkably, despite this marginalization, we still attain powerful sensitivity to axions as the effect of axions is shown to be often qualitatively distinct.

We consider the impact of axion astrophysics on the UV luminosity of low-mass halos, where halos below the halo Jeans critical mass will lack an axion DM component and thus have a higher baryon-to-DM ratio, enhancing UV luminosity. However, we show in Fig. 4.6 that the impacts of axion astrophysics on the UVLF are negligible compared to the axion cosmology through the linear MPS (in particular, when accounting for the cancelling effect from when axion halo pressure suppresses the formation of low-mass halos). We therefore neglect these axion impacts on mean UV luminosity.

Comparison to simulations with even more realistic models of star formation and radiative transfer at high redshifts can further improve this model of UV luminosity [such as those done by 140, 202, 110, 133, 194, 185]. This improved modeling can also be informed by future multi-wavelength studies of high-$z$ galaxies using HST, JWST and the Roman Space Telescope [146], characterizing the star formation process at these times [as discussed in, e.g., 147, 79, 175, 88]. However, both

observations and simulations currently have high uncertainties at redshifts $z > 10$ beyond what we probe with HST data.

### 4.6.3 Preliminary results from James Webb Space Telescope luminosities

There is much debate in the community regarding the unexpected detection of numerous massive high-redshift ($z > 10$) galaxies observed by JWST [213]. Early results claimed to be inconsistent with HST predictions, suggesting that our current models of early star and galaxy formation may be incomplete [see e.g. 32, 49]. If robust, these observations have the potential to place tighter constraints on axion DM physics or to force us to reevaluate our models of halo formation and UV luminosity at higher redshifts.

In order to test whether these preliminary JWST results are in tension with our model, we consider a spectroscopically-confirmed sample of 25 JWST UV sources presented in Table 1 of [87]. We restrict ourselves to only spectroscopically-confirmed sources as photometric samples are known to be contaminated by low-$z$ interlopers. It is only with mid- and far-infrared spectroscopy that redshifts can be definitively determined. Indeed, many of the initial high-$z$ sources that were claimed to be in tension with ΛCDM cosmology were later found to be interlopers and determining the true redshift is still an active area of research [215, 79, 88]. The sources to which we restrict our analysis have spectroscopic redshifts from $8.61 < z < 13.20$, allowing [87] to compute the UVLF at $z = 9$ and $z = 10$. They also compute lower bounds at $z = 12$, and upper bounds at $z = 16$ (from non-detection in their field). Fig. 4.10 shows the current JWST estimates of the UVLF, along with estimates of the UVLF from our model fit to HST. The JWST data are consistent with both the HST data at comparable redshifts and the best-fit UVLF model. We show in the bottom panel that the effect of axions increases with redshift.

As with the HST UVLF (Sec. 4.5.1), we combine the JWST UVLF with the Pantheon supernovae likelihood, along with BBN priors on $\omega_{\rm b}$ and a fixed value of $100\theta_{\rm s} = 1.040827$. We show marginalized posteriors given JWST data in Fig. 4.11. The pale pink contours show constraints on $m_{\rm ax} = 10^{-24}$ eV axions from JWST data alone, while blue contours are from HST UVLF alone. Despite only 25 sources, compared to HST's 24,000 sources, JWST already puts a comparable limit on the axion fraction:

$$f_{\rm ax}[m_{\rm ax} = 10^{-24}{\rm eV}] < 0.52 \ (95\% \ {\rm c.l.}) \quad [{\rm JWST \ UVLF}]. \tag{4.7}$$

This limit is tighter than the *Planck* CMB limit of 0.93 (see Eq. (4.4)), but looser than the HST UVLF limit of 0.28 (see Eq. (4.5)). The magenta contours in Fig. 4.11 indicate joint constraints from HST and JWST UVLF showing that JWST data does not meaningfully improve axion constraints set by HST at this time. Our model (a flexible double power law given in Eq. (1.83) with a redshift-dependent amplitude $\epsilon_\star$ and pivot mass $M_c$) is consistent with both HST and spectroscopic JWST results. These JWST observations do not present any discrepancy with ΛCDM.

Any tests of discrepancy at $z > 10$ will require additional spectroscopic data. The effect of axions (dashed lines in Fig. 4.10) is to suppress the UVLF at all redshifts (from 40% at $z = 8$ to 90% at $z = 16$). If future JWST measurements prove an excess of sources over a larger and more accurately determined volume factor, this will further constrain the axion fraction, particularly since the relative impact of axions is greater at higher redshifts (see the lower panel of Fig. 4.10). Detections of axion suppression will require a large volume factor in order to measure a deficiency

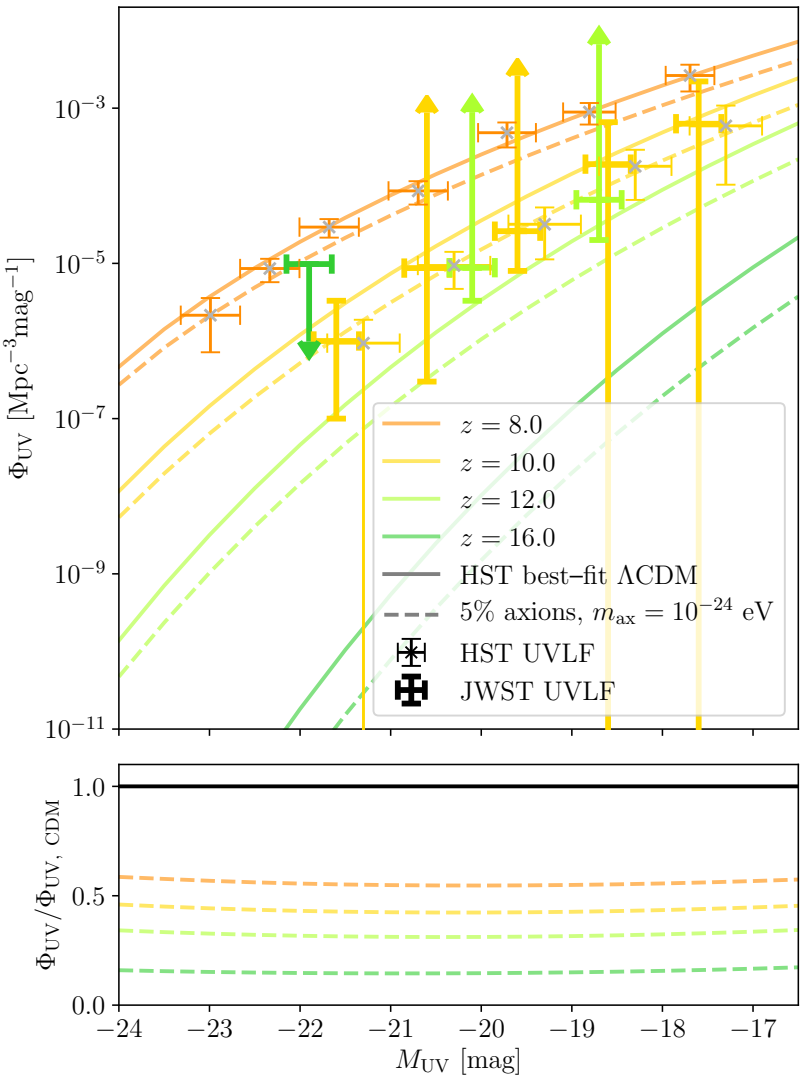


Figure 4.10: JWST estimates of the UVLF at redshifts $z = 10, 12, 16$ in thick error bars from [87]. Down arrows represent upper limits, while up arrows represent lower limits with uncertainties. We also show (in thin error bars) HST estimates of the UVLF at redshifts $z = 8, 10$. The solid curves show the best-fit ΛCDM cosmology given HST data, while the dashed lines are with 5% axion DM and $m_{\rm ax} = 10^{-24}$ eV. The bottom panel shows the ratio of the UVLF in the presence of axions relative to the ΛCDM case. The impacts of axions on the UVLF are proportionally higher at higher redshift, but current spectroscopically-confirmed JWST samples do not have the required sensitivity to distinguish this effect after marginalization over astrophysical uncertainties.

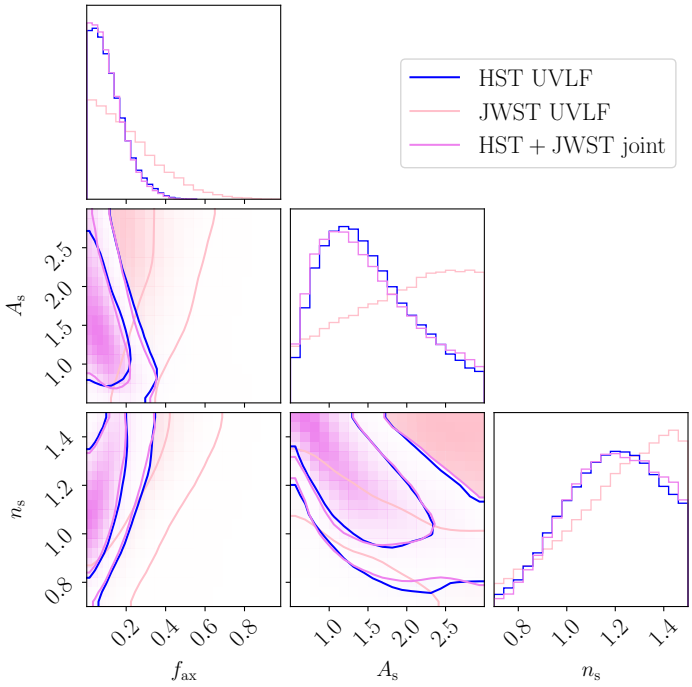


Figure 4.11: As Fig. 4.8, where blue contours show constraints from HST UVLF [30], while pink contours are from a sample of 25 spectroscopically-confirmed galaxies from JWST [87]. The magenta contours represent joint constraints from both HST and JWST. $A_s$ is given in units of $10^{-9}$. While JWST alone sets a limit on the axion fraction, the joint constraints are not meaningfully different than the HST-only case.

of high-$z$ UV sources, while limiting the axion fraction could be achieved with a smaller volume factor. We leave a thorough computation of JWST UVLF forecasts on axions for future study. This approach is also complementary to ongoing efforts to use 21-cm measurements to detect axions at similar scales and redshifts [5, 95, 75].

Observations of abundant structure at high redshifts could imply the presence of extreme axions (i.e. axions with a high starting field angle, resulting in the growth of field perturbations and an overabundance of structure on certain scales), as described in [121] and [17]. Although we do not consider the impacts of extreme axions in this paper, such a comparison could be performed using efficient extreme-axion computations, such as those developed by [208] for the linear MPS.

### 4.6.4 Small-scale structure

Our work also presents evidence for a new observable consequence of mixed-axion DM models: an overabundance of low-mass halos at late times (as shown in Fig. 4.4). Our modeling calculates that this effect is maximized for axion fractions between $5 - 10\%$. This effect is due to the axion component suppressing primordial linear structure on small scales, delaying the hierarchical growth of halos and resulting in an overabundance of low-mass halos that have not yet merged into higher mass ones at late times. The halo masses ($M_h \lesssim 10^9 M_\odot$) and redshifts ($z \lesssim 3$) relevant for this effect are both too low to be measured using the UVLF in this paper. But there is an opportunity to search for these effects in late-time small-scale galaxy structure (e.g., using stellar streams [20], satellite galaxies [148] or strong gravitational lensing [187]). A more detailed treatment of axion astrophysics would be necessary as the effects of axion wave physics would have a significant impact on hierarchical merger histories on small scales. A more thorough computation is left for future study.

## 4.7 Conclusions

The galaxy UV luminosity function is a powerful probe of structure on small scales ($0.5\,\mathrm{Mpc}^{-1} < k < 10\,\mathrm{Mpc}^{-1}$) and high redshifts ($4 \leq z \leq 16$). We demonstrate, for the first time, by using a flexible parametric model relating UV luminosity and halo mass, the use of the UVLF to set world-leading limits on fundamental physics. Our main conclusions are:

1. **The UVLF depends primarily on the mixed-axion linear matter power spectrum** and is largely independent of small-scale axion astrophysics (see Sections 4.3 and 4.4 and Appendices 4.8.2 and 4.8.3).

2. **We set new cosmological constraints on mixed-axion cosmologies** by computing the impacts of axions on the HMF and the UVLF, while robustly marginalizing over uncertainty in the relation between UV luminosity and halo mass. Joint HST UVLF (for $4 \leq z \leq 10$) and *Planck* CMB likelihoods rule out axions with $\log(m_{\rm ax}/\mathrm{eV}) < -21.6$ each as 100% of the DM and limit axions with $\log(m_{\rm ax}/\mathrm{eV}) < -23$ to constitute $\leq 22\%$ of the DM (both limits at 95% credibility; detailed constraints given in Table 4.3). Our results are the first joint constraints combining *Planck* CMB with small-scale measurements, constraining axion DM on a wide range of cosmological scales and bridging the mass gap in axion constraints shown in Fig. 4.1.

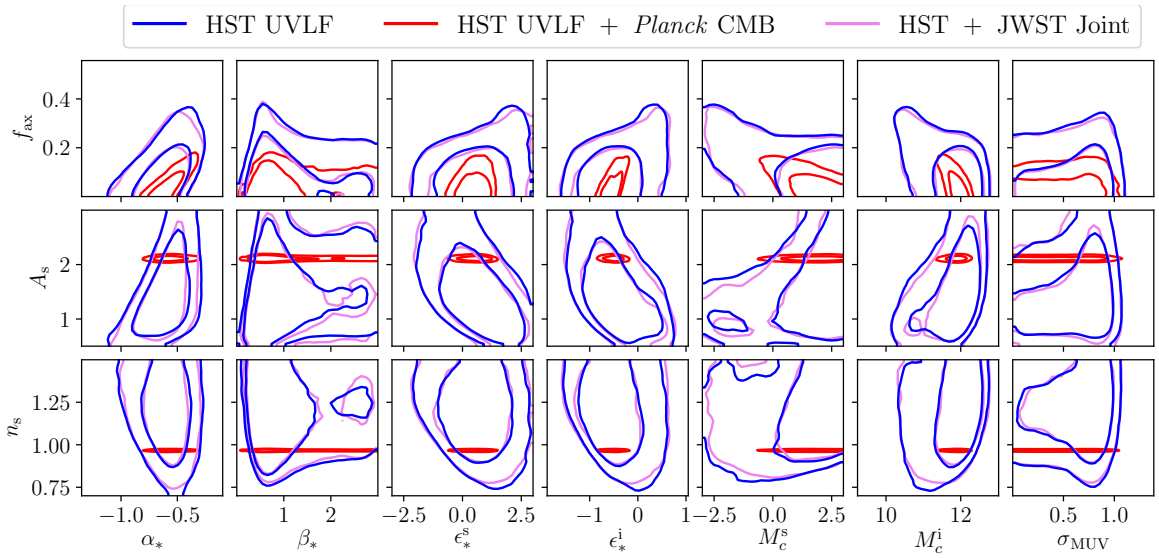


Figure 4.12: Marginalized posterior on cosmological parameters (along the vertical axis: $f_{\rm ax} = \Omega_{\rm ax}/\Omega_{\rm DM}$ for axions with a mass of $10^{-24}$ eV, $A_{\rm s}$ and $n_{\rm s}$) and astrophysical parameters (along the horizontal axis, as defined in Eq. (1.83)). The blue contours are from the HST UVLF, while the red contours are from the HST UVLF plus *Planck* CMB. Imposing the *Planck* likelihood in addition to HST UVLF breaks degeneracies with $A_{\rm s}$ and $n_{\rm s}$ and therefore tightens constraints on the astrophysical parameters of the UVLF model. We also show in magenta the joint HST and JWST UVLF posterior, which is nearly identical to the HST-only case. Inner and outer contours respectively show the 68% and 95% credible regions of the marginalized posterior. $A_{\rm s}$ is given in units of $10^{-9}$. Table 4.1 describes the full datasets that we use.

3. **Current JWST spectroscopic measurements of the UVLF are consistent with ΛCDM** when computed using a flexible parametric model of UV luminosity with redshift-dependent amplitude and pivot mass. As shown in Fig. 4.11, combining HST estimates of the UVLF with spectroscopic JWST data from [87] does not meaningfully improve our constraints over HST alone. However, we do find in Fig. 4.4 that the impact of axions on the HMF and UVLF is more pronounced at higher redshifts, implying that future high-$z$ estimates of the UVLF from JWST have the potential to improve our constraints significantly. More detailed multi-wavelength measurements of high-$z$ galaxies with JWST will also help to refine our picture of star formation at early times, informing our assumptions about how UV luminosity relates to halo mass at high redshifts ($z > 10$). As we enter a new era of high-redshift galaxy science with JWST, the UVLF will continue to improve as a powerful probe of the nature of dark matter.

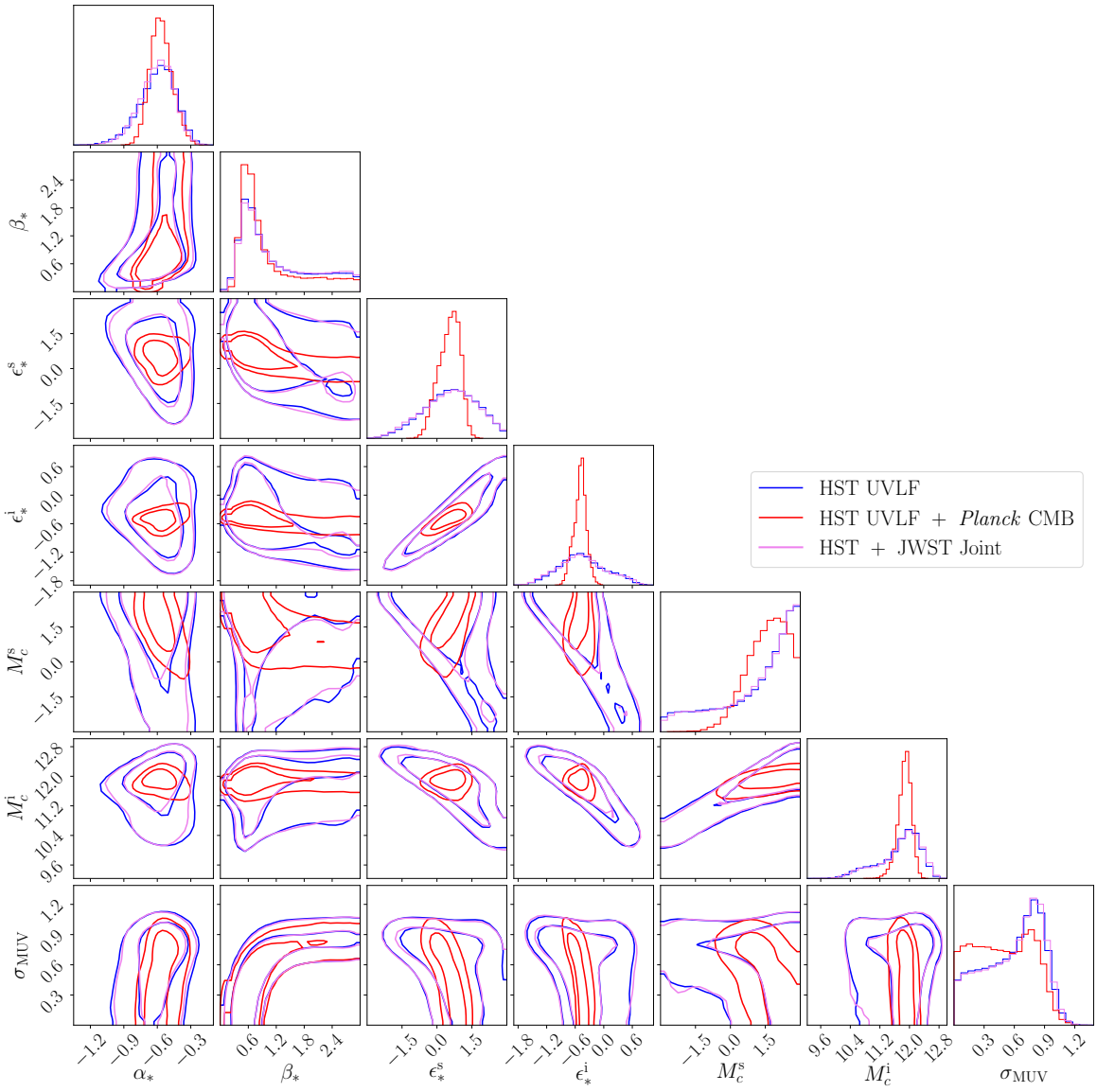


Figure 4.13: Marginalized posterior on astrophysical parameters (as defined in Eq. (1.83)), with the same data combinations as in Fig. 4.12. Inner and outer contours respectively show the 68% and 95% credible regions of the marginalized posterior. Table 4.1 describes the full datasets that we use.

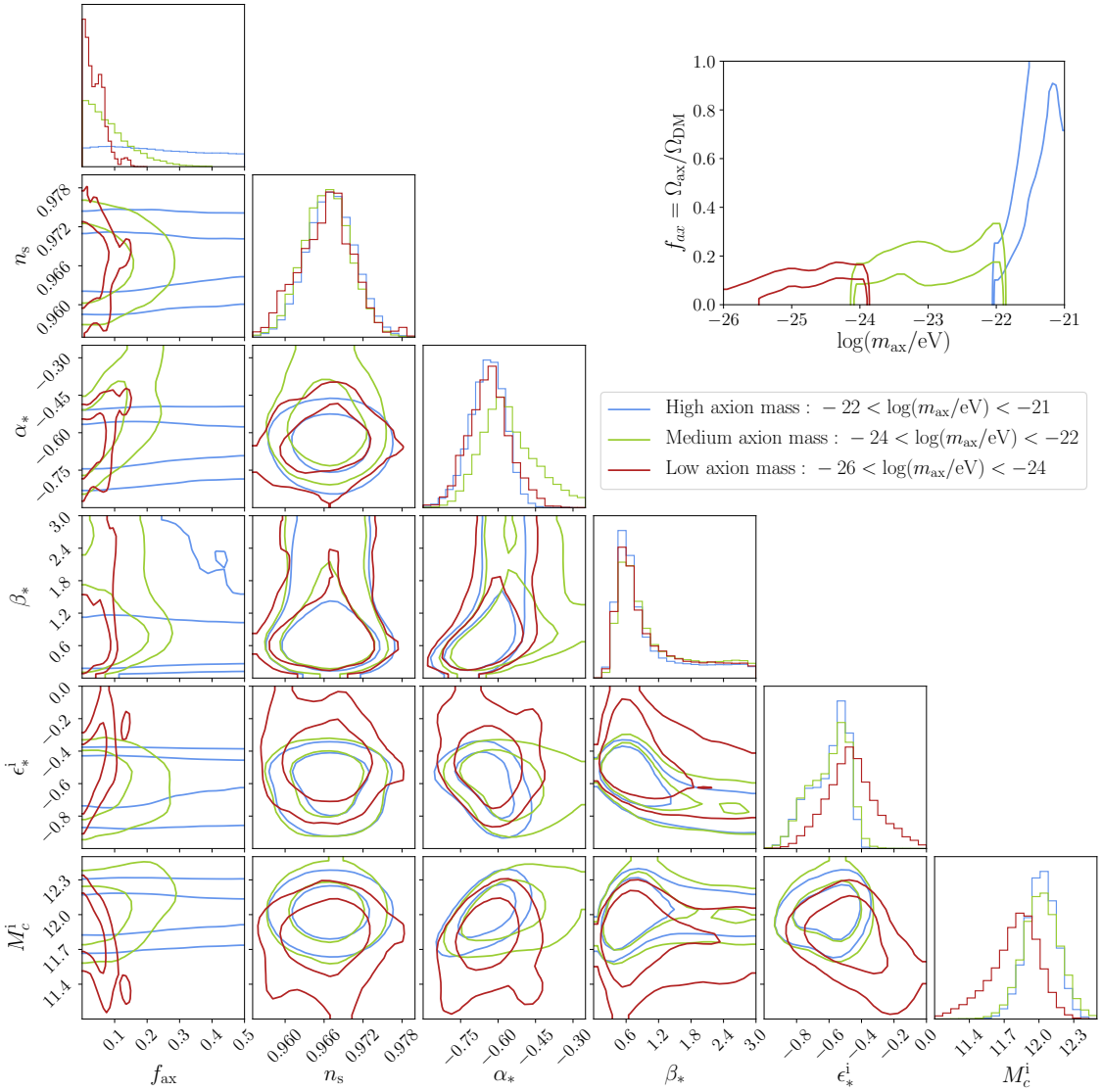


Figure 4.14: Constraints on the axion fraction and some cosmological and astrophysical parameters from joint HST UVLF and *Planck* CMB likelihoods, divided into three axion mass bins as shown in the upper-right subplot. Constraints on high mass axions ($-22 < \log(m_{ax}/eV) < -21$) are shown in blue, medium mass axions ($-24 < \log(m_{ax}/eV) < -22$) are shown in green, and low mass axions ($-26 < \log(m_{ax}/eV) < -24$) are shown in red. Inner and outer contours respectively show the 68% and 95% credible regions of the marginalized posterior.

## 4.8 Appendix

### 4.8.1 Constraints on astrophysical parameters

Figure 4.12 shows constraints on axion fraction, cosmological and UVLF parameters from Table 4.2 for an axion mass of $10^{-24}$ eV. The blue contours are given HST UVLF alone, while red contours are given joint HST UVLF and *Planck* CMB likelihoods. We also show in magenta the constraints given joint HST + JWST UVLF estimates, which are identical to the HST-only results. Fig. 4.13 shows the correlations between all UVLF model parameters, for HST UVLF only, HST UVLF + *Planck* CMB and HST + JWST UVLF. The addition of *Planck* data tightens the constraint on some UVLF parameters by breaking degeneracy with cosmological parameters.

In Fig. 4.14, we show the joint HST UVLF and *Planck* CMB constraints on axions for axion masses in three different ranges. The degeneracy direction of axion fraction and certain astrophysical parameters changes with axion mass bin. Medium mass axions ($-24 < \log(m_{\rm ax}/{\rm eV}) < -22$, in green) have a positive degeneracy with $\alpha_\star$, since their impact on the UVLF primarily occurs at faint luminosities. Low-mass axions ($-26 < \log(m_{\rm ax}/{\rm eV}) < -24$, in red) have a positive degeneracy with $\epsilon^i_\star$, since they suppress the UVLF on a wider range of scales (see Fig. 4.6). It would be powerful to identify complementary datasets that break these degeneracies, bearing in mind that these degeneracies vary with axion mass.

### 4.8.2 An alternative model of the UV luminosity function

In Section 4.4, we discuss our method for relating halo mass to UV luminosity, which follows Method II in [173]. Here, we discuss their Model III and use it to compute constraints on mixed axion cosmologies, demonstrating consistency with Model II. In this alternative model, we relate $M_h$ and $\overline{M_\star}$ using the same double power law as in Eq. (1.83) and the same parameterization of $\alpha_\star, \beta_\star, \epsilon^s_\star, \epsilon^i_\star, M^s_c, M^i_c$. However, we then use an empirically-determined relation between $M_\star$ and $M_{\rm UV}$, which is derived from near-infrared observations of galaxies, presented in [191, 192]. The stellar mass is calculated from stellar synthesis population models compared to the multi-band observations of HST galaxies and this is then compared to the rest-frame UV luminosity. This relation is calculated for galaxies from $z = 4$ to $z = 10$ and is estimated to be accurate to within a factor of two [173].

In Fig. 4.15, we show constraints on cosmological parameters using both the primary (Model II in [174]) and alternative (Model III in [174]) methods of computing the UVLF. We show in green the *Planck* ΛCDM best-fit parameter values for comparison. Both methods give largely consistent constraints on cosmological parameters. However, the alternative method gives slightly tighter constraints on the axion fraction, while also preferring higher values of $n_{\rm s}$ that are mildly inconsistent with *Planck* ΛCDM values. Therefore, we use the primary model of UV luminosity for our fiducial study, due to its greater consistency with *Planck* and more conservative limit on the axion fraction.

### 4.8.3 An alternative model of the halo mass function

In Section 4.3, we use the Sheth-Tormen mass function [186] when computing the HMF, as done in [174]. However, alternative mass functions have been proposed to describe halo formation. Here,

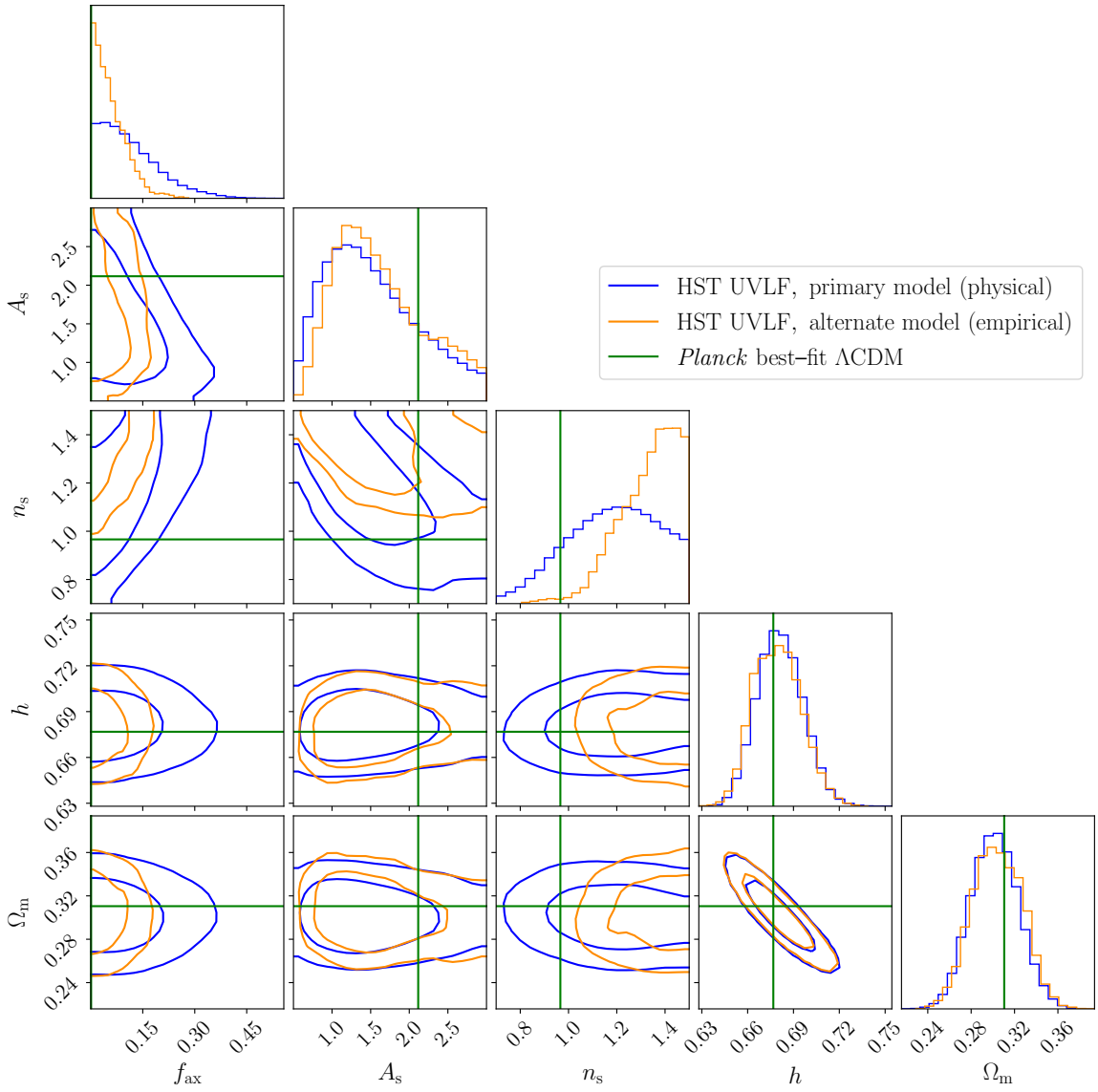


Figure 4.15: Marginalized posterior on cosmological parameters and axion fraction for $m_{\rm ax} = 10^{-24}$ eV using the HST UVLF with two different models of the UVLF. The primary model (in blue) corresponds to Model II in [173], which relates stellar mass and UV luminosity through a physically-motivated argument, while the alternative model (in orange) corresponds to Model III in [173], which relates stellar mass and UV luminosity through empirical estimates at $4 < z < 10$ using HST infrared observations [192]. The green lines show the best-fit ΛCDM cosmological parameters given *Planck* CMB.

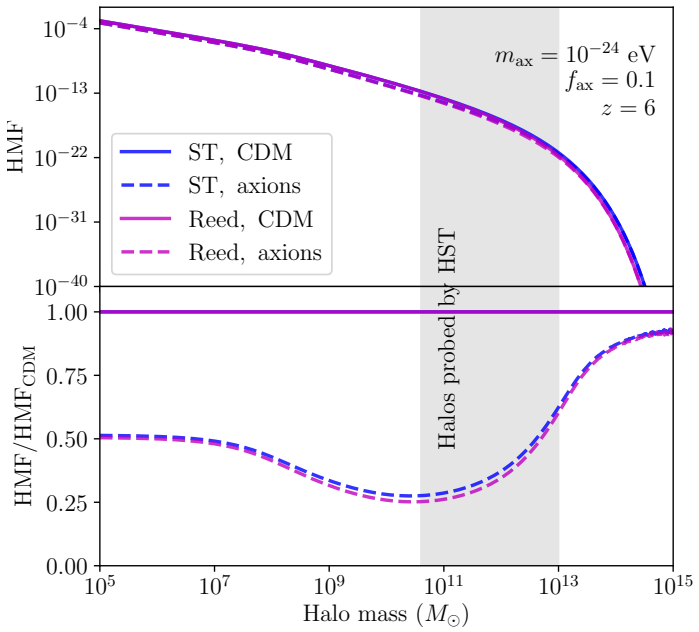


Figure 4.16: The HMF computed using both the Sheth-Tormen (ST, in blue) and Reed (in magenta) multiplicity functions. The solid lines are for a fiducial CDM cosmology, while the dashed lines show axions with $m_{\rm ax} = 10^{-24}$ eV as 10% of the DM. The HMF given each multiplicity function is impacted by axions in almost identical ways, meaning that our final axion constraints are independent of the choice between the two.

we consider the alternative Reed mass function [164] and compare the effects of axions on the HMF using both methods. In the Reed model, Eq. (1.65) is replaced by:

$$f_{\rm Rd}(\sigma_{M_{\rm h}}) = A_{\rm Rd}\sqrt{\frac{2a_{\rm Rd}}{\pi}}\left[1+\left(\frac{\sigma^2_{M_{\rm h}}}{a_{\rm Rd}\delta^2_{\rm Rd}}\right)^{p_{\rm Rd}} + 0.2\exp\left(-\frac{(\ln\sigma^{-1}_{M_{\rm h}} - 0.4)^2}{2(0.6)^2}\right)\right]\frac{\delta_{\rm Rd}}{\sigma_{M_{\rm h}}}\exp\left(-\frac{c_{\rm Rd}a_{\rm Rd}\delta^2_{\rm Rd}}{2\sigma^2_{M_{\rm h}}}\right), \tag{4.8}$$

where $A_{\rm Rd} = 0.3235$, $a_{\rm Rd} = 0.707$, $p_{\rm Rd} = 0.3$, $c_{\rm Rd} = 1.081$ and $\delta_{\rm Rd} = 1.686$ [164, 174].

[174] compares astrophysical and cosmological impacts on the UVLF given the two mass functions. They find that, while the high-$z$ estimates of the UVLF are slightly changed by the Reed mass function, the resulting constraints on cosmology are largely unchanged, likely due to slight shifts in the astrophysical nuisance parameters that account for the changes in the mass function. In Fig. 4.16, we show the HMF given each multiplicity function, for both a CDM cosmology and one with 10% axions and $m_{\rm ax} = 10^{-24}$ eV. In the lower panel, we show that axions impact the HMF given each mass function in an almost identical way. Therefore, since other cosmological parameters are not significantly shifted by the choice of mass function, we conclude that the constraints on axion parameters are also unaffected.

## 4.9 Comparison to the observed galaxy main sequence

Our model connecting halo mass and galaxy UV luminosity (described in Sec. 4.4.1) involves a number of intermediate connections: from halo mass to mean stellar mass in Eq. (1.83), to mean star formation rate in Eq. (1.82), to mean UV luminosity in Eq. (**??**). These connections are varied by nuisance parameters over which we marginalize (Table 4.2). Here, we confirm that our model reproduces observed connections between these intermediate variables, without having seen these additional data.

E.g., the galaxy main sequence is the relation between galaxy stellar mass and star formation rate (SFR). [160] fits a parametric relation to a compendium of galaxy main sequence data for $0 < z < 6$. Fig. 4.17 compares this fit to the prior and posterior on the galaxy main sequence given our UVLF model and HST data. In Eq. 1.82, we assume a linear relation between stellar mass and SFR parameterized by a dynamical time $t_\star$ over which we marginalize, with a redshift dependence given by the Hubble parameter $H(z)$. Since $t_\star$ is degenerate with the amplitude of the stellar mass to halo mass relation $\epsilon_\star$ (Eq. (1.83)), we combine these two variables into one, parameterize the combination with a redshift-dependant power-law relation in Eq. (1.87) and then marginalize over the slope $\epsilon_\star^{\rm s}$ and intercept $\epsilon_\star^{\rm i}$ of this relation. We give the prior and posterior on the slope and intercept in Table 4.2.

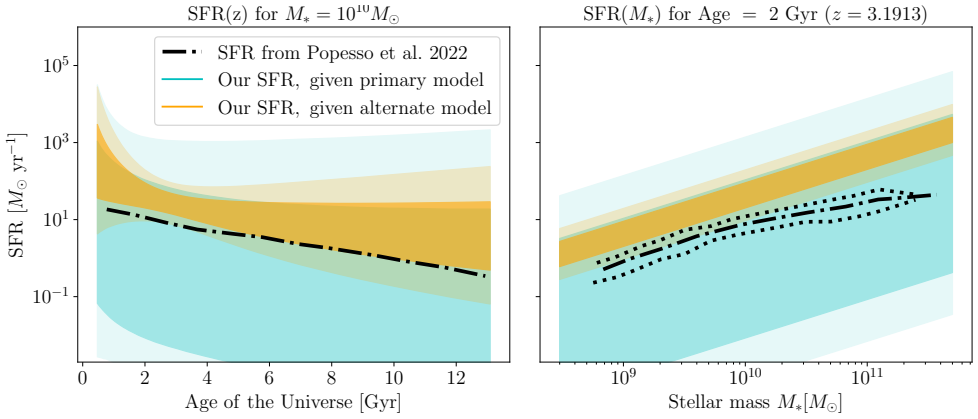


Figure 4.17: The mean galaxy star formation rate (SFR) $\overline{\dot{M}_\star}$ as a function of time (left column) and galaxy stellar mass $M_\star$ (right column). The left panel fixes $M_\star = 10^{10} M_\odot$, while the right panel fixes age of the Universe = 2 Gyr (i.e., $z = 3.1913$ for a *Planck* best-fit cosmology). The black dot-dashed line is the measurement from [160] (their Fig. 1 for the left panel and their Fig. 2 for the right; both a parametric fit to a compendium of data). The dotted black lines on the right panel indicate the $3\sigma$ error bars on the mean SFR from the [160] analysis (note that this is not an estimate of the *scatter* in the SFR). As described in Appendix 4.9, the colored bands indicate our prior and posterior distributions on the galaxy main sequence given our UVLF model and the HST data, i.e., independent of the direct measurements from [160]. The cyan bands show posteriors on the star formation rate from our primary model assuming a uniform distribution on $\epsilon_\star^{\rm s}$ and $\epsilon_\star^{\rm i}$; the orange bands show our posterior on $\epsilon_\star^{\rm s}$ and $\epsilon_\star^{\rm i}$ given the alternative UVLF model presented in Appendix 4.8.2. The darker and lighter shaded regions respectively indicate the 68% and 95% credible regions.

In order to examine the relationship our model is assuming between stellar mass and SFR, we need some way of disentangling $t_\star$ and $\epsilon_\star$, in order to estimate the value of $t_\star$ (and thus, the galaxy main sequence relation) being assumed in our model. We do this in two ways. The first, more

conservative, approach is to divide out the full range of possible $\epsilon_\star$ values by marginalizing over the full uniform prior range of both the slope and intercept, resulting in the full possible range of $t_\star$ values our model could accommodate within the posterior range on the joint parameter. We do this through random draws from the posterior on the slope and intercept of the combined $\epsilon_\star/t_\star$ parameter, divided by random draws from the uniform prior on the slope and intercept of $\epsilon_\star$ to get the full range of possible values for $t_\star$. Another approach is to utilize the alternative model described in Appendix 4.8.2, where the stellar mass is directly related to the UV luminosity through an empirical relation. This method allows us to draw values for the slope and intercept of $\epsilon_\star$ from the posteriors of this alternative model, which we can then use to isolate $t_\star$ and compute estimates of the star formation rate.

The cyan bands in Fig. 4.17 are the $1-$ and $2-\sigma$ limits on the range of models assuming the primary model and a full uniform prior on $\epsilon_\star$ to isolate $t_\star$, while the orange bands are the $1-$ and $2-\sigma$ limits using the posterior range on $\epsilon_\star$ from the alternate model.[3] The black dotted-dashed lines are the best-fit observational galaxy main sequence as estimated by [160], that is a synthesis of results from a number of previous studies, with the error on these estimates shown by the dotted black lines. This comparison is for illustrative purposes only; we do not explicitly calculate stellar mass or star formation rate in our model, and use this relation merely to motivate the functional form of the UVLF over which we then marginalize. However, we can see that our model is flexible enough to accommodate the observed galaxy main sequence within our posterior range and roughly matches the functional dependence of SFR on both redshift (or age of the universe) and stellar mass.

It is worth noting that the estimates of the star formation rate from [160] show a slight decrease in the mass dependence at higher stellar masses which is not captured by our model, as shown in Fig. 4.17. However, we can safely ignore this stellar mass dependence of the star formation rate for two reasons. Firstly, this mass dependence is more pronounced at lower redshifts, as seen in Figures 4 and 5 of [160], while at the redshifts we consider ($z \geq 4$) the effect is minimal. Secondly, even this minimal suppression in the star formation rate at high stellar masses would manifest in the UVLF as a slight reduction in the number density at brighter luminosities, which can already be accounted for by the double power law form of the stellar mass relation we assume. Since the only observable we use in our analysis is the UVLF, any mass-dependence in the star formation rate (or in the UV luminosity scatter, for that matter) would be entirely degenerate with the halo-mass-dependence of the stellar mass we already assume.

[3] We can hypothesize as to why the red bands appear to slightly overestimate the star formation rate relative to the [160] results. Since the red bands are derived from comparing the primary and alternate models of UV luminosity discussed in Appendix 4.8.2, this could be a result of the alternate model preferring lower values of $\epsilon_\star$ relative to the primary model. This is consistent with the alternate model preferring higher values for $n_{\rm s}$ relative to the primary model (and also relative to *Planck* best-fit cosmology), as seen in Fig. 4.15. Higher values of $n_{\rm s}$ and lower values of $\epsilon_\star$ could still give a similar UVLF on small scales, but it would give the impression of a higher inferred star formation rate when compared to the primary model.

# Chapter 5

# Conclusion

Dark matter (DM) is one of the most mysterious substances in the known universe. It has played an essential role in the evolution of the universe, the formation of cosmic structure, and the dynamics of galaxies. Despite this importance, we know almost nothing about its particle characteristics, cosmological origins, or small-scale structure and distribution. This thesis has involved the creation of multiple novel tools that shed light on the nature of DM, allowing us to draw connections between theoretical DM models and concrete astrophysical observables. These tools open up many new scientific opportunities for productive follow-up work, allowing us to probe the fundamental nature of DM in novel ways on a wide range of scales.

In Chapter 2 (Harrison Winch et al. "Using LSST Microlensing to Constrain Dark Compact Objects in Spherical and Disk Configurations". In: *The Astrophysical Journal* 933.2 (July 2022), p. 177. DOI: 10.3847/1538-4357/ac7467. URL: https://dx.doi.org/10.3847/1538-4357/ac7467), we computed sophisticated forecasts for how well LSST would be able to search for DCOs using microlensing. We concluded that LSST with the Rubin Observatory would be able to detect DCOs making up as little as one part in $10^4$ of the DM, as shown in Fig. 2.1. Crucially, we also computed how these constraints would change depending on the spatial distribution of the DCOs. This relates to the fundamental nature of these compact objects - primordial black holes would likely have a spherical NFW galactic distribution, whereas "dark stars" arising from dissipative or mirror sector DM models could form in disk configurations. We computed constraints on dark disks with a variety of shapes, finding that the vertical and radial rescaling of the dark disk could change the constraints by several orders of magnitude, as shown in Fig. 2.8. We also found that tilting the dark disk relative to the baryonic disk could weaken the microlensing constraints with a nontrivial dependence on tilt angle, as shown in Fig. 2.10. These microlensing calculations will be a powerful tool when LSST comes online, allowing us to search for the unique microlensing signatures of these dark disk models, and differentiate them from PBH DM.

There are many ways of potentially expanding on this microlensing work. For example, the current analysis in [210] assumes a single mass for all DCOs, and also assumes no small-scale clumpiness in the DCO distribution. Both of these assumptions could be broken in future versions of the microlensing forecasting code, and it would be interesting to explore how the microlensing forecasts would change in light of this. But perhaps the most significant area of further research is connecting the galactic distribution of DCOs with the fundamental properties of the dissipative DM model that

created them, such the Mirror Sector. As discussed in Chapter 2, the connection between the atomic properties of Mirror Sector particles and the formation of stellar galactic structure is complex, particularly when combined with simultaneous baryonic galactic formation. However, such a connection would allow us to relate microlensing constraints on dark compact disks to the fundamental allowed properties of Mirror Sector physics, placing observational constraints on potential Mirror Sector solutions to the little hierarchy problem.

In Chapter 3 (Harrison Winch et al. "Extreme Axions Unveiled: a Novel Fluid Approach for Cosmological Modeling". In: (Nov. 2023). arXiv: 2311.02052 [astro-ph.CO]), we developed a powerful computational method for modeling extreme axions as an effective cosmological fluid. Extreme axions are a particular type of axion-like DM candidate, consisting of an ultralight scalar field with a periodic potential, and a starting value near the peak of that field potential. This starting configuration results in highly nonlinear behaviour resulting in an enhancement of primordial structure on certain scales, which is a distinctive observational signature. However, modeling the nonlinear perturbation dynamics of these extreme axions near the peak of their potential is computationally intensive, often requiring hours or even days to simulate. We developed a novel method of modeling these extreme axions as a cosmological fluid, utilizing a negative effective sound speed squared to capture the effects of the perturbation enhancements, as shown in Fig. 3.2. Our results were shown to be consistent with the more rigorous field equation solutions, as shown in Fig. 3.3. When combined with various other computational innovations, we were able to compute the $z = 0$ linear matter power spectrum for mixed extreme axion and CDM cosmologies in under a minute, which represents a substantial speed up over previous work. Using our new efficient methods, we were able to simulate a range of possible extreme axion cosmologies, comparing the results to estimates of the linear $z = 0$ matter power spectrum from the eBOSS measurements of the Lyman-$\alpha$ forest. We found that extreme axions were capable of relieving observational constraints on axion mass and fraction for a non-trivial range of starting field values, as shown in Figs. 3.11 and 3.12.

This motivates the reevaluations of existing cosmological constraints on axion DM in light of the possibility of extreme axions, while also enabling such a computation with an efficient and accurate software package. Now that we have developed an efficient fluid formalism for modeling extreme axions, many follow up projects are possible, reevaluating cosmological constraints on axions in light of this extreme axion possibility. For example, we could compute MCMC constraints on mixed extreme axion cosmologies using CMB or Lyman-$\alpha$ forest likelihoods, evaluating how the constraints on axion mass and fraction might become weaker relative to vanilla axion constraints. Given the non-trivial range of starting angles that appear to alleviate tensions with Lyman-$\alpha$ forest data shown in Fig. 3.11, we expect to see a substantial weakening of current constraints, even with a purely uniform prior on starting angle and no fine-tuning.

In Chapter 4 (Harrison Winch et al. "High-redshift, small-scale tests of ultralight axion dark matter using Hubble and Webb galaxy UV luminosities". In: (Apr. 2024). arXiv: 2404.11071 [astro-ph.CO]), we used measurements of galaxy UV luminosities to place strong observational constraints on mixed axion cosmologies for a range of axion masses and DM fractions. The UV luminosity function (UVLF) represents the number of UV galaxies of a given luminosity and redshift, and has been measured by the Hubble space telescope (HST) at redshifts from $4 < z < 10$. The UVLF depends on both the halo mass function (which depends on the underlying distribution of DM, and is sensitive to ultralight axions), as well as the astrophysical model connecting halo mass and

UV luminosity, as illustrated in Fig. 1.4. By marginalizing over a flexible parametric astrophysical model we were able to compute conservative limits on the axion DM fraction allowed by HST at a range of axion masses. For example, we excluded a single axion as all the DM for $m_{\rm ax} < 10^{-21.6}$ eV and limiting axions with $-26 \leq \log(m_{\rm ax}/{\rm eV}) \leq -23$ to be less than 22% of the DM (both at 95% credibility). These constraints not only probe a novel region of axion DM parameter space, as shown in Fig. 4.1, but also utilize observables in a novel range of scales and redshifts, as shown in Fig. 1.2, providing a powerful high-$z$ validation tool for low-$z$ tests of axion DM.

This work involved using HST measurements of the UVLF at redshifts $4 < z < 10$ — however, new data from JWST has the potential to probe even smaller scales and earlier redshifts, where the effect of axions is more pronounced (as seen in Fig. 4.4). The validity of our HMF and UV luminosity models at redshifts $z > 10$ has not been thoroughly tested, particularly for mixed axion models that could contain nontrivial astrophysical effects. Any rigorous forecasts or comparison to JWST data must be preceded by a careful validation of our model against relevant simulations. These could include the THESAN simulations, which model high redshift galaxy formation for both cold and fuzzy DM[110, 185], as well as the Peak Patch simulations that can approximate the impacts of mixed axion DM on high-redshift halo formation [119]. Once we validate our HMF and UVLF model at high redshifts in mixed axion cosmologies, we will be able to compute forecasts and constraints on axion DM using JWST measurements of the UVLF.

The study of DM is a complex endeavour, touching on many areas of particle physics, astrophysics, and mathematics. This thesis has drawn diverse interdisciplinary connections between topics such as mirror-sector particle physics, galactic structure, extreme axion wave mechanics, computational cosmological fluid dynamics, axion halo formation, galaxy UV luminosity, and statistical analysis. These connections have allowed me to develop multiple powerful new tools for the study of DM, including software modules to compute microlensing forecasts on dark compact objects with specific galactic distributions, efficiently model the evolution of extreme axion density perturbations for estimating the linear MPS, and relating galaxy UV luminosities to the primordial mixed-axion MPS. These tools have unlocked new forecasts, modelings, and observational constraints that allow us to shed light on one of the most profound mysteries of modern physics: the nature of dark matter.

# Bibliography


[1] Kevork Abazajian et al. "Snowmass 2021 CMB-S4 White Paper". In: (Mar. 2022). arXiv: 2203.08024 [astro-ph.CO].

[2] L. F. Abbott and P. Sikivie. "A Cosmological Bound on the Invisible Axion". In: *Phys. Lett. B* 120 (1983). Ed. by M. A. Srednicki, pp. 133–136. DOI: 10.1016/0370-2693(83)90638-X.

[3] R. Abbott et al. "GW190521: A Binary Black Hole Merger with a Total Mass of 150 $M_\odot$". In: *Phys. Rev. Lett.* 125 (10 Sept. 2020), p. 101102. DOI: 10.1103/PhysRevLett.125.101102. URL: https://link.aps.org/doi/10.1103/PhysRevLett.125.101102.

[4] T. M. C. Abbott et al. "Dark Energy Survey year 1 results: Cosmological constraints from galaxy clustering and weak lensing". In: *Phys. Rev. D* 98.4 (2018), p. 043526. DOI: 10.1103/PhysRevD.98.043526. arXiv: 1708.01530 [astro-ph.CO].

[5] Zara Abdurashidova et al. "HERA Phase I Limits on the Cosmic 21 cm Signal: Constraints on Astrophysics and Cosmology during the Epoch of Reionization". In: *Astrophys. J.* 924.2 (2022), p. 51. DOI: 10.3847/1538-4357/ac2ffc. arXiv: 2108.07282 [astro-ph.CO].

[6] C. B. Adams et al. "Axion Dark Matter". In: *Snowmass 2021*. Mar. 2022. arXiv: 2203.14923 [hep-ex].

[7] N. Aghanim et al. "Planck 2015 results. XI. CMB power spectra, likelihoods, and robustness of parameters". In: *Astron. Astrophys.* 594 (2016), A11. DOI: 10.1051/0004-6361/201526926. arXiv: 1507.02704 [astro-ph.CO].

[8] N. Aghanim et al. "Planck 2018 results. V. CMB power spectra and likelihoods". In: *Astron. Astrophys.* 641 (2020), A5. DOI: 10.1051/0004-6361/201936386. arXiv: 1907.12875 [astro-ph.CO].

[9] N. Aghanim et al. "Planck 2018 results. VI. Cosmological parameters". In: *Astron. Astrophys.* 641 (2020). [Erratum: Astron.Astrophys. 652, C4 (2021)], A6. DOI: 10.1051/0004-6361/201833910. arXiv: 1807.06209 [astro-ph.CO].

[10] H. Akaike. "A new look at the statistical model identification". In: *IEEE Transactions on Automatic Control* 19.6 (1974), pp. 716–723. DOI: 10.1109/TAC.1974.1100705.

[11] Shadab Alam et al. "Completed SDSS-IV extended Baryon Oscillation Spectroscopic Survey: Cosmological implications from two decades of spectroscopic surveys at the Apache Point Observatory". In: 103.8, 083533 (Apr. 2021), p. 083533. DOI: 10.1103/PhysRevD.103.083533. arXiv: 2007.08991 [astro-ph.CO].

[12] C. Alcock et al. "The MACHO project first year LMC results: The Microlensing rate and the nature of the galactic dark halo". In: *Astrophys. J.* 461 (1996), p. 84. DOI: 10.1086/177039. arXiv: astro-ph/9506113 [astro-ph].

[13] C. Alcock et al. "The MACHO Project: Microlensing Optical Depth toward the Galactic Bulge from Difference Image Analysis". In: *The Astrophysical Journal* 541.2 (Oct. 2000), pp. 734–766. DOI: 10.1086/309484. URL: https://doi.org/10.1086%2F309484.

[14] Luca Amendola et al. "Cosmology and fundamental physics with the Euclid satellite". In: *Living Rev. Rel.* 21.1 (2018), p. 2. DOI: 10.1007/s41114-017-0010-3. arXiv: 1606.00180 [astro-ph.CO].

[15] Luca Amendola and Riccardo Barbieri. "Dark matter from an ultra-light pseudo-Goldstone-boson". In: *Phys. Lett. B* 642 (2006), pp. 192–196. DOI: 10.1016/j.physletb.2006.08.069. arXiv: hep-ph/0509257.

[16] Lauren Anderson et al. "The clustering of galaxies in the SDSS-III Baryon Oscillation Spectroscopic Survey: baryon acoustic oscillations in the Data Releases 10 and 11 Galaxy samples". In: *Mon. Not. Roy. Astron. Soc.* 441.1 (2014), pp. 24–62. DOI: 10.1093/mnras/stu523. arXiv: 1312.4877 [astro-ph.CO].

[17] Asimina Arvanitaki et al. "Large-misalignment mechanism for the formation of compact axion structures: Signatures from the QCD axion to fuzzy dark matter". In: *Phys. Rev. D* 101.8 (2020), p. 083014. DOI: 10.1103/PhysRevD.101.083014. arXiv: 1909.11665 [astro-ph.CO].

[18] Asimina Arvanitaki et al. "String Axiverse". In: *Phys. Rev. D* 81 (2010), p. 123530. DOI: 10.1103/PhysRevD.81.123530. arXiv: 0905.4720 [hep-th].

[19] P. Awad et al. "Probing compact dark matter objects with microlensing in gravitationally lensed quasars". In: 673, A88 (May 2023), A88. DOI: 10.1051/0004-6361/202245615. arXiv: 2304.01320 [astro-ph.GA].

[20] Nilanjan Banik et al. "Novel constraints on the particle nature of dark matter from stellar streams". In: *JCAP* 10 (2021), p. 043. DOI: 10.1088/1475-7516/2021/10/043. arXiv: 1911.02663 [astro-ph.GA].

[21] Nitsan Bar, Kfir Blum, and Chen Sun. "Galactic rotation curves versus ultralight dark matter: A systematic comparison with SPARC data". In: *Phys. Rev. D* 105.8 (2022), p. 083015. DOI: 10.1103/PhysRevD.105.083015. arXiv: 2111.03070 [hep-ph].

[22] Nitsan Bar et al. "Ultralight dark matter in disk galaxies". In: *Phys. Rev. D* 99.10 (2019), p. 103020. DOI: 10.1103/PhysRevD.99.103020. arXiv: 1903.03402 [astro-ph.CO].

[23] J. Barranco and A. Bernal. "Self-gravitating system made of axions". In: *Phys. Rev. D* 83 (2011), p. 043525. DOI: 10.1103/PhysRevD.83.043525. arXiv: 1001.1769 [astro-ph.CO].

[24] Z. G. Berezhiani, A. S. Sakharov, and M. Yu. Khlopov. "Primordial background of cosmological axions". In: *Sov. J. Nucl. Phys.* 55 (1992), pp. 1063–1071.

[25] Zurab Berezhiani. "Mirror world and its cosmological consequences". In: *Int. J. Mod. Phys.* A19 (2004), pp. 3775–3806. DOI: 10.1142/S0217751X04020075. arXiv: hep-ph/0312335 [hep-ph].

[26] Zurab Berezhiani et al. "Evolutionary and structural properties of mirror star MACHOs". In: *Astropart. Phys.* 24 (2006), pp. 495–510. DOI: 10.1016/j.astropartphys.2005.10.002. arXiv: astro-ph/0507153 [astro-ph].

[27] Simeon Bird et al. "Snowmass2021 Cosmic Frontier White Paper: Primordial black hole dark matter". In: *Phys. Dark Univ.* 41 (2023), p. 101231. DOI: 10.1016/j.dark.2023.101231. arXiv: 2203.08967 [hep-ph].

[28] L. Bisigello et al. "The Impact of JWST Broadband Filter Choice on Photometric Redshift Estimation". In: 227.2, 19 (Dec. 2016), p. 19. DOI: 10.3847/0067-0049/227/2/19. arXiv: 1605.06334 [astro-ph.GA].

[29] Diego Blas, Julien Lesgourgues, and Thomas Tram. "The Cosmic Linear Anisotropy Solving System (CLASS). Part II: Approximation schemes". In: 2011.7, 034 (July 2011), p. 034. DOI: 10.1088/1475-7516/2011/07/034. arXiv: 1104.2933 [astro-ph.CO].

[30] R. J. Bouwens et al. "New Determinations of the UV Luminosity Functions from z 9 to 2 Show a Remarkable Consistency with Halo Growth and a Constant Star Formation Efficiency". In: 162.2, 47 (Aug. 2021), p. 47. DOI: 10.3847/1538-3881/abf83e. arXiv: 2102.07775 [astro-ph.GA].

[31] R. J. Bouwens et al. "z 2-9 Galaxies Magnified by the Hubble Frontier Field Clusters. II. Luminosity Functions and Constraints on a Faint-end Turnover". In: 940.1, 55 (Nov. 2022), p. 55. DOI: 10.3847/1538-4357/ac86d1. arXiv: 2205.11526 [astro-ph.GA].

[32] Rychard J. Bouwens et al. "Evolution of the UV LF from z 15 to z 8 using new JWST NIRCam medium-band observations over the HUDF/XDF". In: 523.1 (July 2023), pp. 1036–1055. DOI: 10.1093/mnras/stad1145. arXiv: 2211.02607 [astro-ph.GA].

[33] Jo Bovy. "galpy: A python Library for Galactic Dynamics". In: 216.2, 29 (Feb. 2015), p. 29. DOI: 10.1088/0067-0049/216/2/29. arXiv: 1412.3451 [astro-ph.GA].

[34] Jo Bovy. "Stellar inventory of the solar neighbourhood using Gaia DR1". In: *Monthly Notices of the Royal Astronomical Society* 470.2 (May 2017), pp. 1360–1387. ISSN: 1365-2966. DOI: 10.1093/mnras/stx1277. URL: http://dx.doi.org/10.1093/mnras/stx1277.

[35] Jo Bovy and Scott Tremaine. "On the local dark matter density". In: *Astrophys. J.* 756 (2012), p. 89. DOI: 10.1088/0004-637X/756/1/89. arXiv: 1205.4033 [astro-ph.GA].

[36] Brandon Bozek et al. "Galaxy UV-luminosity function and reionization constraints on axion dark matter". In: *Mon. Not. Roy. Astron. Soc.* 450.1 (2015), pp. 209–222. DOI: 10.1093/mnras/stv624. arXiv: 1409.3544 [astro-ph.CO].

[37] Thejs Brinckmann and Julien Lesgourgues. "MontePython 3: boosted MCMC sampler and other features". In: *Phys. Dark Univ.* 24 (2019), p. 100260. DOI: 10.1016/j.dark.2018.100260. arXiv: 1804.07261 [astro-ph.CO].

[38] Jatan Buch, Shing Chau (John) Leung, and JiJi Fan. "Using Gaia DR2 to Constrain Local Dark Matter Density and Thin Dark Disk". In: *JCAP* 04 (2019), p. 026. DOI: 10.1088/1475-7516/2019/04/026. arXiv: 1808.05603 [astro-ph.GA].

[39] Gustavo Burdman et al. "Colorless Top Partners, a 125 GeV Higgs, and the Limits on Naturalness". In: *Phys. Rev.* D91.5 (2015), p. 055007. DOI: 10.1103/PhysRevD.91.055007. arXiv: 1411.3310 [hep-ph].

[40] Josh Calcino, Juan Garcia-Bellido, and Tamara M. Davis. "Updating the MACHO fraction of the Milky Way dark halowith improved mass models". In: *Mon. Not. Roy. Astron. Soc.* 479.3 (2018), pp. 2889–2905. DOI: 10.1093/mnras/sty1368. arXiv: 1803.09205 [astro-ph.CO].

[41] Francisco X. Linares Cedeño, Alma X. González-Morales, and L. Arturo Ureña-López. "Cosmological signatures of ultralight dark matter with an axionlike potential". In: *Phys. Rev.* D96.6 (2017), p. 061301. DOI: 10.1103/PhysRevD.96.061301. arXiv: 1703.10180 [gr-qc].

[42] J. A. R. Cembranos et al. "Constraints on anharmonic corrections of Fuzzy Dark Matter". In: *JHEP* 08 (2018), p. 073. DOI: 10.1007/JHEP08(2018)073. arXiv: 1805.08112 [astro-ph.CO].

[43] Solène Chabanier, Marius Millea, and Nathalie Palanque-Delabrouille. "Matter power spectrum: from Ly$\alpha$ forest to CMB scales". In: *Mon. Not. Roy. Astron. Soc.* 489.2 (2019), pp. 2247–2253. DOI: 10.1093/mnras/stz2310. arXiv: 1905.08103 [astro-ph.CO].

[44] Z. Chacko, Hock-Seng Goh, and Roni Harnik. "The Twin Higgs: Natural electroweak breaking from mirror symmetry". In: *Phys. Rev. Lett.* 96 (2006), p. 231802. DOI: 10.1103/PhysRevLett.96.231802. arXiv: hep-ph/0506256 [hep-ph].

[45] Zackaria Chacko et al. "Cosmological Signatures of a Mirror Twin Higgs". In: *JHEP* 09 (2018), p. 163. DOI: 10.1007/JHEP09(2018)163. arXiv: 1803.03263 [hep-ph].

[46] Zackaria Chacko et al. "Cosmological Signatures of a Mirror Twin Higgs". In: *JHEP* 09 (2018), p. 163. DOI: 10.1007/JHEP09(2018)163. arXiv: 1803.03263 [hep-ph].

[47] Zackaria Chacko et al. "Cosmology in Mirror Twin Higgs and Neutrino Masses". In: *JHEP* 07 (2017), p. 023. DOI: 10.1007/JHEP07(2017)023. arXiv: 1611.07975 [hep-ph].

[48] Jae Hyeok Chang et al. "Structure Formation and Exotic Compact Objects in a Dissipative Dark Sector". In: *JCAP* 03 (2019), p. 036. DOI: 10.1088/1475-7516/2019/03/036. arXiv: 1812.07000 [hep-ph].

[49] Iryna Chemerynska et al. "JWST UNCOVER: The Overabundance of Ultraviolet-luminous Galaxies at $z > 9$". In: *arXiv e-prints*, arXiv:2312.05030 (Dec. 2023), arXiv:2312.05030. DOI: 10.48550/arXiv.2312.05030. arXiv: 2312.05030 [astro-ph.GA].

[50] Raymond T. Co, Eric Gonzalez, and Keisuke Harigaya. "Axion Misalignment Driven to the Hilltop". In: *JHEP* 05 (2019), p. 163. DOI: 10.1007/JHEP05(2019)163. arXiv: 1812.11192 [hep-ph].

[51] Asantha Cooray and Ravi K. Sheth. "Halo Models of Large Scale Structure". In: *Phys. Rept.* 372 (2002), pp. 1–129. DOI: 10.1016/S0370-1573(02)00276-4. arXiv: astro-ph/0206508.

[52] P. S. Corasaniti et al. "Constraints on dark matter scenarios from measurements of the galaxy luminosity function at high redshifts". In: *Phys. Rev. D* 95.8 (2017), p. 083512. DOI: 10.1103/PhysRevD.95.083512. arXiv: 1611.05892 [astro-ph.CO].

[53] Nathaniel Craig, Seth Koren, and Timothy Trott. "Cosmological Signals of a Mirror Twin Higgs". In: *JHEP* 05 (2017), p. 038. DOI: 10.1007/JHEP05(2017)038. arXiv: 1611.07977 [hep-ph].

[54] Djuna Croon, David McKeen, and Nirmal Raj. "Gravitational microlensing by dark matter in extended structures". In: *Phys. Rev. D* 101.8 (2020), p. 083013. DOI: 10.1103/PhysRevD.101.083013. arXiv: 2002.08962 [astro-ph.CO].

[55] Djuna Croon et al. "Subaru-HSC through a different lens: Microlensing by extended dark matter structures". In: *Phys. Rev. D* 102.8 (2020), p. 083021. DOI: 10.1103/PhysRevD.102.083021. arXiv: 2007.12697 [astro-ph.CO].

[56] Csaba Csáki, Salvator Lombardo, and Ofri Telem. "TASI Lectures on Non-supersymmetric BSM Models". In: *Proceedings, Theoretical Advanced Study Institute in Elementary Particle Physics : Anticipating the Next Discoveries in Particle Physics (TASI 2016): Boulder, CO, USA, June 6-July 1, 2016*. WSP, 2018, pp. 501–570. DOI: 10.1142/9789813233348_0007. arXiv: 1811.04279 [hep-ph].

[57] David Curtin and Jack Setford. "How To Discover Mirror Stars". In: *Phys. Lett. B* 804 (2020), p. 135391. DOI: 10.1016/j.physletb.2020.135391. arXiv: 1909.04071 [hep-ph].

[58] David Curtin and Jack Setford. "Signatures of Mirror Stars". In: *JHEP* 03 (2020), p. 041. DOI: 10.1007/JHEP03(2020)041. arXiv: 1909.04072 [hep-ph].

[59] Francis-Yan Cyr-Racine et al. "Constraints on Large-Scale Dark Acoustic Oscillations from Cosmology". In: *Phys. Rev. D* 89.6 (2014), p. 063517. DOI: 10.1103/PhysRevD.89.063517. arXiv: 1310.3278 [astro-ph.CO].

[60] Neal Dalal and Andrey Kravtsov. "Excluding fuzzy dark matter with sizes and stellar kinematics of ultrafaint dwarf galaxies". In: *Phys. Rev. D* 106.6 (2022), p. 063517. DOI: 10.1103/PhysRevD.106.063517. arXiv: 2203.05750 [astro-ph.CO].

[61] Mariafelicia De Laurentis and Paolo Salucci. "The Accurate Mass Distribution of M87, the Giant Galaxy with Imaged Shadow of Its Supermassive Black Hole, as a Portal to New Physics". In: *Astrophys. J.* 929.1 (2022), p. 17. DOI: 10.3847/1538-4357/ac54b9. arXiv: 2206.01997 [astro-ph.CO].

[62] Mona Dentler et al. "Fuzzy dark matter and the Dark Energy Survey Year 1 data". In: *Mon. Not. Roy. Astron. Soc.* 515.4 (2022), pp. 5646–5664. DOI: 10.1093/mnras/stac1946. arXiv: 2111.01199 [astro-ph.CO].

[63] Luca Di Luzio et al. "The landscape of QCD axion models". In: *Phys. Rept.* 870 (2020), pp. 1–117. DOI: 10.1016/j.physrep.2020.06.002. arXiv: 2003.01100 [hep-ph].

[64] Michael Dine and Willy Fischler. "The Not So Harmless Axion". In: *Phys. Lett. B* 120 (1983). Ed. by M. A. Srednicki, pp. 137–141. DOI: 10.1016/0370-2693(83)90639-1.

[65] A. D. Dolgov. *Massive Primordial Black Holes*. 2019. arXiv: 1911.02382 [astro-ph.CO].

[66] Alex Drlica-Wagner et al. "Probing the Fundamental Nature of Dark Matter with the Large Synoptic Survey Telescope". In: *arXiv e-prints*, arXiv:1902.01055 (Feb. 2019), arXiv:1902.01055. arXiv: 1902.01055 [astro-ph.CO].

[67] Hélion du Mas des Bourboux et al. "The Completed SDSS-IV Extended Baryon Oscillation Spectroscopic Survey: Baryon Acoustic Oscillations with Ly$\alpha$ Forests". In: 901.2, 153 (Oct. 2020), p. 153. DOI: 10.3847/1538-4357/abb085. arXiv: 2007.08995 [astro-ph.CO].

[68] Leanne D. Duffy and Karl van Bibber. "Axions as Dark Matter Particles". In: *New J. Phys.* 11 (2009), p. 105008. DOI: 10.1088/1367-2630/11/10/105008. arXiv: 0904.3346 [hep-ph].

[69] Cora Dvorkin et al. "Dark Matter Physics from the CMB-S4 Experiment". In: *Snowmass 2021*. Mar. 2022. arXiv: 2203.07064 [hep-ph].

[70] Joshua Eby et al. "Axion Stars in the Infrared Limit". In: *JHEP* 03 (2015). [Erratum: JHEP 11, 134 (2016)], p. 080. DOI: 10.1007/JHEP11(2016)134. arXiv: 1412.3430 [hep-th].

[71] Albert Einstein. "Lens-Like Action of a Star by the Deviation of Light in the Gravitational Field". In: *Science* 84.2188 (1936), pp. 506–507. DOI: 10.1126/science.84.2188.506. eprint: https://www.science.org/doi/pdf/10.1126/science.84.2188.506. URL: https://www.science.org/doi/abs/10.1126/science.84.2188.506.

[72] Albert Escrivà, Florian Kuhnel, and Yuichiro Tada. "Primordial Black Holes". In: (Nov. 2022). DOI: 10.1016/B978-0-32-395636-9.00012-8. arXiv: 2211.05767 [astro-ph.CO].

[73] JiJi Fan et al. "Dark-Disk Universe". In: *Phys.Rev.Lett.* 110.21 (2013), p. 211302. DOI: 10.1103/PhysRevLett.110.211302. arXiv: 1303.3271 [hep-ph].

[74] JiJi Fan et al. "Double-Disk Dark Matter". In: *Phys.Dark Univ.* 2 (2013), pp. 139–156. DOI: 10.1016/j.dark.2013.07.001. arXiv: 1303.1521 [astro-ph.CO].

[75] Jordan Flitter and Ely D. Kovetz. "Closing the window on fuzzy dark matter with the 21-cm signal". In: *Phys. Rev. D* 106.6 (2022), p. 063504. DOI: 10.1103/PhysRevD.106.063504. arXiv: 2207.05083 [astro-ph.CO].

[76] R. Foot. "Have mirror stars been observed?" In: *Phys. Lett.* B452 (1999), pp. 83–86. DOI: 10.1016/S0370-2693(99)00230-0. arXiv: astro-ph/9902065 [astro-ph].

[77] Robert Foot, A. Yu. Ignatiev, and R. R. Volkas. "Physics of mirror photons". In: *Phys. Lett.* B503 (2001), pp. 355–361. DOI: 10.1016/S0370-2693(01)00228-3. arXiv: astro-ph/0011156 [astro-ph].

[78] Daniel Foreman-Mackey. "corner.py: Scatterplot matrices in Python". In: *The Journal of Open Source Software* 1.2 (June 2016), p. 24. DOI: 10.21105/joss.00024. URL: https://doi.org/10.21105/joss.00024.

[79] Seiji Fujimoto et al. "CEERS Spectroscopic Confirmation of NIRCam-selected z $\gtrsim$ 8 Galaxy Candidates with JWST/NIRSpec: Initial Characterization of Their Properties". In: *Astrophys. J. Lett.* 949.2 (2023), p. L25. DOI: 10.3847/2041-8213/acd2d9. arXiv: 2301.09482 [astro-ph.GA].

[80] Andrew Gelman and Donald B. Rubin. "Inference from Iterative Simulation Using Multiple Sequences". In: *Statistical Science* 7.4 (1992), pp. 457–472. ISSN: 08834237. URL: http://www.jstor.org/stable/2246093 (visited on 06/11/2024).

[81] Naomi Gendler et al. "Glimmers from the Axiverse". In: (Sept. 2023). arXiv: 2309.13145 [hep-th].

[82] Nicolas J. F. Gillet, Andrei Mesinger, and Jaehong Park. "Combining high-z galaxy luminosity functions with Bayesian evidence". In: *Mon. Not. Roy. Astron. Soc.* 491.2 (2020), pp. 1980–1997. DOI: 10.1093/mnras/stz2988. arXiv: 1906.06296 [astro-ph.GA].

[83] Nathan Golovich et al. *A Reanalysis of Public Galactic Bulge Gravitational Microlensing Events from OGLE-III and IV*. 2020. arXiv: 2009.07927 [astro-ph.GA].

[84] Andrew Gould. "Extending the MACHO Search to approximately 10 6 M sub sun". In: 392 (June 1992), p. 442. DOI: 10.1086/171443.

[85] Kim Griest. "Galactic Microlensing as a Method of Detecting Massive Compact Halo Objects". In: 366 (Jan. 1991), p. 412. DOI: 10.1086/169575.

[86] Daniel Grin et al. "Gravitational probes of ultra-light axions". In: (2019). arXiv: 1904.09003 [astro-ph.CO].

[87] Yuichi Harikane et al. "Pure Spectroscopic Constraints on UV Luminosity Functions and Cosmic Star Formation History from 25 Galaxies at z $_{spec}$ = 8.61-13.20 Confirmed with JWST/NIRSpec". In: 960.1, 56 (Jan. 2024), p. 56. DOI: 10.3847/1538-4357/ad0b7e. arXiv: 2304.06658 [astro-ph.GA].

[88] Cameron Heather et al. "Extreme-value modelling of the brightest galaxies at $z \gtrsim 9$". In: (Apr. 2024). arXiv: 2404.11567 [astro-ph.GA].

[89] Renée Hlozek, David J. E. Marsh, and Daniel Grin. "Using the Full Power of the Cosmic Microwave Background to Probe Axion Dark Matter". In: *Mon. Not. Roy. Astron. Soc.* 476.3 (2018), pp. 3063–3085. DOI: 10.1093/mnras/sty271. arXiv: 1708.05681 [astro-ph.CO].

[90] Renée Hlozek et al. "A search for ultralight axions using precision cosmological data". In: *Phys. Rev. D* 91.10 (2015), p. 103512. DOI: 10.1103/PhysRevD.91.103512. arXiv: 1410.2896 [astro-ph.CO].

[91] Renée Hlozek et al. "The Atacama Cosmology Telescope: A Measurement of the Primordial Power Spectrum". In: 749.1, 90 (Apr. 2012), p. 90. DOI: 10.1088/0004-637X/749/1/90. arXiv: 1105.4887 [astro-ph.CO].

[92] Renée Hložek et al. "A search for ultralight axions using precision cosmological data". In: *Phys. Rev. D* 91 (10 May 2015), p. 103512. DOI: 10.1103/PhysRevD.91.103512. URL: https://link.aps.org/doi/10.1103/PhysRevD.91.103512.

[93] Renée Hložek et al. "Future CMB tests of dark matter: Ultralight axions and massive neutrinos". In: *Phys. Rev. D* 95.12 (2017), p. 123511. DOI: 10.1103/PhysRevD.95.123511. arXiv: 1607.08208 [astro-ph.CO].

[94] C.J. Hogan and M.J. Rees. "AXION MINICLUSTERS". In: *Phys.Lett.B* 205 (1988), pp. 228–230. DOI: 10.1016/0370-2693(88)91655-3.

[95] Selim C. Hotinli, David J. E. Marsh, and Marc Kamionkowski. "Probing ultralight axions with the 21-cm signal during cosmic dawn". In: *Phys. Rev. D* 106.4 (2022), p. 043529. DOI: 10.1103/PhysRevD.106.043529. arXiv: 2112.06943 [astro-ph.CO].

[96] Wayne Hu. "Structure formation with generalized dark matter". In: *Astrophys. J.* 506 (1998), pp. 485–494. DOI: 10.1086/306274. arXiv: astro-ph/9801234.

[97] Wayne Hu, Rennan Barkana, and Andrei Gruzinov. "Cold and fuzzy dark matter". In: *Phys. Rev. Lett.* 85 (2000), pp. 1158–1161. DOI: 10.1103/PhysRevLett.85.1158. arXiv: astro-ph/0003365 [astro-ph].

[98] Hsinhao Huang, Hsi-Yu Schive, and Tzihong Chiueh. "Cosmological simulations of two-component wave dark matter". In: *Mon. Not. Roy. Astron. Soc.* 522.1 (2023), pp. 515–534. DOI: 10.1093/mnras/stad998. arXiv: 2212.14288 [astro-ph.CO].

[99] Lam Hui et al. "Ultralight scalars as cosmological dark matter". In: *Phys. Rev. D* 95.4 (2017), p. 043541. DOI: 10.1103/PhysRevD.95.043541. arXiv: 1610.08297 [astro-ph.CO].

[100] Vid Iršič et al. "The Lyman $\alpha$ forest power spectrum from the XQ-100 Legacy Survey". In: *Mon. Not. Roy. Astron. Soc.* 466.4 (2017), pp. 4332–4345. DOI: 10.1093/mnras/stw3372. arXiv: 1702.01761 [astro-ph.CO].

[101] Vid Iršič et al. "First constraints on fuzzy dark matter from Lyman-$\alpha$ forest data and hydrodynamical simulations". In: *Phys. Rev. Lett.* 119.3 (2017), p. 031302. DOI: 10.1103/PhysRevLett.119.031302. arXiv: 1703.04683 [astro-ph.CO].

[102] Zeljko Ivezić. "LSST survey: millions and millions of quasars". In: *Proceedings of the International Astronomical Union* 12.S324 (2016), pp. 330–337. DOI: 10.1017/S1743921316012424.

[103] Zeljko Ivezić et al. "LSST: From Science Drivers to Reference Design and Anticipated Data Products". In: *The Astrophysical Journal* 873.2 (Mar. 2019), p. 111. ISSN: 1538-4357. DOI: 10.3847/1538-4357/ab042c. URL: http://dx.doi.org/10.3847/1538-4357/ab042c.

[104] Željko Ivezić et al. "LSST: From Science Drivers to Reference Design and Anticipated Data Products". In: 873.2, 111 (Mar. 2019), p. 111. DOI: 10.3847/1538-4357/ab042c. arXiv: 0805.2366 [astro-ph].

[105] Joerg Jaeckel, Viraf M. Mehta, and Lukas T. Witkowski. "Monodromy Dark Matter". In: *JCAP* 1701.01 (2017), p. 036. DOI: 10.1088/1475-7516/2017/01/036. arXiv: 1605.01367 [hep-ph].

[106] Karsten Jedamzik. "Primordial Black Hole Dark Matter and the LIGO/Virgo observations". In: *JCAP* 09 (2020), p. 022. DOI: 10.1088/1475-7516/2020/09/022. arXiv: 2006.11172 [astro-ph.CO].

[107] A. Jenkins et al. "The Mass function of dark matter halos". In: *Mon. Not. Roy. Astron. Soc.* 321 (2001), p. 372. DOI: 10.1046/j.1365-8711.2001.04029.x. arXiv: astro-ph/0005260.

[108] Samson A. Johnson et al. "Predictions of the Nancy Grace Roman Space Telescope Galactic Exoplanet Survey. II. Free-floating Planet Detection Rates". In: *The Astronomical Journal* 160.3 (Aug. 2020), p. 123. ISSN: 1538-3881. DOI: 10.3847/1538-3881/aba75b. URL: http://dx.doi.org/10.3847/1538-3881/aba75b.

[109] Marc Kamionkowski and Adam G. Riess. "The Hubble Tension and Early Dark Energy". In: (Nov. 2022). arXiv: 2211.04492 [astro-ph.CO].

[110] R. Kannan et al. "Introducing the thesan project: radiation-magnetohydrodynamic simulations of the epoch of reionization". In: *Mon. Not. Roy. Astron. Soc.* 511.3 (2022), pp. 4005–4030. DOI: 10.1093/mnras/stab3710. arXiv: 2110.00584 [astro-ph.GA].

[111] M. Khlopov, B. A. Malomed, and Ia. B. Zeldovich. "Gravitational instability of scalar fields and formation of primordial black holes". In: *Mon. Not. Roy. Astron. Soc.* 215 (1985), pp. 575–589.

[112] Takeshi Kobayashi et al. "Lyman-$\alpha$ constraints on ultralight scalar dark matter: Implications for the early and late universe". In: *Phys. Rev. D* 96.12 (2017), p. 123514. DOI: 10.1103/PhysRevD.96.123514. arXiv: 1708.00015 [astro-ph.CO].

[113] Edward W. Kolb and Igor I. Tkachev. "Axion miniclusters and Bose stars". In: *Phys. Rev. Lett.* 71 (1993), pp. 3051–3054. DOI: 10.1103/PhysRevLett.71.3051. arXiv: hep-ph/9303313.

[114] Eric David Kramer and Lisa Randall. "Interstellar Gas and a Dark Disk". In: *Astrophys.J.* 829.2 (2016), p. 126. DOI: 10.3847/0004-637X/829/2/126. arXiv: 1603.03058 [astro-ph.GA].

[115] Eric David Kramer and Lisa Randall. "Updated Kinematic Constraints on a Dark Disk". In: *Astrophys.J.* 824.2 (2016), p. 116. DOI: 10.3847/0004-637X/824/2/116. arXiv: 1604.01407 [astro-ph.GA].

[116] Pavel Kroupa. "On the variation of the initial mass function". In: 322.2 (Apr. 2001), pp. 231–246. DOI: 10.1046/j.1365-8711.2001.04022.x. arXiv: astro-ph/0009005 [astro-ph].

[117] Alex Laguë et al. "Constraining ultralight axions with galaxy surveys". In: *JCAP* 01.01 (2022), p. 049. DOI: 10.1088/1475-7516/2022/01/049. arXiv: 2104.07802 [astro-ph.CO].

[118] Alex Laguë et al. "Cosmological simulations of mixed ultralight dark matter". In: *Phys. Rev. D* 109.4 (2024), p. 043507. DOI: 10.1103/PhysRevD.109.043507. arXiv: 2310.20000 [astro-ph.CO].

[119] Alex Laguë et al. "Evolving ultralight scalars into non-linearity with Lagrangian perturbation theory". In: *Mon. Not. Roy. Astron. Soc.* 504.2 (2021), pp. 2391–2404. DOI: 10.1093/mnras/stab601. arXiv: 2004.08482 [astro-ph.CO].

[120] Adrian Lee et al. "The Simons Observatory". In: *Bulletin of the American Astronomical Society*. Vol. 51. Sept. 2019, 147, p. 147. DOI: 10.48550/arXiv.1907.08284. arXiv: 1907.08284 [astro-ph.IM].

[121] Ka-Hou Leong et al. "Testing extreme-axion wave-like dark matter using the BOSS Lyman-alpha forest data". In: *Mon. Not. Roy. Astron. Soc.* 484.3 (2019), pp. 4273–4286. DOI: 10.1093/mnras/stz271. arXiv: 1810.05930 [astro-ph.CO].

[122] Antony Lewis and Sarah Bridle. "Cosmological parameters from CMB and other data: A Monte Carlo approach". In: 66 (2002), p. 103511. DOI: 10.1103/PhysRevD.66.103511. arXiv: astro-ph/0205436 [astro-ph].

[123] Francisco X. Linares Cedeño, Alma X. González-Morales, and L. Arturo Ureña-López. "Ultralight DM bosons with an axion-like potential: scale-dependent constraints revisited". In: *JCAP* 01 (2021), p. 051. DOI: 10.1088/1475-7516/2021/01/051. arXiv: 2006.05037 [astro-ph.CO].

[124] Francisco X. Linares Cedeño and Luis Arturo Ureña-lópez. "One-parametric description for scalar field dark matter potentials". In: *Astron. Nachr.* 342.1-2 (2021). Ed. by C. A. Zen Vasconcellos et al., pp. 404–410. DOI: 10.1002/asna.202113942. arXiv: 2102.05074 [astro-ph.CO].

[125] Adrian Liu et al. "Snowmass2021 Cosmic Frontier White Paper: 21cm Radiation as a Probe of Physics Across Cosmic Ages". In: (Mar. 2022). arXiv: 2203.07864 [astro-ph.CO].

[126] Bin Liu, Huanyuan Shan, and Jiajun Zhang. "New galaxy UV luminosity constraints on warm dark matter from JWST". In: (Apr. 2024). arXiv: 2404.13596 [astro-ph.CO].

[127] S. López et al. "XQ-100: A legacy survey of one hundred $3.5 \lesssim z \lesssim 4.5$ quasars observed with VLT/X-shooter". In: 594, A91 (Oct. 2016), A91. DOI: 10.1051/0004-6361/201628161. arXiv: 1607.08776 [astro-ph.GA].

[128] LSST Science Collaboration et al. "LSST Science Book, Version 2.0". In: *arXiv e-prints*, arXiv:0912.0201 (Dec. 2009), arXiv:0912.0201. arXiv: 0912.0201 [astro-ph.IM].

[129] Limin Lu et al. "The lyman-alpha forest at Z 4: keck hires observations of q 0000-26". In: *Astrophys. J.* 472 (1996), p. 509. DOI: 10.1086/526756. arXiv: astro-ph/9606033.

[130] D. H. Lyth. "Axions and inflation: Sitting in the vacuum". In: *Phys. Rev. D* 45 (1992), pp. 3394–3404. DOI: 10.1103/PhysRevD.45.3394.

[131] Piero Madau and Mark Dickinson. "Cosmic Star Formation History". In: *Ann. Rev. Astron. Astrophys.* 52 (2014), pp. 415–486. DOI: 10.1146/annurev-astro-081811-125615. arXiv: 1403.0007 [astro-ph.CO].

[132] Mathew S. Madhavacheril, Neelima Sehgal, and Tracy R. Slatyer. "Current Dark Matter Annihilation Constraints from CMB and Low-Redshift Data". In: *Phys. Rev. D* 89 (2014), p. 103508. DOI: 10.1103/PhysRevD.89.103508. arXiv: 1310.3815 [astro-ph.CO].

[133] Umberto Maio and Matteo Viel. "JWST high-redshift galaxy constraints on warm and cold dark matter models". In: *Astron. Astrophys.* 672 (2023), A71. DOI: 10.1051/0004-6361/202345851. arXiv: 2211.03620 [astro-ph.CO].

[134] Yao-Yuan Mao et al. "Snowmass2021: Vera C. Rubin Observatory as a Flagship Dark Matter Experiment". In: (Mar. 2022). arXiv: 2203.07252 [hep-ex].

[135] David J. E. Marsh. "Axion Cosmology". In: *Phys. Rept.* 643 (2016), pp. 1–79. DOI: 10.1016/j.physrep.2016.06.005. arXiv: 1510.07633 [astro-ph.CO].

[136] David J. E. Marsh. "The Axiverse Extended: Vacuum Destabilisation, Early Dark Energy and Cosmological Collapse". In: *Phys. Rev. D* 83 (2011), p. 123526. DOI: 10.1103/PhysRevD.83.123526. arXiv: 1102.4851 [astro-ph.CO].

[137] David J. E. Marsh and Jens C. Niemeyer. "Strong Constraints on Fuzzy Dark Matter from Ultrafaint Dwarf Galaxy Eridanus II". In: *Phys. Rev. Lett.* 123.5 (2019), p. 051103. DOI: 10.1103/PhysRevLett.123.051103. arXiv: 1810.08543 [astro-ph.CO].

[138] David J. E. Marsh and Joe Silk. "A Model For Halo Formation With Axion Mixed Dark Matter". In: *Mon. Not. Roy. Astron. Soc.* 437.3 (2014), pp. 2652–2663. DOI: 10.1093/mnras/stt2079. arXiv: 1307.1705 [astro-ph.CO].

[139] Stephen P. Martin. "A Supersymmetry primer". In: *Adv. Ser. Direct. High Energy Phys.* 21 (2010). Ed. by Gordon L. Kane, pp. 1–153. DOI: 10.1142/9789812839657_0001. arXiv: hep-ph/9709356.

[140] Ian G. McCarthy et al. "The BAHAMAS project: Calibrated hydrodynamical simulations for large-scale structure cosmology". In: *Mon. Not. Roy. Astron. Soc.* 465.3 (2017), pp. 2936–2965. DOI: 10.1093/mnras/stw2792. arXiv: 1603.02702 [astro-ph.CO].

[141] Philip Mocz et al. "Cosmological structure formation and soliton phase transition in fuzzy dark matter with axion self-interactions". In: *Mon. Not. Roy. Astron. Soc.* 521.2 (2023), pp. 2608–2615. DOI: 10.1093/mnras/stad694. arXiv: 2301.10266 [astro-ph.CO].

[142] R. N. Mohapatra and Vigdor L. Teplitz. "Structures in the mirror universe". In: *Astrophys. J.* 478 (1997), pp. 29–38. DOI: 10.1086/303762. arXiv: astro-ph/9603049 [astro-ph].

[143] Rabindra N. Mohapatra and Vigdor L. Teplitz. "Mirror matter MACHOs". In: *Phys. Lett.* B462 (1999), pp. 302–309. DOI: 10.1016/S0370-2693(99)00789-3. arXiv: astro-ph/9902085 [astro-ph].

[144] Cristina Mondino et al. "Astrometric Weak Lensing with Gaia DR3 and Future Catalogs: Searches for Dark Matter Substructure". In: (Aug. 2023). arXiv: 2308.12330 [astro-ph.CO].

[145] Cristina Mondino et al. "First Results on Dark Matter Substructure from Astrometric Weak Lensing". In: *Phys. Rev. Lett.* 125.11 (2020), p. 111101. DOI: 10.1103/PhysRevLett.125.111101. arXiv: 2002.01938 [astro-ph.CO].

[146] Mireia Montes et al. "Optimizing Roman's High Latitude Wide Area Survey for Low Surface Brightness Astronomy". In: (June 2023). arXiv: 2306.09414 [astro-ph.GA].

[147] Julian B. Muñoz et al. "Breaking degeneracies in the first galaxies with clustering". In: *Mon. Not. Roy. Astron. Soc.* 526.1 (2023), pp. L47–L55. DOI: 10.1093/mnrasl/slad115. arXiv: 2306.09403 [astro-ph.CO].

[148] Ethan O. Nadler et al. "Dark Matter Constraints from a Unified Analysis of Strong Gravitational Lenses and Milky Way Satellite Galaxies". In: *Astrophys. J.* 917.1 (2021), p. 7. DOI: 10.3847/1538-4357/abf9a3. arXiv: 2101.07810 [astro-ph.CO].

[149] Julio F. Navarro, Carlos S. Frenk, and Simon D. M. White. "The Structure of Cold Dark Matter Halos". In: *The Astrophysical Journal* 462 (May 1996), p. 563. ISSN: 1538-4357. DOI: 10.1086/177173. URL: http://dx.doi.org/10.1086/177173.

[150] Dylan Nelson et al. "The IllustrisTNG simulations: public data release". In: *Comput. Astrophys. Cosmol.* 6.1 (2019), p. 2. DOI: 10.1186/s40668-019-0028-x. arXiv: 1812.05609 [astro-ph.GA].

[151] Fabrizio Nesti and Paolo Salucci. "The Dark Matter halo of the Milky Way, AD 2013". In: *JCAP* 1307 (2013), p. 016. DOI: 10.1088/1475-7516/2013/07/016. arXiv: 1304.5127 [astro-ph.GA].

[152] Hiroko Niikura et al. "Microlensing constraints on primordial black holes with Subaru/HSC Andromeda observations". In: *Nature Astron.* 3.6 (2019), pp. 524–534. DOI: 10.1038/s41550-019-0723-1. arXiv: 1701.02151 [astro-ph.CO].

[153] Bohdan Paczynski. "Gravitational microlensing by the galactic halo". In: *Astrophys. J.* 304 (1986), pp. 1–5. DOI: 10.1086/164140.

[154] Priyank Parashari and Ranjan Laha. "Primordial power spectrum in light of JWST observations of high redshift galaxies". In: *Mon. Not. Roy. Astron. Soc.* 526.1 (2023), pp. L63–L69. DOI: 10.1093/mnrasl/slad107. arXiv: 2305.00999 [astro-ph.CO].

[155] Chan-Gyung Park, Jai-chan Hwang, and Hyerim Noh. "Axion as a cold dark matter candidate: Low-mass case". In: 86.8, 083535 (Oct. 2012), p. 083535. DOI: 10.1103/PhysRevD.86.083535. arXiv: 1207.3124 [astro-ph.CO].

[156] Jaehong Park et al. "Inferring the astrophysics of reionization and cosmic dawn from galaxy luminosity functions and the 21-cm signal". In: *Mon. Not. Roy. Astron. Soc.* 484.1 (2019), pp. 933–949. DOI: 10.1093/mnras/stz032. arXiv: 1809.08995 [astro-ph.GA].

[157] R. D. Peccei and Helen R. Quinn. "Constraints imposed by CP conservation in the presence of pseudoparticles". In: *Phys. Rev. D* 16 (6 Sept. 1977), pp. 1791–1797. DOI: 10.1103/PhysRevD.16.1791. URL: https://link.aps.org/doi/10.1103/PhysRevD.16.1791.

[158] Jorge Pinochet and Michael Van Sint Jan. "Einstein ring: weighing a star with light". In: *Physics Education* 53.5 (Sept. 2018), p. 055003. DOI: 10.1088/1361-6552/aac7b9. arXiv: 1801.00001 [physics.pop-ph].

[159] Ofelia Pisanti et al. "Primordial Deuterium after LUNA: concordances and error budget". In: *JCAP* 04 (2021), p. 020. DOI: 10.1088/1475-7516/2021/04/020. arXiv: 2011.11537 [astro-ph.CO].

[160] P. Popesso et al. "The main sequence of star-forming galaxies across cosmic times". In: 519.1 (Feb. 2023), pp. 1526–1544. DOI: 10.1093/mnras/stac3214. arXiv: 2203.10487 [astro-ph.GA].

[161] Vivian Poulin, Tristan L. Smith, and Tanvi Karwal. "The Ups and Downs of Early Dark Energy solutions to the Hubble tension: a review of models, hints and constraints circa 2023". In: (Feb. 2023). arXiv: 2302.09032 [astro-ph.CO].

[162] Vivian Poulin et al. "Cosmological implications of ultralight axionlike fields". In: *Phys. Rev. D* 98.8 (2018), p. 083525. DOI: 10.1103/PhysRevD.98.083525. arXiv: 1806.10608 [astro-ph.CO].

[163] John Preskill, Mark B. Wise, and Frank Wilczek. "Cosmology of the Invisible Axion". In: *Phys. Lett. B* 120 (1983). Ed. by M. A. Srednicki, pp. 127–132. DOI: 10.1016/0370-2693(83)90637-8.

[164] Darren Reed et al. "The halo mass function from the dark ages through the present day". In: *Mon. Not. Roy. Astron. Soc.* 374 (2007), pp. 2–15. DOI: 10.1111/j.1365-2966.2006.11204.x. arXiv: astro-ph/0607150.

[165] Beth A. Reid et al. "Cosmological constraints from the clustering of the Sloan Digital Sky Survey DR7 luminous red galaxies". In: 404.1 (May 2010), pp. 60–85. DOI: 10.1111/j.1365-2966.2010.16276.x. arXiv: 0907.1659 [astro-ph.CO].

[166] R Michael Rich et al. "The Blanco DECam bulge survey. I. The survey description and early results". In: *Monthly Notices of the Royal Astronomical Society* 499.2 (Aug. 2020), pp. 2340–2356. DOI: 10.1093/mnras/staa2426. URL: https://doi.org/10.1093%2Fmnras%2Fstaa2426.

[167] R. Michael Rich. "The Large Synoptic Survey Telescope and Milky Way Science". In: *Rediscovering Our Galaxy*. Ed. by Cristina Chiappini et al. Vol. 334. IAU Symposium. Aug. 2018, pp. 233–241. DOI: 10.1017/S1743921317009413. arXiv: 1712.02885 [astro-ph.IM].

[168] Keir K. Rogers, Cora Dvorkin, and Hiranya V. Peiris. "Limits on the Light Dark Matter–Proton Cross Section from Cosmic Large-Scale Structure". In: *Phys. Rev. Lett.* 128.17 (2022), p. 171301. DOI: 10.1103/PhysRevLett.128.171301. arXiv: 2111.10386 [astro-ph.CO].

[169] Keir K. Rogers and Hiranya V. Peiris. "Strong Bound on Canonical Ultralight Axion Dark Matter from the Lyman-Alpha Forest". In: *Phys. Rev. Lett.* 126.7 (2021), p. 071302. DOI: 10.1103/PhysRevLett.126.071302. arXiv: 2007.12705 [astro-ph.CO].

[170] Keir K. Rogers and Vivian Poulin. "$5\sigma$ tension between Planck cosmic microwave background and eBOSS Lyman-alpha forest and constraints on physics beyond $\Lambda$CDM". In: (Nov. 2023). arXiv: 2311.16377 [astro-ph.CO].

[171] Keir K. Rogers et al. "Ultra-light axions and the $S_8$ tension: joint constraints from the cosmic microwave background and galaxy clustering". In: *JCAP* 06 (2023), p. 023. DOI: 10.1088/1475-7516/2023/06/023. arXiv: 2301.08361 [astro-ph.CO].

[172] Anton Rudakovskyi et al. "Constraints on warm dark matter from UV luminosity functions of high-z galaxies with Bayesian model comparison". In: *Mon. Not. Roy. Astron. Soc.* 507.2 (2021), pp. 3046–3056. DOI: 10.1093/mnras/stab2333. arXiv: 2104.04481 [astro-ph.CO].

[173] Nashwan Sabti, Julian B. Muñoz, and Diego Blas. "Galaxy luminosity function pipeline for cosmology and astrophysics". In: *Phys. Rev. D* 105.4 (2022), p. 043518. DOI: 10.1103/PhysRevD.105.043518. arXiv: 2110.13168 [astro-ph.CO].

[174] Nashwan Sabti, Julian B. Muñoz, and Diego Blas. "New Roads to the Small-scale Universe: Measurements of the Clustering of Matter with the High-redshift UV Galaxy Luminosity Function". In: *Astrophys. J. Lett.* 928.2 (2022), p. L20. DOI: 10.3847/2041-8213/ac5e9c. arXiv: 2110.13161 [astro-ph.CO].

[175] Nashwan Sabti, Julian B. Muñoz, and Marc Kamionkowski. "Insights from HST into Ultra-massive Galaxies and Early-Universe Cosmology". In: *Phys. Rev. Lett.* 132.6 (2024), p. 061002. DOI: 10.1103/PhysRevLett.132.061002. arXiv: 2305.07049 [astro-ph.CO].

[176] Sedighe Sajadian and Radosław Poleski. "Predictions for the Detection and Characterization of Galactic Disk Microlensing Events by LSST". In: 871.2, 205 (Feb. 2019), p. 205. DOI: 10.3847/1538-4357/aafa1d. arXiv: 1806.06372 [astro-ph.IM].

[177] Sedighe Sajadian and Radosław Poleski. "Predictions for the Detection and Characterization of Galactic Disk Microlensing Events by LSST". In: *The Astrophysical Journal* 871.2 (Feb. 2019), p. 205. DOI: 10.3847/1538-4357/aafa1d. URL: https://doi.org/10.3847%2F1538-4357%2Faafa1d.

[178] Hsi-Yu Schive et al. "Contrasting Galaxy Formation from Quantum Wave Dark Matter, $\psi$DM, with $\Lambda$CDM, using Planck and Hubble Data". In: *Astrophys. J.* 818.1 (2016), p. 89. DOI: 10.3847/0004-637X/818/1/89. arXiv: 1508.04621 [astro-ph.GA].

[179] E. F. Schlafly et al. "The DECam Plane Survey: Optical Photometry of Two Billion Objects in the Southern Galactic Plane". In: *The Astrophysical Journal Supplement Series* 234.2 (Feb. 2018), p. 39. DOI: 10.3847/1538-4365/aaa3e2. URL: https://doi.org/10.3847%2F1538-4365%2Faaa3e2.

[180] Katelin Schutz et al. "Constraining a Thin Dark Matter Disk with Gaia". In: *Phys. Rev. Lett.* 121.8 (2018), p. 081101. DOI: 10.1103/PhysRevLett.121.081101. arXiv: 1711.03103 [astro-ph.GA].

[181] Katelin Schutz et al. "Constraining a Thin Dark Matter Disk withGaia". In: *Physical Review Letters* 121.8 (Aug. 2018). ISSN: 1079-7114. DOI: 10.1103/physrevlett.121.081101. URL: http://dx.doi.org/10.1103/PhysRevLett.121.081101.

[182] Bodo Schwabe et al. "Simulating mixed fuzzy and cold dark matter". In: *Phys. Rev. D* 102.8 (2020), p. 083518. DOI: 10.1103/PhysRevD.102.083518. arXiv: 2007.08256 [astro-ph.CO].

[183] D. M. Scolnic et al. "The Complete Light-curve Sample of Spectroscopically Confirmed SNe Ia from Pan-STARRS1 and Cosmological Constraints from the Combined Pantheon Sample". In: *Astrophys. J.* 859.2 (2018), p. 101. DOI: 10.3847/1538-4357/aab9bb. arXiv: 1710.00845 [astro-ph.CO].

[184] Sanjib Sharma et al. "Galaxia: A Code to Generate a Synthetic Survey of the Milky Way". In: 730.1, 3 (Mar. 2011), p. 3. DOI: 10.1088/0004-637X/730/1/3. arXiv: 1101.3561 [astro-ph.GA].

[185] Xuejian Shen et al. "THESAN-HR: Galaxies in the Epoch of Reionization in warm dark matter, fuzzy dark matter and interacting dark matter". In: (Apr. 2023). arXiv: 2304.06742 [astro-ph.GA].

[186] Ravi K. Sheth and Giuseppe Tormen. "Large scale bias and the peak background split". In: *Mon. Not. Roy. Astron. Soc.* 308 (1999), p. 119. DOI: 10.1046/j.1365-8711.1999.02692.x. arXiv: astro-ph/9901122.

[187] Tatyana Shevchuk, Ely D. Kovetz, and Adi Zitrin. "New Bounds on Fuzzy Dark Matter from Galaxy-Galaxy Strong-Lensing Observations". In: (Aug. 2023). arXiv: 2308.14640 [astro-ph.CO].

[188] J. Skowron et al. "OGLE-2011-BLG-0265Lb: A Jovian Microlensing Planet Orbiting an M Dwarf". In: 804.1, 33 (May 2015), p. 33. DOI: 10.1088/0004-637X/804/1/33. arXiv: 1410.8252 [astro-ph.EP].

[189] J. Skowron et al. "OGLE-2017-BLG-0373Lb: A Jovian Mass-Ratio Planet Exposes A New Accidental Microlensing Degeneracy". In: *Acta Astronomica* 68.1 (Mar. 2018), pp. 43–61. DOI: 10.32023/0001-5237/68.1.2. arXiv: 1802.10067 [astro-ph.EP].

[190] Tristan L. Smith, Vivian Poulin, and Mustafa A. Amin. "Oscillating scalar fields and the Hubble tension: a resolution with novel signatures". In: *Phys. Rev. D* 101.6 (2020), p. 063523. DOI: 10.1103/PhysRevD.101.063523. arXiv: 1908.06995 [astro-ph.CO].

[191] Mimi Song et al. "The Evolution of the Galaxy Stellar Mass Function at z = 4-8: A Steepening Low-mass-end Slope with Increasing Redshift". In: 825.1, 5 (July 2016), p. 5. DOI: 10.3847/0004-637X/825/1/5. arXiv: 1507.05636 [astro-ph.GA].

[192] Mauro Stefanon et al. "Galaxy Stellar Mass Functions from z 10 to z 6 using the Deepest Spitzer/Infrared Array Camera Data: No Significant Evolution in the Stellar-to-halo Mass Ratio of Galaxies in the First Gigayear of Cosmic Time". In: 922.1, 29 (Nov. 2021), p. 29. DOI: 10.3847/1538-4357/ac1bb6. arXiv: 2103.16571 [astro-ph.GA].

[193] Gary Steigman. "CMB constraints on the thermal WIMP mass and annihilation cross section". In: *Phys. Rev. D* 91 (8 Apr. 2015), p. 083538. DOI: 10.1103/PhysRevD.91.083538. URL: https://link.aps.org/doi/10.1103/PhysRevD.91.083538.

[194] Guochao Sun et al. "Bursty Star Formation Naturally Explains the Abundance of Bright Galaxies at Cosmic Dawn". In: 955.2, L35 (Oct. 2023), p. L35. DOI: 10.3847/2041-8213/acf85a. arXiv: 2307.15305 [astro-ph.GA].

[195] Peter Svrcek and Edward Witten. "Axions In String Theory". In: *JHEP* 06 (2006), p. 051. DOI: 10.1088/1126-6708/2006/06/051. arXiv: hep-th/0605206.

[196] Max Tegmark and Matias Zaldarriaga. "Separating the early universe from the late universe: Cosmological parameter estimation beyond the black box". In: *Phys. Rev. D* 66 (2002), p. 103508. DOI: 10.1103/PhysRevD.66.103508. arXiv: astro-ph/0207047.

[197] Max Tegmark and Matias Zaldarriaga. "The Fast Fourier Transform Telescope". In: *Phys. Rev. D* 79 (2009), p. 083530. DOI: 10.1103/PhysRevD.79.083530. arXiv: 0805.4414 [astro-ph].

[198] Tisserand et al. "Limits on the Macho content of the Galactic Halo from the EROS-2 Survey of the Magellanic Clouds ***". In: *A&A* 469.2 (2007), pp. 387–404. DOI: 10.1051/0004-6361:20066017. URL: https://doi.org/10.1051/0004-6361:20066017.

[199] I.I. Tkachev. "On the possibility of Bose star formation". In: *Phys.Lett.B* 261 (1991), pp. 289–293. DOI: 10.1016/0370-2693(91)90330-S.

[200] L. Arturo Ureña-López. "Scalar field dark matter with a cosh potential, revisited". In: (2019). arXiv: 1904.03318 [astro-ph.CO].

[201] Matteo Viel et al. "Warm dark matter as a solution to the small scale crisis: New constraints from high redshift Lyman-$\alpha$ forest data". In: *Phys. Rev. D* 88 (2013), p. 043502. DOI: 10.1103/PhysRevD.88.043502. arXiv: 1306.2314 [astro-ph.CO].

[202] Mark Vogelsberger et al. "High-redshift JWST predictions from IllustrisTNG: dust modelling and galaxy luminosity functions". In: 492.4 (Mar. 2020), pp. 5167–5201. DOI: 10.1093/mnras/staa137. arXiv: 1904.07238 [astro-ph.GA].

[203] Sophie M. L. Vogt, David J. E. Marsh, and Alex Laguë. "Improved mixed dark matter halo model for ultralight axions". In: *Phys. Rev. D* 107.6 (2023), p. 063526. DOI: 10.1103/PhysRevD.107.063526. arXiv: 2209.13445 [astro-ph.CO].

[204] Christopher Wegg, Ortwin Gerhard, and Matthieu Portail. "MOA-II Galactic microlensing constraints: the inner Milky Way has a low dark matter fraction and a near maximal disc". In: 463.1 (Nov. 2016), pp. 557–570. DOI: 10.1093/mnras/stw1954. arXiv: 1607.06462 [astro-ph.GA].

[205] Steven Weinberg. "A New Light Boson?" In: *Phys. Rev. Lett.* 40 (4 Jan. 1978), pp. 223–226. DOI: 10.1103/PhysRevLett.40.223. URL: https://link.aps.org/doi/10.1103/PhysRevLett.40.223.

[206] Frank Wilczek. "Problem of Strong $P$ and $T$ Invariance in the Presence of Instantons". In: *Phys. Rev. Lett.* 40 (1978), pp. 279–282. DOI: 10.1103/PhysRevLett.40.279.

[207] Harrison Winch. "LSST Microlensing Sensitivity Prediction Code". In: *https://github.com/HarrisonWinch96/Dark* (Dec. 2020).

[208] Harrison Winch et al. "Extreme Axions Unveiled: a Novel Fluid Approach for Cosmological Modeling". In: (Nov. 2023). arXiv: 2311.02052 [astro-ph.CO].

[209] Harrison Winch et al. "High-redshift, small-scale tests of ultralight axion dark matter using Hubble and Webb galaxy UV luminosities". In: (Apr. 2024). arXiv: 2404.11071 [astro-ph.CO].

[210] Harrison Winch et al. "Using LSST Microlensing to Constrain Dark Compact Objects in Spherical and Disk Configurations". In: *The Astrophysical Journal* 933.2 (July 2022), p. 177. DOI: 10.3847/1538-4357/ac7467. URL: https://dx.doi.org/10.3847/1538-4357/ac7467.

[211] L. Wyrzykowski et al. "Black hole, neutron star and white dwarf candidates from microlensing with OGLE-III". In: *Monthly Notices of the Royal Astronomical Society* 458.3 (Feb. 2016), pp. 3012–3026. ISSN: 1365-2966. DOI: 10.1093/mnras/stw426. URL: http://dx.doi.org/10.1093/mnras/stw426.

[212] L. Wyrzykowski et al. "The OGLE view of microlensing towards the Magellanic Clouds – I. A trickle of events in the OGLE-II LMC data*". In: *Monthly Notices of the Royal Astronomical Society* 397.3 (July 2009), pp. 1228–1242. ISSN: 0035-8711. DOI: 10.1111/j.1365-2966.2009.15029.x. eprint: https://academic.oup.com/mnras/article-pdf/397/3/1228/3723741/mnras0397-1228.pdf. URL: https://doi.org/10.1111/j.1365-2966.2009.15029.x.

[213] Haojing Yan et al. "First Batch of z ≈ 11-20 Candidate Objects Revealed by the James Webb Space Telescope Early Release Observations on SMACS 0723-73". In: 942.1, L9 (Jan. 2023), p. L9. DOI: 10.3847/2041-8213/aca80c. arXiv: 2207.11558 [astro-ph.GA].

[214] Xiao-hu Yang, H. J. Mo, and Frank C. van den Bosch. "Constraining galaxy formation and cosmology with the conditional luminosity function of galaxies". In: *Mon. Not. Roy. Astron. Soc.* 339 (2003), p. 1057. DOI: 10.1046/j.1365-8711.2003.06254.x. arXiv: astro-ph/0207019.

[215] Jorge A. Zavala et al. "Dusty Starbursts Masquerading as Ultra-high Redshift Galaxies in JWST CEERS Observations". In: 943.2, L9 (Feb. 2023), p. L9. DOI: 10.3847/2041-8213/acacfe. arXiv: 2208.01816 [astro-ph.GA].

[216] Ui-Han Zhang and Tzihong Chiueh. "Cosmological Perturbations of Extreme Axion in the Radiation Era". In: *Phys. Rev. D* 96.6 (2017), p. 063522. DOI: 10.1103/PhysRevD.96.063522. arXiv: 1705.01439 [astro-ph.CO].

[217] Ui-Han Zhang and Tzihong Chiueh. "Evolution of linear wave dark matter perturbations in the radiation-dominated era". In: *Phys. Rev.* D96.2 (2017), p. 023507. DOI: 10.1103/PhysRevD.96.023507. arXiv: 1702.07065 [astro-ph.CO].